A STUDY ON MATERIALS IN ENERGY SCIENCE USING MICROFLUIDICS WITH *IN SITU* RAMAN SPECTROSCOPY

DISSERTATION

Submitted in Partial Fulfillment of

the Requirements for

the Degree of

DOCTOR OF PHILOSOPHY (Materials Chemistry)

at the

NEW YORK UNIVERSITY
TANDON SCHOOL OF ENGINEERING

by

Weiqi Chen

September 2019

Approved:

_____
Department Chair Signature

8/26/2019
_____
Date

ProQuest Number: 22619886

ProQuest 22619886

Approved by the Guidance Committee:

Major: Materials Chemistry
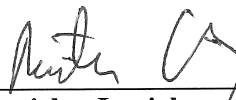
Ryan L. Hartman
Associate Professor
Department of Chemical and
Biomolecular Engineering

8/12/2019
Date

Rastislav Levicky
Professor
Department of Chemical and
Biomolecular Engineering

8/12/2019
Date

Iwao Teraoka
Professor
Department of Chemical and
Biomolecular Engineering

8-12-2019
Date

Michael D. Ward
Silver Chair Professor of Chemistry
Department of Chemistry

08/12/2019
Date

Microfilm or copies of this dissertation may be obtained from:

Vita

In the year of 1991, Weiqi Chen (陈玮琪) was born in Xiamen, China, to Shunshui Chen (陈顺水) and Meigan Chen (陈美柑). In 2013, he received a B.S. in Material Chemistry from the Department of Chemistry at Nankai University in Tianjin, China. From October 2012 to June 2013, he conducted research on Energy Storage by Microporous Materials as an undergraduate researcher advised by Professor Niu Li in National Key Laboratory of Advanced Energy Material, China. From June 2014 to Aug 2014, he engaged in research on Synthesis of Graphene Materials through Chemical Methods as a research technician in Xiamen G-CVD Graphene Technology Co., Ltd. In 2015, he completed his master program and was granted the M.S. in Materials Science and Engineering from Herbert Wertheim College of Engineering at the University of Florida in Gainesville, Florida. In 2015, he was admitted into the Doctoral Program in Materials Chemistry at the Chemical and Biomolecular Engineering Department in NYU Tandon School of Engineering in Brooklyn, New York. In September 2015, he joined the Flow Chemistry with Microsystems Laboratory led by Professor Ryan L. Hartman and continued his thesis research throughout his doctoral program. From September 2015 to August 2018, he conducted the research on Crystallization and Dissolution Kinetics Study of Methane Hydrate in Microfluidic Reactor, funded by the MRSEC Program of the National Science Foundation under Award Number DMR-1420073. Since April 2017, he engaged in the Joint Industry Project and conducted the research on Mechanistic Study of Asphaltenes Deposition and Dissolution Processes by Microfluidic System. The project and himself were funded by Anadarko Petroleum Corporation, and Nalco Champion, an Ecolab Company.

Acknowledgement

My four-year experience in Brooklyn has been saturated with love, joyful and happy memories. I would like to sincerely thank my advisor Dr. Ryan L. Hartman for the opportunity of becoming a member in Flow Chemistry with Microsystems Laboratory. Throughout the whole Ph.D. study, he continuously supports me with motivation, guidance, patience, wisdom, and trust. His enthusiasm, self-discipline, and integrity have made a deep impression on me. I am truly grateful to have Dr. Hartman as my advisor.

My special thanks to my thesis committee members: Dr. Michael Ward, Dr. Rastislav Levicky, and Dr. Iwao Teraoka for their insightful comments and encouragement to keep me on track. Their wide-ranging knowledge has guided me to think and reflect on questions from various perspectives. I feel privileged to have associated with them in my life.

My special thanks to NYU MRSEC for funding and supporting of methane hydrate project, and Anadarko Petroleum Cooperation and Nalco Champion, an Ecolab company for funding and supporting of asphaltenes project. I express my deep gratitude to Dr. Yogesh Kapoor, Dr. Nikhil Joshi from Anadarko Petroleum Cooperation and Dr. Andrew Yen, Dr. Christopher Russell, Dr. Priyanka Juyal from Nalco Champion, an Ecolab company for the constant support and making this work possible. Their kindness of sharing their extensive industry experience and knowledge has brought the practical impacts to this work. I would like to extend my special thanks to Dr. Andrew Yen and Dr. Yogesh Kapoor for the help with hydrocarbon samples and fruitful discussion on the project.

My special acknowledges to the Advanced Science Research Center Nanofabrication facility of the Graduate Center at the City University of New York, and the Singh Center

v

for Nanotechnology at University of Pennsylvania. The powerful nanofabrication facility and helpful staff members ease the process of the sophisticated fabrication of our designed microfluidics devices.

My warmest thanks to my mentors Dr. Chuntian Hu and Dr. Bruno Pinho for their patience and tolerance towards my annoying questions. In the meantime, they have taught me how to become an independent researcher and how to maintain a healthy and productive Ph.D. life. I would like to acknowledge Priyangi Vashistha and Tony Guo for their dedication and contribution to the asphaltenes project. I would like to extend my special thanks to Tianyi Hua, Benjamin Rizkin, Yukun Liu and Filip Popovic for the invaluable discussion; to Jasmine Sabio for her precious helps with microreactor fabrication. My warmest thanks to the rest of my fellow lab mates for bearing with me through the good time and bad time during my Ph.D. study.

My greatest gratitude to my beloved family for their love and faith. They cheer for my every little achievement and support my every little decision. The strength they give me makes me feel safe and drives me forward, even though we are tens of thousands of miles apart.

Last but not least, to the love of my life, Yao Wang, who has enlightened my life and brought joys and troubles, trusts me with her life and makes sure that I don't have personal time: Thank you for being my sunshine, my muse, my cheerleader, my launderer, my chef, and my boss. But most of all, thank you for being with me, I love you.

To my wife, Yao Wang

ABSTRACT

A STUDY ON MATERIALS IN ENERGY SCIENCE USING MICROFLUIDICS WITH *IN SITU* RAMAN SPECTROSCOPY

by

Weiqi Chen

Advisor: Prof. Ryan L. Hartman, Ph.D.

Submitted in Partial Fulfillment of the Requirements for

the Degree of Doctor of Philosophy (Materials Chemistry)

September 2019

Energy is an integrated part of modern civilization of human. Despite the soaring development of renewable energy, the reliance on fossil fuel energy will last for decades. Flow assurance problem in the petroleum industry, caused by the phase transition, becomes increasingly important as light crude oil is draining. However, the complex chemical environment, composition, and operation conditions of wellbore and pipeline region make it a challenging problem to study, especially in traditional experimental setup without *in situ* characterization. In response, three microsystems integrated with *in situ* Raman spectroscopy are utilized to provide a gateway to understand the complex phase behaviors of two notorious materials: methane gas hydrate and asphaltenes. The sequential chapters are organized by different materials and microfluidic systems. Chapter 1 provides the introduction to the field of gas hydrate, asphaltenes, and microfluidics. Chapter 2& 3 covers the kinetics research on methane hydrate crystallization and dissociation, respectively. Chapter 4 presents the mechanistic study on asphaltenes dissolution by the aromatic solvent in porous media, while Chapter 5 introduces a novel automated microsystem for asphaltenes study. The thesis is concluded by providing conclusions and future development in Chapter 6.

Table of Content

Chapter 1

From fossil fuels to microfluidic – Introduction and background

Chapter 2

Crystallization Kinetics Study of Methane (sI) Hydrate in A Thermoelectrically-cooled Microreactor

Chapter 3

Methane Hydrate Intrinsic Dissociation Kinetics Measured in A Microfluidic System by Means of *in-Situ* Raman Spectroscopy

Chapter 4

Dissolution Mechanism Study of Asphaltenes in Porous Media with Presence of H-ZSM 5 Aluminosilicates by Using in-Situ Raman Spectroscopy in Microfluidic System

Chapter 5

An Automated Microfluidic System for the Investigation of Asphaltenes Deposition and Dissolution in Porous Media

Chapter 6

Conclusion and Future Development

Appendix A

Dissociation kinetics calculated based on equilibrium reaction and mass transfer rate

Appendix B

Pressure drop measurement of asphaltenes deposition in porous media, validation of bed occupancy and sheet size measurement, characterization of asphaltenes samples

Appendix C

Fabrication and characterization of AUTO^3-μPBR, distribution of bed occupancy and sheet size at different regions

Appendix D

MATLAB codes

List of Figures

xxii

xxiii

xxiv

xxviii

Chapter 1

From fossil fuels to microfluidic –

Introduction and background

1.1 Hydrocarbon energy resource and flow assurance

Energy has been a predominant driving force behind the development of human civilization as we know it. During the agrarian era, wood served as a major fuel to provide warmth and sustenance for humans to survive. When James Watt improved the steam engine in 1776, which led to Industrial Revolution later, wood or coal were used to power the steam engine. However, coal soon became the preferred fuel as it was cheaper to produce and easier to distribute, in addition to having a higher energy density. The environmental concerns on air pollution by burning coal and invention of new technologies urged a shift in energy sources from coal to oil. As the gusher of Spindletop first blew into the air, humans entered into the new oil economy. The electric light bulb and automobile industry drove the increasing demand for oil. During World War I, oil played a major role in fueling military vehicles and became a critical military asset. Prior to the 1920s, the natural gas was considered as a waste by-product of oil production and flared on-site. Soon people realized the value of natural gas and began to use them it as a fuel source for industrial and residential heating and power. The three most important fossil fuels in human history enlightened the development of human society and drove innovation in innumerable other fields.

As the development of human society continues to soar exponentially, the demand for energy has been rising for years. From 1820 to 2010, the world energy consumption was estimated to increase at least 25 times. This increase is highly correlated with the growth of world population and is expected to continue for at least several more decades. According to the U.S. Energy Information Administration's latest International Energy Outlook 2019 (IEO 2019), the world energy consumption is projected to grow by 28%

(a)

Energy consumption by energy source in Unite State (2018)
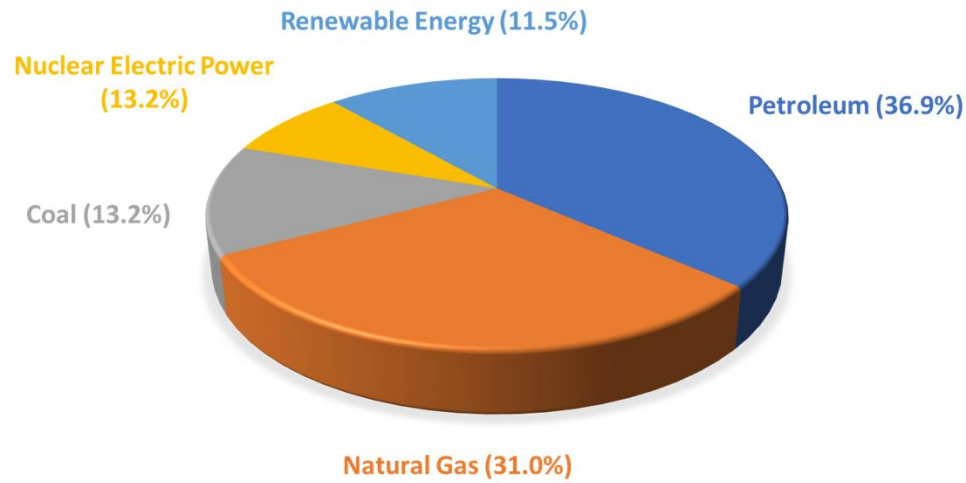
(b)
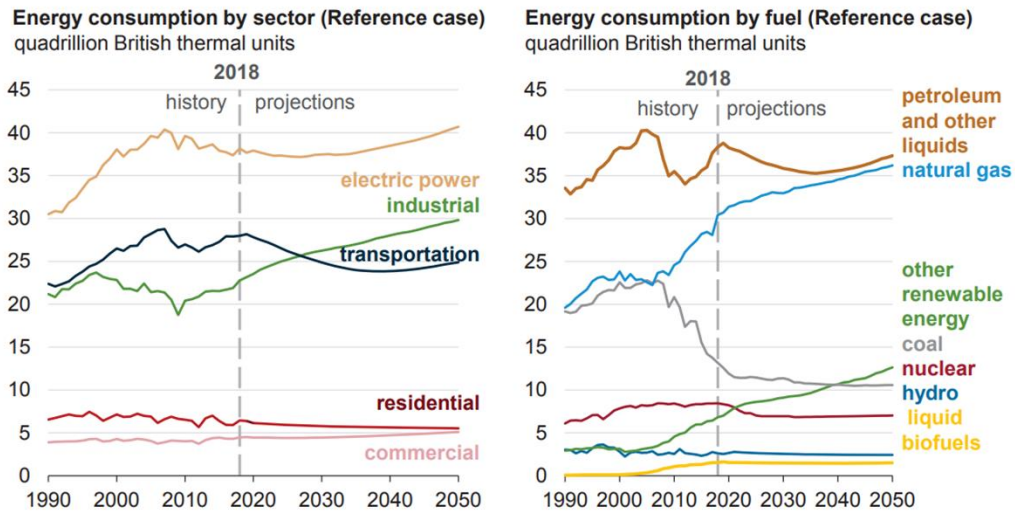
Figure 1.1 (a) Energy consumption by energy source in Unite State in 2018. Fossil fuels contribute 81.1 % of total energy consumption. (b) Left: Energy consumption by sector in Unite State from 1990 to 2050 (predicted). Right: Energy consumption by fuel in Unite State from 1990 to 2050 (predicted).[1]

between 2015 and 2050.[1] Despite the enormous development in the renewal and clean energy, we will still reply on hydrocarbon energy sources, mainly the fossil fuels, for quite

a long time due to the economic efficiency. As shown in Figure 1.1 (a), in 2018, 81.1 % of energy consumption in U.S. was came from fossil fuels: 36.9 % petroleum, 31.0 % natural gas, and 13.2 % coal. This reliance on hydrocarbon energy source is expected to exist at least till 2050 as shown in Figure 1.1 (b), according to EIA's report.[1]

However, the easy-to-access hydrocarbon resource have already been depleted, which has triggered the desire for exploitation of the remainder, for instance, heavy oil and bitumen.[2] The requirement of sophisticated technologies for the exploitation of these energy resources increases to an unprecedent level. Subsea engineering is one of the breakthrough technologies besides horizontal drilling and hydraulic fracturing, which enables the deepwater production of oil and gas. Offshore facilities for oil and gas involve tremendous costs, easily in excess of US $ 1 billion. The wells and flowlines comprise 39% and 38% of the total cost, respectively.[3,4] Thereby, the failure of operation could lead to devastating economic impacts to the project. Flow assurance, a term developed since around 1995, is the major concern as it could have severe impacts on profit and safety during the offshore oil and gas production. It refers to the successful flow of hydrocarbon stream from reservoir to the point of sale, which involved the elimination of blockage formation in pipelines. The complex crude oil phases transition due to changes of conditions in the upstream portion of the petroleum supply chain could be problematic and lead to failure of flow assurance. The phase transition of crude oil results in formation of solid deposits like gas hydrate, asphaltenes, wax, organic scale, and diamonoids.[5] (see Figure 1.2) The inappropriate handling of these solid precipitants could lead to economic loss and serious safety issues, for instance, fracturing of pipes due to improper dissociation of gas hydrate by one-side depressurization. It is these safety and economic reasons that

- 4 -
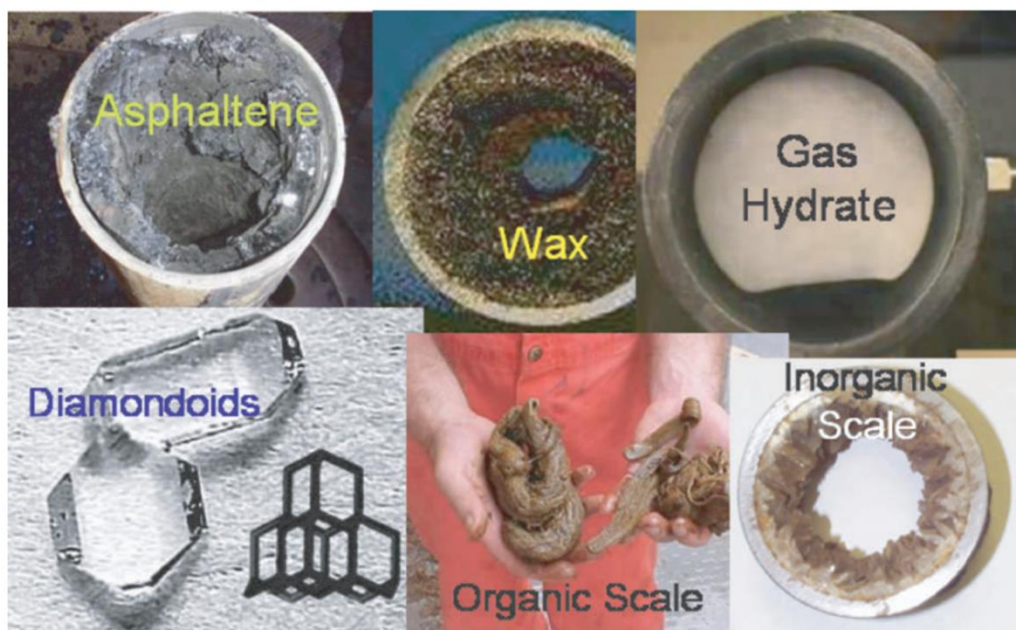
Figure 1.2 Various solids materials that obstruct oil pipelines.[5]

triggered us to study the two of the most common solids materials in petroleum science: gas hydrate and asphaltenes.

1.2 Gas hydrate, a promising crystalline material

Gas hydrate, or clathrate hydrates, are crystalline solid materials with a structure resembling hexagonal ice (Ih). In gas hydrate structure, a 'cage' formed by H-bonded water cluster (host) entraps small guest molecules. Depending on the fit of guest molecule within the water cage, gas hydrate could form different structures: sI through sVII, sT and sH. Among these structures, sI, sII and sH are the most common structures as shown in Figure 1.3.[6,7] When the guest molecules are natural gas, the crystalline solids are named natural gas hydrate. The most common natural gas hydrate are methane, ethane, propane, and carbon dioxide hydrate. The history of gas hydrate could be dated back to 1810, when Sir
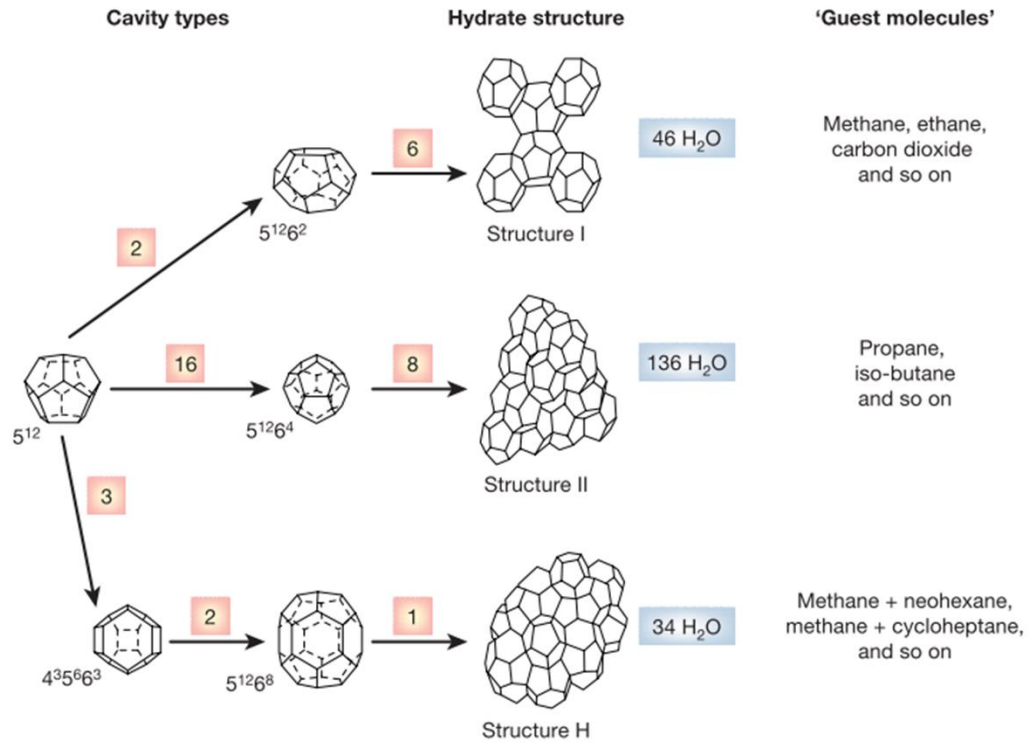
Figure 1.3 Three common clathrate hydrate unit crystal structures.[6]

Humphrey Davy discovered chlorine hydrate. By the time, the study of gas hydrate was only treated as the satisfaction of a scientific curiosity. The second milestone of gas hydrate was in 1934, when Hammerschmidt identified the hydrates as the cause of pipeline plugs in the petroleum industry. Since then, there has been a continued industrial interest to research on this 'problematic' materials.

As offshore oil exploration plays an increasing role in the industry these days, deepwater flow assurance is a major technical problem in the field. Formation of hydrate is the top deepwater flow assurance problem.[4] In the mid-1960s, the discovery of gas hydrate in deep oceans, permafrost regions and in extraterrestrial environments started a new era of gas hydrate study. Figure 1.4 indicates the influence of these two incidents as driving forces to stimulate the research interests in this area. Nowadays, it is believed that even with the
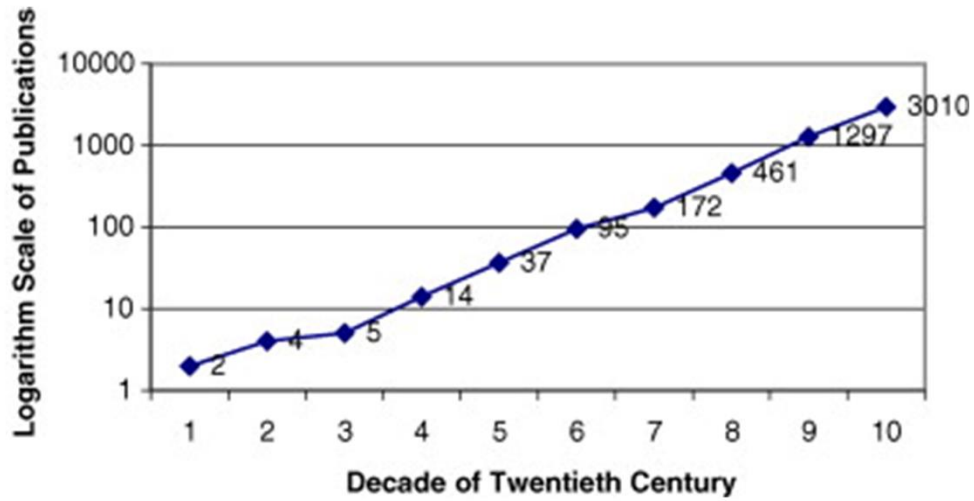
Figure 1.4 Number of hydrate-related publication by decade in the 20th century.[4]

most conservative estimation, the amount of energy stored in the natural gas hydrates is at

least twice that of all other fossil fuels combined.[7] Figure 1.5 shows the broad distribution

of natural gas hydrate in the nature. Although methane hydrate only contains 42% of the

energy density of liquefied methane, it has an energy density equivalent to compressed gas
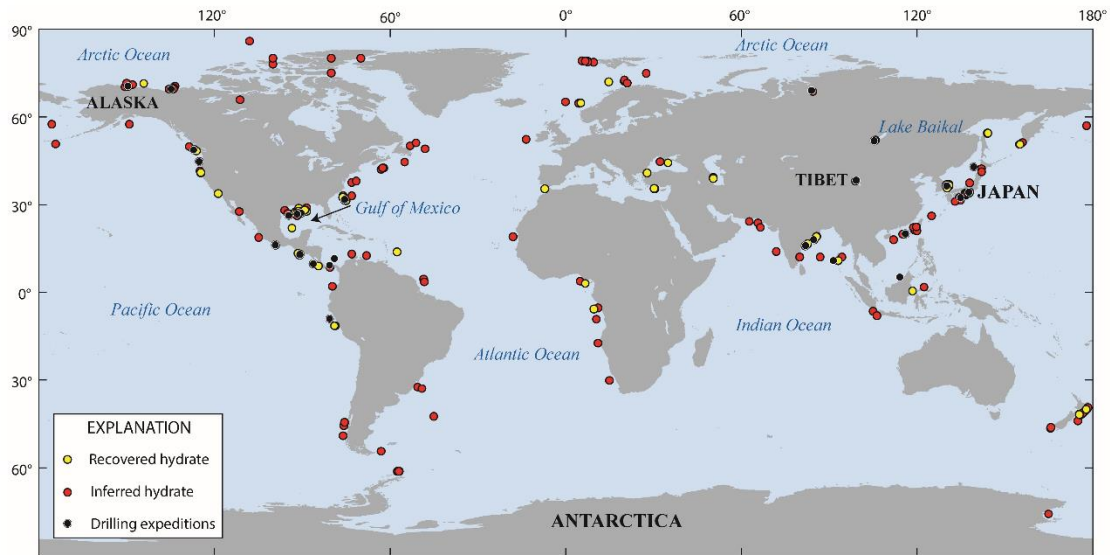
Figure 1.5 Global distribution of natural gas hydrate. (from USGS)

(e.g. at 18 MPa at room temperature). This excellent energy density makes hydrates a promising material for gas storage and transportation. To realize the potential of this promising material, a thorough understanding of its thermodynamic and kinetic behavior through *in-situ* study is rather important.

The comprehensive understanding of thermodynamic properties of gas hydrates is the most basic yet powerful knowledge in the gas hydrate research. In practice, there are only eight natural gas components in industry, but these form countless mixtures with different compositions. Although it might be possible to experimentally measure the phase transition boundary of gas hydrate, it requires tremendous amounts of efforts and resources to accomplish and could be inaccurate, considering the results are sensitive to experimental conditions. Therefore, accurate thermodynamic models not only provide an understanding of time-independent properties of gas hydrate, but also have wide use in industry. In 1957, van der Waals and Platteeuw used the statistical thermodynamics method to link the microscopic and macroscopic properties.[8] This method laid the foundation of the method currently used. Since then, there were many efforts investing an improvement of the accuracy of these models. Focus has been mainly on refinement of chemical potentials through considering different factors, such as different potential models,[9,10] presence of oil,[11] or lattice distortion.[12,13] Several programs were developed and commercialized for the prediction of hydrate properties. The average absolute errors in temperature for five of the most common programs vary from 0.40 to 0.66 K, which could satisfy most engineering purposes.[6] However, it has been shown in some cases of industrial practice that the risk management is a more economical method than avoidance of gas hydrate formation.[4] The

former method deals with time-dependent properties of gas hydrate, while the latter one is based on thermodynamics.

Since mid-1990s, there has been a significant increase in the amount of effort dedicated to the kinetic study of gas hydrates at different scales with diverse techniques. Macroscopic measurement, including gas consumption rate measurement, particle size measurement by light scattering,[14–18] and differential scanning calorimetry measurement (DSC), have been first to applied to the kinetic study. There methods could provide quantitative information about the process but with limited insights on microscopic properties. The imaging techniques, such as scanning electron microscopy (SEM),[19,20] magnetic resonance imaging (MRI),[21] and X-ray computed tomography (CT),[22] have been applied to track and obtain spatial, time-resolved images during hydrate formation or dissociation. Coupled with image analysis, one could readily obtain the necessary quantitative information from mesoscale observations. Time-resolved microscopic measurement utilized the most sophisticated experimental techniques and is usually accompanied by complicated deconvolution processes. The reward of these methods however is the priceless *in situ* information on molecule scale, such as crystal structure. Neutron diffraction,[23–25] X-ray diffraction,[26] nuclear magnetic resonance (NMR),[27,28] and Raman spectroscopy have been applied to the field.[29,30] Thanks to the exponential improvement in the computation capability, computer simulations provide a whole new methodology to approach the traditional scientific and engineering problem, which are also being applied to study the early stage of hydrate formation and different effects on hydrate dissociation kinetics.[31,32] Although these studies obtain great achievements towards the understanding of time-dependent properties of gas hydrate, there are still some limitations in the study.

- 9 -

Unlike the time-independent properties, the kinetics studies of gas hydrate formation and dissociation are more challenging and possess higher requirements for system design. In the laboratory scale, it is common practice to use the magnetic stirring bar to improve the mixing properties of system. This simple yet effective mixing method works well for homogeneous reaction but fails to provide adequate mixing with heterogeneous phases such as gas hydrates. In addition, stainless steel has poor thermal conductivity. During intrinsic kinetic studies, it is hard or even impossible to eliminate the heat transfer and mass transfer resistance. Therefore, almost every kinetics study should be considered as a transient process where both intrinsic kinetics and transport properties play roles. Unfortunately, even at laboratory scale, the temperature profiles for most experimental setups are unpredictable. These are the major reasons why the kinetic data and models are often dependent on the experimental setup. Accurate data acquired from a well-controled system is needed for the development of comprehensive kinetics models.

1.3 Asphaltenes, a useful but problematic material

Asphaltenes, the most aromatic portion of heavy oil, are notorious for high viscosity, low stability, and low distillate yields. The history of asphaltenes could be dated back to 1837, when Boussingault noticed the distillation residue of some bitumens had asphalt-like properties in eastern France and Peru. He then coined the word "asphaltenes". Although asphaltene could be used in road construction, waterproofing, and roofing, they are mostly considered as problematic for their tendency to cause formation damage, which refers to the reduction in permeability during petroleum production processes. The deposition of asphaltenes could happen in multiple facilities and equipment types: the wellbore area, in production tubing, flowlines, separators, pumps, tanks, and other safety handling

equipment. The impairment in the permeability adversely influences the transportation of crude oil and results in production rate decline, undesired economical loss, and even health, safety and environment issues. The heavy crude oils with high content of asphaltenes are common in worldwide production as light crude oils are depleting. Locations reported to have high asphaltenes content containing crude oils include the southern and central regions of Alberta, the Norwegian sector of the North Sea, West Texas and Alaska, Saudi Arabia, and the southern producing regions of Mexico. The regions presented to have the most serious problems with asphaltenes deposition include the oilfields of Venezuela, the Persian Gulf, the Adriatic Sea, and the U.S. Gulf of Mexico.[33] As the heavy crude oil plays an increasingly important role in the petroleum market, the flow assurance problems caused by asphaltene precipitation and deposition will be critical to the industry in the years to come.

In reality, the complexity of asphaltenes' composition and structure made it difficult to resolve the problem with single solution. The widely accepted definition of asphaltenes is based on its solubility: the portion of crude oil that is soluble in aromatic solvent (e.g. toluene, xylenes) and insoluble in alkaline solvent (e.g. n-heptane). Figure 1.6 shows a typical definition of SARA (saturate, aromatic, resin, asphaltenes) composition of crude oil. This broad definition requires the understanding of asphaltenes molecules should not be limited to a simple chemical structure. Despite the broad variance in molecular structure, asphaltenes molecules share some common chemical features. The most important feature of asphaltenes molecules' chemical structure is the presence of the aromatic polycyclic clusters cores. These aromatic cores make the asphaltenes molecules soluble in aromatic solvent. Although there are some debates on whether the archipelago or the island structure
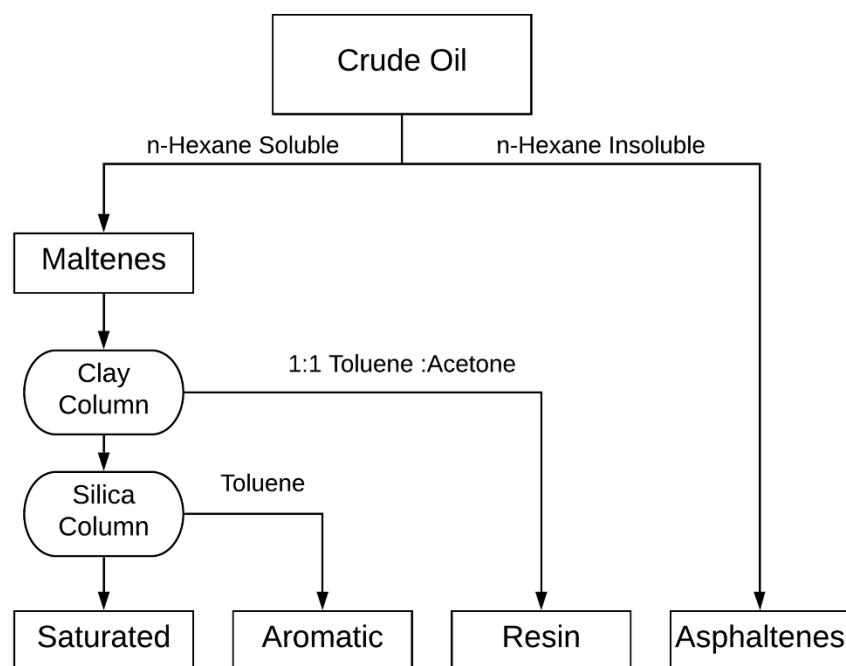
Figure 1.6 Saturated, aromatic, resin, and asphaltenes (SARA) analysis based on ASTM D2007 standard.

of asphaltenes is more properly representative, the atomic force microscopy of single asphaltenes molecule deciphers that most asphaltenes have island structure.[34] In addition, asphaltenes molecules contain heteroatoms (e.g. N, O, S), which constitute different functional groups in structure. Besides that, a trace amount of metals (e.g. V, Fe, Ni) could lead to the complex structure of asphaltenes molecules.[34] These elements lead to at least five different types of interactions between asphaltenes molecules: acid-basic interaction, hydrogen bonding interaction, π-π stacking interaction, Van der Waals interaction and chelation interaction.[35] Furthermore, it is widely reported that the asphaltenes properties are different depending the source or origin. The asphaltenes molecules collected from coal have small alkane fraction and small ring systems, while the ones collected from oil have

large alkane fraction and large ring systems.[36–38] The asphaltenes collected from different geological sites could have different critical nanoaggregation concentrations.[39–41] This diversity of asphaltenes molecules further complicates asphaltene research by requiring researchers to consider each case study individually. Last but not least, the complex environment in the reservoirs and production tubing results in multiple parameters needed to be considered during the deposition and precipitation of asphaltenes. For example, changes in pressure, temperature, and composition in the crude oil could all lead to asphaltenes deposition or impairment.

The wellbore area is where the most frequent deposition happens resulting in a potential production loss.[42] There are at least three pathways via which the deposition of asphaltenes in the rock texture could result in formation damage: 1) reducing pore cross-section area and blocking pore throats; 2) alternating the surface chemistry of rock and changing the wettability; 3) stabilizing water-in-oil emulsions and decreasing the mobility of hydrocarbon compounds.[33] Therefore, these are the main focuses of asphaltenes study in the field-scale and laboratory-scale investigations. From an economic point of view, it is desirable to prevent formation damage from the beginning, such as maintaining the operating pressure above the asphaltenes onset pressure (AOP) and usage of asphaltenes inhibitors, rather than to applying remediation methodology after deposition occurs. Several field studies have shown that the prevention methods can be less expensive and more efficient than remediation procedures.[33] However, as we stated in the beginning of the chapter, it could be challenging to avoid all the solids from precipitation as they have different phase behaviors. Therefore, remediation of formation damage caused by asphaltene deposition cannot be avoided. Regardless, the development of both prevention

and remediation strategy relies on the understanding of asphaltene deposition onto the porous media, which could be obtained through laboratory research.

It is generally accepted that the two mechanisms govern the deposition of asphaltenes onto the porous media: adsorption mechanism and hydrodynamic bridging mechanism.[43] (see Figure 1.7) The adsorption mechanism describes the asphaltenes deposition onto the surface of substrates through formation of an adsorption layer. The hydrodynamic bridging mechanism, or mechanical entrapment mechanism, states the large asphaltenes aggregate particles could cause the clogging of pore throats. Therefore, extensive research efforts and
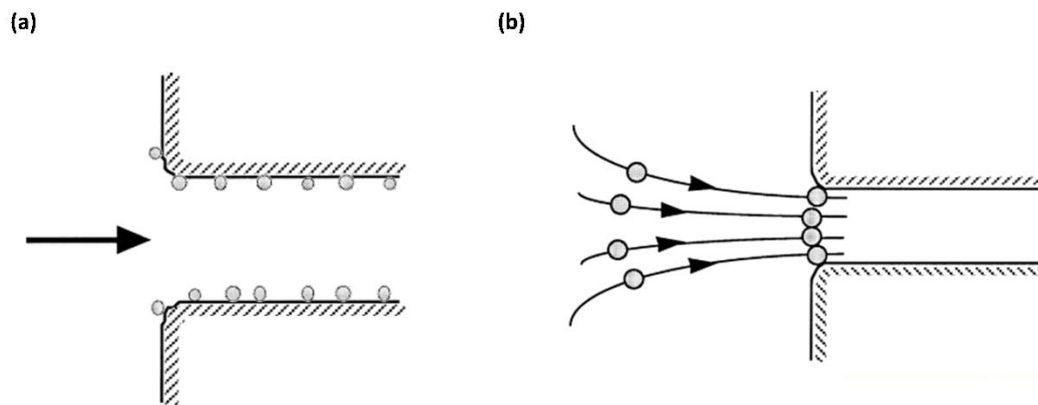
Figure 1.7 Two mechanisms of deposition onto porous media: (a) adsorption, and (b) hydrodynamic bridging.[42]

resources have been applied to study the adsorption of asphaltenes onto surfaces and asphaltenes aggregation phenomenon.[44–47] The common surfaces used for the study of asphaltenes adsorption include 1) metal materials, such as stainless steel, gold, aluminum etc.[48,49]; 2) mineral materials, such as clay, quartz, sandstones, alumino-silicate et al.[50–57]; (3) inorganic sorbent, such as metal oxides et al.[58–62]; (4) typical soil.[63] The asphaltenes in

toluene solution or mixtures with n-heptane are the typical model oil for adsorption study. The major technique for determining the adsorption of asphaltenes is UV-Vis spectroscopy, which could estimate the amount of deposited asphaltenes through comparing the absorbance difference before and after adsorption.[61,64–67] In the meantime, other techniques being applied to adsorption study of asphaltenes include quartz crystal microbalances (QCM),[49,68,69] Near-Infrared or Fourier transform infrared (FT-IR) spectroscopy,[70] atomic force microscopy (AFM),[50,55] contact angle measurement,[52,71] and so on. These adsorption studies have revealed the importance of intermolecular interactions between asphaltenes molecules and surface materials, which mainly depend on the structure characteristic of the molecules.[46] These studies could also benefit the practical application of the absorbents for asphaltenes elimination from crude oils.

The study on asphaltenes aggregation, however, contributes more toward the fundamental knowledge of the process. A modified Yen model, or Yen-Mullins model, of asphaltenes aggregation is now widely accepted as it dictates the behaviors of asphaltenes and matches well with the experimental results.[44,72,73] Figure 1.8 shows the hierarchy architecture of asphaltenes aggregation: molecules, nanoaggregates, and cluster. Critical nanoaggregate concentration (CNAC) is one of the important parameters for the aggregation process, above which the nanoaggregation happens and properties of the fluid change, such as absorption characteristics and interfacial properties. Different techniques have been utilized to characterize the formation of the asphaltene aggregates, including small-angle X-ray scattering (SAXS),[74,75] small-angle neutron scattering (SANS),[76–78] NMR,[79–81] near-infrared (NIR) spectroscopy,[82–84], light scattering,[85,86] and microscopy methods such as scanning electron microscopy (SEM),[87,88] tunneling electron microscopy
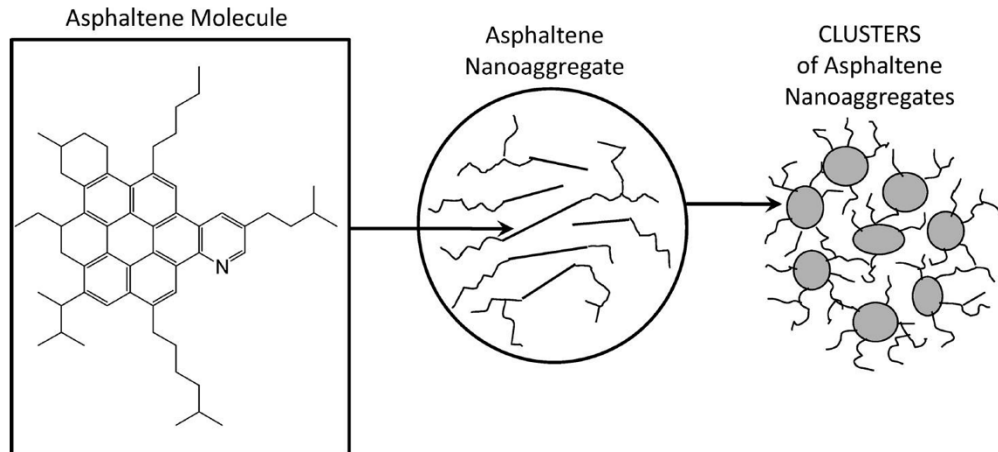
Figure 1.8 Modified Yen model of asphaltenes aggregates. [71]

(TEM),[87,89,90] atomic force microscopy (AFM).[91] These studies have confirmed that the asphaltenes' aggregation behaviors and structures are dependent on the material source, solvent types and thermodynamic conditions.

Research about asphaltene adsorption, aggregation, and emulsion all contribute to a deeper understanding of asphaltene phase behaviors under different conditions. To correlate laboratory knowledge to field practice, an asphaltenes deposition study under flow conditions should be applied. Capillary tests are the most common model system for asphaltene deposition studies.[92–96] Stainless steel capillary tubes resemble the industrial pipes and possess better heat transfer properties, while glass capillaries have the advantage of imaging the process. Packed-bed reactors can act as a replica of a reservoir to study deposition in porous media.[97–101] The pressure drop measurement and residence time distribution (RTD) measurements are two powerful methods to characterize the deposition of asphaltenes onto porous media. These studies provide important insights towards how does asphaltenes deposition alter the permeability and porosity of porous media. However,

the complexity of the porous media environment adds to the challenges of understanding the behaviors of asphaltenes without in situ characterization. Furthermore, the deposition study in the traditional setup is time-consuming, let alone the variety of asphaltenes sources makes the laboratory study inextensible without characterizing each source sample. Therefore, it motivates the development of new a platform for high throughput laboratory methodology with access to high fidelity, transient information for asphaltenes deposition study.

1.4 Microfluidics have much to offer

Microfluidic science deals with manipulation, characterization and observation of fluids in a system with geometrically small features, typically in the range of ten to several hundreds of microns. These features are often realized in microreactors. The history of microfluidics and microreactors could be dated back to 1951, when Siemens-Elema patented the first inkjet printer. In the 1960s, the introduction of MEMS technology added a whole new possibility to the microfluidic field. In 1979, the first 'Lab-on-a-Chip' was introduced by S. Terry.[102] After decades of development and improvement, microfluidic science has made tremendous progress in the fabrication of microreactors.

Nowadays, a variety of materials could be chosen from to manufacture the designed microreactors depending on the intended applications, including stainless steel, ceramic, glass, polymer, and silicon. Stainless steel microreactors have been widely used in production-related chemical processes because of their excellent chemical resistant and durability.[103,104] Ceramic microreactors provide excellent resistant to high temperature and often are applied to fuel related process, such as microburners.[105,106] However, compared with stainless steel microreactors, ceramic microreactors are usually fragile and need more

- 17 -

cared when handling. Glass microreactors have an apparent advantage of transparency, which provides an easy-to-access window for process analytic technology, although they are also fragile. Polymer is properly the most popular material, Poly-dimethysiloxane (PDMS) for example, for fabrication of microreactor, especially in biochemical processes research. The ease of fabrication provides a feasible solution to satisfy the sterile requirement of biology processes, where disposable utensils are common practice.[107,108] With the emergence and development of 3D-printing technology, the fabrication of polymer microreactors is further simplified by elimination the need for making moulds.[109] The rapid turn-around from design to application offered by polymer microreactors has attracted interests in prototyping.[110,111] However, the poor mechanical properties, low thermal conductivity and chemical compatibilies limit the application of polymer materials in chemical processes involving high pressure, high temperature or non-aqueous environments. Silicon, on the other hand, offers good mechanical properties and the best thermal conductivity among the materials mentioned.[112–114] Accompanied by the enormous development in MEMS technology, the fabrication of complex and sophisticated microreactor designs was realized in silicon reactors.[115,116] After deposition of silicon dioxide or other materials, such as Teflon, it provides excellent chemical compatibilies for chemical processes.[117] The capability of bonding with glass materials, such as Pyrex 7740 or Borofloat 33, brings the advantages of transparency. Advanced wet and dry etching processes introduce control of not only the size, but also the morphology of channels in the wafer. Multi-step etching enables the possibility of 3D networking of silicon reactors.

The achievements in microfabrication led to advanced microreactors capable of fulfilling diverse potentials. Microreactors have advantages of being easier to handle, offer

- 18 -

safer manipulation of chemicals and have less chemical usage and higher throughput when compared with conventional reaction system. The miniaturization of reactors provides the benefit of supreme mass and heat transfer rates. Combined with precise control, it makes it possible to study reactions under harsh conditions, which is difficult or unsafe to perform with conventional reaction system, especially when unknown conditions could lead to runaway reactions. Also, the elimination of mass transfer and heat transfer resistance could reveal intrinsic information about reactions, which might be overlooked in conventional chemical methods. Furthermore, the reduction of required chemical volumes in the experiment leads to decrease in economic costs and hazardous wastes in most studies, such as heterogeneous noble metal catalyst study. Last but not least, the capability of integration with process analytical technology (PATs) provides a versatile experimental setup to access the high fidelity, transient, *in-situ* information in short periods of time. The high throughput performance of microreactors leads to reduced labor requirements and time consumption for each experiment. Integrated microsystems with analysis technology have been developed for many different techniques, including optical microscopy, electrochemical analysis, and nuclear magnetic resonance (NMR), absorption spectroscopy (UV-Vis and IR), and Raman spectroscopy.

Optical microscopy offers the most straightforward information regarding the researched process through observation. This characterization technique could often offer insights with higher quality information, such as flow patterns.[118,119] The limitation of this method is also very obvious, the human eyes. Unfortunately, while our eyes could only detect certain wavelength in the spectrum (visible light), we could not differentiate lots of chemical species as they are clear in this range. Therefore, we must utilize other techniques

with detectors to obtain quantitative information. Electrochemical analysis determines the chemical reactivity of the system based on the loss or gain of electron. It provides vital information regarding the mechanisms and kinetics of a chemical process. Among all the characterization techniques, electrochemical analysis is one of the simplest to integrate with microfluidic system, which makes it ideal for point-of-care applications.[120,121] Determined by the absorption of radio frequency by nuclei, nuclear magnetic resonance (NMR) provides very useful information about chemical structures of molecules. The major drawback of NMR characterization is the low sensitivity since the difference in population between the ground state and the excited state is low. The high-resolution spectra could be obtained through an enhanced magnetic field, which results in complex and expensive NMR machines with extensive support facilities and large footprints. These reasons limit the application of NMR spectroscopy in microfluidics.[122] Absorption spectroscopy (UV-Vis and IR) identifies the chemical species through the absorption of incident light due to the energy change during the transitions between different electronic states (UV-Vis) or different vibrational states (IR). UV-Vis is one of the most common characterization techniques in the lab for its simplicity, ease of operation, convenience and economy while offering useful and high-resolution data.[123] The change in intensity could be used to determine the concentration of the species through the Beer-Lambert law, while the shift in absorption wavelength could provide insights towards nanostructure of the matter, such as size and shape of nanoparticles.[124] UV-Vis could only provide limited chemical information about the molecules, whereas IR spectroscopy could provide fingerprint information for organic compounds. Furthermore, different setup modes (transmission mode, reflection mode, and attenuated total reflection mode) combined with

different acquisition modes (single point acquisition, mapping acquisition, and imaging acquisition) make IR spectroscopy a powerful instrument in microfluidic studies. [125–129] However, the broad and huge IR absorption peak of water limits the application of IR spectroscopy in aqueous environments. Raman spectroscopy, considered as complimentary to IR spectroscopy, could be an alternative powerful characterization technique. Similar to IR absorption spectroscopy, Raman spectroscopy could also identify the vibrational and rotational energy of chemical bonds to provide information on chemical structure and chemical environment of the molecules. Depending on the symmetry of the molecules, some vibration modes are only IR active, some modes are only Raman active, with some modes being both IR active and Raman active. In general, Raman scattering is considered as a weak signal because its intensity is only equivalent to 10^{-6} of the incident light. Due to developments in hardware, especially the laser light, Raman spectroscopy has greatly overcome its natural shortcomings. The utilization of surface enhanced resonance even makes Raman spectroscopy one of the most sensitive instruments, which could detect a single molecule.[130] In the meanwhile, Raman spectroscopy could be applied to characterize different phases of samples (gas, liquid, solid) with little requirement for sample preparation. Raman spectroscopy is non-constructive and offers high spatial resolution and high spectroscopic resolution with rapid acquisition. These features make Raman spectroscopy an invaluable tool for characterization in medicine, biotechnology, materials science and so on.[131,132] Combined with the unique property of microfluidics, the integration of Raman spectroscopy and microreactors will have an increasingly important role in the research applications.

1.5 The scope of this work

In this work, we explore the potential of using integrated microfluidics with *in situ* Raman spectroscopy as a platform to study two major materials causing the flow assurance problems: gas hydrates and asphaltenes. Our goal is to access the high throughput information to help to understand and resolve the problems encounter in industry. In each study, we simulated different real-world environments through the design of microreactors. In the gas hydrate study, the spiral channel with relatively long residence time is designed to study the phase behaviors under different conditions. In the asphaltenes study, a packed-bed microreactor is packed with quartz particles to serve as a scaled-down porous media of reservoir in petroleum industry. The microreactors used in this study were all made of silicon through standard MEMS fabrication technology either by a contractor or myself. Although Pyrex 7740 glass from Corning possessed better mechanical properties (higher yield stress), Borofloat 33 glass was used to seal the microchannel in this work as Pyrex 7740 was discontinued by the company. Nevertheless, we managed to conduct our experiment at our desired conditions (< 100 bar). Combined with thermo-electrical module, we were able to control the temperature of the system in a rapid fashion (~ 1.0 K/s) for a wide range (-20 °C to 80 °C). These features help us to conquer some engineering obstacles that could not be overcome in traditional large-scale experiments. In the meantime, better control of the system minimizes experimental error and enables us to conduct the experiments under varying conditions with high accuracy. For example, in the gas hydrate project, the fact that the induction time of crystallization could take any time from few minutes to more than 24 hours, due to the stochastic nature of nucleation, makes it an unpleasant experience for an experimentalist to conduct research on. Here, we are able to

- 22 -

control the formation of hydrate within seconds with thermal cycling of the microsystem. Furthermore, the kinetics of hydrate crystallization and dissociation were measured up to an accuracy of ±0.01 °C, which is unachievable in larger scale system. Last but not least, the integration with *in situ* Raman spectroscopy provides us with high fidelity, transient information about the processes. For instance, in the asphaltenes project, we are able to identify the different mechanisms of asphaltenes deposition and reveal the importance of π-π stacking interaction through the *in-situ* characterization of porous media during the asphaltenes deposition and dissolution processes. More details on the advantages of using the microfluidics system shall be found in the later chapters.

The utilization of microfluidic systems saves researchers time when obtaining useful information from first-principles research through process intensification. However, this does not necessarily mean the labor required for a researcher will decrease, as the expectation more data increases. Additionally, it requires a higher degree of attention as a larger volume of data is being generated and analyzed. The realization of automation in microfluidic systems could not only save labor, but also minimize the experimental errors due to human factors. In our work, we showed that we could increase the experimental efficiency even further through integrating automation with microfluidic systems. This builds confidence to tackle the complex and industrially-relevant chemical problems such as asphaltenes, where a huge variety of chemicals are present. Furthermore, it could be revolutionary to scientists in general, as more effort could now be put into understanding the problem rather than spending time on repetitive and tedious data collection.

Reference

(1)   U.S. Energy Information Administration. *Annual Energy Outlook 2019*; 2019.

(2)   Sheu, E.; Mullins, O. C. *Asphaltenes Fundamentals and Applications*, 1st edn.; Springer Science+ Business Media, LLC, 1995.

(3)   Sloan, D.; Koh, C.; Sum, A. K.; Ballard, A. L.; Creek, J.; Eaton, M.; Lachance, J.; Norm, M.; Palermo, T.; Shoup, G.; et al. *Natural Gas Hydrates in Flow Assurance*; Gulf Professional Publishing: Burlington, 2010.

(4)   Sloan, E. D. A Changing Hydrate Paradigm—from Apprehension to Avoidance to Risk Management. *Fluid Phase Equilib.* **2005**, *228–229*, 67–74.

(5)   Mullins, O. C.; Sheu, E. Y.; Hammami, A.; Marshall, A. G. *Asphaltenes, Heavy Oils, and Petroleomics*; Springer Science+ Business Media, LLC: New York, 2007.

(6)   Sloan, E. D.; Koh, A. C. *Clathrate Hydrates of Natural Gases*, 3rd edn.; CRC Press Taylor & Francis Group, 2007.

(7)   Sloan, E. D. Fundamental Principles and Applications of Natural Gas Hydrates. *Nature* **2003**, *426* (6964), 353–363.

(8)   Platteeuw, J. C.; Waals, J. H. Van Der. Thermodynamic Properties of Gas Hydrates. *Mol. Phys. An Int. J. Interface Between Chem. Phys.* **1957**, 91–96.

(9)   Mckoy, V.; Sinanoglu, O. Theory of Dissociation Pressures of Some Gas Hydrates. *J. Chem. Phys.* **1963**, *38* (12), 2946–2956.

(10) Child, W. C. Thermodynamic Functions for Metastable Ice Structures. *J. Phys. Chem.* **1964**, *68* (7), 1834–1838.

(11) Avlonitis, D.; Danesh, A.; Todd, A. C. Prediction of VL and VLL Equilibria of Mixtures Containing Petroleum Reservoir Fluids and Methanol with a Cubic EoS. *Fluid Phase Equilib.* **1994**, *94*, 181–216.

(12) Westacott, R. E.; Rodger, P. M. Full-Coordinate Free-Energy Minimisation for Complex Molecular Crystals : Type I Hydrates. *Chem. Phys. Lett.* **1996**, *262*, 47– 51.

(13) Zele, S. R.; Lee, S. Y.; Holder, G. D. A Theory of Lattice Distortion in Gas Hydrates. *J.Phys.Chem.B.* **1999**, *103* (46), 10250–10257.

(14) Clarke, M.; Bishnoi, P. R. Determination of the Intrinsic Rate of Ethane Gas Hydrate Decomposition. *Chem. Eng. Sci.* **2000**, *55*, 4869–4883.

(15) Clarke, M.; Bishnoi, P. R. R. Determination of the Activation Energy and Intrinsic Rate Constant of Methane Gas Hydrate Decomposition. *Can. J. Chem. Eng.* **2001**, *79* (1), 143–147.

(16) Clarke, M. A.; Bishnoi, P. R. Determination of the Intrinsic Rate Constant and Activation Energy of CO 2 Gas Hydrate Decomposition Using In-Situ Particle Size Analysis. *Chem. Eng. Sci.* **2004**, *59*, 2983–2993.

(17) Parent, J. S.; Bishnoi, P. Investigations Into the Nucleation Behaviour of Methane Gas Hydrates. *Chem. Eng. Commun.* **1996**, *144* (1), 51–64.

(18) Monfort, J. P.; Nzihou, A. Light Scattering Kinetics Study of Cyclopropane

Hydrate Growth. *J. Cryst. Growth* **1993**, *128*, 1182–1186.

(19)   Staykova, D. K.; Kuhs, W. F.; Salamatin, A. N.; Hansen, T. Formation of Porous
        Gas Hydrates from Ice Powders : Diffraction Experiments and Multistage Model.
        J.Phys.Chem.B **2003**, *107*, 10299–10311.

(20)   Stern, La. A.; Kirby, S. H.; Circone, S.; Durham, W. B. Scanning Electron
        Microscopy Investigations of Laboratory-Grown Gas Clathrate Hydrates Formed
        from Melting Ice , and Comparison to Natural Hydrates. *Am. Mineral.* **2004**, *89*,
        1162–1175.

(21)   Moudrakovski, I. L.; Mclaurin, G. E.; Ratcliffe, C. I.; Ripmeester, J. A. Methane
        and Carbon Dioxide Hydrate Formation in Water Droplets : Spatially Resolved
        Measurements from Magnetic Resonance Microimaging. *J.Phys.Chem.B* **2004**,
        108, 17591–17595.

(22)   Gupta, A.; Kneafsey, T. J.; Moridis, G. J.; Seol, Y.; Kowalsky, M. B.; Sloan, E. D.
        Composite Thermal Conductivity in a Large Heterogeneous Porous Methane
        Hydrate Sample. *J.Phys.Chem.B* **2006**, *110*, 16384–16392.

(23)   Henning, R. W.; Schultz, A. J.; Thieu, V.; Halpern, Y. Neutron Diffraction Studies
        of CO $_2$ Clathrate Hydrate: Formation from Deuterated Ice. *J. Phys. Chem. A*
        2000, *104* (21), 5066–5071.

(24)   Koh, C. A.; Wisbey, R. P.; Wu, X.; Westacott, R. E.; Soper, A. K. Water Ordering
        around Methane during Hydrate Formation Theoretical Studies of the Kinetics of
        Methane Hydrate Crystallization in External Electromagnetic Fields Water
        Ordering around Methane during Hydrate Formation. *J. Chem. Phys. J. Chem.*

- 26 -

Phys. J. Chem. Phys **2000**, *113* (10).

(25)   Halpern, Y.; Thieu, V.; Henning, R. W.; Wang, X.; Schultz, A. J. Time-Resolved

in Situ Neutron Diffraction Studies of Gas Hydrate: Transformation of Structure II

(SII) to Structure I (SI). *J.Am.Chem.Soc.* **2001**, *123* (10), 12826–12831.

(26)   Uchida, T.; Takeya, S.; Wilson, L. D.; Tulk, C. A.; Ripmeester, J. A.; Nagao, J.;

Ebinuma, T.; Narita, H. Measurements of Physical Properties of Gas Hydrates and

in Situ Observations of Formation and Decomposition Processes via Raman

Spectroscopy and X-Ray Diffraction. *Can. J. Phys.* **2008**, *81*, 351–357.

(27)   Gupta, A.; Dec, S. F.; Koh, C. A.; Sloan, E. D. NMR Investigation of Methane

Hydrate Dissociation. *J. Phys. Chem. C* **2007**, *111* (5), 2341–2346.

(28)   Moudrakovski, I. L.; Sanchez, A. A.; Ratcliffe, C. I.; Ripmeester, J. A. Nucleation

and Growth of Hydrates on Ice Surfaces : New Insights from Xe NMR

Experiments with Hyperpolarized Xenon. *J.Phys.Chem.B* **2001**, *105*, 12338–

12347.

(29)   Sum, A. K.; Burruss, R. C.; Sloan, E. D. Measurement of Clathrate Hydrates via

Raman Spectroscopy. *J. Phys. Chem. B* **1997**, *101* (38), 7371–7377.

(30)   Subramanian, S.; Sloan, E. D. Trends in Vibrational Frequencies of Guests

Trapped in Clathrate Hydrate Cages. *J.Phys.Chem.B* **2002**, *106*, 4348–4355.

(31)   English, N. J.; Johnson, J. K.; Taylor, C. E. Molecular-Dynamics Simulations of

Methane Hydrate Dissociation. *J. Chem. Phys.* **2005**, *123* (10), 244503–264507.

(32)   English, N. J.; Phelan, G. M. Molecular Dynamics Study of Thermal-Driven

Methane Hydrate Dissociation. *J. Chem. Phys.* **2009**, *131* (10), 074704.

(33)   Eskin, D.; Mohammadzadeh, O.; Akbarzadeh, K.; Taylor, S. D.; Ratulowski, J. Reservoir Impairment by Asphaltenes: A Critical Review. *Can. J. Chem. Eng.* **2016**, *94* (6), 1202–1217.

(34)   Schuler, B.; Meyer, G.; Peña, D.; Mullins, O. C.; Gross, L. Unraveling the Molecular Structures of Asphaltenes by Atomic Force Microscopy. *J. Am. Chem. Soc.* **2015**, *137* (31), 9870–9876.

(35)   Gray, M. R.; Tykwinski, R. R.; Stryker, J. M.; Tan, X. Supramolecular Assembly Model for Aggregation of Petroleums Asphaltenes. *Energy Fuels* **2011**, *25* (7), 3125–3134.

(36)   Groenzin, H.; Mullins, O. C. Molecular Size and Structure of Asphaltenes from Various Sources. *Energy Fuels* **2000**, *14*, 677–684.

(37)   Ballard Andrews, A.; Shih, W.-C.; Mullins, O. C.; Norinaga, K. Molecular Size Determination of Coal-Derived Asphaltene by Fluorescence Correlation Spectroscopy. *Appl. Specroscopy* **2011**, *65*, 1348–1356.

(38)   Buch, L.; Groenzin, H.; Buenrostro-Gonzalez, E.; Andersen, S. I.; Lira-Galeana, C.; Mullins, O. C. Molecular Size of Asphaltene Fractions Obtained from Residuum Hydrotreatment. *Fuel* **2003**, *82*, 1075–1084.

(39)   Zeng, H.; Song, Y.; Johnson, D. L.; Mullins, O. C. Critical Nanoaggregate Concentration of Asphaltenes by Direct-Current (DC) Electrical Conductivity. *Energy Fuels* **2009**, No. 23, 1201–1208.

(40) Andreatta, G.; Bostrom, N.; Mullins, O. C. High-Q Ultrasonic Determination of the Critical Nanoaggregate Concentration of Asphaltenes and the Critical Micelle Concentration of Standard Surfactants. *Langmuir* **2005**, *21*, 2728–2736.

(41) Andreatta, G.; Goncalves, C. C.; Buffin, G.; Bostrom, N.; Quintella, C. M.; Arteaga-larios, F.; Perez, E.; Mullins, O. C. Nanoaggregates and Structure - Function Relations in Asphaltenes. *Energy Fuels* **2005**, *19* (6), 1282–1289.

(42) Mcmullen, J. P.; Jensen, K. F. Rapid Determination of Reaction Kinetics with an Automated Microfluidic System. *Org. Process Res. Dev.* **2011**, *15*, 398–407.

(43) Ramachandran, V.; Fogler, H. S. Plugging by Hydrodynamic Bridging during Flow of Stable Colloidal Particles within Cylindrical Pores. *J. Fluid Mech.* **1999**, *385*, 129–156.

(44) Mullins, O. C. The Asphaltenes. *Annu. Rev. Anal. Chem.* **2011**, *4* (1), 393–418.

(45) Akbarzadeh, K.; Hammami, A.; Kharrat, A.; Zhang, D.; Allenson, S.; Creek, J.; Kabir, S.; Jamaluddin, J.; Marshall, A.; Rodgers, R.; et al. Asphaltenes-Problematic but Rich in Potential. *Oilf. Rev.* **2007**, 22–43.

(46) Adams, J. J. Asphaltene Adsorption, a Literature Review. *Energy Fuels* **2014**, *28* (5), 2831–2856.

(47) Buckley, J. S. Asphaltene Deposition. *Energy Fuels* **2012**, *26*, 4086–4090.

(48) Abdallah, W. A.; Taylor, S. D. Surface Characterization of Adsorbed Asphaltene on a Stainless Steel Surface. *Nucl. Instruments Methods Physcis Res. B* **2007**, *258*, 213–217.

(49) Ekholm, P.; Blomberg, E.; Claesson, P.; Auflem, I. H.; Sjöblom, J.; Kornfeldt, A. A Quartz Crystal Microbalance Study of the Adsorption of Asphaltenes and Resins onto a Hydrophilic Surface. *J. Colloid Interface Sci.* **2002**, *247* (2), 342–350.

(50) Toulhoat, H.; Prayer, C.; Rouquet, G. Characterization by Atomic Force Microscopy of Adsorbed Asphaltenes. *Colloids Surfaces A Physicochem. Eng. Asp.* **1994**, *91*, 267–283.

(51) Drummond, C.; Israelachvili, J. Fundamental Studies of Crude Oil – Surface Water Interactions and Its Relationship to Reservoir Wettability. *J. Pet. Sci. Eng.* **2004**, *45*, 61–81.

(52) González, G.; Moreira, M. B. C. The Wettability of Mineral Surfaces Containing Adsorbed Asphaltene. *Colloids and Surfaces* **1991**, *58* (3), 293–302.

(53) Pernyeszi, T.; Patzk, A.; Berkesi, O.; Dekany, I. Asphaltene Adsorption on Clays and Crude Oil Reservoir Rocks. *Colloids Surfaces A Physicochem. Eng. Asp.* **1998**, *137*, 373–384.

(54) Tong, Z. X.; Morrow, N. R.; Xie, X. Spontaneous Imbibition for Mixed-Wettability States in Sandstones Induced by Adsorption from Crude Oil. *J. Pet. Sci. Eng.* **2003**, *39*, 351–361.

(55) Kumar, K.; Dao, E.; Mohanty, K. K. AFM Study of Mineral Wettability with Reservoir Oils. *J. Colloid Interface Sci.* **2005**, *289* (1), 206–217.

(56) Pernyeszi, T.; Dekany, I. Sorption and Elution of Asphaltenes from Porous Silica Surfaces. *Colloids Surfaces A Physicochem. Eng. Asp.* **2001**, *194*, 25–39.

(57)   Bantignies, J.; Moulin, C. C. dit; Dexpert, H. Asphaltene Adsorption on Kaolinite Characterized by Infrared and X-Ray Absorption Spectroscopies. *J. Pet. Sci. Eng.* **1998**, *20*, 233–237.

(58)   Jeon, Y. W.; Yi, S. H.; Choi, S. J. Adsorption of Asphaltene Functionalities and Asphaltene on Geothite. *Fuel Sci. Technol. Int.* **1995**, *13* (2), 195–214.

(59)   Cosultchi, A.; Rossbach, P.; Hernandez-Calderon, I. XPS Analysis of Petroleum Well Tubing Adherence. *Surf. Interface Anal.* **2003**, *35*, 239–245.

(60)   Nassar, N. N.; Hassan, A.; Pereira-almao, P. Comparative Oxidation of Adsorbed Asphaltenes onto Transition Metal Oxide Nanoparticles. *Colloids Surfaces A Physicochem. Eng. Asp.* **2011**, *384*, 145–149.

(61)   Nassar, N. N. Asphaltene Adsorption onto Alumina Nanoparticles: Kinetics and Thermodynamic Studies. *Energy Fuels* **2010**, *24* (8), 4116–4122.

(62)   Nassar, N. N. . b; Hassan, A. . b; Pereira-Almao, P. . b. Metal Oxide Nanoparticles for Asphaltene Adsorption and Oxidation. *Energy Fuels* **2011**, *25* (3), 1017–1023.

(63)   Szymula, M.; Marczewski, A. W. Adsorption of Asphaltenes from Toluene on Typical Soils of Lublin Region. *Appl. Surf. Sci.* **2002**, *196*, 301–311.

(64)   González, G.; Middea, A. Asphaltenes Adsorption by Quartz and Feldspar. *J. Dispers. Sci. Technol.* **1987**, *8* (5–6), 525–548.

(65)   Marczewski, A. W.; Szymula, M. *Adsorption of Asphaltenes from Toluene on Mineral Surface*; 2002; Vol. 208.

(66)   Saraji, S.; Goual, L.; Piri, M. Adsorption of Asphaltenes in Porous Media under

Flow Conditions. *Energy Fuels* **2010**, *24* (11), 6009–6017.

(67)   Franco, C. A.; Nassar, N. N.; Ruiz, M. A.; Pereira-Almao, P.; Cortes, F. B.
        Nanoparticles for Inhibition of Asphaltenes Damage: Adsorption Study and
        Displacement Test on Porous Media. *Energy Fuels* **2013**, *27* (6), 2899–2907.

(68)   Dudášová, D.; Silset, A.; Sjöblom, J. Quartz Crystal Microbalance Monitoring of
        Asphaltene Adsorption / Deposition. *J. Dispers. Sci. Technol.* **2008**, No. 29, 139–
        146.

(69)   Abudu, A.; Goual, L. Adsorption of Crude Oil on Surfaces Using Quartz Crystal
        Microbalance with Dissipation (QCM-D) under Flow Conditions. *Energy Fuels*
        2009, *23* (3), 1237–1248.

(70)   Syunyaev, R. Z.; Balabin, R. M.; Akhatov, I. S.; Safieva, J. O. Adsorption of
        Petroleum Asphaltenes onto Reservoir Rock Sands Studied by Near-Infrared
        (NIR) Spectroscopy. *Energy Fuels* **2009**, *23* (3), 1230–1236.

(71)   Gonzalez, G.; Travalloni-Louvisse, A. M. Adsorption of Asphaltenes and Its
        Effect on Oil Production. *SPE Prod. Facil.* **1993**, *8* (02), 91–96.

(72)   Mullins, O. C. The Modified Yen Model. *Energy Fuels* **2010**, *24* (6), 2179–2207.

(73)   Mullins, O. C.; Sabbah, H.; Pomerantz, A. E.; Barre, L.; Andrews, a. B.; Ruiz-
        Morales, Y.; Mostowfi, F.; McFarlane, R.; Goual, L.; Lepkowicz, R.; et al.
        Advances in Asphaltene Science and the Yen − Mullins Model. *Energy Fuels*
        2012, *26*, 3986−4003.

(74)   Fenistein, D.; Barre, L. Experimental Measurement of the Mass Distribution of

Petroleum Asphaltene Aggregates Using Ultracentrifugation and Small-Angle X-Ray Scattering. *Fuel* **2001**, *80*, 283–287.

(75)   Espinat, D.; Fenistein, D.; Barre, L.; Frot, D.; Briolant, Y. Effects of Temperature and Pressure on Asphaltenes Agglomeration in Toluene . A Light , X-Ray , and Neutron Scattering Investigation. *Energy Fuels* **2004**, *18*, 1243–1249.

(76)   Roux, J.; Broseta, D.; Deme, B. SANS Study of Asphaltene Aggregation : Concentration and Solvent Quality Effects. *Langmuir* **2001**, *17* (8), 5085–5092.

(77)   Tanaka, R.; Hunt, J. E.; Winans, R. E.; Thiyagarajan, P. Aggregates Structure Analysis of Petroleum Asphaltenes with Small-Angle Neutron Scattering. *Energy Fuels* **2003**, *17* (5), 127–134.

(78)   Hoepfner, M. P.; Bô, V.; Fávero, F.; Haji-Akbari, N.; Fogler, H. S. The Fractal Aggregation of Asphaltenes. *Langmuir* **2013**, *29*, 8799–8808.

(79)   Norinaga, K.; Wargardalam, V. J.; Takasugi, S.; Iino, M.; Matsujawa, S. Measurement of Self-Diffusion Coefficient of Asphaltene in Pyridine by Pulsed Field Gradient Spin - Echo 1 H NMR. *Energy Fuels* **2001**, *15* (2), 1317–1318.

(80)   Ostlund, J. A.; Andersson, S. I.; Nyden, M. Studies of Asphaltenes by the Use of Pulsed- Field Gradient Spin Echo NMR. *Fuel* **2001**, *80*, 1529–1533.

(81)   Lisitza, N. V; Freed, D. E.; Sen, P. N.; Song, Y. Study of Asphaltene Nanoaggregation by Nuclear Magnetic Resonance (NMR). *Energy Fuels* **2009**, *23* (16), 1189–1193.

(82)   Joshi, N. B.; Mullins, O. C.; Jamaluddin, A.; Creek, J.; McFadden, J. Asphaltene

Precipitation from Live Crude Oil. *Energy Fuels* **2001**, *15* (7), 979–986.

(83)   Aske, N.; Kallevik, H.; Johnsen, E. E.; Sjo, J. Asphaltene Aggregation from Crude Oils and Model Systems Studied by High-Pressure NIR Spectroscopy. *Energy Fuels* **2002**, *16* (7), 1287–1295.

(84)   Gharfeh, S.; Yen, A.; Asomaning, S.; Blumer, D. Asphaltene Flocculation Onset Determinations for Heavy Crude Oil and Its Implications. *Pet. Sci. Technol.* **2004**, *22*, 1055–1072.

(85)   Nielsen, B. B.; Svrcek, W. Y.; Mehrotra, A. K. Effects of Temperature and Pressure on Asphaltene Particle Size Distributions in Crude Oils Diluted with N-Pentane. *Ind. Eng. Chem. Res* **1994**, *33*, 1324–1330.

(86)   Yarranton, H. W.; Ortiz, D. P.; Barrera, D. M.; Baydak, E. N.; Barre, L.; Frot, D.; Eyssautier, J.; Zeng, H.; Xu, Z.; Dechaine, G.; et al. On the Size Distribution of Self-Associated Asphaltenes. *Energy Fuels* **2013**, *27*, 5083–5106.

(87)   Trejo, F.; Ancheyta, J.; Rana, M. S.; Petro, M. Structural Characterization of Asphaltenes Obtained from Hydroprocessed Crude Oils by SEM and TEM. *Energy Fuels* **2009**, *23* (5), 429–439.

(88)   Luo, P.; Wang, X.; Gu, Y. Fluid Phase Equilibria Characterization of Asphaltenes Precipitated with Three Light Alkanes under Different Experimental Conditions. *Fluid Phase Equilib.* **2010**, *291* (2), 103–110.

(89)   Perez-Hernandez, R.; Mendoza-Anaya, D.; Mondragon-Galicia, G.; Espinosa, M. E.; Rodriguez-Lugo, V.; Lozada, M.; Arenas-Alatorre, J. Microstructural Study of

Asphaltene Precipitated with Methylene Chloride and N-Hexane. *Fuel* **2003**, *82*, 977–982.

(90)   Sharma, A.; Groenzin, H.; Tomita, A.; Mullins, O. C. Probing Order in Asphaltenes and Aromatic Ring Systems by HRTEM. *Energy Fuels* **2002**, *16* (17), 490–496.

(91)   Batina, N.; Manzano-Martinez, J. C.; Andersen, S. I.; Lira-Galeana, C. AFM Characterization of Organic Deposits on Metal Substrates from Mexican Crude Oils. *Energy Fuels* **2003**, *17* (2), 532–542.

(92)   Wang, J.; Buckley, J. S.; Creek, J. L. Asphaltene Deposition on Metallic Surfaces. *J. Dispers. Sci. Technol.* **2004**, *253* (3), 287–298.

(93)   Boek, E. S.; Ladva, H. K.; Crawshaw, J. P.; Padding, J. T. Deposition of Colloidal Asphaltene in Capillary Flow: Experiments and Mesoscopic Simulation. *Energy Fuels* **2008**, *22*, 805–813.

(94)   Lawal, K. A.; Crawshaw, J. P.; Boek, E. S.; Vesovic, V. Experimental Investigation of Asphaltene Deposition in Capillary Flow. *Energy Fuels* **2012**, *26*, 2145–2153.

(95)   Hoepfner, M. P.; Limsakoune, V.; Chuenmeechao, V.; Maqbool, T.; Fogler, H. S. A Fundamental Study of Asphaltene Deposition. *Energy Fuels* **2013**, *27*, 725–735.

(96)   Chaisoontornyotin, W.; Haji-Akbari, N.; Scott Fogler, H.; Hoepfner, M. P. Combined Asphaltene Aggregation and Deposition Investigation. *Energy Fuels* **2016**, *30*, 1979–1986.

(97) Lin, Y.-J.; He, P.; Tavakkoli, M.; Thunduvila Mathew, N.; Yit Fatt, Y.; Chai, J. C.; Goharzadeh, A.; Vargas, F. M.; Lisa Biswal, S. Examining Asphaltene Solubility on Deposition in Model Porous Media. *Langmuir* **2016**, *32*, 8729–8734.

(98) Hu, C.; Morris, J. E.; Hartman, R. L. Microfluidic Investigation of the Deposition of Asphaltenes in Porous Media. *Lab chip* **2014**, *14* (12), 2014–2022.

(99) Hu, C.; Hartman, R. L. High-Throughput Packed-Bed Microreactors with In-Line Analytics for the Discovery of Asphaltene Deposition Mechanisms. *AIChE J.* **2014**, *60* (10), 3534–3546.

(100) Hu, C.; Shaughnessy, K. H.; Hartman, R. L. Influence of Water on the Deprotonation and the Ionic Mechanisms of a Heck Alkynylation and Its Resultant E-Factors. *React. Chem. Eng.* **2016**, *1* (1), 65–72.

(101) Hu, C.; Yen, A.; Joshi, N.; Hartman, R. L. Packed-Bed Microreactors for Understanding of the Dissolution Kinetics and Mechanisms of Asphaltenes in Xylenes. *Chem. Eng. Sci.* **2016**, *140*, 144–152.

(102) Terry, S. C.; Jerman, J. H.; Angell, J. B. A Gas Chromatographic Air Analyzer Fabricated on a Silicon Wafer. *IEEE Trans. Electron Devices* **1979**, *26* (12), 1880–1886.

(103) Iglesia, O. de la; Sebastian, V.; Mallada, R.; Nikolaidis, G.; Coronas, J.; Kolb, G.; Zapf, R.; Hessel, V.; Santamaria, J. Preparation of Pt/ZSM-5 Films on Stainless Steel Microreactors. *Catal. Today* **2007**, *125*, 2–10.

(104) Rebrov, E. V; Seijger, G. B. F.; Calis, H. P. A.; Croon, M. H. J. M. De; Bleek, C.

M. Van Den; Schouten, J. C. The Preparation of Highly Ordered Single Layer ZSM-5 Coating on Prefabricated Stainless Steel Microchannels. *Appl. Catal. A Gen.* **2001**, *206*, 125–143.

(105) Norton, D. G.; Wetzel, E. D.; Vlachos, D. G. Fabrication of Single-Channel Catalytic Microburners : Effect of Confinement on the Oxidation of Hydrogen / Air Mixtures. *Ind.Eng.Chem.Res* **2004**, *43*, 4833–4840.

(106) Norton, D. G.; Vlachos, D. G. Hydrogen Assisted Self-Ignition of Propane / Air Mixtures in Catalytic Microburners. *Proc. Combust. Inst.* **2005**, *30* (2), 2473–2480.

(107) Oh, K.; Chung, J.; Devasia, S.; Riley, J. J. Bio-Mimetic Silicone Cilia for Microfluidic Manipulation. *Lab Chip* **2009**, *9*, 1561–1566.

(108) Park, T.; Lee, S.; Seong, H.; Choo, J.; Lee, K.; Kim, Y. S.; Ji, W. H.; Hwang, S. Y.; Gweon, D.-G.; Lee, S. Highly Sensitive Signal Detection of Duplex Dye-Labelled DNA Oligonucleotides in a PDMS Microfluidic Chip : Confocal Surface-Enhanced Raman Spectroscopic Study. *Lab Chip* **2005**, *5*, 437–442.

(109) Urrios, A.; Parra-cabrera, C.; Bhattacharjee, N.; Gonzalez-suarez, A. M.; Rigat-brugarolas, L. G.; Nallapatti, U.; Samitier, J.; Deforest, C. A.; Posas, F.; Garcia-Cordero, J. L.; et al. 3D-Printing of Transparent Bio-Microfluidic Devices in PEG-DA. *Lab Chip* **2016**, *16*, 2287–2294.

(110) Anderson, J. R.; Chiu, D. T.; Jackman, R. J.; Cherniavskaya, O.; Mcdonald, J. C.; Wu, H.; Whitesides, S. H.; Whitesides, G. M. Fabrication of Topologically Complex Three-Dimensional Microfluidic Systems in PDMS by Rapid

Prototyping. *Anal.Chem.* **2000**, *72* (14), 3158–3164.

(111) Wu, H.; Odom, T. W.; Chiu, D. T.; Whitesides, G. M. Fabrication of Complex Three-Dimensional Microchannel Systems in PDMS. *J.Am.Chem.Soc.* **2003**, *125* (19), 554–559.

(112) Marre, S.; Adamo, A.; Basak, S.; Aymonier, C.; Jensen, K. F. Design and Packaging of Microreactors for High Pressure and High Temperature Applications. *Ind. Eng. Chem. Res.* **2010**, *49* (22), 11310–11320.

(113) Jensen, K. F. Silicon-Based Microchemical Systems : Characteristics and Applications. *MRS Bull.* **2006**, *31*, 101–107.

(114) Hartman, R. L.; McMullen, J. P.; Jensen, K. F. Deciding Whether to Go with the Flow: Evaluating the Merits of Flow Reactors for Synthesis. *Angew. Chem Int. Ed.* **2011**, *50* (33), 7502–7519.

(115) Hartman, R. L.; Sahoo, H. R.; Yen, B. C.; Jensen, K. F. Distillation in Microchemical Systems Using Capillary Forces and Segmented Flow. *Lab Chip* **2009**, *9* (13), 1843–1849.

(116) Hartman, R. L.; Jensen, K. F. Microchemical Systems for Continuous-Flow Synthesis. *Lab Chip* **2009**, *9* (17), 2495–2507.

(117) Kuhn, S.; Hartman, R. L.; Sultana, M.; Nagy, K. D.; Marre, S.; Jensen, K. F. Teflon-Coated Silicon Microreactors : Impact on Segmented Liquid À Liquid Multiphase Flows. *Langmuir* **2011**, *27*, 6519–6527.

(118) Atencia, J.; Beebe, D. J. Controlled Microfluidic Interfaces. *Nature* **2005**, *437*,

648–655.

(119) Zhao, C.; Middelberg, A. P. J. Two-Phase Microfluidic Flows. *Chem. Eng. Sci.*
       2011, *66* (7), 1394–1411.

(120) Sassa, F.; Morimoto, K.; Satoh, W.; Suzuki, H. Electrochemical Techniques for
       Microfluidic Applications. *Electrophoresis* **2008**, *29* (9), 1787–1800.

(121) Rackus, D. G.; Shamsi, M. H.; Wheeler, A. R. Electrochemistry, Biosensors and
       Microfluidics: A Convergence of Fields. *Chem. Soc. Rev* **2015**, *44*, 5320–5340.

(122) Gomez, M. V.; De La Hoz, A. NMR Reaction Monitoring in Flow Synthesis.
       Beilstein J. Org. Chem **2017**, *13*, 285–300.

(123) Pena-Pereira, F.; Costas-Mora, I.; Romero, V.; Lavilla, I.; Bendicho, C. Advances
       in Miniaturized UV-Vis Spectrometric Systems. *Trends Anal. Chem.* **2011**, *30*
       (10), 1637–1648.

(124) Begum, R.; Farooqi, Z. H.; Naseem, K.; Ali, F.; Batool, M.; Xiao, J.; Irfan, A.
       Applications of UV/Vis Spectroscopy in Characterization and Catalytic Activity of
       Noble Metal Nanoparticles Fabricated in Responsive Polymer Microgels: A
       Review. *Crit. Rev. Anal. Chem.* **2018**, *48* (6), 503–516.

(125) Perro, A.; Lebourdon, G.; Henry, S.; Lecomte, S.; Servant, L.; Marre, S.
       Combining Microfluidics and FT-IR Spectroscopy: Towards Spatially Resolved
       Information on Chemical Processes. *React. Chem. Eng* **2016**, *1*, 577–594.

(126) Moore, J. S.; Jensen, K. F. Automated Multitrajectory Method for Reaction
       Optimization in a Microfluidic System Using Online IR Analysis. *Org. Process*

Res. Dev. **2012**, *16*, 1409–1415.

(127) Chan, K. L. A.; Niu, X.; Demello, A. J.; Kazarian, S. G. Generation of Chemical

Movies: FT-IR Spectroscopic Imaging of Segmented Flows. *Anal. Chem.* **2011**,

83, 3606–3609.

(128) Chan, K. L. A.; Kazarian, S. G. FT-IR Spectroscopic Imaging of Reactions in

Multiphase Flow in Microfluidic Channels. *Anal. Chem.* **2012**, *84*, 4052–4056.

(129) Gabrienko, A. A.; Lai, C. H.; Kazarian, S. G. In Situ Chemical Imaging of

Asphaltene Precipitation from Crude Oil Induced by N-Heptane. *Energy Fuels*

2014, *28*, 964–971.

(130) Nie, S.; Emory, S. R. Probing Single Molecules and Single Nanoparticles by

Surface Enhanced Raman Scattering. *Science* **1997**, *275*, 1102–1106.

(131) Berger, A.; Wang, Y.; Feld, M. S. Rapid, Noninvasive Concentration

Measurements of Aqueous Biological Analytes by near-Infrared Raman

Spectroscopy. *Appl. Opt.* **1996**, *35* (1), 209–212.

(132) Chrimes, A. F.; Khoshmanesh, K.; Stoddart, P. R.; Mitchell, A.; Kalantar-zadeh,

K. Microfluidics and Raman Microscopy: Current Applications and Future

Challenges. *Chem. Soc. Rev.* **2013**, *42* (13), 5880.

Chapter 2

Crystallization Kinetics Study of Methane (sI) Hydrate in A Thermoelectrically-cooled Microreactor

2.1 Introduction

Because of the discovery of its present in the nature environment, the formation of gas hydrate has successfully attracted extensive research interest since 1960s.[1] Gas hydrate formation kinetics, like the crystallization of other materials, are generally thought to involve two stages: nucleation followed by crystal growth. During the stage of nucleation, the system could persist being in nonequilibrium state, so call metastable state, for a long period of time without formation of hydrate. From a molecular level perspective, the nucleation process is entropy disfavoured as disorderly gas phase and liquid phase rearrange into the orderly hydrate crystal structure. According to classical nucleation theory, in the event of homogeneous nucleation, the cluster of molecules needs to reach the critical size to overcome the energy barrier before trigger the nucleation as a nucleus. This energy barrier ΔG could be expressed through the sum of the surface excess energy ΔG_S and volume excess free energy ΔG_V,[2]

$$\Delta G = \Delta G_S + \Delta G_V = 4\pi r^2 \sigma + \frac{4}{3}\pi r^3 \Delta g_V \qquad (2.1)$$

Where, σ is the surface tension (positive value) and Δg_V is the free energy change per unit volume (negative value). The critical radius of clusters could be obtained through calculation of maximum value for equation (2.1). The typical critical cluster size of a nucleus calculated by Larson et al,[2,3] is on order of 10 nm. While Englezos et al. calculated the critical size of methane hydrate to be 30-170 Å through modification of classical nucleation theory through calculating the value of Δg_V through the fugacity.[4,5] Although homogeneous nucleation is barely happened in practice, the equation 2.1 provides us the insights toward the difficulty of

nucleation.[6] In the meanwhile, the solubility of nonpolar gases, such as methane and ethane, in liquid water is very small. For instance, the mole fraction of hydrocarbon in the aqueous phase is always less than 0.001, while the guest composition in hydrate phase could be as high as 0.15. As a result, the incident of nucleation in the bulk phase is unusual. Numerous researchers have confirmed the nucleation and initial crystal growth typically happened at the gas-liquid interface, where the max gas to water ratio is located.[7–10] This discrepancy in concentration further adds the difficulty to the nucleation of gas hydrate when compared with salt crystallization from supersaturated solution. The stochastic nature of nucleation makes the prediction of induction times an arduous endeavour. The nucleation time of methane hydrate, as an example, can range from 12 min to more than 24 hrs.[11,12]

On the other hand, the experimental measurement of crystal growth is possible. Growth can be described by three steps: 1) propagation of hydrate thin film at the hydrocarbon/water interface, 2) film development, 3) hydrate film solidification, and 4) bulk conversion.[13,14] Figure 2.1 shows a conceptual picture of hydrate thin film transformation mechanisms. At the beginning of the crystal growth, a porous thin film of hydrate with tens of microns is propagated at the interface of gas-liquid until it covers.[13] Then the liquid and gas are transferred through the pore in the hydrate film and crystalize at their encounter, which results in the film thickening. Later, the pore inside the hydrate film will be annealed through the crystallization. The nonporous hydrate film acts as mass transfer barrier at the interface and makes the bulk conversion an extremely long process without agitation of the system. The time range of each step is on the order of 10 s for propagation, 10 min for film
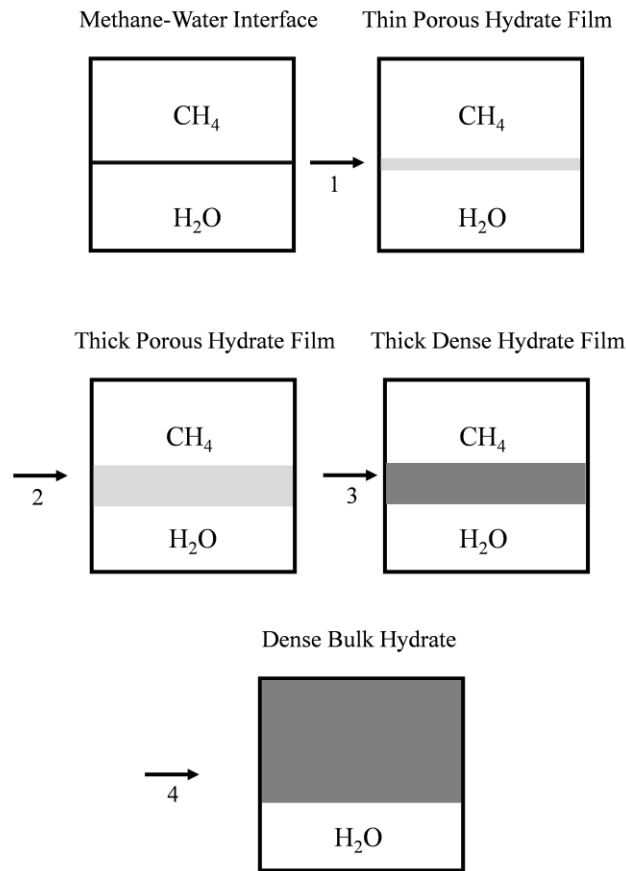
Figure 2.1 Schematic of the proposed mechanism of hydrate conversion at the interface of methane-water. Step 1: Propagation of a thin porous hydrate film at the interface of hydrocarbon-water. Step 2: Film development in thickness as methane and water transport through the pores and crystalize at the encounter. Step 3: Hydrate film solidification as the pores are annealed by crystallization. Step 4: Bulk conversion.

development, 10 hrs for film solidification, and infinite long for bulk conversion. To complicate matters, hydrate crystallization, like many reactions occurring at gas-liquid-solid interfaces, is a complex process that can be influenced by intrinsic kinetics, mass transfer, and heat transfer.

Models have been developed that describe hydrate growth based on different driving forces.[15–20] However, existing models only fit the data within their own parameter space, and they are commonly apparatus dependent.[1] Heat and mass transfer limitations not only influence growth, but they can also be difficult to quantify in the batch reactors designed to study hydrates. Sub-cooling, which is defined as the temperature difference below phase boundary temperature, is considered as the major driving force in heat-transfer based model. Propagation rates of methane, carbon dioxide, and cyclopentane hydrates have been reported,[13,17,19] and heat transfer-dominated models describe growth for sub-cooling in the range of 6 to 12 K.[17,18,20] Existing models, however, fall short of non-linear extrapolations at lower sub-cooling. Recall that the solubility of methane in water is infinitesimal (*e.g.*, S = 0.0974 mol/kg methane in water, at 50 bar and 273.15 K.)[21] compared to many solutes. The resultant driving forces for heat and mass transport at the gas-liquid-solid crystallization interface are miniscule, and the molecular diffusivity decreases with increasing sub-cooling. Under these conditions, the focus of the present work, an order of magnitude less heat is required to form methane hydrates. Understanding the kinetics in this regime, however, requires novel laboratory techniques and more comprehensive models that also consider the influence of mass transport limitations.

Microfluidics with *in situ* spectroscopic techniques are exceptional tools to study the crystallization. Some state-of-art work have been done to achieve on-chip crystallization analyses on different materials by utilizing the in situ techniques, including biomacromolecules by X-ray Diffraction (XRD),[22] Matrix-assisted Laser

- 45 -

Desorption Ionization-Mass Spectrometry (MALDI-MS)[23] and inorganic compound by Fourier Transform-Infrared Specroscopy (FTIR),[24] Laser Scanning Confocal Microscopy (LSCM).[25] The small characteristic length-scales, high surface-to-volume ratios, laminar flows ($Re \sim 1$), well-defined fluid dynamics, and controlled interfaces make it possible to safely understanding contributions of heat and mass transfer resistances at hydrate forming temperatures (270.65-283.25 K) and pressures (30.0-80.9 bar). Moreover, devices constructed of silicon (*i.e.*, with a high enough thermal conductivity) allow for isothermal operation and stepwise changes in the reactor temperature. Materials that permit the transmission of light, such as glassy borosilicates (*e.g.*, Pyrex®) and quartz, allow *in situ* observation and measurement by Raman spectroscopy.[26–30] As an example, quiescent micro-models of 2D porous media provide direct visual evidence to answer many key questions concerning the mechanism of hydrate formation and distribution in sediments, which are difficult to study otherwise.[31] As previous works suggest, hydrate growth is a competition between kinetic and transport limitations, but comprehensive models should consider both. Microfluidic systems have much to offer the study of hydrate crystallizations.

In the present work, we report the design of a thermoelectrically-cooled microreactor for the study of methane (sI) hydrate crystal growth kinetics. Precise control of conditions with the microsystem enabled the discovery of a previously unknown transition from heat-transfer-limited crystallization to mixed heat and mass-transfer-limited crystal growth at the methane-water-hydrate interface. A comprehensive model was derived from first principles and fitted to our

experimental rate data. The molecular diffusivity of methane within the thin film was discovered to follow Stokes-Einstein, while calculated Hatta and Beta numbers confirm that diffusion should not be neglected. Our discoveries introduce novel laboratory methods for the study of methane hydrate crystallizations and principle understanding of crystal growth under conditions that require an order of magnitude less heat than previously investigated.[17]

2.2 Experimental section

2.2.1 Design of a thermoelectrically-cooled microreactor

Microreactors were designed using a procedure described previously.[32–34] Two-
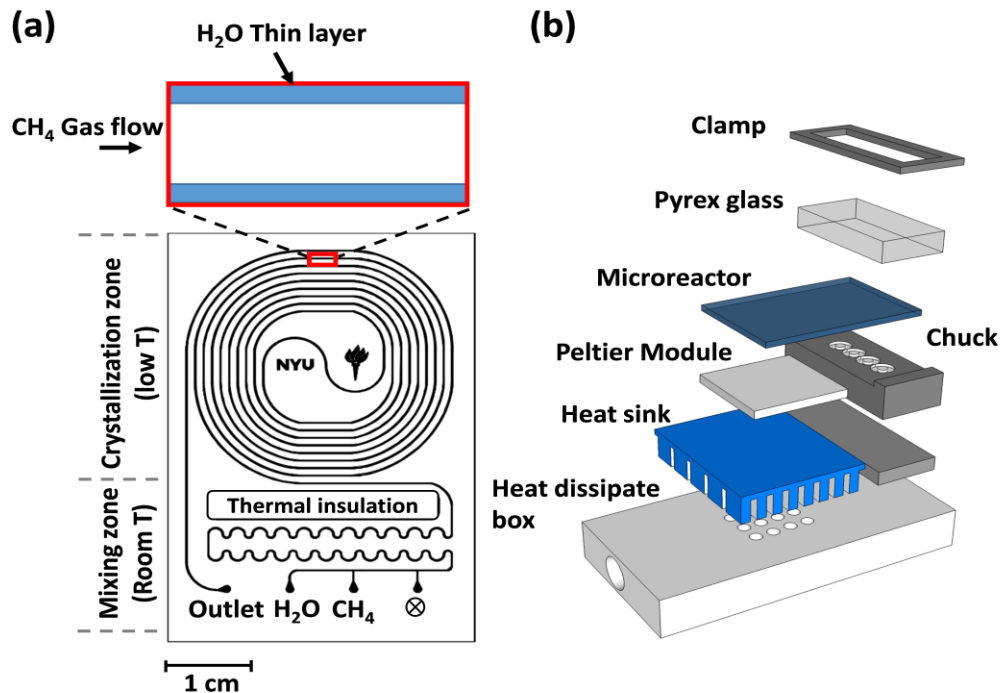
Figure 2.2 (a) Two-dimensional design of the microreactor. (b) Thermoelectric cooling system assembly.

dimensional masks were designed by AutoCAD. Microchannels (cross-section of

- 47 -

200 µm x 200 µm) were then etched in silicon using traditional microelectronics processing techniques by Little Things Factory GmbH Elsoff, Germany. Pyrex® (1 mm thick) was bonded to the substrate to create the 3D microstructures. As shown in Figure 2.2 (a), the design includes mixing (4.5 µL) and crystallization (27.7 µL) zones, which were separated by a thermal insulation through-etch. Operation at flowrates in the range of 2 to 80 µL/min enabled residence times from 0.4 min to 16.1 min.

A thermoelectric cooling system was designed to enable stepwise temperature changes and isothermal operation. Stainless steel compression chucks (Figure 2.2 (b)), designed in AutoCAD and manufactured by AC Manufacturing Santa Clara, California, enabled the delivery of fluids to and from the devices.[35] A thermoelectric module (TEC, TE Technology HP-127-1.4-1.5-74, max. 65W) was used in the present study. The backside of the microreactor was attached onto the cool side of the TEC with thermal paste (see Figure 2.1 (b)) to maximize the cooling rate of 1.05 K/s. The device temperature was monitored by a thermocouple (TE Technology MP-2444) and controlled by a PID controller (TE Technology RS485). A stream of in-house air was flow through air dryer and liquid coolant bath in sequence to obtain the dry and cool air. Then the cool air was continuously delivered to a heat dissipate box to maximize the driving force for heat transfer, thereby maximize the cooling rate. In addition, the dry air helps to resolve the potential condensation problem by flushing the entire testing environment.

The temperature distribution across the microreactor was further characterized by an IR thermal camera (ICI 9640P). The total of 40 test points of 7 test regions on the
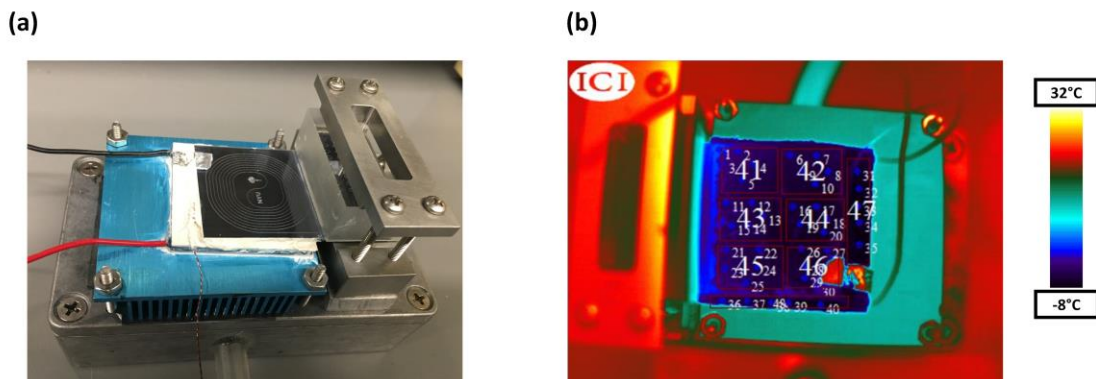
Figure 2.3 (a) Image of microsystem assembly (b) IR image of temperature distribution across the microsystem. The temperature distribution across the experiment observation zone is 0.1033 K.

crystallization zone were selected for a set testing temperature of -8 ºC. As shown in Figure 2.3 (b), the surface of microreactor was cooled to the setting temperature despite the environment and other components of microsystem, including stainless steel compression chucks, stayed at room temperature. This indicates the well thermal insulation between crystallization zone of the microreactor from the environment. The results from IR camera shows the temperature distribution across the observation zone is 0.1033 K, which represents the experimental error in the temperature measurement in our work. The pressure of the inlet and outlet of microreactor, the pressure and flowrates of both high-pressure pumps, and the temperature of the microsystem were monitored and recorded by a data acquisition module (National Instruments cDAQ-9171) with an in-house LabView program. The assembled microsystem was placed inside a Class 1 laser enclosure for *in situ* Raman spectroscopy. [28] Here, the laser enclosure not only blocks the laser from potentially damaging experimentalist's eyes, but also serves the purpose of isolating

the testing environment from the atmosphere to maintain the dryness as New York
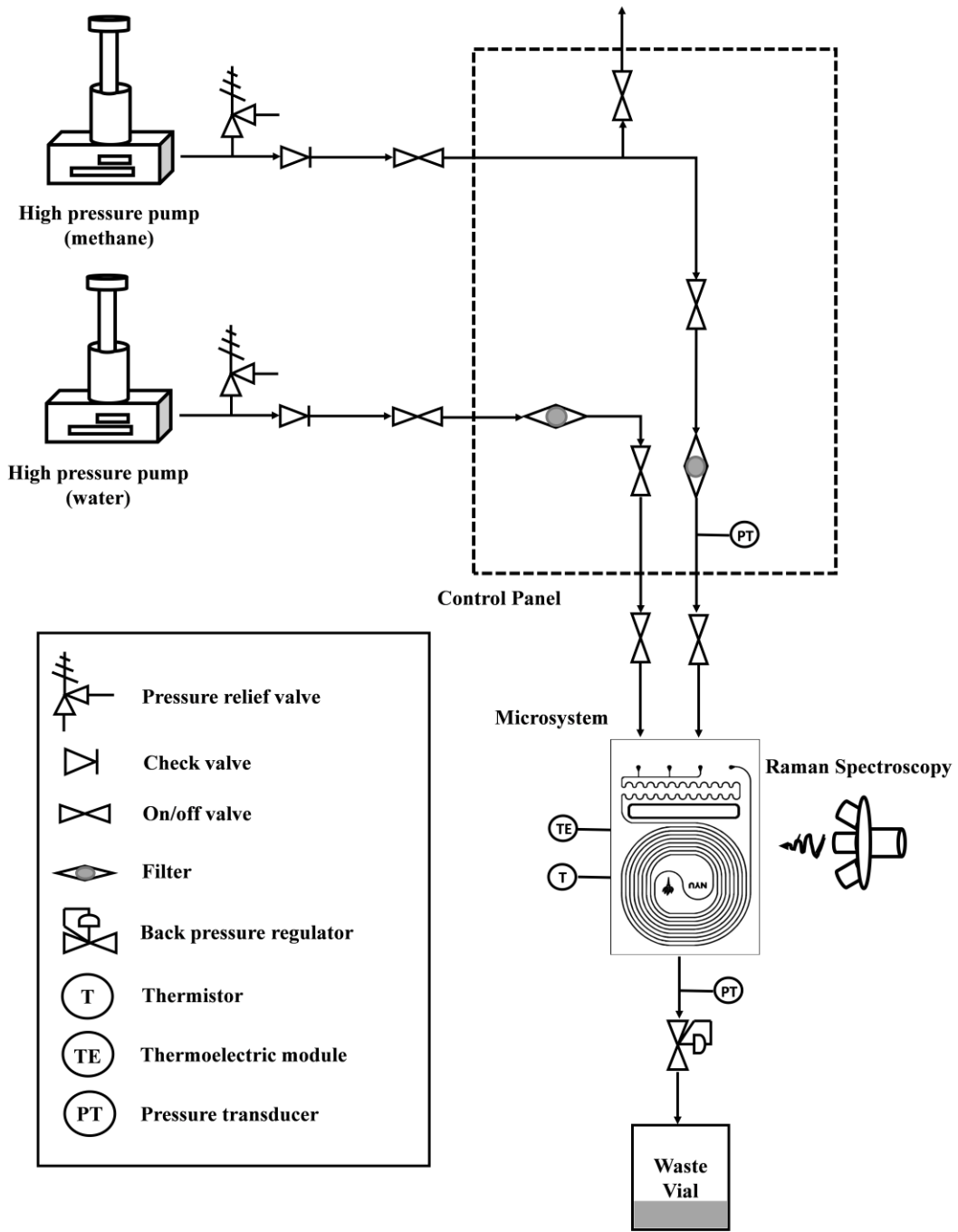
Figure 2.4 Process flow diagram of the experimental apparatus for the study of methane (sI) hydrate crystallizations.

City could be very humid in the summer.

2.2.2 Experimental apparatus

The experimental apparatus is illustrated in Figure 2.4. As can be seen, methane and deionized water were delivered to the microsystem by two high-pressure syringe pumps (Teledyne ISCO 65DM). A back-pressure regulator (Equilibar ZF1SNN8, max. 200 bars) connected at downstream was used to maintain a constant pressure. Two pressure transducers (WIKA A-10, max. 207 bar, accuracy $\pm$ 0.5%) were installed upstream and downstream of the microsystem to monitor the inlet and outlet pressures, respectively. The pressure drop of the microreactor was calculated as the difference between the transducers. The pressure drops across the microfluidic is negligible when compared to the pressure of measurement. The pressure of the system was read from the pressure transducer at the downstream and assumed to be constant throughout the experiment. Data were recorded by a National Instruments cDAQ-9171 with an in-house LabView program.

2.2.3 Methane hydrate formation

High purity deionized water used in this work was produced by a Milli-Q system (Milli-pore). Methane (>99.99 % purity) was purchased from Airgas. Melt ice was used as a source to trigger the crystallization of methane hydrates. First, all wetted parts were pressurized (30 to 80 bars) by deionized water. Then water pump was stop while methane was injected into the system (at different flowrates from 2 to 80 μL/min) to create the methane-water interface. The purpose of stop water pump was
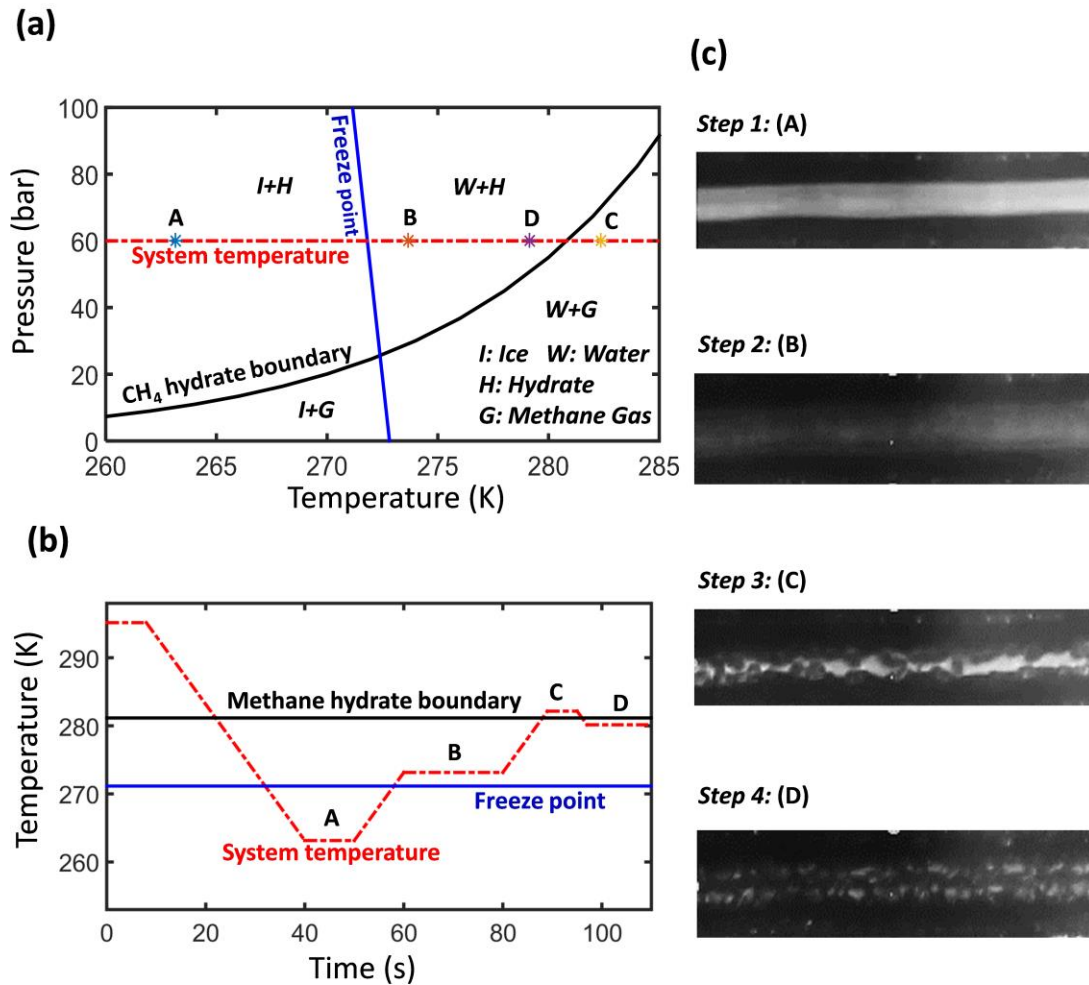
Figure 2.5 Methane hydrate crystallized from ice and methane by stepwise control of the temperature at 60 bar. (a) Phase diagram of methane hydrate from the NIST clathrate hydrate database. The corresponding operation conditions of the microsystem are denoted by "A", "B", "C", and "D".. (b) Microreactor temperature step changes. (c) Example video frames of a microchannel taken at each temperature condition. Step 1: ice formation; Step 2: ice transformation into methane hydrate; Step 3: dissociation of methane hydrate; Step 4: methane hydrate formation.

to avoid the segment flow, which could potentially cause the clogging of microfluidic channels during the methane hydrate formation. Methane hydrates

were then formed at constant pressures according to the following procedure shown graphically in Figure 2.5:

   1) The microsystem was cooled down to 263.15 K for 5 s to form ice. The presence of solid in water phase indicated the formation of ice.

   2) The temperature of the microsystem was then increased to 273.65 K: thermodynamic conditions at which ice is expected to melt and transform into methane hydrate.

   3) The microsystem was heated to 1.00 K above the phase boundary, until no hydrate crystals were optically observed (until the crystals were less than 2.78 µm).

   4) With hydrate nuclei now formed, the microsystem was then cooled down to the desired sub-cooling temperature to study the crystal growth rates.

2.2.4 *In situ* Raman spectroscopy

The spectra of methane hydrate were acquired by *in situ* confocal Raman spectroscopy (Horiba LabRam HR evolution, Jobin-Yvon). The excitation source was a Diode-Pumped Solid-State (DPSS) laser system emitting light at 532 nm with 48 mW power. A 10x objective lens (MPlanN Olympus, 0.25NA, 10.6 mm WD) and CCD Synapse EM detector were used to acquired spectra. The grating was 1800 grooves/mm and the exposure time was 10 s. The deconvolution of the spectra was done by in-house developed MATLAB program integrated with third party codes, such as GSTools (import '.spc' files) ipf (deconvolution of spectra). A linear baseline correction was applied to all peaks.

2.2.5 Phase boundary measurements

The phase boundary temperatures of methane hydrate at different pressures were measured using microscopy. The temperature was not recorded until methane hydrate was observed to be stable, neither growing nor dissociating inside the microchannel. The process was repeated at least 3 times for every pressure with an accuracy of ± 0.01 K.

2.2.6 Propagation rate measurements

Propagation rate measurements were taken once the temperature was stabilized at the desired sub-cooling degree (±0.05 K). The propagation rate of the methane hydrate along the methane-water interface (in the axial direction of the microreactor) was observed and recorded by CCD camera. The accuracy of the CCD camera was 2.78 µm/pixel and 15 fps. The corresponding accuracy of propagation rate measurements was 0.20 µm/s.

2.2.7 Dimensionless analysis

The dimensionless analysis was applied to estimate the significance of intrinsic kinetics, heat transfer, and mass transfer to the overall methane hydrate propagation process. The Hatta modulus M_H, or Hatta number, is the dimensionless number to compare the reaction rate and mass diffusion rate,

$$M_H = \sqrt{\frac{maximum\ reaction\ rate}{maximum\ mass\ diffusion\ rate}} = \sqrt{\frac{k\prime C_m}{\frac{D}{\delta_s}C_m}} = \sqrt{\frac{k\prime}{k_c}} \qquad (2.2)$$

- 54 -

Here, k' is the apparent specific crystallization rate constant, k_c is the mass transport coefficient of methane, D is the diffusivity of methane in water, C_m is the concentration of methane at the interface, and δ_s is the thickness of the thin film layer.

The beta number β_B is the dimensionless number to estimate the importance of heat transfer during a process,

$$\beta_B = \frac{heat\ generated\ rate}{heat\ remove\ rate} = \frac{r_i \Delta H}{r_h} = \frac{\frac{k'AC_m M_{CH4}}{\omega_{CH4}} \Delta H}{h'A(T_{eq}-T_b)^n} = \frac{k'C_m M_{CH4} \Delta H}{\omega_{CH4} h'(T_{eq}-T_b)^n} \qquad (2.3)$$

Here, ΔH is the enthalpy change during the crystallization, r_i and r_h are the crystallization rate of methane hydrate and heat transfer rate, respectively. The detail on notation and derivation for the expression of crystallization rate and heat transfer rate could be found in the section 2.3.6.

The Lewis number Le is a dimensionless number defined as the ratio of thermal diffusivity to mass diffusivity. It is used to characterize fluid flows where there is simultaneous heat and mass transfer.

$$Le = \frac{thermal\ diffusivity}{mass\ diffusivity} = \frac{\kappa}{\rho D c_p} \qquad (2.4)$$

Here, κ is the thermal conductivity of water (0.58 W/m·K), ρ is the water density (1.00 x10^3 kg/m^3) and c_p is the specific heat of water (4.18x10^3 J/kg·K).[36] And the values of κ, ρ and c_p are assumed to be constant in the range of experimental conditions.

- 55 -

2.3 Results and discussion

2.3.1 Methane hydrate formation

The nucleation of methane (sI) hydrates is a stochastic process that can take from 10 mins to up to 24 hrs. Different methods have been reported to induce the nucleation of hydrates within minutes by utilizing confined water or additives.[19,37] In the present work, the swift change and precise control of the temperature by design of the microsystem enable methane hydrate crystallizations from melt ice within seconds.

Temperature cycling of the microsystem to form hydrates required approximately 10 mins. Compared with larger-scale batch methods, our use of a microsystem improved the experimental efficiency and accuracy under mild sub-cooling, while acquiring sufficient amounts of data in short time periods. Furthermore, the microsystem was free of additives and confined water, which could influence hydrate crystallizations.

Figure 2.5 (c) shows the snapshots of a microchannel captured during each step of the hydrate formation process depicted in Figure 2.5 (a) & (b). During the first step, the sharp contrast between ice along the microchannel walls and methane gas in the bulk indicated the formation of ice. No sign of methane hydrate was observed during this step (confirmed by *in situ* Raman spectroscopy). At the second step, the temperature was above the freezing point of water, and methane hydrate crystallized all over the microchannel (also confirmed by *in situ* Raman spectroscopy). At the third step, where the temperature was 1.0 K greater than the equilibrium

Table 2.1 Experimental phase boundary measured using the microsystem.

Pressure (bar)	T_{eq} (K)	$T_{eq}{}^i$ (K)
30.0	274.65	274.32
39.6	277.65	277.02
49.5	279.65	279.19
60.8	281.35	281.20
71.5	283.15	282.79
80.9	284.25	283.88
1.0^{ii}	0.10	0.00

i Data retrieved from the NIST clathrate hydrate database

ii Freeze point of pure water

temperature, methane hydrate dissociated. At the final step, methane hydrate recrystallized while sub-cooled conditions were achieved. These observations are consistent with the 'memory effect' reported by other scientists, which supports that water from the melted hydrate forms hydrate easier than the fresh water.[38–41] Noteworthy is that the memory effect ceased at higher temperatures, *e.g.*, upon heating to 10.0 K above the equilibrium temperature (instead of 1.0 K). This implies that the memory effect originated from methane hydrate seed crystals that are stable at 1.0 K above equilibrium conditions.

The phase boundary was estimated by repeating the third and the fourth steps at different pressures. Table 2.1 summarizes the measured phase boundary temperature compared to data from the NIST clathrate hydrate database.[42] As can be seen, the difference is less than 0.5 K. Note that the data from literature is also experimental, which could depend on the accuracy of the apparatus. The measured freeze point of

water, also reported in Table 2.1, further indicated the reliability of our microsystem. To obtain the accurate sub-cooling temperature, the measured phase boundary was used as the equilibrium temperature throughout this work.

2.3.2 Raman spectra of methane hydrate

In situ Raman spectroscopy was used to characterize the formation of methane hydrate within the microsystem. Figure 2.6 shows the Raman spectra. One observes that deconvolution of the spectral shifts confirmed that crystals formed, *e.g.*, at 70
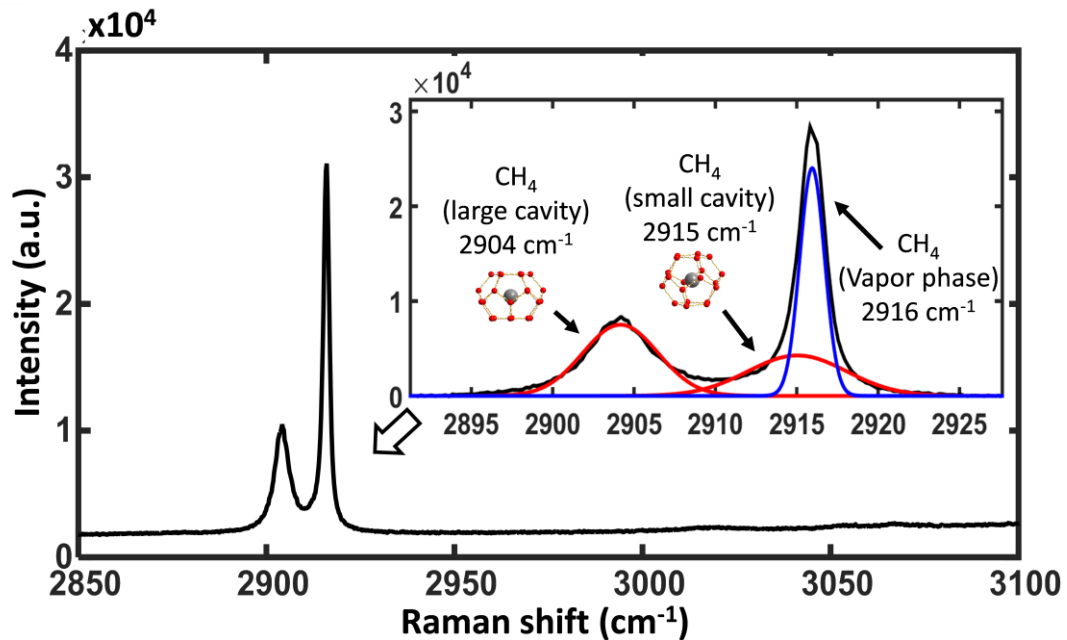
Figure 2.6 Raman Spectra of the v_1 stretching mode of methane vapor and methane (sI) hydrate cavities at 70 bars. Deconvolution of the shifts confirms the presence of small 5^{12} cavities (red, at 2915 cm^{-1}) and the large $5^{12}6^2$ cavities (red, at 2904 cm^{-1}) in methane hydrate. The deconvoluted peak (blue) at 2916 cm^{-1} indicates the presence of methane in vapor phase.

bar, were methane hydrate. Characteristic shifts of methane hydrate at 2904 cm^{-1} and 2915 cm^{-1} were measured in the presence of methane gas at 2916 cm^{-1}. The full width of half maximum (FWHM) of the peaks for hydrate and methane gas were 2.7 cm^{-1}, 3.6 cm^{-1} and 0.9 cm^{-1}, respectively. The methane gas shift correlated well with the v_1 symmetric C-H stretching mode of methane molecules. [43] Shifts at 2904 cm^{-1} and 2915 cm^{-1} confirmed the presence of the small cavity (5^{12}) and the large cavity ($5^{12}6^2$) that build the sI structure, which is consistent with the results reported by Sum. [44]

Besides crystal identification, *in situ* Raman also provided insight on the crystal growth. The area of characteristic Raman peak correlates with the concentration of analyte in a relation derived by Wopenka and Pasteris,[44–46] which is similar to Beer-Lambert's law:

$$A = C\sigma\eta = C \cdot F \tag{2.5}$$

where A is the area of the characteristic Raman peak, σ is the Raman cross sections, and η is the instrument factor. The product of σ and η yields the 'Raman quantification factor' F. We acquired Raman spectra on the same spot for 30 mins at 2-min intervals after the formation of hydrate was observed at 70 bar. (see Figure 2.7) Since we focused on the same spot over time, the normalized ratio of the Raman peak revealed the relative crystal growth rate of methane hydrate. During the first 6 mins, the methane hydrate crystal was propagating along the interface of methane and water at certain thickness. The almost unchanged area of the Raman shift implied that 1) propagation on a time scale of seconds rather than minutes, and 2) the initial layer of hydrate film was homogeneous. The thickness of the initial growth
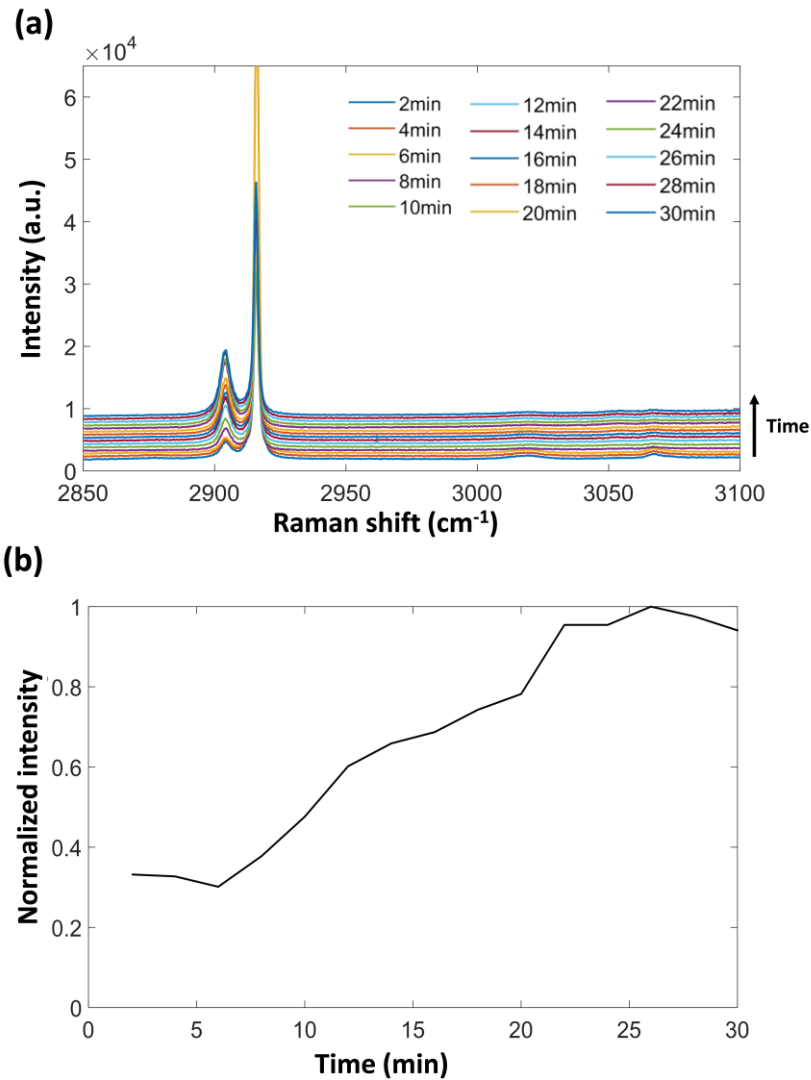
Figure 2.7 (a) Raman spectra on same spot of channel taken for 30 min with 2-min interval. The intensity of signature peak at 2904 cm^{-1} over time is proportional to the methane hydrate growth in the perpendicular direction to the CH_4/H_2O interface. (b) Normalized intensity of 2904 cm^{-1} peak over time. During first 6 minutes, the unchanged intensity indicates the initial thin film thickness could be assumed to be constant during the propagation stage. The increase of intensity from 6 minutes to 26 minutes shows the process of thin film thickening.

was a function of pressure and sub-cooling temperature.[18,47,48] During the next 20 mins, the increase of Raman peak intensity indicated the growth of thin film in thickness (or the density increased). Overall, the thin film development took several minutes, and these observations are in agreement with the phenomena described by Taylor.[13]

2.3.3 Propagation rate measurements

The propagation of hydrate at the methane-water interface was next examined to understand which physical and chemical rate processes govern it. The solubility of hydrocarbons in aqueous solution are usually very low (*e.g.*, $C_{methane}/C_{water} = 1/571$, at 50 bar and 273.15 K).[49] Compared with the ratio in sI hydrate, which ranges from 5.75 to 6.29, the dissolved methane has less chance to form the clathrate hydrate in bulk water. Our previous work has shown that confined liquid-liquid interfaces between two immiscible phases are comprised of mixture layers of tens of micrometres in thickness,[28] which is anticipated to be influenced by temperature and pressure in gas-liquid systems. The initial thickness of methane hydrate films have also been reported in the range of tens of micrometres.[13,20,48] These facts support that the propagation of hydrate in our microsystem occurred at the interface of methane and water.[31] Once propagation commenced in the direction tangential to the methane-water layered interface, surface renewal was then required to continue crystallization. However, the thin film at the methane hydrate-water interface would also serve as a mass transfer barrier that limited the flux of methane for surface renewal. Heat transfer in microfluidics can also be dominated by conduction rather

- 61 -
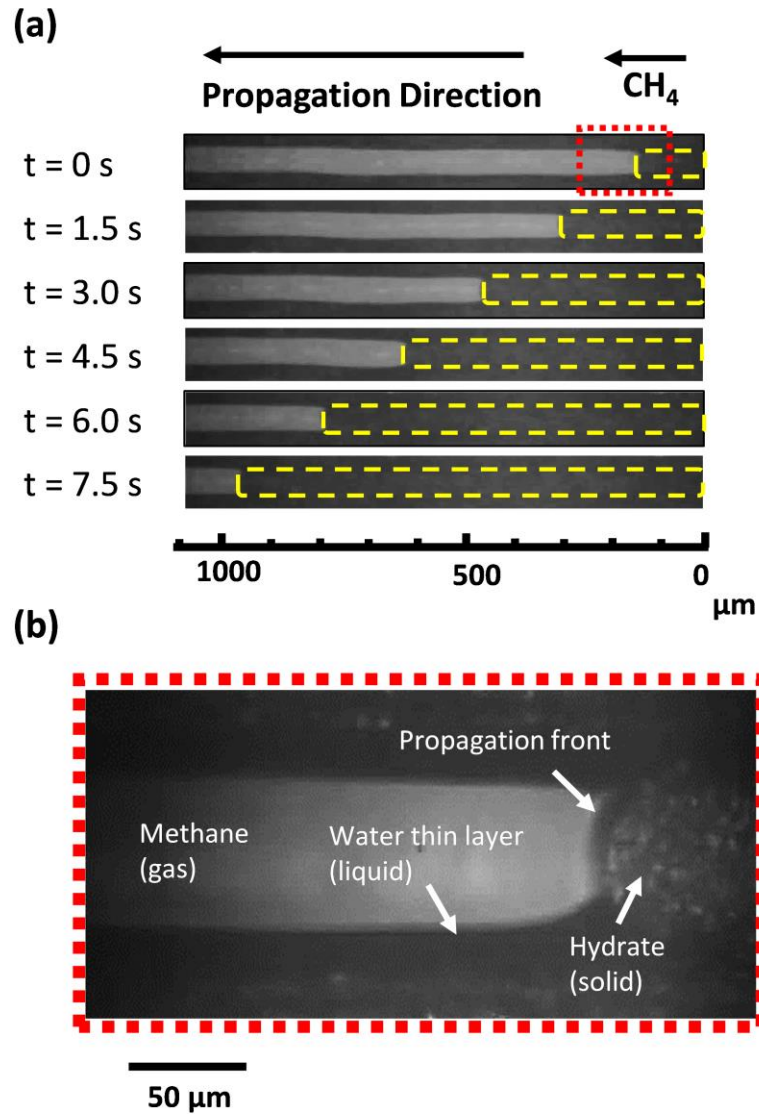
Figure 2.8 (a) Snapshots of methane hydrate propagation along a microchannel at a pressure of 60.8 bar and sub-cooling temperature of 3.0 K. The flowrate of methane in this example was 2.5 mg/min, and the video recorded at 15 fps. The directions of propagation and methane flow are indicated by the arrows. (b) Magnification of the region highlighted in (a). Three phases (methane free gas, water liquid and hydrate solid) coexist inside the microchannel.

than convection. The preceding facts explain why methane hydrate crystallization

kinetics measured in microfluidics could be different from quiescent systems.[5,50,51] These important points support that the study of propagation kinetics in microfluidics could provide new insights on clathrate hydrate crystal kinetics.

The propagation rate of methane hydrate at different flowrates, sub-cooling temperatures, and pressures was investigated. Annular flow established a thin film of water along the microchannel walls while methane gas flowed tangential in the centre of the microchannel. The microfluidics ensured steady-state hydrate propagation without the risk of clogging the device. Figure 2.8 shows an example propagation rate measurement at 60 bar and sub-cooling temperature of 3.0 K. The phase boundaries of the hydrate film are highlighted by dashed-lines. As can be seen, frame-by-frame analysis of the micrographs provided axial propagation with accuracy of 15 fps (or about 0.20 µm/s).

2.3.4 Influence of pressure drop on methane hydrate formation

The formation of methane hydrate crystals could deposit onto the microchannel and increase the pressure drop across the microreactor. It could eventually cause the clogging of the microchannel. Another concern is the increase of pressure drop could invalidate the assumption of constant pressure in the microreactor and results in inaccurate data. Figure 2.9 shows an example of pressure drop measurement of the microfluidic system during the methane hydrate formation. Compared with the pressure of system P, the pressure drop ΔP is negligible while measuring the propagation rate. Allowing hydrate formation to continue for extended periods (an order of magnitude longer than the time scale of the propagation rate measurement)

(a)

(b)
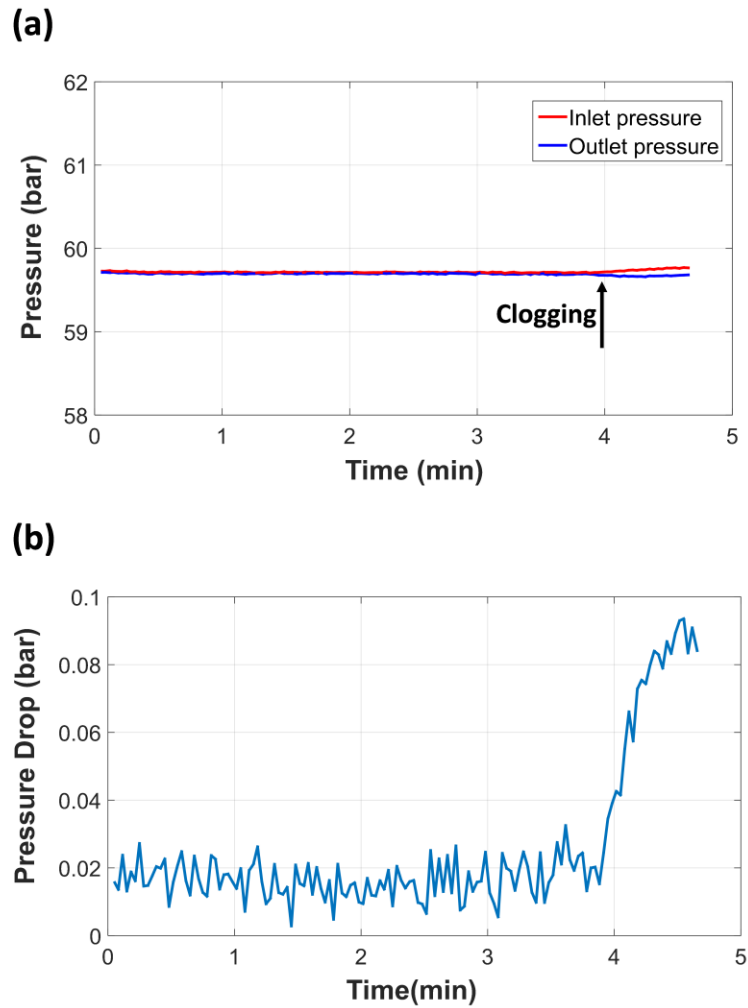
Figure 2.9 The pressure profile of the microfluidic system during methane hydrate formation at 59.8 bar, sub-cooling temperature of 1.0 K, and methane flow rate of 20 μL/min. (a) Inlet and outlet pressure of the microfluidic system in the first 5 min of methane hydrate formation. (b) The pressure difference across the microfluidic system. The increase of pressure drop at around 4 min indicates the onset of constriction. Even after 4 min, $\frac{\Delta P}{P} \cong$ 0.0017, which confirms that the pressure drop is negligible.

can lead to constriction. When compared with the results from Raman spectroscopy in figure 2.7, it shows that the change in pressure drop during the propagation stage

of methane hydrate formation is negligible, whereas the change in pressure drop become significant during the hydrate layer thickening stage.

2.3.5 Influence of the flowrate of methane

The influence of the methane flowrate was studied at 60 bar and 2.0 K sub-cooling. The flowrate was increased in separate experiments from 2 to 200 µL/min (or 98 µg/min to 9812 µg/min). Reynolds number (Re) ranged from 0.7 to 69.0. Based on traditional film theory, the mass transfer coefficient k_c across the methane gas film (at the methane-water interface tangential to the direction of propagation) would increase with the increase of Re. Under the same pressure and temperature, the increase of Re would also increase the methane flux across the gas film. Figure 2.10 (a) shows that the propagation rate remained unchanged when the flowrate of methane increased.

The results suggest that 1) mass transfer across the gas film, which is perpendicular to the direction of propagation, does not affect the propagation rate, and 2) there is enough methane within the gas film to form the hydrate. Any mass transfer limitations in our system are therefore confined within the thin film layers where both water and methane are present. Within layers beyond the gas film of the interface, the solubility of methane decreases by orders of magnitude and so does the driving force of the flux. A similar analogy can be made that no external mass transfer limitations exist, but internal mass transfer limitations (within the stagnant film) could still influence the crystallization.

2.3.6 Influence of pressure and sub-cooling temperature
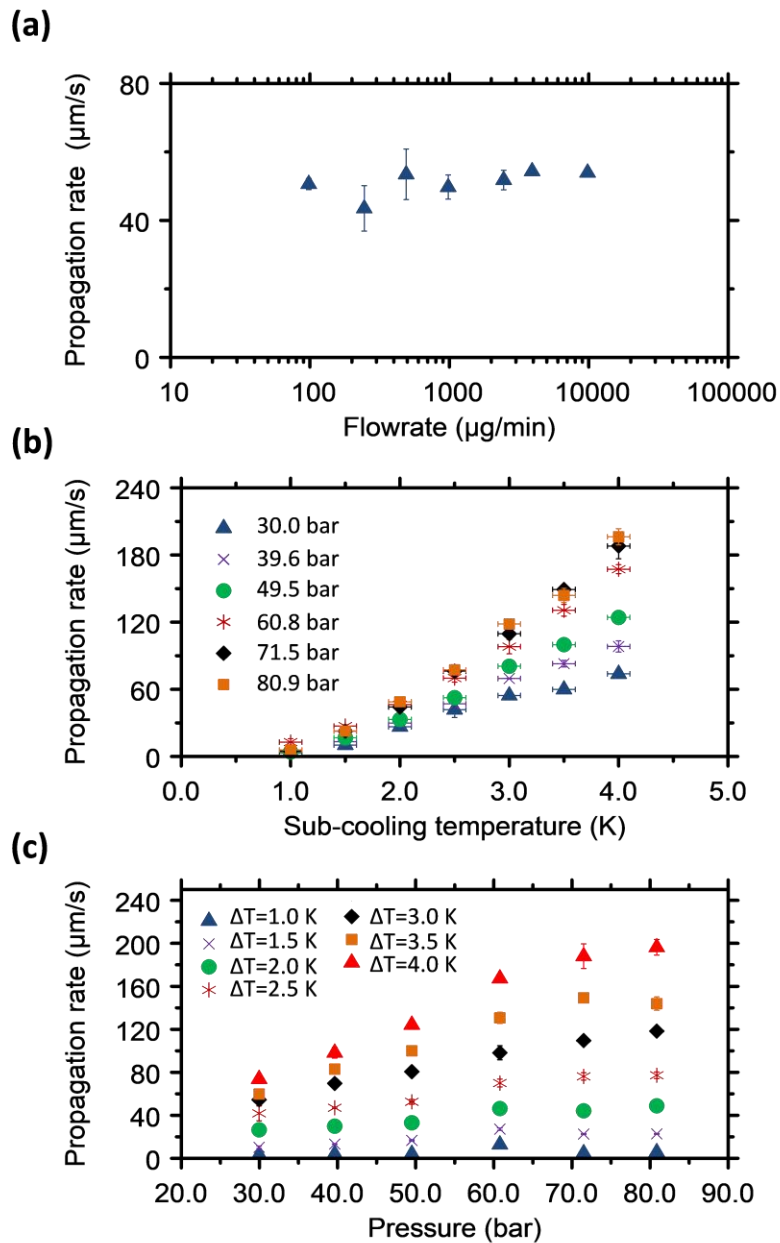
Figure 2.10 (a) Propagation rates of methane hydrate measured at different flowrates of methane (at 60.8 bar and 2.0 K sub-cooling). (b) Propagation rates measured for different sub-cooling temperatures at constant pressure (methane flowrate = 2453 µg/min). (c) Propagation rates measured at different pressures at constant sub-cooling temperatures (methane flowrate = 2453 µg/min).

Figure 2.10 (b) & (c) report the propagation rates of methane hydrate for different pressures (from 30.0 to 80.9 bar) and sub-cooling temperatures (from 1.0 K to 4.0 K) at a flowrate of 2453 μg/min. As can be seen, the propagation rate increases when the sub-cooling temperature increases at constant pressure. The propagation rate also increased with an increase in the pressure for constant sub-cooling in the range of 4.0 K. These general observations are in good agreement with those reported for moderate to high sub-cooling temperatures. [13,17,20] Closer examination of propagation at low sub-cooling temperatures motivates the need for new predictive models derived from first principles. Figure 2.10 (b) can be divided into at least two regions: low sub-cooling temperatures and moderate sub-cooling temperatures. At low sub-cooling (*e.g.*, $\Delta T < 2.0$ K), the propagation rate at different pressures followed a similar trend, independent of the pressure, with respect to the sub-cooling temperature. These observations support that heat transfer controlled the propagation. At moderate sub-cooling (*e.g.*, 2.0 K $< \Delta T < 4.0$ K), the propagation rate increased as pressure increased at a fixed sub-cooling temperature. The heat transfer alone could not account for this phenomenon. Recall that the intrinsic crystal growth rate and the flux of methane are both functions of the methane concentration. The concentration of methane at the interface is expected to increase with an increase in the pressure. Furthermore, an increase in the sub-cooling is expected to decrease the molecular diffusivity of methane within the thin film by a significant factor (see Figure 2.11).[52] This implies that at moderate sub-cooling temperatures, the crystal growth kinetics should consider intrinsic growth, mass transfer, and heat

- 67 -

transfer. Based on this information, we can now derive (from first principles) a theoretical model for hydrate growth for low to moderate sub-cooling.
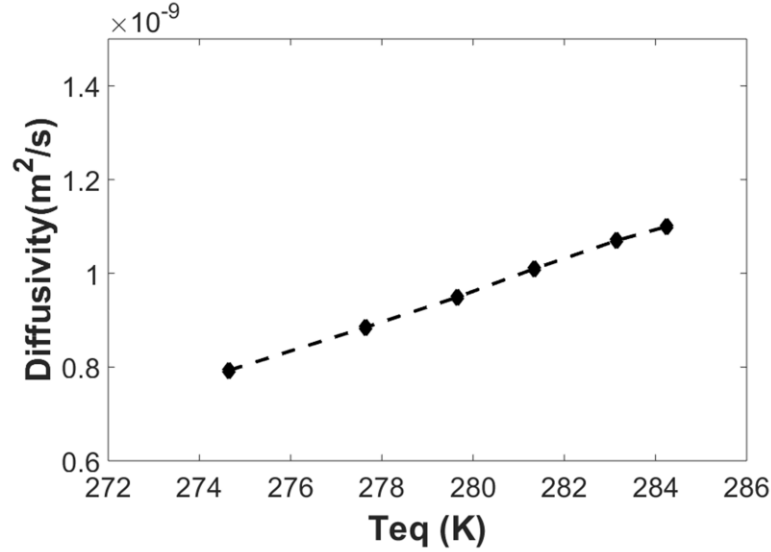
Figure 2.11 The correlation of diffusivity to temperature based on Stokes-Einstein equation.

2.3.7 Theoretical prediction of hydrate growth kinetics

The growth of methane hydrate is a complex process that can be governed by heat transfer, mass transfer, intrinsic crystallization, or a combination of all three. Here we consider the steady-state propagation of a crystalline film of the same thickness at the methane-water interface and axially down the length of a microchannel. The crystal growth rate is determined by the rate-limiting step among the heat transfer and crystallization rate. One can derive the following expression for the overall crystal growth rate (r_t) based on electrical analog as describe in literature:[52]

$$r_t = \frac{1}{\left[\left(\frac{1}{r_h}\right)+\left(\frac{1}{r_c}\right)\right]} \tag{2.6}$$

- 68 -

where r_h is the heat transfer rate and r_c is the crystallization rate. Here r_c could be the intrinsic rate, a mixed mass-transfer-crystallization rate, or a mass transfer rate. One should consider each contribution to fully understand the propagation of hydrate crystals.

2.3.7.a Heat transfer rate

The crystallization of methane hydrate is an exothermic process. The liberation of the heat of crystallization is essential to keep the propagation front below temperatures where hydrates are thermodynamically stable (*i.e.*, the phase boundary temperature). Figure 2.12 (a) illustrates hydrate propagation along the methane-water interface. As shown, the temperature profile depends on the phase boundary temperature (T_{eq}), the temperature of the adsorption layer-stagnant film interface (T_i), and the temperature of the bulk liquid ahead of the propagating film (T_b). Here, the energy balance on the interface was applied to obtain the expression of the propagation rate based on conductive heat transfer domination of the process. The energy balance on the adsorption layer yields the rate of heat transfer across the adsorption layer,

$$\left(\frac{dq}{dt}\right)_i = h_i A(T_{eq} - T_i) \qquad (2.7)$$

where A is the cross-sectional area of the film and h_i is the heat transfer coefficient of the adsorption layer, defined by,

$$h_i = \frac{\kappa_i}{\delta_i} \qquad (2.8)$$

- 69 -
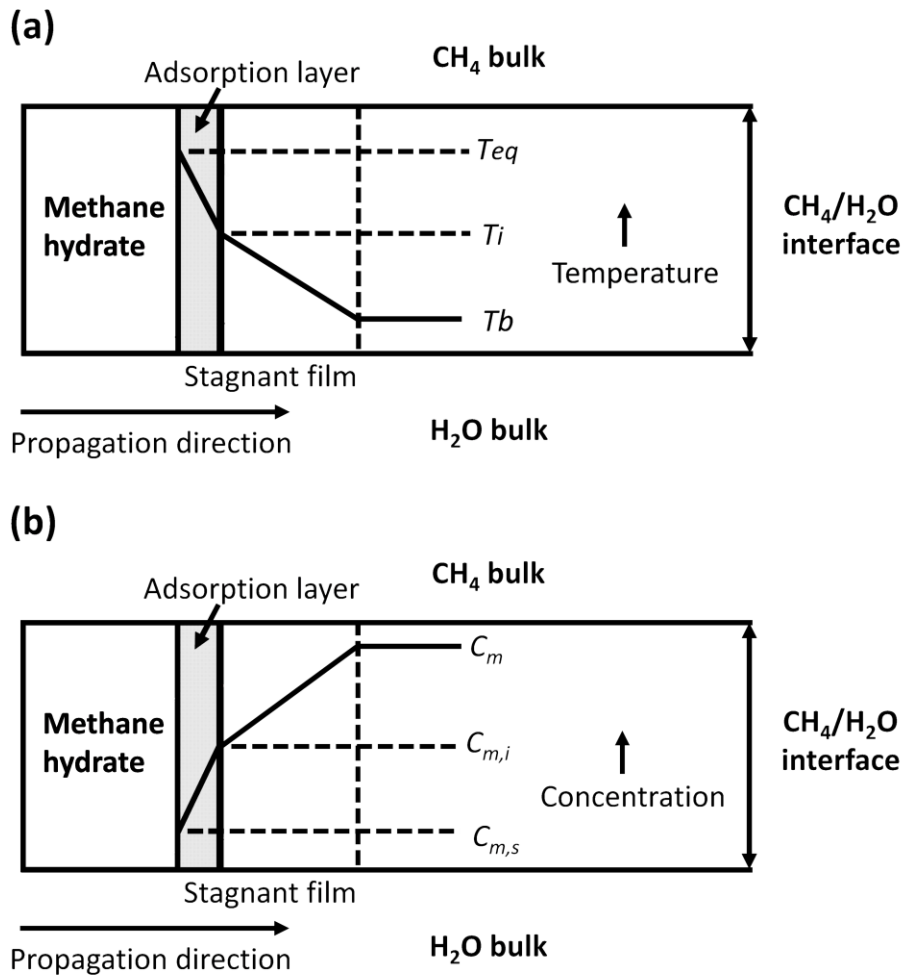
Figure 2.12 Schematic of the methane hydrate propagation interface. (a) The temperature profile depends on the phase boundary temperature (T_{eq}), the temperature of the adsorption layer-stagnant film interface (T_i), and the temperature of the bulk liquid ahead of the propagating film (T_b). (a) Fickian diffusion through the film is driven by the difference between the concentration at the adsorption layer-stagnant film interface ($C_{m,s}$) and the bulk methane concentration (C_m) ahead of the propagating front.

Here κ_i is the thermal conductivity and δ_i is the thickness of the adsorption layer. Similarly, the rate of heat transfer across the stagnant film can be expressed as,

- 70 -

$$\left(\frac{dq}{dt}\right)_s = h_s A(T_i - T_b) \tag{2.9}$$

$$h_s = \frac{\kappa_s}{\delta_s} \tag{2.10}$$

Here h_s is the heat transfer coefficient of the stagnant film, κ_s is the thermal conductivity, and δ_s is the thickness of the stagnant film. At steady-state, the heat transfer rate in either the adsorption layer or the stagnant film is equal. Since the temperature at the interface T_i and the thicknesses δ_i and δ_s are difficult to directly measure, equations 2.7 and 2.9 may be expressed by,[6]

$$\left\{ \begin{array}{l} r_h = h' A(T_{eq} - T_b)^n \\ \quad = h_i A(T_{eq} - T_i) \\ \quad = h_s A(T_i - T_b) \end{array} \right\} \tag{2.11}$$

where h' is the effective heat transfer coefficient and the exponent n is the order of the overall heat transfer process. Values of n have previously been reported in the range of 1.5 to 2.5 for heat-transfer-dominated hydrate crystallizations.[6] The heat generated can be further expressed in terms of the propagation rate ($\frac{dx}{dt}$) and the enthalpy of hydrate crystallization (ΔH),

$$\left(\frac{dq}{dt}\right)_g = \frac{dm}{dt}\Delta H = \frac{dx}{dt}A\rho_H\Delta H \tag{2.12}$$

where ρ_H is the hydrate density (~920 kg/m^3), and ΔH is 436.5 kJ/kg.[1] Equation 2.12 implies the relationship between the heat required and propagation rate of methane hydrate. Based on our conditions, an order of magnitude smaller propagation rate (minimum 3.1 μm/s) was observed than propagation rate in previous work (minimum 21 μm/s).[17] The rate of heat added or removed by

conduction from the microreactor indeed is proportional to the temperature gradient (i.e., the driving force). It is important to note that we examined sub-cooling temperatures on the order of 1 K whereas previous works have focused primarily on sub-cooling on the order of 10 K. Thus, the present work examines conditions where methane hydrates form even when the rate of heat removed from the system is an order of magnitude less than conventional experiments designed to study hydrates. The thermal conductivity of our silicon reactor is also 1 to 2 orders of magnitude larger than the thermal conductivities of reactor materials (e.g., glass and stainless steel) used previously to study hydrates. Upon substitution of equation 2.12 into 2.11, one can obtain the propagation rate when heat transfer controls crystal growth,

$$\frac{dx}{dt} = \frac{h'(T_{eq} - T_b)^n}{\rho_H \Delta H} \tag{2.13}$$

2.3.7.b Mixed mass-transfer-crystallization kinetics.

From the molecular-level prospective, the crystallization of hydrate is the rearrangement of water clusters and their surface integration at a gas-liquid-solid interface. Crystallization occurs at the propagation front, and thus methane must diffuse to the adsorption layer (see Figure 2.12 (b)). Therefore, the potential exists for mass transfer within the methane-water interface to control the hydrate propagation, especially for mild sub-cooling. Equating the intrinsic crystal growth rate r_i to the flux W_i gives,[52]

$$r_i = W_i a = ka C_{w,s}^{\alpha} C_{m,s}^{\beta} \tag{2.14}$$

- 72 -

where k is the specific crystallization rate, a is the interface area per unit volume, $C_{w,s}$ and $C_{m,s}$ are concentrations of water and methane at the adsorption layer-stagnant film interface, and α and β are the reaction orders of water and methane, respectively. Here we assume that methane is the limiting reactant due to its low solubility. The resultant mixed mass-transfer-crystallization limited rate for first order kinetics is written as,

$$r_c = k_{eff} a C_m \tag{2.15}$$

where C_m is the concentration of methane at the interface, and k_{eff} is the effective specific crystallization rate, defined as,

$$k_{eff} = \frac{k' k_C}{k' + k_C} \tag{2.16}$$

where k_C is the mass transport coefficient of methane,

$$k_C = \frac{D}{\delta_s} \tag{2.17}$$

and D is the diffusivity of methane within thin film. The apparent specific crystallization rate constant in excess water (k') is readily available by the Arrhenius expression,

$$k' = k C_{w,s}^{\alpha} = A exp\left[-\frac{E_a}{RT_{eq}}\right] \tag{2.18}$$

where E_a is the activation energy, and A is the pre-exponential factor. From equation 2.16, when mass transfer controls crystallization $k_{eff} = k_C$, and when crystallization

is intrinsic $k_{eff} = k'$. The rate of methane hydrate formation $\left(\frac{dm}{dt}\right)_g$ could be expressed in terms of propagation rate $\frac{dx}{dt}$ through the equation,

$$\left(\frac{dm}{dt}\right)_g = \frac{dx}{dt} a \rho_H \qquad (2.19)$$

A mass balance was performed on methane yields the relationship between the methane consumption rate and the methane hydrate formation rate,

$$\frac{r_c M_{CH4}}{\omega_{CH4}} = \left(\frac{dm}{dt}\right)_g \qquad (2.20)$$

where ω_{CH4} is the weight fraction of methane in the hydrate (~0.13), and M_{CH4} is the molecular weight of methane (0.016 kg/mol). Combination of equation 2.15, 2.16, 2.19 and 2.20, one could obtain the expression of propagation rate at the front when mixed mass-transfer-crystallization-limited kinetics control the hydrate film growth,

$$\frac{dx}{dt} = \left(\frac{k'k_C}{k'+k_C}\right)\left(\frac{M_{CH4}}{\omega_{CH4}\rho_H}\right) C_m \qquad (2.21)$$

Here ω_{CH4} is the weight fraction of methane in the hydrate (~0.13), and M_{CH4} is the molecular weight of methane (0.016 kg/mol).

Finally, one can consider the combined role of heat transfer, mass transfer, and the intrinsic kinetics when predicting methane hydrate crystal growth. Combining equations (2.21) and (2.13) into (2.6) gives the overall propagation rate:

$$\frac{dx}{dt} = \frac{1}{\left[\left(\frac{\rho_H \Delta H}{h'(T_{eq}-T_b)^n}\right)+\left(\frac{k'+k_C}{k'k_C}\right)\left(\frac{\omega_{CH4}\rho_H}{M_{CH4}C_m}\right)\right]} \qquad (2.22)$$

The resulting model has four unknown parameters (h', k', k_C, and n), which are readily obtained using nonlinear regression based on the least-squares method.

- 74 -

Fitting the parameters revealed interesting and useful results. The value of *n* was discovered to be constant and equal to 2.5 for all conditions, which is consistent with the values reported by Mullin (*n* = 1.5-2.5) for heat transfer dominated crystallizations. [6] The non-unity value of *n* indicates the non-linear temperature gradient across the stagnant film, likely due to changes in the thermal conductivity brought about by the concentration gradient of methane across the stagnant film.[53] Recall that heat transfer in our microsystem is dominated by conduction. Table 2.2 summarizes the fitted kinetic parameters of equation (2.22). As expected, values of *h'* increased as the pressure of the system increased, in good agreement with literature for heat-transfer-limited models.[53] Calculation of the activation energy of surface integration, available by equation (2.18), was found to be 64.83 kJ/mol and slightly higher than the values reported by Mullin (40-60 kJ/mol).[6] The resultant pre-exponential factor (A) was calculated to be 3.25×10^9 m/s. Estimation of the thickness of the stagnant film based on equation (2.17), $\delta_S = 0.13$ µm, was possible by values of k_C. Binary diffusion of methane in water is expected to follow the correlation:[52]

$$D(T_2) = D(T_1) \left(\frac{\mu_1}{\mu_2}\right)\left(\frac{T_2}{T_1}\right) \tag{2.23}$$

From equation (2.23), the diffusivity of methane in water was correlated with the temperature. As expected, the molecular diffusivity decreases with an increase in the viscosity or a decrease in the phase boundary temperature.

The true contribution of heat transfer, mass transfer, and intrinsic crystal growth can be distinguished by dimensionless analysis. Estimation of the Lewis number

(*Le*) in the range of 128-207 is some indication that mass transport influenced the kinetics (see Table 2.2). Since the driving force for heat transfer

Table 2.2 Fitted model parameters and dimensionless values at different experimental conditions

T_{eq} (K)	P (bar)	$h' \times 10^3$ (W·K$^{2.5}$·m^{-2})	$k' \times 10^3$ (m/s)	$k_c \times 10^3$ (m/s)	M_H	$\beta_B{}^a$	$\beta_B{}^b$
274.65	30.0	2.36	1.48	5.98	0.50	0.79	25.1
277.65	39.6	2.55	2.01	6.70	0.55	1.31	41.4
279.65	49.5	2.65	2.46	7.18	0.59	1.92	60.6
281.35	60.8	3.09	2.91	7.59	0.62	2.40	75.6
283.15	71.5	3.44	3.54	8.07	0.66	3.08	97.0
284.25	80.9	3.57	3.86	8.31	0.68	3.69	116

a Calculated at maximum sub-cooling temperature in the study (4.0 K)

b Calculated at minimum sub-cooling temperature in the study (1.0 K)

is three orders of magnitude less than that for mass transfer at low sub-cooling temperature, ($\Delta C \approx 1.5 \times 10^3$ mol/m^3 at 60 bar, $\Delta T = 2.0$ K) the potential exists for either heat or mass transfer resistances to control the process. Calculation of the Beta number (β_B) reveals which contribution dominates.[54] As can be seen in Table 2.2, values of β_B range from 0.79-116 for our experimental conditions. At moderate sub-cooling, the intrinsic crystal growth rate was less than or approximately the same order of magnitude as the heat transfer rate. At low sub-cooling, the intrinsic crystal growth rate was at least two orders of magnitude greater than the heat transfer
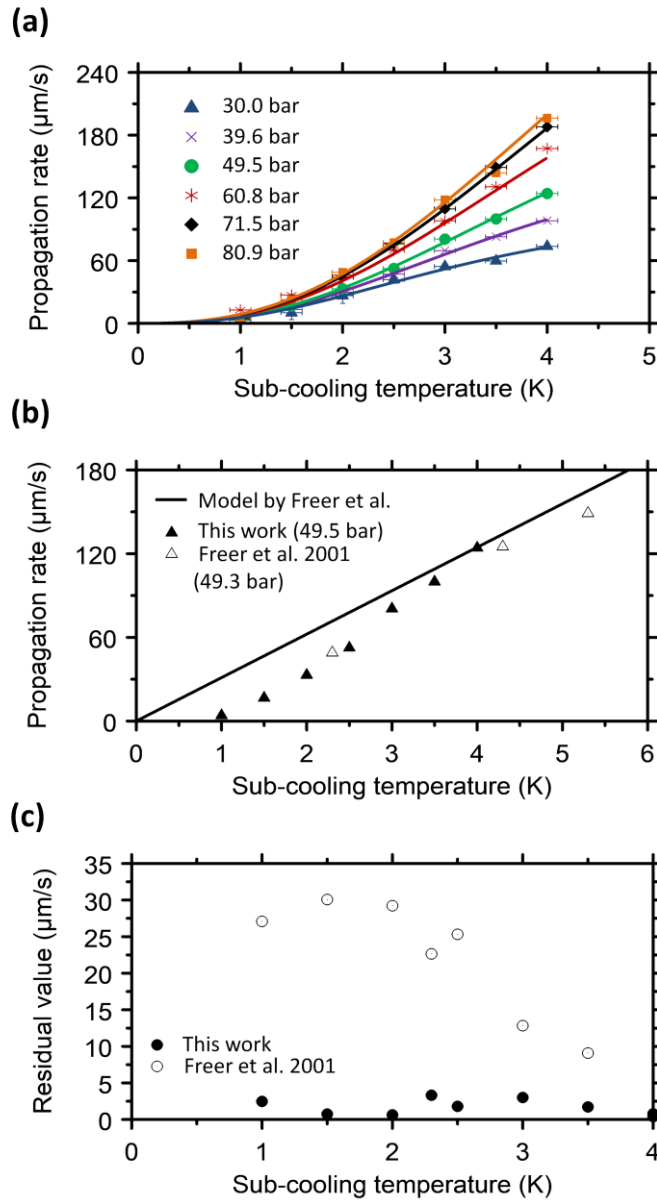
Figure 2.13 (a) A comparison of mixed heat and mass-transport-limited model with experiment. (b) Extrapolation of a heat transfer dominated model by Freer et al. to data in the present study at 49.5 bar for sub-cooling from 1.0 to 4.0 K. (c) Residuals calculated for mixed heat-transfer-crystallization-limited (empty circles) and mixed heat-transfer-mass-transfer-crystallization-limited (filled circles) kinetics. The data shows the contribution of mass transfer limitations.

rate. A similar analogy can be made by estimation of the Hatta number (M_H). Values $0.02 < M_H < 2.0$ indicate mixed mass-transfer-reaction-rate limitations. From Table 2.2, M_H values ranged from 0.50-0.68, confirming indeed that mass transfer resistances influenced the hydrate crystal growth.

Figure 2.13 (a) shows a comparison of the mixed heat-transfer-mass-transfer-crystallization-limited model with the measured propagation rates. Different colours denote the propagation rates at each pressure with their corresponding predictions. The model appears to be in excellent agreement with the data, which is further validated by a comparison of heat transfer-crystallization-limited kinetics[17,18,20]. At first glance (Figure 2.13 (b)) extrapolation of a mixed heat-transfer-limited model to sub-cooling < 4.0 K does not accurately describe our work. Calculation of the residuals, shown in Figure 2.13 (c), further confirms that mixed-transport limitations are more important as the sub-cooling temperature is decreased. Here, the residuals are the difference between the theoretical values predicted by models and our experimental values. Although the model presented here was derived for methane (sI) hydrate crystallization, one could extend the same approach to discover transport limited kinetics of other multiphase, high-pressure, and sub-cooled flash crystallizations with knowledge of the properties of the materials.

2.4 Conclusion

The present work established a new methodology to study the growth of methane (sI) hydrate thin films. Design of a thermoelectrically-cooled microreactor allowed stepwise changes in the crystal growth temperature, and in turn reduced the

experiment time from hours-to-days to seconds-to-minutes. The results indicated that the propagation rate is dependent on both temperature and pressure rather than the flowrate of methane. It was discovered that external mass transfer resistances can be neglected, yet the diffusive flux within the stagnant film ahead of crystal propagation is an important consideration.

Dimensional analyses revealed the influence of heat and mass transfer. Estimations of the Lewis number supports that the diffusive flux could influence hydrate crystal growth, while calculation of the Hatta number demonstrates conclusively a mixed-mass-transfer-crystallization-limited process. Further evaluation of the Beta number revealed that heat transfer resistances and intrinsic crystal growth are of similar magnitude, depending on the sub-cooling temperature (in the range of 1.0-4.0 K). A comprehensive model was derived, from first principles, that describes the contributions of heat transfer, mass transfer, and intrinsic crystal growth. Comparison with previous work confirmed that mass transfer resistances should not be neglected when predicting methane hydrate crystal growth for sub-cooling from 1.0-4.0 K. The discoveries reported in this study could help advance the science of other multiphase, high-pressure, and sub-cooled crystallizations.

Reference

(1)   Sloan, E. D.; Koh, A. C. *Clathrate Hydrates of Natural Gases*, 3rd Edn.; CRC Press Taylor & Francis Group, 2007.

(2)   Larson, M. A.; Garside, J. Solute Clustering and Interfacial Tension. *J. Cryst. Growth* **1986**, *76* (1), 88–92.

(3)   Larson, M. A.; Garside, J. Solute Clustering in Supersaturated Solutions. *Chem. Eng. Sci.* **1986**, *41* (5), 1285–1289.

(4)   Englezos, P.; Kalogerakis, N.; Dholabhai, P. D. D.; Bishnoi, P. R. R. Kinetics of Formation of Methane and Ethane Gas Hydrates. *Chem. Eng. Sci.* **1987**, *42* (11), 2647–2658.

(5)   Englezos, P.; Kalogerakis, N.; Dholabhai, P. D.; Bishnoi, P. R. Kinetics of Gas Hydrate Formation from Mixtures of Methane and Ethane. *Chem. Eng. Sci.* **1987**, *42* (11), 2659–2666.

(6)   Mullin, J. *Crystallization*, 4th edn.; Butterworth-Heinemann, A division of Reed Educational and Professional Publishing Ltd, 2001.

(7)   Huo, Z.; Freer, E.; Lamar, M.; Sannigrahi, B.; Knauss, D. .; Sloan, E. . Hydrate Plug Prevention by Anti-Agglomeration. *Chem. Eng. Sci.* **2001**, *56* (17), 4979– 4991.

(8)   Moon, C.; Taylor, P. C.; Rodger, P. M. Molecular Dynamics Study of Gas Hydrate Formation. *J. Am. Chem. Soc.* **2003**, *125*, 4706–4707.

(9)   Kashchiev, D.; Firoozabadi, A. Nucleation of Gas Hydrates. *J. Cryst. Growth* **2002**, *243* (3–4), 476–489.

- 80 -

(10)   Østergaard, K. K.; Tohidi, B.; Burgass, R. W.; Danesh, A.; Todd, A. C. Hydrate Equilibrium Data of Multicomponent Systems in the Presence of Structure-II and Structure-H Heavy Hydrate Formers. *J. Chem. Eng. Data* **2001**, *46* (3), 703–708.

(11)   Skovborg, P.; Ng, H. J.; Rasmussen, P.; Mohn, U. Measurement of Induction Times for the Formation of Methane and Ethane Gas Hydrates. *Chem. Eng. Sci.* **1993**, *48* (3), 445–453.

(12)   Fandiño, O.; Ruffine, L. Methane Hydrate Nucleation and Growth from the Bulk Phase: Further Insights into Their Mechanisms. *Fuel* **2014**, *117*, 442–449.

(13)   Taylor, C. J.; Miller, K. T.; Koh, C. A.; Dendy Sloan Jr, E. Macroscopic Investigation of Hydrate Film Growth at the Hydrocarbon/Water Interface. *Chem. Eng. Sci.* **2007**, *62*, 6524–6533.

(14)   Takeya, S.; Hori, A.; Hondoh, T.; Uchida, T. Freezing-Memory Effect of Water on Nucleation of CO2 Hydrate Crystals. *J. Phys. Chem. B* **2000**, *104* (17), 4164–4168.

(15)   Skovborg, P.; Rasmussen, P. A Mass Transport Limited Model for the Growth of Methane and Ethane Gas Hydrates. *Chem. Eng. Sci.* **1994**, *49* (8), 1131–1143.

(16)   Buanes, T.; Kvamme, B.; Svandal, A. Computer Simulation of CO2 Hydrate Growth. *J. Cryst. Growth* **2006**, *287* (2), 491–494.

(17)   Freer, E. M.; Selim, M. S.; Dendy Sloan Jr, E. Methane Hydrate Film Growth Kinetics. *Fluid Phase Equilib.* **2001**, *185*, 65–75.

(18)   Mochizuki, T.; Mori, Y. H. Clathrate-Hydrate Film Growth along Water/Hydrate-Former Phase Boundaries-Numerical Heat-Transfer Study. *J. Cryst. Growth* **2006**, *290* (2), 642–652.

(19)   Gayet, P.; Dicharry, C.; Marion, G.; Graciaa, A.; Lachaise, J.; Nesterov, A. Experimental Determination of Methane Hydrate Dissociation Curve up to 55 MPa by Using a Small Amount of Surfactant as Hydrate Promoter. *Chem. Eng. Sci.* **2005**, *60*, 5751–5758.

(20)   Uchida, T.; Ebinuma, T.; Kawabata, J.; Narita, H. Microscopic Observations of Formation Processes of Clathrate-Hydrate Films at an Interface between Water and Carbon Dioxide. *J. Cryst. Growth* **1999**, *204*, 348–356.

(21)   Duan, Z.; Møller, N.; Greenberg, J.; Weare, J. H. The Prediction of Methane Solubility in Natural Waters to High Ionic Strength from 0 to 250C and from 0 to 1600 Bar. *Geochim. Cosmochim. Acta* **1992**, *56* (4), 1451–1460.

(22)   Dhouib, K.; Malek, K.; Pfleging, W.; Gauthier-manuel, B.; Duffait, R.; Gieg, R. Microfluidic Chips for the Crystallization of Biomacromolecules by Counter-Diffusion and on-Chip Crystal X-Ray Analysis. *Lab Chip* **2009**, *9* (9), 1412–1421.

(23)   Aijian, A.; Chatterjee, D.; Garrell, R. Lab on a Chip Fluorinated Liquid-Enabled Protein Handling and Surfactant-Aided Crystallization for Fully in Situ Digital Microfluidic MALDI-MS Analysis. *Lab Chip* **2012**, *12*, 2552–2559.

(24)   Li, S.; Ihli, J.; Marchant, W. J.; Zeng, M.; Chen, L.; Wehbe, K.; Cinque, G.; Cespedes, O.; Kapur, N.; Meldrum, F. C. Synchrotron FTIR Mapping of Mineralization in a Microfluidic Device. *Lab Chip* **2017**, *17*, 1616–1624.

(25)   Mies, M. J. M.; Rebrov, E. V; Jansen, J. C.; Croon, M. H. J. M. De; Schouten, J. C. Method for the in Situ Preparation of a Single Layer of Zeolite Beta Crystals on a Molybdenum Substrate for Microreactor Applications. *J. Catal.* **2007**, *247*, 328–338.

(26) Liu, N.; Aymonier, C.; Lecoutre, C.; Garrabos, Y.; Marre, S. Microfluidic Approach for Studying CO 2 Solubility in Water and Brine Using Confocal Raman Spectroscopy. *Chem. Phys. Lett.* **2012**.

(27) Fletcher, P. D. I.; Haswell, S. J.; Zhang, X. Monitoring of Chemical Reactions within Microreactors Using an Inverted Raman Microscopic Spectrometer. *Electrophoresis* **2003**, *24* (18), 3239–3245.

(28) Pinho, B.; Hartman, R. L. Microfluidics with In Situ Raman Spectroscopy for the Characterization of Immiscible Non-Polar/Aqueous Interfaces. *React. Chem. Eng.* **2016**, *2*, 189–200.

(29) Chan, J. W.; Winhold, H.; Lane, S. M.; Huser, T. Optical Trapping and Coherent Anti-Stokes Raman Scattering (CARS) Spectroscopy of Submicron-Size Particles. *IEEE J. Sel. Top. Quantum Electron.* **2005**, *11* (4), 858–863.

(30) Leung, S.-A.; Winkle, R. F.; Wootton, R. C. R.; deMello, A. J. A Method for Rapid Reaction Optimisation in Continuous-Flow Microfluidic Reactors Using Online Raman Spectroscopic Detection. *Analyst* **2005**, *130* (1), 46.

(31) Tohidi, B.; Anderson, R.; Clennell, M. B.; Burgass, R. W.; Biderkab, A. B. Visual Observation of Gas-Hydrate Formation and Dissociation in Synthetic Porous Media by Means of Glass Micromodels. *Geology* **2001**, *29* (9), 867–870.

(32) Hartman, R. L.; Jensen, K. F. Microchemical Systems for Continuous-Flow Synthesis. *Lab Chip* **2009**, *9* (17), 2495–2507.

(33) Marre, S.; Adamo, A.; Basak, S.; Aymonier, C.; Jensen, K. F. Design and Packaging of Microreactors for High Pressure and High Temperature Applications. *Ind. Eng. Chem. Res.* **2010**, *49* (22), 11310–11320.

- 83 -

(34) Hu, C.; Hartman, R. L. High-Throughput Packed-Bed Microreactors with In-Line Analytics for the Discovery of Asphaltene Deposition Mechanisms. *AIChE J.* **2014**, *60* (10), 3534–3546.

(35) Hu, C.; Morris, J. E.; Hartman, R. L. Microfluidic Investigation of the Deposition of Asphaltenes in Porous Media. *Lab chip* **2014**, *14* (12), 2014–2022.

(36) NIST Standard Reference Databse #69.

(37) Casco, M. E.; Silvestre-Albero, J.; Ramírez-Cuesta, A. J.; Rey, F.; Jordá, J. L.; Bansode, A.; Urakawa, A.; Peral, I.; Martínez-Escandell, M.; Kaneko, K. Methane Hydrate Formation in Confined Nanospace Can Surpass Nature. *Nat. Commun.* **2015**, *6*.

(38) Ohmura, R.; Ogawa, M.; Yasuoka, K.; Mori, Y. H. Statistical Study of Clathrate-Hydrate Nucleation in a Water/Hydrochlorofluorocarbon System: Search for the Nature of the "Memory Effect." *J. Phys. Chem. B* **2003**, *107* (22), 5289–5293.

(39) Vysniauskas, A.; Bishnoi, P. R. A Kinetic Study of Methane Hydrate Formation. *Chem. Eng. Sci.* **1983**, *38* (7), 1061–1072.

(40) Lederhos, J. P.; Long, J. P.; Sum, A.; Christiansen, R. L.; Sloan, E. D. Effective Kinetic Inhibitors for Natural Gas Hydrates. *Chem. Eng. Sci.* **1996**, *51* (8), 1221–1229.

(41) Parent, J. S.; Bishnoi, P. Investigations Into the Nucleation Behaviour of Methane Gas Hydrates. *Chem. Eng. Commun.* **1996**, *144* (1), 51–64.

(42) Korenlein, K.; Muzny, C. D.; Kazakov, A.; Diky, V. V.; Chirico, R. D.; Sloan, E. D.; Frenkel, M. Clathrate Hydrate Physical Property Database.

(43) Long, D. A. *Raman Spectroscopy*; McGraw-Hill, Inc., 1977.

- 84 -

(44) Sum, A. K.; Burruss, R. C.; Sloan, E. D. Measurement of Clathrate Hydrates via Raman Spectroscopy. *J. Phys. Chem. B* **1997**, *101* (38), 7371–7377.

(45) Wopenka.B., P. J. D. Raman Intensities and Detection Limits of Geochemically Relevant Gas Mixtures for a Laser Raman Microprobe. *Anal. Chem.* **1987**, *59*, 2165–2170.

(46) Wopenka.B., P. J. D. Limitations to Quantitative Analysis of Fluid Inclusions in Geological Samples by Laser Raman Microprobe Spectroscopy. *Appl. Specroscopy* **1986**, *40* (2), 144–151.

(47) Ohmura, R.; Kashiwazaki, S.; Mori, Y. H.; Rousseau, R. W. Measurements of Clathrate-Hydrate Film Thickness Using Laser Interferometry. *J. Cryst. Growth* **2000**, *218*, 372–380.

(48) Li, S.-L.; Sun, C.-Y.; Liu, B.; Feng, X.-J.; Li, F.-G.; Chen, L.-T.; Chen, G. Initial Thickness Measurements and Insights into Crystal Growth of Methane Hydrate Film. *AIChE* **2013**, *59*, 2145–2154.

(49) Duan, Z.; Møller, N.; Greenberg, J.; Weare, J. H. The Prediction of Methane Solubility in Natural Waters to High Ionic Strength from 0 to 250C and from 0 to 1600 Bar. *Geochim. Cosmochim. Acta* **1992**, *56* (4), 1451–1460.

(50) Long, J. P.; Sloan, E. D. Hydrates in the Ocean and Evidence for the Location of Hydrate Formation. *Int. J. Thermophys.* **1996**, *17* (1), 1–13.

(51) Sloan, E. D. Fundamental Principles and Applications of Natural Gas Hydrates. *Nature* **2003**, *426* (6964), 353–363.

(52) Fogler, H. S. *Elements of Chemical Reaction Engineering*, 4th Edn.; Pearson Education Inc., 2006.

(53)   Roder, H. M. Thermal Conductivity of Methane for Temperatures between 110 and 310 K with Pressures to 70 MPa. *Int. J. Thermophys.* **1985**, *6* (2), 119–142.

(54)   Hartman, R. L.; McMullen, J. P.; Jensen, K. F. Deciding Whether to Go with the Flow: Evaluating the Merits of Flow Reactors for Synthesis. *Angew. Chem Int. Ed.* **2011**, *50* (33), 7502–7519.

Chapter 3

Methane Hydrate Intrinsic Dissociation Kinetics Measured in A Microfluidic System by Means of *in-Situ* Raman Spectroscopy

The text and figures in this chapter are partially from the paper: Chen, W., and Hartman, R.L., Methane Hydrate Intrinsic Dissociation Kinetics Measured in a Microfluidic System by Means of in Situ Raman Spectroscopy, *Energy Fuels*, **2018**, *32*, 11761-11771.

3.1 Introduction

While the knowledge about methane hydrate formation could assist in risk management during the petroleum production, the knowledge about hydrate dissociation provide the guidance for the resolution of plugging problem inside the pipeline. When a hydrate plug occurs inside the flowline, four types of plug removal method could be applied to remediate the problem after careful evaluation of safety implications: 1) Hydraulic methods, such as depressurization; 2) Chemical methods, such as injection of inhibitors or reactive chemicals that generate heat; 3) Thermal methods, such as direct electrical heating; 4) Mechanical methods, such as drilling etc. When improper removal operation is applied based on an inaccurate assessment, it could cause economic loss and even loss of life. Sloan (2007) pointed out in his book that three characteristics lead to hydrate safety problems: [1]

1. The unmelt hydrate plug could be dislodged at high velocity by upstream pressure. Hydrate density is similar to ice, which could lead to high momentum. This high momentum can fracture the pipe. Besides that, extreme plug momentum and gas compression can cause pipe rupture downstream of the hydrate path.

2. There is no method could predict how many hydrate plugs are formed inside the pipeline. Between adjunct plugs, high differential pressure could be trapped.

3. Density of gas inside hydrate is relatively high (164 volumes (STP) gas per volume of hydrate). Therefore, any confinement could cause the rapid increase of gas pressure during the dissociation.

Figure 3.1 shows two ways a plug can rupture a pipeline. The problem of flow assurance caused by hydrate plug will be increasingly important as the petroleum industry expands
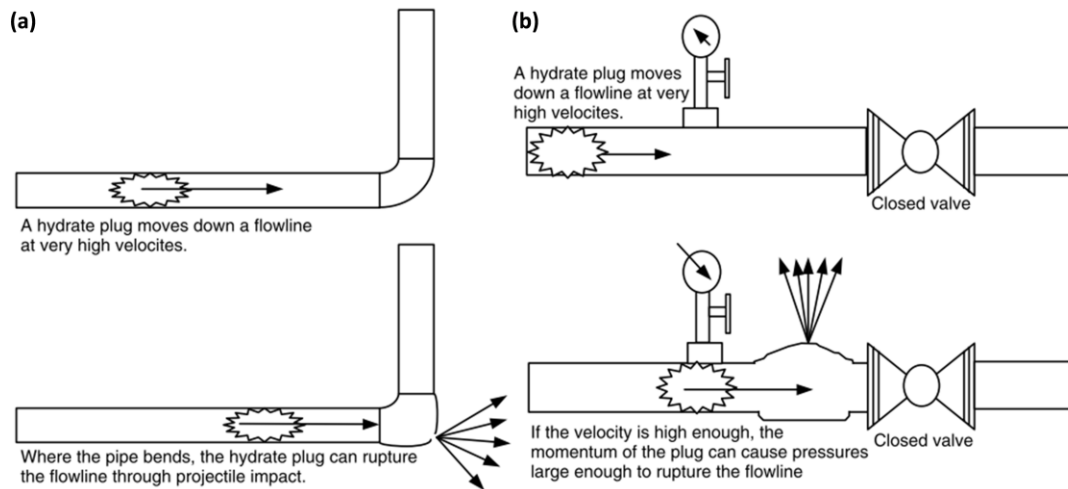
Figure 3.1 Two ways a hydrate plug can rupture a pipeline via (a) the high momentum impact to the pipe bends by high velocity the hydrate plug; (b) combination of high momentum impact and rapid pressurization at confinement space during dissociation.[1]

the production from far-reach regions, such as ultra-deepwater and the arctic. The conceptual understanding combined with knowledge on time-dependent properties of hydrate dissociation process is the key towards the safe operation of hydrate plug removal.

From macroscopic point of view, it is now widely accepted that the dissociation of a hydrate plug inside the channel happens in the radial direction typically rather than previously suggested axial direction. (See Figure 3.2) The major reasons for this phenomenon are: 1) the materials used for pipeline, such as stainless steel, possess relatively high thermal conductivity; 2) dissociation is an endothermal process; 3) the radial plug dimensions are always smaller than longitudinal dimensions; 4) the surface area in the radial direction is larger than in the axial direction, resulting in larger temperature transfer rate in radial direction. X-ray computed tomography (CT) measurement was applied to observe the dissociation of a methane hydrate core.[2] The result provided a direct
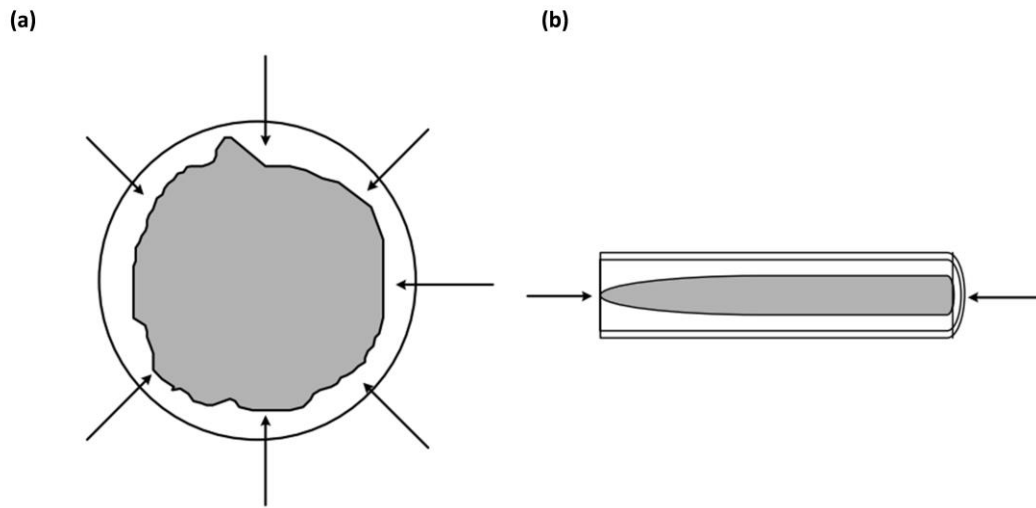
Figure 3.2 Hydrate dissociates in the (a) radial direction and (b) axial direction of the pipe.[1]

evidence towards the radial dissociation model, whereas no evidence of axial dissociation was observed. During the dissociation process, the dissociation front of hydrate would start from outer layer and move inward. The water phase from melt hydrate surrounds the hydrate core and acts as heat transfer media for energy to transfer from pipeline to the dissociation front since the dissociation is an endothermal process. Conduction heat transfer followed Fourier's Law is the dominated mechanism for the process as the water phase is often considered as stationary. From molecular point of view, the process of hydrate dissociation involves the breakage of hydrogen bonding among host water molecules, and van der Waals interaction forces between guest molecules and water molecules. The hydrate is then decomposed into hydrocarbon gas and water. The dissociation process usually happened at low pressure, at which the concentration of gas in hydrate is larger than in free gas. In addition to the fact that hydrocarbon gases have low solubility in water, gases would diffuse from water phase and become bulk gas phase. The process involves heat transfer, mass transfer and intrinsic kinetics.

- 90 -

Considerable attention has been given to the kinetics study of methane hydrate dissociation.[1,3–28] Although numerous models on methane hydrate dissociation kinetics have been developed, many are specific to the constraints of the experimental apparatus used to derive the models. Hydrate dissociation has been studied using non-adiabatic systems where heat transfer by the surroundings influences the kinetics.[13,14,18,19] Heat transfer profiles can vary from one experimental apparatus to another, which makes the validation of computationally-derived models a challenge. Moreover, sensitive and step-input control of the dissociation temperature is difficult to achieve in conventional batch systems due to their large thermal mass and the heat transfer being controlled by convection and conduction. As a consequence, the depressurization method is the most common way to study methane hydrate dissociation. However, during the depressurization, the disturbance of the system is stochastic and introduces another unpredictable factor.[13,18] These reasons motivate the design of novel laboratory techniques that utilize the temperature change method to study methane hydrate dissociation.

In addition to the heat transfer design, the method of characterization is also important for the study of methane hydrate dissociation. In general, there are two common methods of measuring the dissociation rate: i) measurement of the volume of gas released and ii) direct measurement of the crystal dissociating by an analytical method such as Raman spectroscopy. Measurement of the gas volume provides the overall dissociation rate, while Raman spectroscopy can yield *in-situ* information. Raman spectroscopy has been widely used to study the dissociation of methane hydrates.[4,9,12,18] However, heat effects caused by laser light were sometimes ignored. Precautionary measurements must be conducted, as we will introduce later in our findings, to ensure that such heat effects have negligible

influence on dissociation rate measurements, as fractional changes in the temperature can drastically influence whether heat transfer controls the kinetics. New methods of studying methane hydrate dissociation with better control of system's conditions are needed, and in-situ characterization can play an important role.

Microfluidics with *in-situ* spectroscopy are appropriate tools for studying the kinetics of chemical processes.[29] Miniaturization can create ideal heat and mass transfer conditions by increasing of the surface contact area and forcing conductive heat transfer only. In the present work, methane hydrate dissociation kinetics were studied by a microfluidic device with thermoelectric cooling that is capable of incremental changes in the temperature of the system within a few seconds.[30] The isothermal conditions helped to distinguish the contribution of heat transfer and intrinsic kinetics during the dissociation of methane hydrate. Our results indicated the contribution of heat transfer and intrinsic kinetics depended on the initial methane hydrate film thickness, temperature of the system, pressure, and the time. Our findings report kinetics where the contribution of intrinsic kinetics dominated over heat transfer, which is contrary to previous investigations. Where the initial thickness of methane hydrate is as thin as tens-of-microns, the dissociation process was dominated by intrinsic kinetics. Furthermore, we provided a possible explanation to the *"memory effect"* of methane hydrate crystallization that had been reported in the literature, which stated that hydrate forms more easily from melting hydrate than fresh water.

3.2 Experimental section

3.2.1 Design and assembly of microfluidic system

Design and fabrication of the microfluidic system used the same methodology as described in previous literature.[30–32] In brief, a two-dimensional design of the microreactor was created by AutoCAD (Figure 3.3 (a)). Then traditional microelectronics processing techniques were applied to etch the 400x400 μm cross-section microchannels on a 0.725-
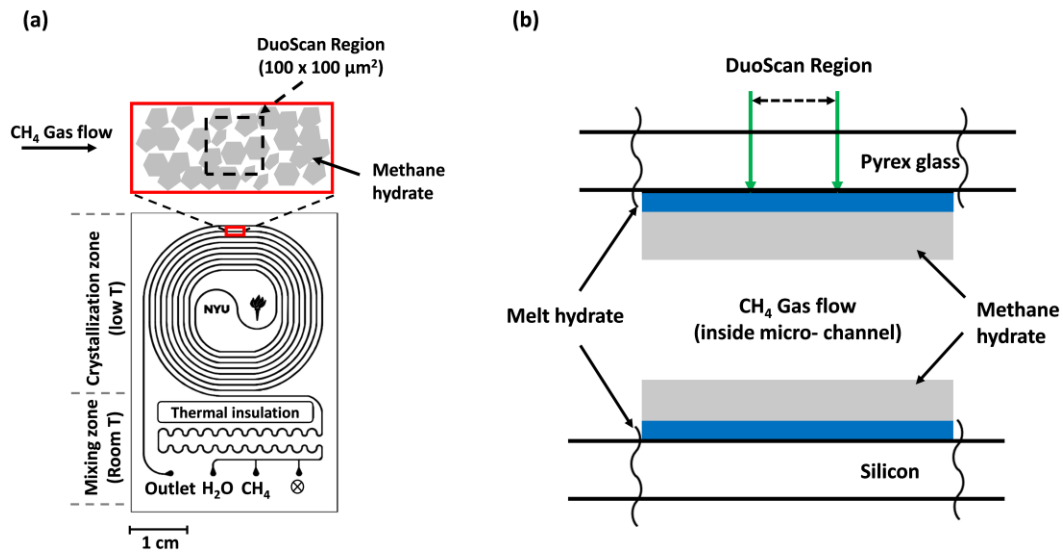
Figure 3.3 (a) Schematic and design of microreactor with serpentine channel. Methane hydrate dissociates inside the microchannels with methane gas flowing. The DuoScan acquisition mode of Raman spectroscopy is applied to monitor the growth/dissociation of methane hydrate at a 100 x 100 μm^2 region inside microchannel. (b) Schematic of the cross-section inside the microchannel. Methane hydrate dissociates in the radial direction of the channel.

mm thick silicon wafer by Little Things Factory GmbH, Elsoff, Germany. A 1-mm Pyrex®

glass was anodically bonded to the wafer to create three-dimensional microchannels. A through-hole etch on the silicon wafer was used as thermal isolation to separate the entrance temperature conditions (18.0 μL) from the crystallization zone (110.8 μL). The materials of construction enable operation of the device at elevated pressure (up to ~80 bar).

The microsystem, integrated with thermoelectric cooling and a stainless-steel compression fitting, was designed to control the temperature of the system and the delivery of the fluids. The combination of the TEC device (TE Technology HP-127-1.4-1.5-74, max. 65 W), thermistor (TE Technology MP-2444), and PID controller (TE Technology RS485) was used to control the temperature in increments of 0.1 K. In a previous study, we had shown that the change over the temperature could be as fast as 1.05 K s^{-1} with the microreactor separated from the thermoelectric module by thermal paste.[30] A stream of cooled and dry air was continuously injected through the microsystem to dissipate the heat generated by the hot side of Peltier module and to avoid any condensation of water caused by operation at sub-cooled temperatures. The lowest temperature that could be achievable in our setup was 251.15 K. In-house design stainless steel compression fittings were manufactured by AC Manufacturing Santa Clara, California. A Pyrex block was placed between the compression chuck and microreactor to ensure the compression stress was distributed evenly at the fluidic injection ports.

The experimental setup is similar to the study for hydrate crystallization kinetics (refer to Figure 2.4 for process flow diagram). The pressure of the microsystem was controlled and maintained by a membrane back-pressure regulator (Equilibar ZF1SNN8, max. 200 bars). Real-time pressure measurements were acquired by two pressure transducers, which

were installed upstream and downstream of the microsystem. Two high-pressure pumps (Teledyne ISCO 65DM) were used to deliver the methane and de-ionized water into the microsystem at preset constant flow rates. Data were recorded by a National Instruments cDAQ-9171 with a proprietary LabVIEW program.

3.2.2 Hydrate formation

Methane (>99.99% purity) was obtained from Airgas. High purity de-ionized water was produced by a Milli-Q system (Milli-Pore). After initializing the system, de-ionized water was pumped into the microreactor through the high-pressure ISCO pump at a flowrate of 200 μL/min. Then the system was pressurized with de-ionized water to the set pressure of back pressure regulator. After reaching the experimental pressure, delivery of de-ionized water was the stopped. Methane was then delivered by another high-pressure ISCO pump at varied flow rates to generate the annular flow with de-ionized water flowing along the microchannel's walls. The flow regime and water film layer could be manipulated by controlling the ratio of superficial velocity of gas and liquid.[33]

   In this work, we followed the same procedure reported previously to crystallize the hydrates within a matter of minutes.[30] At first, the temperature of the system was cooled down to 253.15 K. The sudden change of the refractive index, which is captured by the microscope, indicates the formation of ice within seconds. Then the temperature of the system was increased to 273.65 K, a point where methane hydrate is thermodynamically stable, while ice is not. This triggered the transition of ice to methane hydrate. One could observe the methane, which was flowing in the center of the channel, attended this transition as methane hydrate covered the whole microchannels. This process was allowed

to continue for at least ten minutes to ensure enough methane hydrate had formed for subsequent dissociation tests.

The dissociation of methane hydrate occurred under isothermal conditions in this study. The temperature of the microreactor was increased until it reached the equilibrium temperature under the system's pressure. After stable behavior was observed for 1 minute, the temperature of the system was increased again to the desired dissociation temperature. Only when the temperature was stable again, we started our measurement of the methane hydrate dissociation rate. Figure 3.4 shows the experimental condition in this work in the methane hydrate phase diagram. In a typical experiment, the temperature of the microreactor took less than 3 seconds to stabilize again, which was at least an order of magnitude less than the observed time-scale of crystal dissociation.
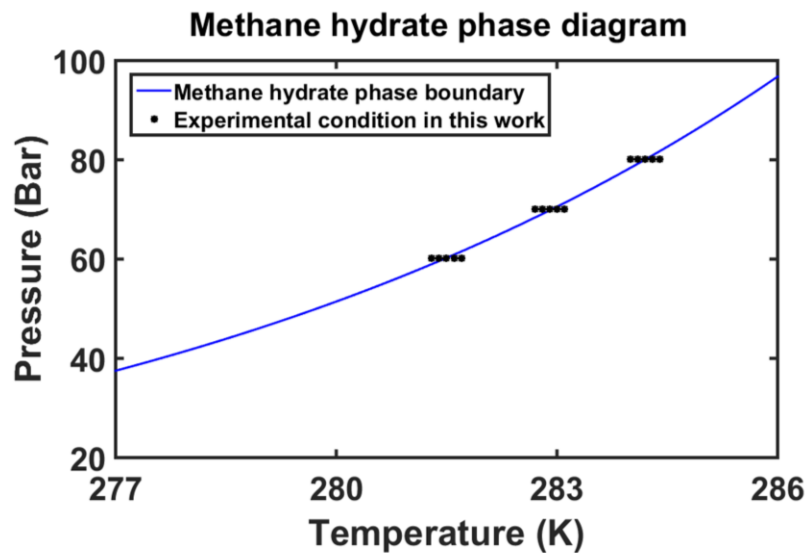
Figure 3.4 Methane hydrate phase diagram. The dissociation of methane hydrate is measured at 0.1 K interval around phase boundary.

3.2.3 *In situ* Raman spectroscopy

In situ Raman spectroscopy (Horiba LabRam HR Evolution, Jobin-Yvon) was used as the main characterization method of the methane hydrate dissociation rate. The instrument was equipped with a Diode-Pumped Solid-State (DPSS) laser system with a 532-nm wavelength excitation line at full power of 100 mW. A CCD detector (Synapse EM) and a 10x objective lens (MPlanN Olympus, 0.25 NA, 10.6-mm WD) were selected to acquire the spectra in a backscattering configuration. The grating was 600 grooves per millimeter. The acquisition time and power of laser light were found to be optimized at 10 s and 10 mW, which is described later in the text. The DuoScan mode was adopted to increase the coverage of the scan area and to mitigate any heat effect caused by laser. A 100 x 100 μm^2 area was scanned during the acquisition of each spectrum. For each dissociation rate measurement, the Raman spectrum was acquired at 10 s intervals for 30 minutes. Optimization of Raman parameters to avoid the heat effect was done under different power of laser light. An in-house developed MATLAB program was used to process the spectrum data. A linear baseline correction was applied to all the spectra, while ImageJ software was used to process the image data.

3.3 Results and discussion

3.3.1 Microscope observation and optimization of Raman parameters

The *in-situ* microscope was used to observe the process of methane hydrate dissociation. Figure 3.5 shows the methane hydrate dissociation process under 60.0 bar and 281.7 K, which is 0.3 K above the equilibrium temperature. The dissociation of methane hydrate
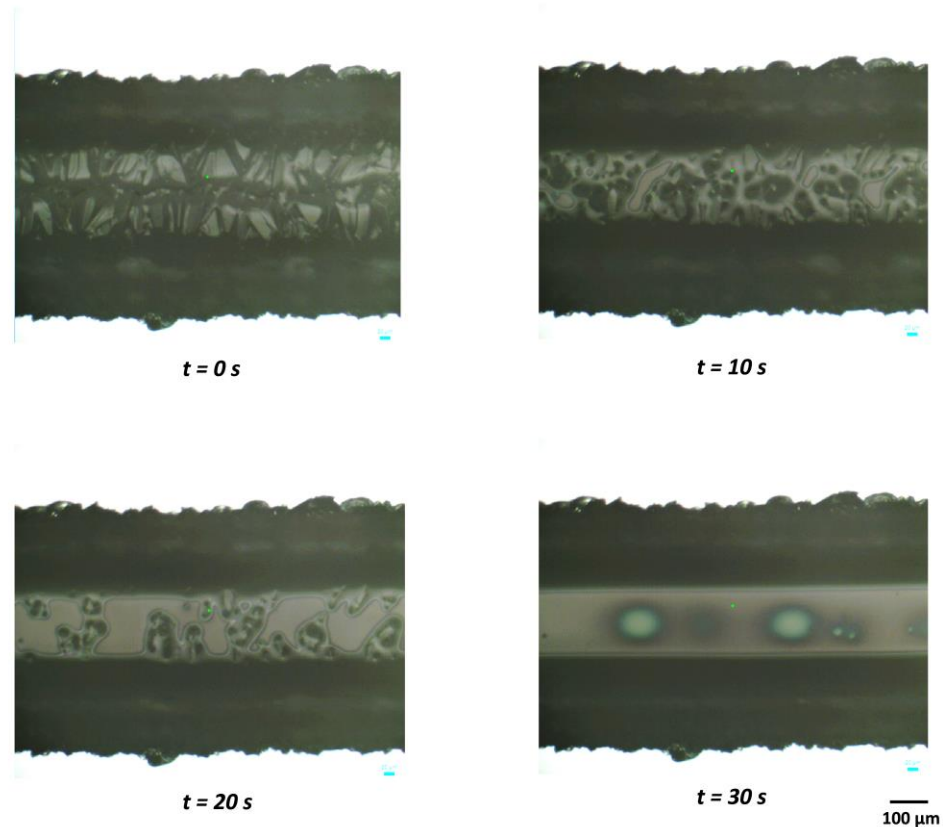
Figure 3.5 Microscope images of methane hydrate dissociation inside the microchannels at 60.0 bar and 281.7 K. The dissociation of methane hydrate is complete within 30 s.

happened homogeneously due to the isothermal conditions of our system. Recall that the thermal conductivity of silicon is one order of magnitude greater than stainless steel and two orders greater than glass. The hydrate dissociated radially as described in the literature.[1,34] The dissociation process was complete within 30 seconds, which indicates the sensitivity of the dissociation process to the temperature. Note that microscope images could only provide planar information, while the thickness of the methane hydrate crystal inside the microchannels could have varied. Therefore, *in-situ* Raman spectroscopy was used to provide information on the concentration profile, ultimately yielding the hydrate

film thickness as a fitted parameter.[9,18,35] Before proceeding, however, optimization of the spectroscopic parameters that would be needed in our study was performed, mainly the acquisition time and laser power. Considering the acquisition, longer acquisition time would increase the intensity of the peaks in the Raman spectrum, which lead to increase in the signal to noise ratio. However, if the acquisition time was too long, the tradeoff would be the loss of time dependent information. Here, we defined the dimensionless number, τ, as,

$$\boldsymbol{\tau} = \frac{t_c}{t_{aq}} \tag{3.1}$$

where t_c is the characteristic time for the incident (such as, dissociation in our case), and t_{aq} is the acquisition time. Only when τ was > 3, the trend of the experimental could be captured with acceptable tolerance. As shown in the Figure 3.5, the dissociation was completed in 30 s. Therefore, the acquisition time was selected as 10 s in our case to optimize the Raman signal.

Although Raman spectroscopy is commonly referred to as a non-invasive characterization method, the focus spot of laser light could raise the temperature of a certain point at high enough power. This increase in temperature could potentially influence our dissociation rate measurement by providing extra thermal energy. This is significantly important since later one will see that the dissociation rate is rather sensitive to the temperature difference. To minimize this effect, we optimized the Raman parameters, mainly the power of incident laser light, under the phase boundary condition, where methane hydrate should either grow or dissociate. The confirmation of phase boundary was described in our previous work.[30]

Figure 3.6 Shows the comparison of microscopy images of the microchannel before and after the treatment of laser light under different power of laser lights. The images were then analyzed through ImageJ to calculate the area of the microchannel that were covered by hydrate crystal. Under 40 mW of laser light, 36.21 % region of scan area was melted
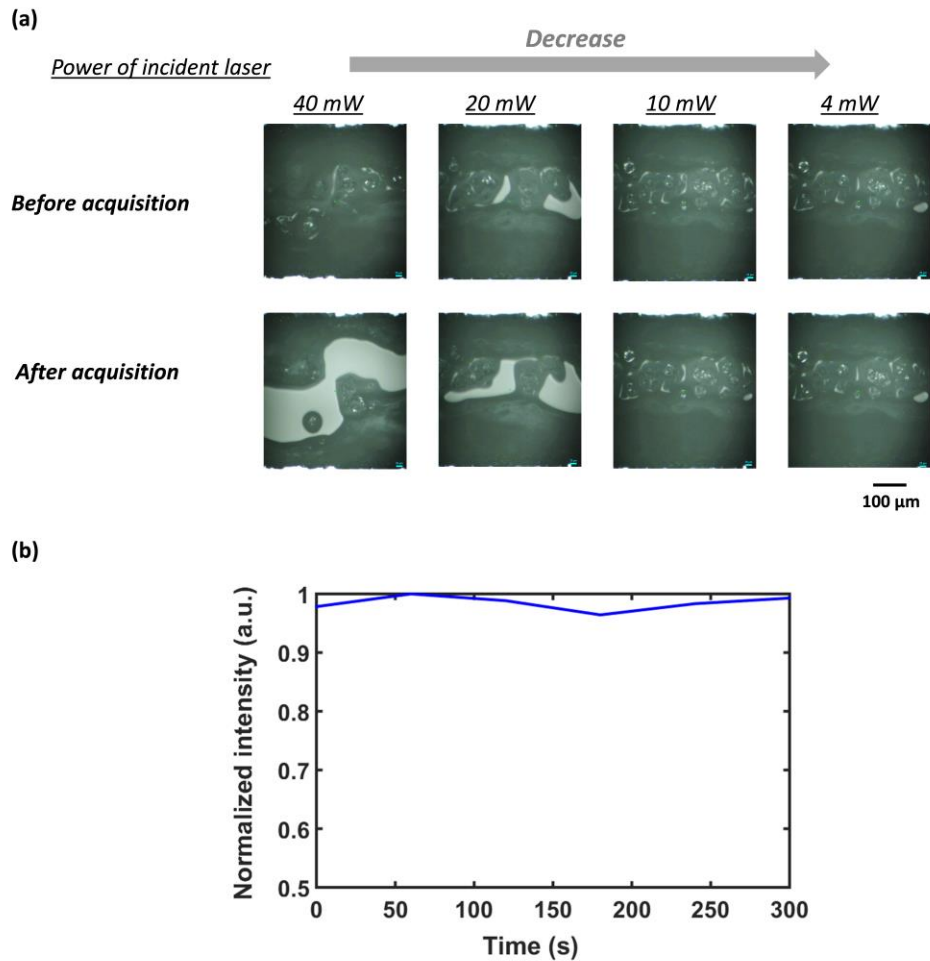
Figure 3.6 (a) Microscope image of methane hydrate inside the microchannels under exposure to different powers (4 to 40 mW) of incident laser light with wavelength of 532 nm for 10 s. (b) Normalized intensity of 2905 cm^{-1}peak at first 5 min confirm the heat effect of incident laser could be neglected at laser power of 10 mW and acquisition time of 10 s.

because of the heat effect. The same incident happened under 20 mW of laser light, 8.95 % region of scan area was melted. When the power of laser light was reduced to 10 mW or 4 mW, the heat effect on the methane hydrate dissociation were considered as negligible, which could be viewed from microscope images in Figure 3.6 (a). In our case, 10 mW was considered an acceptable threshold value for the heat effect. However, decrease of the incident laser power would lead to the decrease of the peak intensity (or signal-to-noise ratio) when all other parameters stay the same. Therefore, to assure the quality of Raman spectra, 10 mW was selected as the power to use during our study. As we mention earlier, the microscopy images could only be used as 2D reference, while the uncertainty about the thickness of hydrate still exists. Therefore, the result was further confirmed by acquiring the Raman spectra over the same spot for 5 minutes. As shown in Figure 3.6 (b), 1.7 % of error is acceptable and the laser has negligible effect on hydrate dissociation.

3.2.2 Methane hydrate dissociation rate measurement

Figure 3.7 shows the *in-situ* Raman spectra of the melting methane hydrate. The 2905 cm^{-1} and 2917 cm^{-1} shifts in the Raman spectra match the signature peaks of methane hydrate (sI) and the free gas, respectively. The Raman peak of methane hydrate (FHWM $\approx$ 6.99 cm^{-1}) is broader than the peak of methane gas (FHWM $\approx$ 3.25 cm^{-1}) due to the present of hydrogen bonding in the hydrate structure. Besides the finger print information, Raman spectra also provided quantitative information. The intensity of the peak could be correlated to the concentration of the analytes through Wopenka's equation.[36–38] In this study, we measured the normalized intensity of the 2905 cm^{-1} peak to access the information about the dissociation rate of methane hydrate. As the dissociation proceeded,
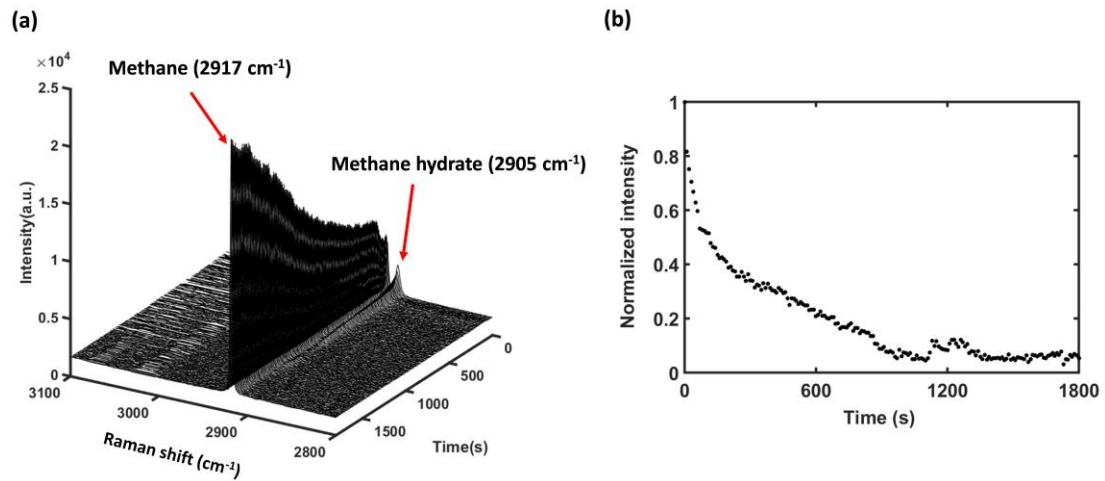
Figure 3. 7 (a) Raman spectra of initial 30 min of methane hydrate dissociation at 60.2 bar and 281.5 K. The decrease of methane hydrate peak (2905 cm^{-1}) and increase of methane gas peak (2917 cm^{-1}) indicates the dissociation of methane hydrate into methane gas. (b) Corresponding normalized intensity of 2905 cm^{-1} for the initial 30 min.

methane hydrate (sI) decomposed into water and free methane gas. As a result, one could spot the decrease in the intensity of 2905 cm^{-1} and the increase in the intensity of 2917 cm^{-1}. Figure 3.7 (b) shows the corresponding normalized intensity of 2905 cm^{-1} peak versus time. The decrease rate of 2905 cm^{-1} was about 2.96 ±0.68 times to the increase rate of 2917 cm^{-1} due to the methane density difference between free gas and hydrate. The standard deviation was caused by the sensitivity of the measurement and unpredictable evaporation rate of water molecules. The occupancy of methane in hydrate could be calculated through the measured density and theoretical density. The occupancy of methane in the hydrate is about 0.962 in our case, which agrees with reported value in the literature.[38]

- 102 -

3.2.3 Influence of fluid flow

In nature, methane hydrate is usually in contact with a free gas reservoir.[20,21] Understanding the influence of free gas fluid flow is important for exploration of methane hydrate. In our experiment, we studied the influence of fluid flow by measuring methane hydrate dissociation rates under different flow conditions at 80.1 bar and 284.2 K. As the flow rates of free gas methane increased from 2.00 μL/min to 20.00 μL/min, Reynold's number of the system increased from 0.42 to 4.16. However, as shown in Figure 3.8, the average dissociation rate of methane hydrate (sI) did not change by a significant margin. Table 3.1 lists the average dissociation rate of initial 200 s of methane hydrate at varies flow conditions. There was only a 7.1 % increase in the average dissociation as the Reynold's number increased by an order of magnitude. The results suggested that the fluid flow had only a minor effect on the dissociation of methane hydrate in the range of our experimental conditions. These results also support that external film mass transfer resistances were
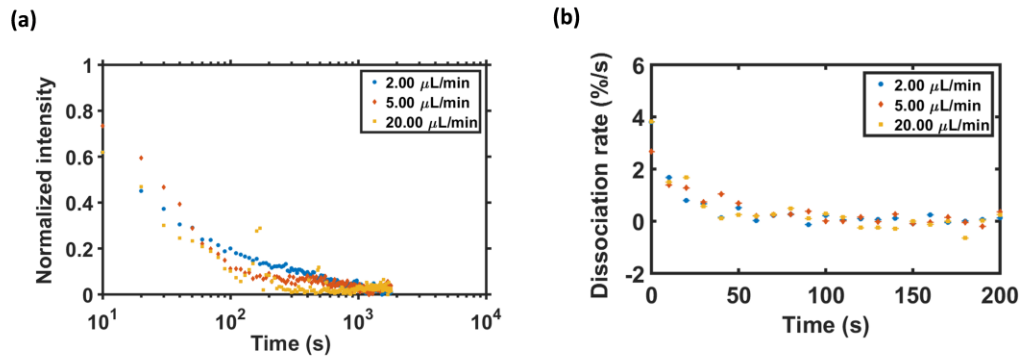
Figure 3.8 (a) Normalized intensity of 2905 cm^{-1} peak at initial 30 mins of methane hydrate dissociation at 80.1 bar and 284.2 K under different flow rate of methane. (b) Calculated dissociation rate at first 200 s of methane hydrate dissociation at 80.1 bar and 284.2 K under different flow rate of methane.

negligible. When experiment extend for longer period, the hydrate thin film existing between water film and gas would melt and result in exposing the water to free gas. This could lead to the evaporation effect of water. Therefore, for long experiment period, one would need to scale up the experimental system. Furthermore, for higher Reynold's number, the pressure drop of the system might increase significantly to

Table 3.1 Average dissociate rate of initial 200 s of methane hydrate at different flow rates of methane.

Flowrate (µL/min)	Reynold number	Mean dissociate rate of initial 200 s (%/s)
2.00	0.42	0.42
5.00	1.04	0.45
20.00	4.16	0.45

a point where the system could not be assumed as isobaric condition. Based on these reasons, we studied the dissociation rate of methane hydrate at the flow rate of 2.00 µL/min.

3.2.4 Influence of the temperature and pressure

We applied the same methodology to study the effect of the temperature and pressure at the flow rate of 2.00 µL/min. Figure 3.9 reports the normalized intensity of methane hydrates during the dissociation processes at varied temperatures ($[T_{eq}$ -0.1K] to $[T_{eq}$ +0.3K]) and pressures (60.2 bar, 70.3 bar and 80.1 bar). As could be seen, the dissociation rate of methane hydrate increases as the temperature of the system increases at constant pressure. This is because dissociation of methane hydrate is an endothermal process, the increase of temperature would lead to the increase in the heat transfer rate and
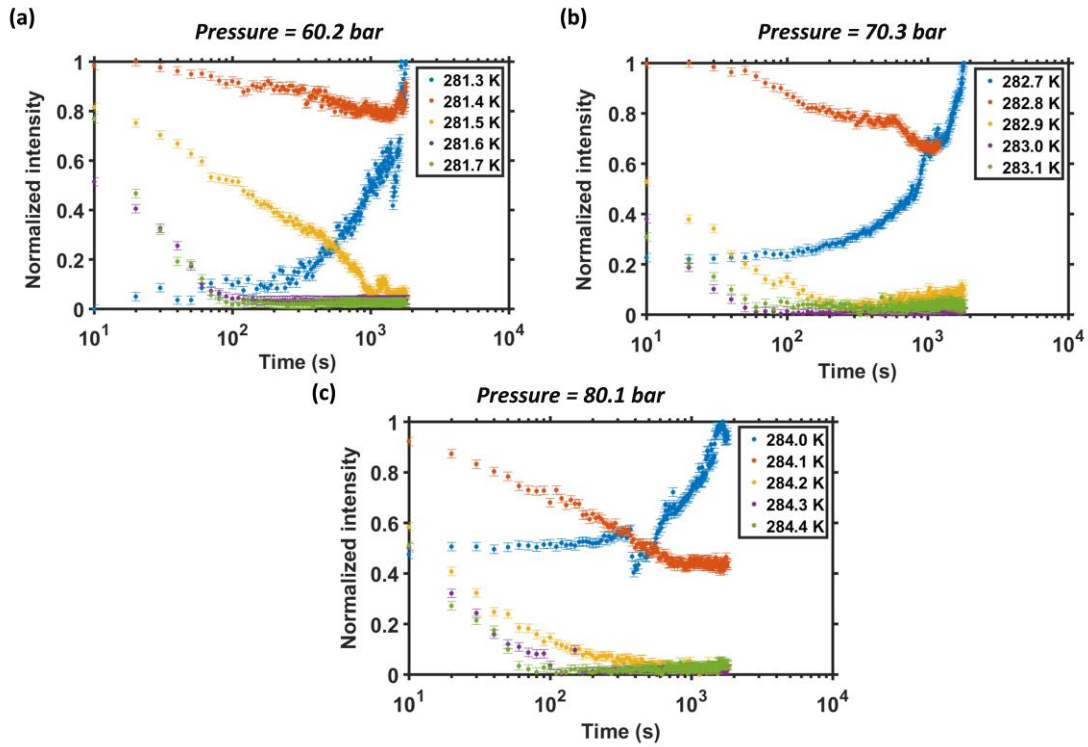
Figure 3.9 Normalized intensity of 2905 cm^{-1} peak at initial 30 mins of methane hydrate dissociation at (a) 60.2 bar (b) 70.3 bar, and (c) 80.1 bar.

intrinsic kinetics, which are the dominant processes reported in the literature.[7,25,39,40] Besides that, our results confirmed just how sensitive the dissociation of methane hydrate is to the temperature. On the other hand, the dissociation rate of methane hydrate did not show significant change at different pressure while the temperature difference from the phase boundary stayed the same. At three different pressures in present work, the dissociation rates all behaved very sensitive to the temperature near the phase boundary when comparing the condition of T_{eq} and [T_{eq}+0.1K]. In the meanwhile, when the temperature difference from the phase boundary exceed 0.2 K, the dissociation rates were all less sensitive to the temperature when comparing the condition of [T_{eq}+0.2K] and [T_{eq}+0.3K]. This implied that the temperature would be the most important factor during

- 105 -

the dissociation of methane hydrate while the pressure or concentration of free gas methane had negligible effect on the dissociation except altering the phase boundary (for the conditions of our study). Based on this information, we could develop the theoretical model to describe the dissociation of methane hydrate.

3.2.5 Kinetic model

Heat transfer, mass transfer, and intrinsic kinetics could all play important roles in methane hydrate dissociation. Here, we first consider each driving force independent of one another to build a comprehensive model from first principles.

3.2.5.a Mass transfer rate

Unlike crystallization, where it requires the both methane and water molecules to constitute the crystal structure, the decomposition of methane hydrate could happen at enough energy provided. It was reported that mass transfer of methane molecules from the dissociation interface restricted the dissociation process at temperatures < 0 ℃, owing to the formation of an ice film that decreased the molecular flux.[5,41] The phenomenon had been previously reported by scientists: the so called *"Self-Preservation"* effect.[18,42–45] However, since no ice forms above its melting point, mass transfer resistance can be considered negligible.[5] This assumption is readily evaluated by calculation of the methane flux through the liquid film surrounding the dissociating hydrate crystal. In this film, the driving force is the lowest due to a reduced solubility of methane in liquid water where the molecular diffusivity is also less than the gas phase. Based on our calculations, diffusion of methane across the thin film of water would occur in 0.021 s, which is three orders magnitude than the time scale of any measured hydrate dissociation rate (~10 s). As a consequence, we

could proceed by deriving the dissociation rate model based on the heat transfer rate and intrinsic kinetics.

3.2.5.b Heat transfer rate

The dissociation of methane hydrate is endothermic. As long as the temperature is above the phase boundary one can expect dissociation. Figure 3.10 illustrates schematically the microchannel cross-section during dissociation. In the present work, the dissociation propagates from the wall towards the center of the microchannel. Conductive heat transfer from the wall (at a constant temperature) provided the necessary energy for the dissociation. Here, a temperature gradient existed from the wall to a dissociation front, and in between the film was comprised of dissociated water and methane. The driving force for the heat transfer was the difference between the system temperature (T) and the phase boundary temperature (T_{eq}). Here, one-dimensional Fourier's Law and an energy balance at the dissociation front were performed to derive the normalized number of moles of
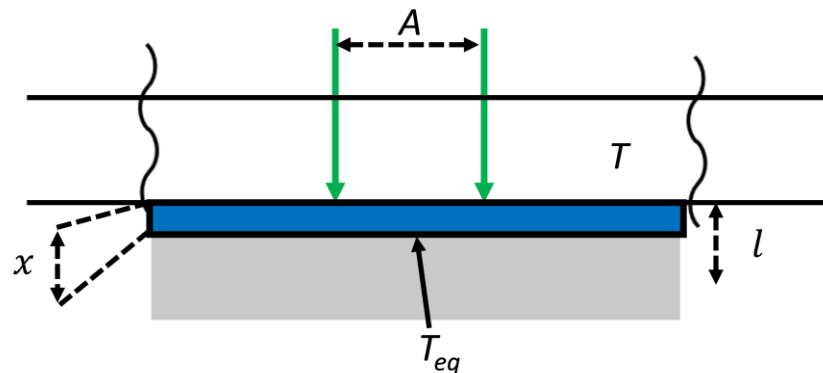
Figure 3.10 Schematic of temperature profile of the microchannel cross-section (top of the channel) during the methane hydrate dissociation process.

dissociated hydrate. The amount of energy required for the dissociation per unit time $(\frac{dq}{dt})_r$, could be expressed as following,

$$(\frac{dq}{dt})_r = \frac{dx}{dt} \cdot A \cdot \rho_H \cdot \Delta H \tag{3.2}$$

where, x is the thickness of melt hydrate, A is cross-section area, (in our case is the DuoScan area, 100 x 100 μm^2), ρ_H is the density of methane hydrate ($\sim$ 920 kg/m^3), and ΔH is the enthalpy of methane hydrate dissociation (436.5 kJ/kg).

Since the conductive heat transfer is dominated, we used one dimensional Fourier's Law to express the energy transfer rate $(\frac{dq}{dt})_t$, as following,

$$(\frac{dq}{dt})_t = \kappa \cdot A \cdot \frac{\Delta T}{x} \tag{3.3}$$

where, κ is the thermal conductivity of melt methane hydrate, and ΔT is the temperature difference between system and equilibrium temperature. The value of thermal conductivity will depend on whether heat transfer is comparable to intrinsic kinetics. If intrinsic kinetics dominate, then the thermal conductivity could be approximated by the value of water (κ_w = 0.58 W/ (m K)). If the heat transfer rate is significant, then the value of thermal conductivity of the mixture (κ_t) should be applied. Here, we used COMSOL Multiphysics to estimate the thermal conductivity equal to 0.47 W/ (m K) as shown in Figure 3.11.

In terms of energy balance, we could combine equations (S1) and (S2) as $(\frac{dq}{dt})_r = (\frac{dq}{dt})_t$. Then we could obtain the following expression for x by applying mathematical treatment like integral,

- 108 -
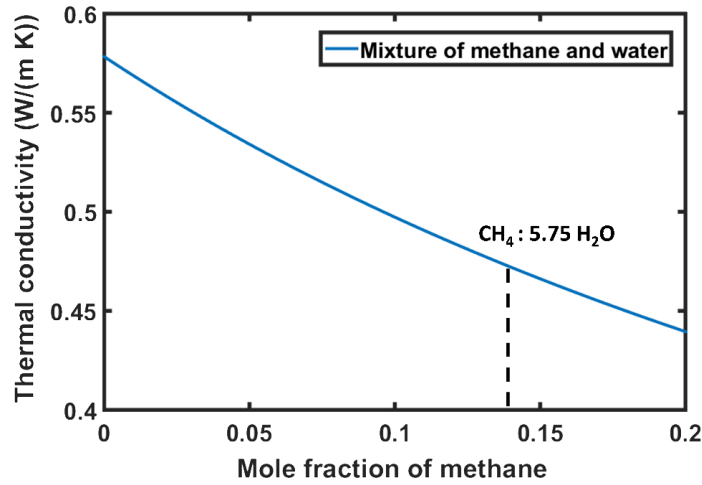
Figure 3.11 Thermal conductivity of methane and water mixture as a function of mole fraction of methane. Thermodynamic property package in Chemical Reaction Engineering Module of COMSOL Multiphysics was used for the calculation.

$$x = \sqrt{\frac{2t \cdot \kappa \cdot \Delta T}{\rho_H \cdot \Delta H}} \tag{3.4}$$

The normalized mass of dissociation methane hydrate could be expressed as below,

$$\frac{n_d}{n_0} = \frac{x \cdot A \cdot \rho_H}{l \cdot A \cdot \rho_H} = \frac{x}{l} = \frac{1}{l} \sqrt{\frac{2t \cdot \kappa \cdot (T - T_{eq})}{\rho_H \cdot \Delta H}} \tag{3.5}$$

where n_d and n_0 are the number of moles of dissociated hydrate and initial hydrate, respectively, and l is the initial thickness of the methane hydrate on the wall. In literature, any methane gas released from the dissociated methane hydrate is assumed to blow away just as soon as the first and subsequent crystals dissociate when intrinsic kinetics govern the process. In this scenario, the thermal conductivity can be approximated by that of water $(0.58 \text{ W/(m} \cdot K))$. However, if the heat transfer rate is comparable to the intrinsic kinetics (as we will later see), then a mixture of methane and water could be trapped within a thin

- 109 -

film between the microchannel walls and the undissociated hydrate crystal. In this case, the thermal conductivity is that of the mixture (0.47 W/(m· K)).

3.2.5.c Intrinsic kinetics

The dissociation of methane hydrate into methane and water can be described by a first-order reaction.[5] Here, we used the rate law to express the dissociation process in terms of the concentration of methane hydrate, yielding the normalized molar ratio of dissociated hydrate,

$$\frac{n_d}{n_0} = 1 - \exp(-k_d t) \tag{3.6}$$

where k_d is the rate constant for dissociation of methane hydrate. It is important to note here that the rate exhibits Arrhenius temperature dependence where the temperature of the dissociating hydrate was assumed uniform and its surface area constant throughout dissociation (*i.e.*, hydrate crystals grown on an isothermal flat plate dissociated from the bottom up). These reasonable approximations provide an estimate of the intrinsic dissociation rate. During the dissociation of methane hydrate, a metastable supersaturated thin film, consisting of water and supercritical methane, could be formed in between the microchannel walls and the undissociated hydrate crystal. This thin film has the potential to recrystallize into methane hydrate. Therefore, an equilibrium between methane hydrate dissociation and crystallization was derived. Our fitted results demonstrate conclusively that equilibrium constant, K_{eq}, is sufficiently large (*i.e.*, ~1×10^{45}) that the dissociation rate of equation (3.6) dominated. (see Appendix A) Therefore, any recrystallization of methane hydrate was considered negligible in our study.

3.2.5.d Combined heat transfer and intrinsic kinetic model

Combining equations (3.5) and (3.6) gives the overall dissociation rate of methane hydrate based on the normalized hydrate intensity,

$$\frac{I_H}{I_0} = \frac{n_H}{n_0} = 1 - \frac{1}{\frac{l}{\sqrt{\frac{2t \cdot \kappa \cdot \Delta T}{\rho_H \cdot \Delta H}}} + \frac{1}{1 - \exp(-k_d t)}} \tag{3.7}$$

Table 3.2 Fitting parameters of the mixed heat transfer and intrinsic kinetic model (equation (3.7)).

Experimental conditions	Initial methane hydrate thickness l (µm)	Intrinsic kinetic constant k_d (s⁻¹)
60.2 bar, ΔT=0.1 K	133.7	0.045
60.2 bar, ΔT=0.2 K	3.8	0.048
60.2 bar, ΔT=0.3 K	9.7	0.042
70.3 bar, ΔT=0.1 K	15.7	0.055
70.3 bar, ΔT=0.2 K	2.3	0.070
70.3 bar, ΔT=0.3 K	11.1	0.049
80.1 bar, ΔT=0.1 K	2.5	0.064
80.1 bar, ΔT=0.2 K	11.5	0.064
80.1 bar, ΔT=0.3 K	6.8	0.063

where l and k_d are fitting parameters obtained through non-linear regression using the least squares method. It is worth to note that each fitting parameters in the equation (3.7) possess a physical meaning. Values of l and k_d for each experimental condition are tabulated as Table 3.2. The results show that the initial thickness of methane hydrate on the wall is in the range of 2.3 – 133.7 μm, which is consistent with the depth of the microchannel (400 μm). The Arrhenius temperature dependence of k_d provided an estimate of the dissociation activation energy (E_a),

$$k_d = k_0 \exp(-\frac{E_a}{RT_{eq}}) \tag{3.8}$$

calculated as 90.95 ± 12.15 kJ/mol and within experimental error of previously reported values of 78.1 kJ/mol and 81 kJ/mol.[15,39] As can be seen in Figures 3.12 and 3.13, a fitted comparison shows good agreement between the model and the experimentally measured normalized intensity.
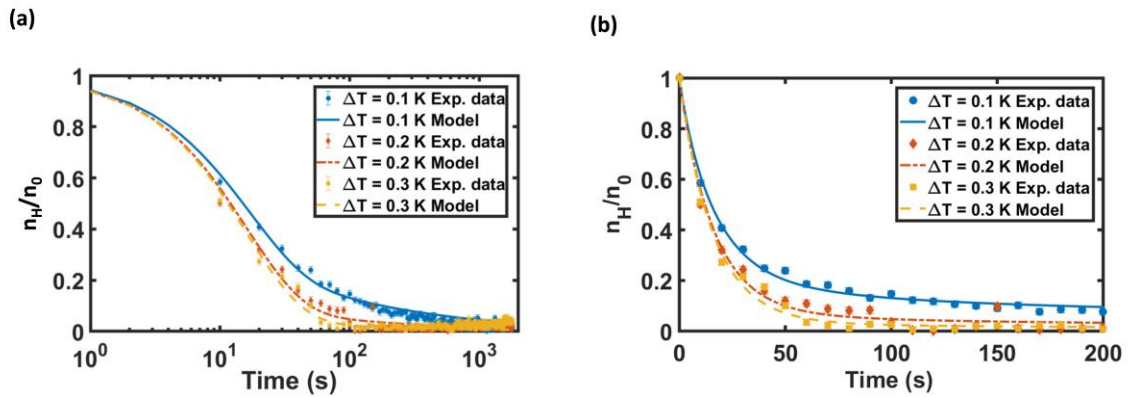
Figure 3.12 (a) Comparison of experimental data and model prediction (by equations (3.4) and (3.5)) at 80.1 bar and different temperature. (b) The data expanded for the first 200 s of dissociation.

The roles of heat transfer and intrinsic kinetics were further evaluated by considering the contribution fraction of each process. Since both are transient processes, the contribution fraction is a function of time, the initial methane hydrate thickness, and the temperature difference between the system and the phase boundary. The ratio of the contribution fraction of each process could be estimated by,

$$\frac{\omega_h}{\omega_i} = l \cdot [1 - \exp(-k_d t)] \cdot \sqrt{\frac{\rho_H \cdot \Delta H}{2t \cdot \kappa \cdot \Delta T}} \tag{3.9}$$

where ω_h and ω_i are the contribution fractions of heat transfer and the intrinsic kinetic, respectively. From this expression, we could see that the contribution of each effect is dependent on the initial methane hydrate thickness and temperature difference, which can
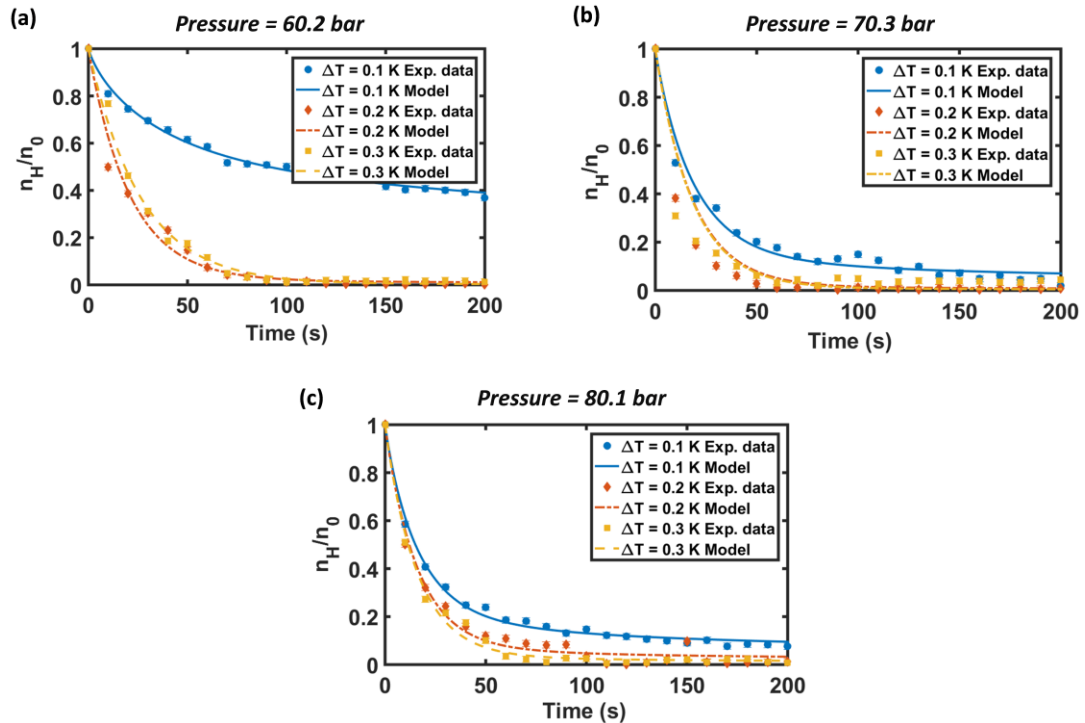
Figure 3.13 Comparison of experimental data and model prediction at (a) 60.2 bar, (b) 70.3 bar, and (c) 80.1 bar.

vary from one experimental apparatus to another. When the initial methane hydrate thickness increased, the contribution of heat transfer to the overall dissociation rate increased. This is because as the initial thickness increases, the required heat transfer distance is larger as other conditions stay the same. On the other hand, when the temperature difference increased, the intrinsic kinetics would have had a greater contribution, since the rate of heat transfer increases as the temperature difference increases. From equation (3.9), one could estimate the transition from heat-transfer to intrinsically-limited dissociation based on the initial thickness of the methane hydrate. Thus, understanding the initial thickness and its relationship to the experimental apparatus is critical. This could explain why dissociation models derived in previous studies vary.[3,5,7,21,40] Figure 3.14 reports the ratio of $\frac{\omega_h}{\omega_i}$ as a function of time and initial thickness of methane hydrate at different pressures and temperatures. The value of $\frac{\omega_h}{\omega_i}$ indicates that for a very thin film, intrinsic kinetics dominates the dissociation. These results are in good agreement with the micrographs shown in Figure 3.5, where the methane hydrate decomposes into islands of greater initial thickness. When heat transfer is faster than the intrinsic kinetics, the decomposition inside the crystal bulk region could be expected. As shown in Figure 3.14, extrapolation of the data to initial thicknesses > 100 μm shows a switch in the governing mechanism. This explains why in larger-scale laboratory equipment the heat transfer rate dominates kinetic measurements. These observations also showed the exclusive advantage of using microfluidics to create thin methane hydrate films on the order of 1-10 microns. The knowledge could be applied to the area where thin-layer hydrate is formed or dissociated. For instance, microstructure of hydrate seed could be applied to promote the formation of hydrate in natural gas storage application, and a layer

$\Delta T = 0.1\ K$ $\Delta T = 0.2\ K$ $\Delta T = 0.3\ K$

60.2 *bar*

70.3 *bar*

80.1 *bar*

This study   -·-·- **Model prediction**
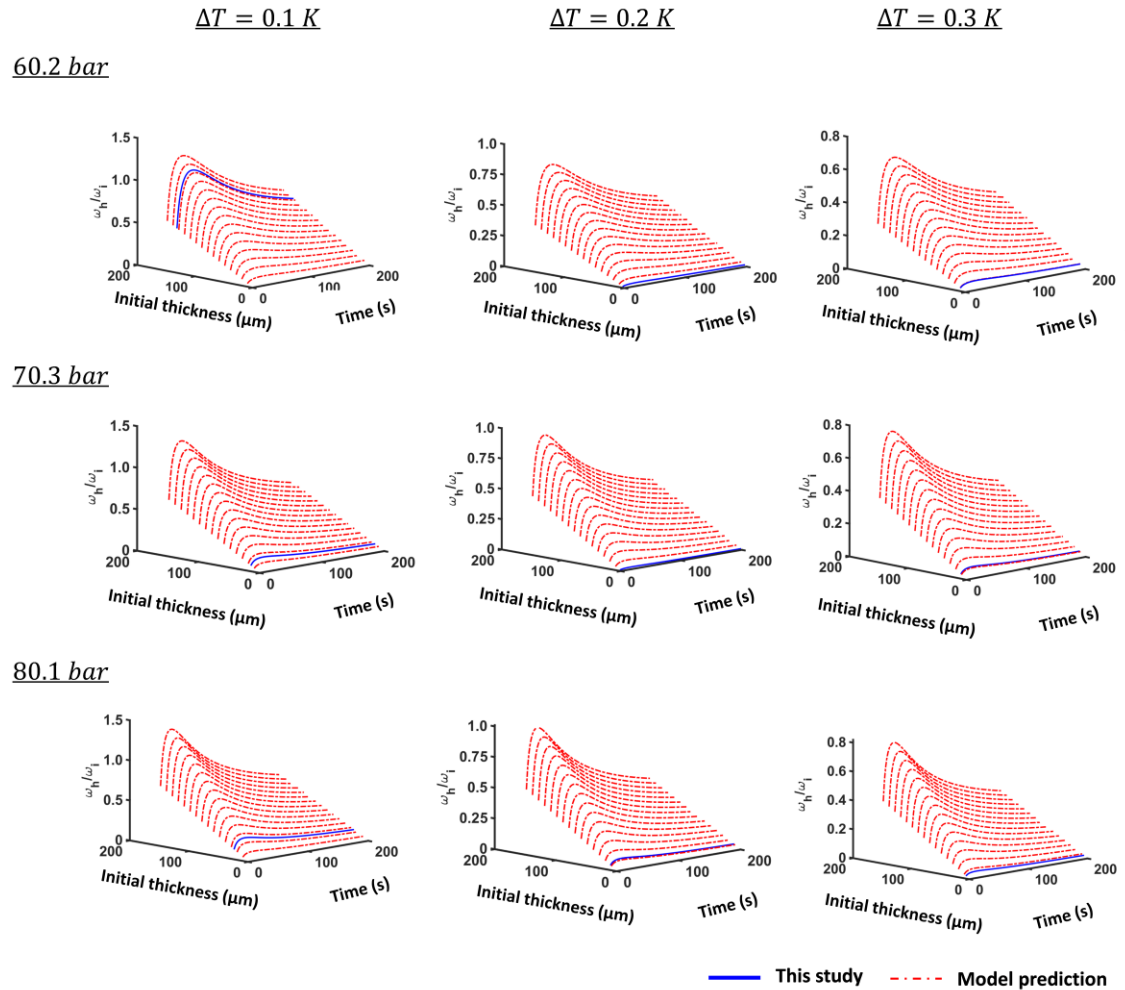
Figure 3.14 Plots of ω_h/ω_i ratios as a function of time and initial thickness at various pressure and temperature. The figures illustrate the contribution of heat transfer and intrinsic kinetics on dissociation.

of hydrate with thickness about 10 microns could be formed as a shell surrounding the water droplet inside the pipeline in flow insurance problem.[46] Due to the increase of accuracy by deleting the heat transfer resistance, the theoretical model derived would potentially provide better prediction to the larger system, where the heat transfer profile is

well known. Furthermore, Figure 3.14 confirms that the dissociation, initially determined by the intrinsic kinetics, in some cases switched as ratios of $\frac{\omega_h}{\omega_i}$ have maxima. Increased pressure at constant temperature increased the maxima, while decreased ΔT increased the maxima. The maxima of Figure 3.10 also provided an explanation of the "*memory effect*" that had been reported in the literature. It is the residual of un-dissociated methane hydrate crystals that promote heterogeneous nucleation. The intrinsic kinetics dominate at the end of dissociation where the low methane hydrate concentration limits the dissociation rate. In other words, the complete consumption of all residual methane hydrate crystals would require a very long period of time, and as a result cause the "*memory effect*".

3.4 Conclusions

The present work utilized a novel microfluidic approach to study the dissociation of methane (sI) hydrate under the isothermal conditions created by a thermoelectric cooling device. The heat effect of the laser power on hydrate dissociation was studied for the first time in this work and quantified to identify where it can be neglected. The results demonstrated an optimum value of laser power to achieve the highest signal to noise ratio without influencing the methane hydrate dissociation. Mass transfer resistances were also found to be negligible. The methodology was applied to study the methane hydrate dissociation kinetics under various pressures and temperatures.

Our findings demonstrate that microfluidics can be exploited to measure dissociation kinetics with unusual sensitivity, within a tenth of a degree Kelvin of the thermodynamic phase boundary. A tenth of a degree below the boundary results in hydrate crystallization while a tenth of a degree above dissociates micron-thick crystalline films prepared by

thermoelectrically-cooled microfluidics. Measurements by *in-situ* Raman spectroscopy revealed that the method can be used to directly estimate the dissociation kinetics. The use of microfluidics enabled the crystallization of micron-thick films that when dissociated were controlled by the intrinsic kinetics rather than by conductive heat transfer. A comprehensive kinetic model derived from first principles was reported, and the equilibrium constant was found to be sufficiently large that any re-crystallization was negligible. Furthermore, the contribution of heat transfer increased as the initial hydrate film thickness increased, while the contribution decreased as the temperature driving force increased. Three-dimensional mapping of the dimensionless ratio of the heat transfer rate to the intrinsic dissociation rate revealed a possible explanation for the "*memory effect*" referenced in gas hydrate science. Under circumstances where dissociation is controlled by intrinsic kinetics, complete dissociation of nuclei requires an infinite reaction time. Methane hydrate dissociation in microfluidics has an advantage by switching from heat-transfer-dominated-dissociation (in conventional laboratory batch systems) to intrinsic kinetics. This work supports that microfluidics with *in-situ* Raman spectroscopy are excellent laboratory tools to understand methane hydrate dissociation, with potentially much broader utility to the field.

Reference

(1)   Sloan, E. D.; Koh, A. C. *Clathrate Hydrates of Natural Gases*, 3rd edn.; CRC Press Taylor & Francis Group, 2007.

(2)   Gupta, A.; Moridis, G. J.; Kneafsey, T. J.; Sloan, E. D. Modeling Pure Methane Hydrate Dissociation Using a Numerical Simulator from a Novel Combination of X-Ray Computed Tomography and Macroscopic Data. *Energy Fuels* **2009**, *23* (12), 5958–5965.

(3)   Kim, H. C.; Bishnoi, P. R.; Heidemann, R. A.; Rizvi, S. S. H. Kinetics of Methane Hydrate Decomposition. *Chem. Eng. Sci.* **1987**, *42* (7), 1645–1653.

(4)   Zhou, X.; Long, Z.; Liang, S.; He, Y.; Yi, L.; Li, D.; Liang, D. In Situ Raman Analysis on the Dissociation Behavior of Mixed CH4–CO2 Hydrates. *Energy Fuels* **2016**, *30*, 1279–1286.

(5)   Sun, C.-Y.; Chen, G.-J. Methane Hydrate Dissociation above 0 C and below 0 C. *Fluid Phase Equilib.* **2006**, *242*, 123–128.

(6)   Gupta, A.; Dec, S. F.; Koh, C. A.; Sloan, E. D. NMR Investigation of Methane Hydrate Dissociation. *J. Phys. Chem. C* **2007**, *111* (5), 2341–2346.

(7)   Jamaluddin, A. K. M.; Kalogerakis, N.; Bishnoi, P. R. Modelling of Decomposition of a Synthetic Core of Methane Gas Hydrate by Coupling Intrinsic Kinetics with Heat Transfer Rates. *Can. J. Chem. Eng.* **1989**, *67* (6), 948–954.

(8)   Circone, S.; Stern, L. a; Kirby, S. H. The Effect of Elevated Methane Pressure on

Methane Hydrate Dissociation. *Am. Mineral.* **2004**, *89*, 1192–1201.

(9)   Yoon, J.-H.; Kawamura, T.; Yamamoto, Y.; Komai, T. Transformation of Methane Hydrate to Carbon Dioxide Hydrate: In Situ Raman Spectroscopic Observations. *J. Phys. Chem. A* **2004**, *108* (23), 5057–5059.

(10)   Yousif, M. H.; Abass, H. H.; Selim, M. S.; Sloan, E. D. Experimental and Theoretical Investigation of Methane-Gas-Hydrate Dissociation in Porous Media. *SPE Reserv. Eng.* **1991**, *6* (01), 69–76.

(11)   Gayet, P.; Dicharry, C.; Marion, G.; Graciaa, A.; Lachaise, J.; Nesterov, A. Experimental Determination of Methane Hydrate Dissociation Curve up to 55 MPa by Using a Small Amount of Surfactant as Hydrate Promoter. *Chem. Eng. Sci.* **2005**, *60*, 5751–5758.

(12)   Liu, C.; Lu, H.; Ye, Y.; Ripmeester, J. A.; Zhang, X. Raman Spectroscopic Observations on the Structural Characteristics and Dissociation Behavior of Methane Hydrate Synthesized in Silica Sands with Various Sizes. *Energy Fuels* **2008**, *22* (6), 3986–3988.

(13)   Misyura, S. Y. Effect of Heat Transfer on the Kinetics of Methane Hydrate Dissociation. *Chem. Phys. Lett.* **2013**, *583*, 34–37.

(14)   Oyama, H.; Konno, Y.; Masuda, Y.; Narita, H. Dependence of Depressurization-Induced Dissociation of Methane Hydrate Bearing Laboratory Cores on Heat Transfer. *Energy Fuels* **2009**, *23*, 4995–5002.

(15)   Clarke, M.; Bishnoi, P. R. R. Determination of the Activation Energy and Intrinsic

Rate Constant of Methane Gas Hydrate Decomposition. *Can. J. Chem. Eng.* **2001**, *79* (1), 143–147.

(16) Goel, N. In Situ Methane Hydrate Dissociation with Carbon Dioxide Sequestration: Current Knowledge and Issues. *J. Pet. Sci. Eng.* **2006**, *51*, 169–184.

(17) Wang, S.; Yang, M.; Wang, P.; Zhao, Y.; Song, Y. In Situ Observation of Methane Hydrate Dissociation under Different Backpressures. *Energy Fuels* **2015**, *29*, 3251–3256.

(18) Komai, T.; Kang, S. P.; Yoon, J. H.; Yamamoto, Y.; Kawamura, T.; Ohtake, M. In Situ Raman Spectroscopy Investigation of the Dissociation of Methane Hydrate at Temperatures Just below the Ice Point. *J. Phys. Chem. B* **2004**, *108* (23), 8062–8068.

(19) Pang, W. X.; Xu, W. Y.; Sun, C. Y.; Zhang, C. L.; Chen, G. J. Methane Hydrate Dissociation Experiment in a Middle-Sized Quiescent Reactor Using Thermal Method. *Fuel* **2009**, *88*, 497–503.

(20) Hong, H.; Pooladi-Darvish, M. Simulation of Depressurization for Gas Production from Gas Hydrate Reservoirs. *J. Can. Pet. Technol.* **2005**, *44* (11), 39–46.

(21) Hong, H.; Bishnoi, P. R. Modelling of Gas Production From Hydrates in Porous Media. *J. Can. Pet. Technol.* **2003**, *42* (11), 45–56.

(22) Lin, W.; Chen, G.-J.; Sun, C.-Y.; Guo, X.-Q.; Wu, Z.-K.; Liang, M.-Y.; Chen, L.-T.; Yang, L.-Y. Effect of Surfactant on the Formation and Dissociation Kinetic Behavior of Methane Hydrate. *Chem. Eng. Sci.* **2004**, *59*, 4449–4455.

(23) Tohidi, B.; Anderson, R.; Clennell, M. B.; Burgass, R. W.; Biderkab, A. B. Visual

Observation of Gas-Hydrate Formation and Dissociation in Synthetic Porous Media by Means of Glass Micromodels. *Geology* **2001**, *29* (9), 867–870.

(24)   Chen, L.; Sloan, E. D.; Koh, C. A.; Sum, A. K. Methane Hydrate Formation and Dissociation on Suspended Gas Bubbles in Water. *J. Chem. Eng. Data* **2013**, *59* (4), 1045–1051.

(25)   Tsypkin, G. G. Mathematical Models of Gas Hydrates Dissociation in Porous Media. *Ann. N. Y. Acad. Sci.* **2006**, *912* (1), 428–436.

(26)   Kawamura, T.; Ohga, K.; Higuchi, K.; Yoon, J. H.; Yamamoto, Y.; Komai, T.; Haneda, H. Dissociation Behavior of Pellet-Shaped Methane-Ethane Mixed Gas Hydrate Samples. *Energy Fuels* **2003**, *17*, 614–618.

(27)   English, N. J.; Johnson, J. K.; Taylor, C. E. Molecular-Dynamics Simulations of Methane Hydrate Dissociation. *J. Chem. Phys.* **2005**, *123* (10), 244503–264507.

(28)   English, N. J.; Phelan, G. M. Molecular Dynamics Study of Thermal-Driven Methane Hydrate Dissociation. *J. Chem. Phys.* **2009**, *131* (10), 074704.

(29)   Hartman, R. L.; McMullen, J. P.; Jensen, K. F. Deciding Whether to Go with the Flow: Evaluating the Merits of Flow Reactors for Synthesis. *Angew. Chem Int. Ed.* **2011**, *50* (33), 7502–7519.

(30)   Chen, W.; Pinho, B.; Hartman, R. L. Flash Crystallization Kinetics of Methane (SI) Hydrate in a Thermoelectrically-Cooled Microreactor. *Lab Chip* **2017**, *17* (17), 3051–3060.

(31)   Marre, S.; Adamo, A.; Basak, S.; Aymonier, C.; Jensen, K. F. Design and Packaging

of Microreactors for High Pressure and High Temperature Applications. *Ind. Eng. Chem. Res.* **2010**, *49* (22), 11310–11320.

(32)   Hu, C.; Morris, J. E.; Hartman, R. L. Microfluidic Investigation of the Deposition of Asphaltenes in Porous Media. *Lab chip* **2014**, *14* (12), 2014–2022.

(33)   Günther, A.; Jensen, K. F. Multiphase Microfluidics: From Flow Characteristics to Chemical and Materials Synthesis. *Lab Chip* **2006**, *6* (12), 1487–1503.

(34)   Davies, S. R.; Selim, M. S.; Sloan, E. D.; Bollavaram, P.; Peters, D. J. Hydrate Plug Dissociation. *AIChE J.* **2006**, *52* (12), 4016–4027.

(35)   Pelletier, M. J. Quantiative Analysis Using Raman Spectroscpoy. *Appl. Spectrosc.* **2003**, *57*, 20A-42A.

(36)   Wopenka.B., P. J. D. Limitations to Quantitative Analysis of Fluid Inclusions in Geological Samples by Laser Raman Microprobe Spectroscopy. *Appl. Specroscopy* **1986**, *40* (2), 144–151.

(37)   Wopenka.B., P. J. D. Raman Intensities and Detection Limits of Geochemically Relevant Gas Mixtures for a Laser Raman Microprobe. *Anal. Chem.* **1987**, *59*, 2165–2170.

(38)   Sum, A. K.; Burruss, R. C.; Sloan, E. D. Measurement of Clathrate Hydrates via Raman Spectroscopy. *J. Phys. Chem. B* **1997**, *101* (38), 7371–7377.

(39)   Kim, H. C.; Bishnoi, P. R.; Heidemann, R. A.; Rizvi, S. S. . Kinetics of Methane Hydrate Decomposition. *Chem. Eng. Sci.* **1987**, *42* (7), 1645–1653.

(40) Selim, M. S.; Sloan, E. D. Heat and Mass Transfer during the Dissociation of Hydrates in Porous Media. *AIChE J.* **1989**, *35* (6), 1049–1052.

(41) Bai, D.; Zhang, D.; Zhang, X.; Chen, G. Origin of Self-Preservation Effect for Hydrate Decomposition: Coupling of Mass and Heat Transfer Resistances. *Sci. Rep.* **2015**, *5*, 14599.

(42) Stern, L. A.; Circone, S.; Kirby, S. H.; Durham, W. B. Anomalous Preservation of Pure Methane Hydrate at 1 Atm. *J. Phys. Chem. B* **2001**, *105*, 1756–1762.

(43) Takeya, S.; Shimada, W.; Kamata, Y.; Ebinuma, T.; Uchida, T.; Nagao, J.; Narita, H. In Situ X-Ray Diffraction Measurements of the Self-Preservation Effect of CH4 Hydrate. *J.Phys.Chem.A* **2001**, *105*, 9756–9759.

(44) Everett, S. M.; Rawn, C. J.; Keffer, D. J.; Mull, D. L.; Payzant, E. A.; Phelps, T. J. Kinetics of Methane Hydrate Decomposition Studied via in Situ Low Temperature X-Ray Powder Diffraction. *J. Phys. Chem. A* **2013**, *117* (17), 3593–3598.

(45) Giavarini, C.; Maccioni, F. Self-Preservation at Low Pressures of Methane Hydrates with Various Gas Contents. *Ind. Eng. Chem. Res.* **2004**, *43* (20), 6616–6621.

(46) Li, S.-L.; Sun, C.-Y.; Liu, B.; Feng, X.-J.; Li, F.-G.; Chen, L.-T.; Chen, G. Initial Thickness Measurements and Insights into Crystal Growth of Methane Hydrate Film. *AIChE* **2013**, *59*, 2145–2154.

Chapter 4

Dissolution Mechanism Study of Asphaltenes in Porous Media with Presence of H-ZSM 5 Aluminosilicates by Using in-Situ Raman Spectroscopy in Microfluidic System

The text and figures in this chapter are partially from the paper: Chen, W., Vashistha P., Yen, A., Joshi, N., Kapoor, Y., and Hartman, R.L., Asphaltenes Dissolution Mechanism Study by in Situ Raman Characterization of a Packed-Bed Microreactor with HZSM-5 Aluminosilicates, *Energy Fuels*, **2018**, *32*, 12205-12217.

4.1 Introduction

Wellbore/reservoir region is the place where asphaltenes deposition problem has the most adverse economic impacts.[1] In the meantime, wellbore/reservoir region is the most complex region in terms of its physical characteristic and chemical environment. The wellbore/reservoir region is usually composed of diverse types of oxide compounds, such as ZrO_2, $CaCO_3$, TiO_2, SiO_2, MgO, Al_2O_3, CeO_2.[2,3] These compounds create not only an intricate porous media, but also diverse chemical environment. The previous work done by Chaisoontornyotin et al. showed that, in the presence of inorganic solids, the asphaltenes precipitation rate would be altered by the introduction of heterogeneous nucleation in addition to homogeneous aggregation.[4] Understanding the influence of chemical environment on asphaltenes deposition and dissolution in porous media could provide great insights toward development of better remediation strategy, which could increase the oil production efficiency by mitigating the flow assurance problem caused by asphaltenes deposition. For this purpose, the combination of quartz particles and fine aluminosilicate particles (HZSM-5) is used as replica of reservoir. HZSM-5, commonly used as a zeolite material, is a readily available synthetic porous material with tunable Al_2O_3 to SiO_2 ratio. The increase of Al_2O_3 content in HZSM-5 increases the surface acidity of the porous media as Al site acts as Brønsted acid. In this work, the HZSM-5 fine particles with Al_2O_3 to SiO_2 ratio of 0, 1/91, 1/26 are applied to investigate the deposition/dissolution of asphaltenes in the porous media.

Two distinguished models were applied to describe the deposition of asphaltenes in porous media: adsorption and mechanical entrapment. Adsorption is a reversible process that describes how dissolved asphaltene molecules get adsorbed onto the surface from the

bulk media, while mechanical entrapment is a physical phenomenon that describes the blocking of pore throats with precipitated asphaltene clusters.[5] The first mechanism is dependent on the diffusion characteristics of asphaltene molecules in the solution, while the second mechanism is dependent both on the collisions between asphaltene molecules and its diffusion rate in the bulk fluid. The previous findings in the literature suggests that diffusion limitations or other barriers influence the asphaltenes deposition in the porous media or a narrow capillary.[6,7]Both kinetic mechanisms could occur concurrently when asphaltenes are deposited in porous media. Therefore, differentiating the occurrence of both mechanisms is challenging. For example, when the concentration of asphaltenes increases, this will lead to an increased amount of asphaltenes adsorbed on the surface, while also causing mechanical entrapment, because of the presence of a larger amount of asphaltenes nanoaggregates. Both blocking and thickening of asphaltenes at the pore throat will lead to an increase in pressure drop across the porous media and flow resistance. Because of these similarities, it is challenging to estimate each effect without an in situ characterization method.

Although mechanical methods could be applied to remediate the wellbore and pipeline from asphaltenes deposits, they have limited application, because of their physical properties. Since the solubility of asphaltenes increases with the increased aromaticity of the solvent, aromatic solvents such as toluene and xylenes are commonly used to resolve the asphaltenes deposit. Besides the aromatic solvent, cosolvents, amphiphile solvent, and polymer dispersant have been studied and applied for the dissolution of asphaltenes. Although xylenes have proven to have some negative environmental and health impacts for human beings (such as toxicity toward the musculoskeletal system, gastrointestinal

- 126 -

system, respiratory system, and so on),[8] xylenes are among the most common solvents used in the field, primarily because of their reasonable dissolution ability and accessibility. It is this reason why xylene was selected as the solvent in this work.

The reduced characteristic length scales of microfluidics and the high surface-to-volume ratios not only minimize the heat- and mass-transfer resistances, but they can also serve as a model system volume of porous media.[9] These advantages can generate high-throughput information with precise control over the conditions, which is why microsystems have helped advance other fields.[10–17] Information about intrinsic reaction kinetics is readily available that might otherwise be overlooked in the conventional chemical systems.[18–20] A well-controlled microfluidic modeled porous media with consolidated posts had been applied by Lin et al., to investigate the asphaltenes deposition behavior under various conditions, such as different concentrations of precipitant and the presence of different dispersants. The results revealed the importance of asphaltenes solubility, diffusion rate and intermolecular forces on the deposition behaviors, which otherwise might be difficult to visualize in macroscopic systems.[21,22] The miniaturization can also enable in situ characterization within a reasonable amount of time. Raman spectroscopy is a powerful method to detect the vibrational and rotational information on chemical bonds, distinguishing mixtures of molecular components. The spectroscopy has also been used to identify the molecular information on materials, such as the sheet size of asphaltenes.[23–25] Our previous work has shown that utilization of online characterization and in situ Raman spectroscopy can provide local information about asphaltenes deposition in micro-packed bed reactors.[25–28]

- 127 -

In the present work, a micro-packed bed reactor with in situ Raman spectroscopy was used to study the dissolution of asphaltenes. The online ubiquitous platform provided information about the deposition and the dissolution, while the *in situ* Raman spectroscopy provided local molecular information within the porous media. Analyses of the sheet size distributions and the occupancy revealed new insight on the dissolution mechanism. The results of the present work could provide useful understanding for the design of near-wellbore squeeze treatments.

4.2 Experimental Section

4.2.1 Design of the micro-packed bed reactor (µPBR)

The two-dimensional masks were designed on AutoCAD. The micro-packed bed reactor featured a connected 9.9-µL triangle and 48.0-µL rectangle packing zone. An on-chip frits section with 30 rows x 250 columns of micropillars (20 µm diameter) was added near the exit of the microreactor to immobilize the quartz particles. The microchannels were dry etched onto the silicon through standard microelectronic processing techniques by Micronit. A 1-mm thick Pyrex glass was anodically bonded on the top of the silicon as the cap of the microchannels.

The porous media inside the micro-packed bed reactor was created by injecting the quartz particles with average diameter of 29.5 ± 7.8 µm. The quartz particles with desired size were prepared from 30-40 mesh quartz sands with mortar and pestle in the presence of water. After drying in oven for 10 min and cool down to room temperature, the grounded quartz particles were sieved by using a sonic sifter for 20 min per batch. The quartz

particles in between 500 mesh and 625 mesh were collected. Around 5 g of quartz particles were dispersed in 15 mL ethanol under ultrasonic bath for 5 min. After sat for 1 min, the ultrafine quartz particles suspended in the ethanol were eliminated while the ones precipitated at the bottom were collected. The gravity separation procedure was repeated until no quartz particles were suspended after 1 min. The result quartz particles were then manually injected into the μPBR.

4.2.2 Zeolites HZSM-5 injection

The HZSM-5 type zeolites with two different Al_2O_3/SiO_2 ratios were selected to inject into the porous media to study the effect of fine particles. The 0.0038 g zeolites were dispersed in 250 mL isopropanol for 10 min in ultrasonic bath. Our previous dynamic light scattering (DLS) data showed that the nanoparticles of zeolites were stable for at least 24 hours without aggregation.[25] The zeolites solution was then delivered into the μPBR by ISCO pump at the flow rate of 40.00 μL/min for 25 hours. Approximately 0.91 mg (~1.25 μL) of zeolites was injected into the μPBR, which corresponds to 65.57% of surface coverage on quartz particles. It was worth to note that we assumed all the zeolites were retained in the porous media as the zeolite solution became clear after passing through the packed bed.

4.2.3 Materials and chemicals

Toluene (>99.9%, purity) was purchased from BDH Chemicals VWR. Ethanol (>99.5%, purity), isopropanol (99.7%, purity), and acetone (99.8%, purity) were purchased from Milipore. n-Heptane (99%, purity), Xylene (>98.5%, purity), and cyclohexane (>99.7%, purity) were purchased from Alfa Aesar. Quartz sand (30-40 mesh) was purchased from

VWR International. The zeolites HZSM-5 with different ratio of Al_2O_3 to SiO_2 were purchased from ACS Material. The zeolites are 300-nm nano crystals with pore size of 5 angstrom and a Brunauer-Emmett-Teller (BET) specific surface area of 362 $m^2 \cdot g^{-1}$. The crude oil was kindly provided by Nalco Champion, Sugar Land, TX, USA. The preparation of asphaltene from crude oil was described in detail in our previous work.[26–29] In brief, the hydrocarbon sample was dissolved in toluene for 20 min under ultrasonic treatment. The solution was then filtered through Whatman grade 1 filter to get rid of the non-soluble impurities after setting for 30 min. Twice volume amount of n-heptane was added to the filtered solution and left overnight. Asphaltenes sample were precipitated out and filtered by Whatman grade 1 filter. The sample and filter paper were oven-dried at 60 for 24 hr. The final sample were scratched from the filter paper and collected in a vial for future use.

4.2.4 Asphaltenes deposition and dissolution on µPBR.

The process flow diagram of asphaltenes deposition and dissolution are shown in Figure 4.1 (c) & (d) , respectively. During the deposition of asphaltenes, two ISCO pumps were utilized to deliver 4.0 g/L asphaltenes in toluene and n- heptane at constant flow rates of 24 µL/min and 16 µL/min, respectively. The fluids were mixed at a stainless-steel T-union, which was placed inside the ultrasonic bath to prevent the asphaltenes aggregation prior to the µPBR. The in-line check valves were installed upstream of T-union in both lines to prevent the back flow of fluid. The pressure drop across the µPBR was increased as asphaltenes precipitated and deposited onto the surface of the quartz. (see Appendix B) The deposition process of asphaltenes was complete once the pressure drops of the µPBR reached 6.0 bar.
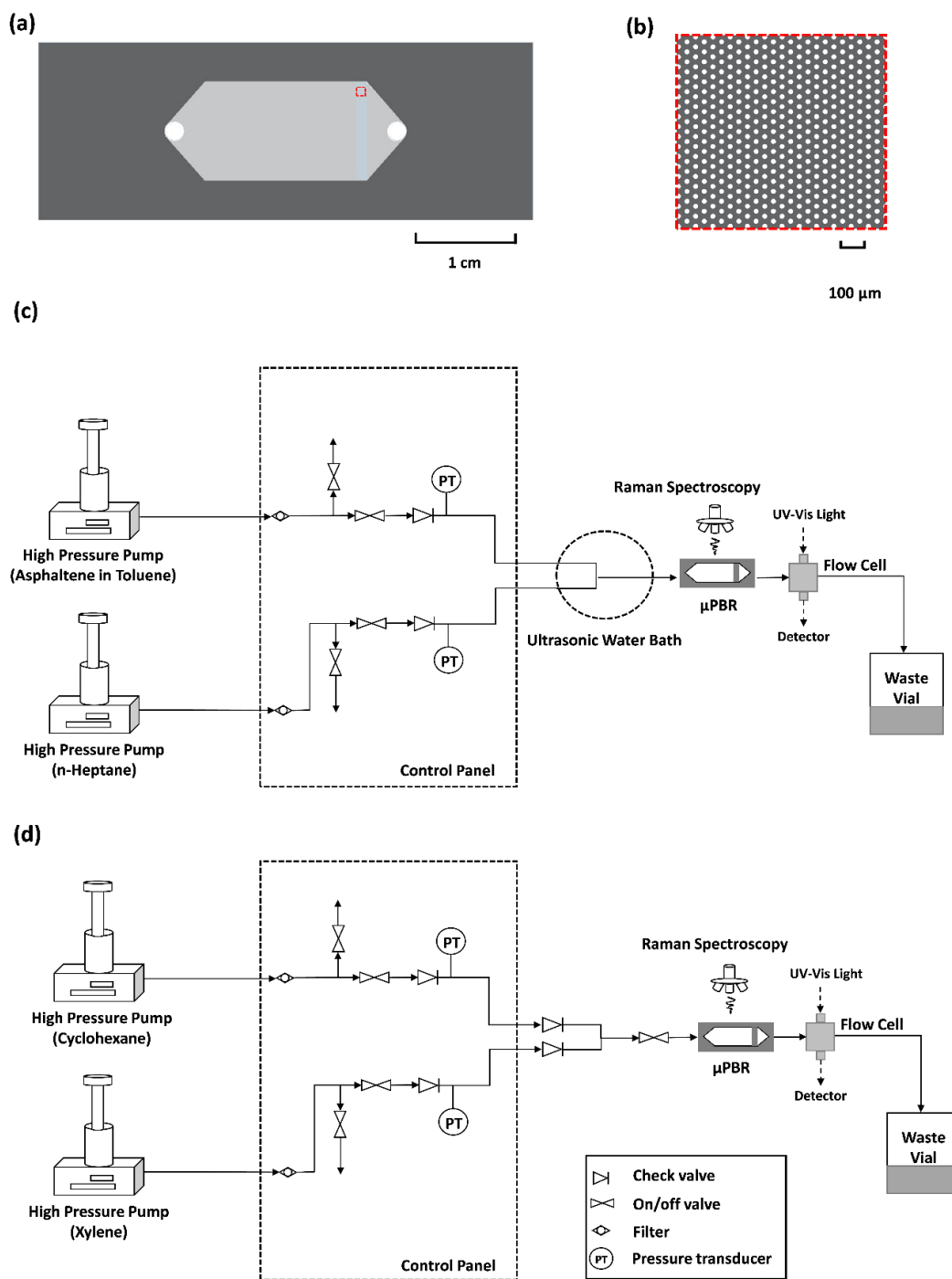
Figure 4.1 (a) Design of micro-packed bed reactor. (b) Enlarged image of the on-chip frit section. Process flow diagram for (c) asphaltenes deposition and (d) asphaltenes dissolution study.

During the dissolution of asphaltenes, two ISCO pumps were utilized to deliver the cyclohexane and xylenes to the μPBR by a stepwise dissolution strategy, which is described in detail below. The controller was set to programmatically deliver the fluids for different volume. A house design flow cell integrated with UV-Vis spectroscopy was installed at the downstream of the μPBR to measure the concentration of dissolved asphaltenes through absorbance measurement. A National Instruments cDAQ-9171 system integrated with an in-house LabView program was used to acquire the record the data regarding the pressures and flowrates.

4.2.5 Stepwise dissolution of asphaltenes

The stepwise strategy was utilized to study the extent of asphaltene dissolved with respect to pore volume of aromatic solvent. For each trial, at least five programs were applied until concentration of dissolved asphaltene is below the detection limits of UV-Vis, which is 2.95 mg/L. All the programs contain the three same steps as below, except the volume of

Table 4.1 Different Program and Corresponding Pore Volume of Xylenes Injected and Dissolution Time.

Program	Pore volume of xylenes injected (V_0)	Dissolution time (min)
1	10	6
2	50	30
3	500	300
4	1000	600
5	1000	600
6	1000	600

xylene injection is different:

(1) Cyclohexane was injected into the µPBR at a flow rate of 40.00 µL/min for 30 min (or 50 pore volumes) to prewet the µPBR.

(2) The cyclohexane pump was stopped, and xylenes were injected into the µPBR at flow rate of 40.00 µL/min for different periods, depending on the program. The injection time and corresponding pore volume is listed in Table 4.1. Programs 4, 5, and 6 have the same pore volume. An example of the program is shown at Figure 4.2.

(3) The xylenes pump was stopped, and cyclohexane was injected into the µPBR at flow rate of 40.00 µL/min for 30 min (or 50 pore volumes) to purge out all the dissolved asphaltenes.
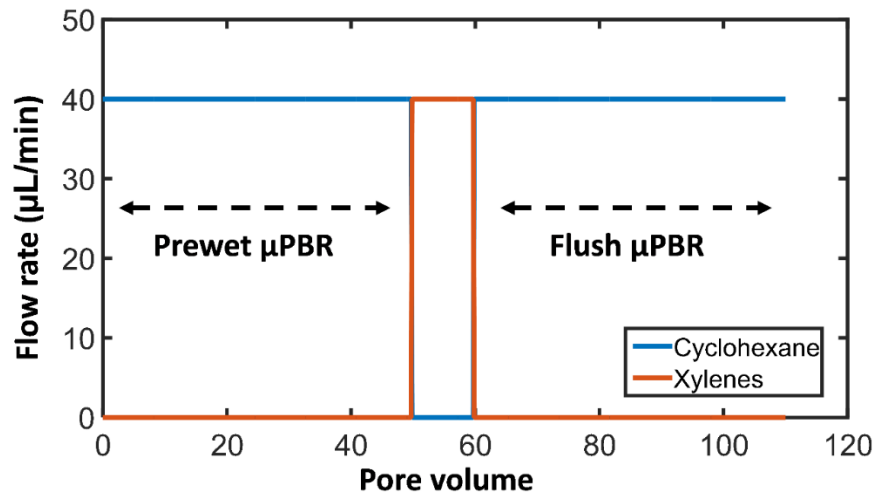
Figure 4.2 Stepwise injection of cyclohexane and xylenes for asphaltenes dissolution study. Different pore volumes of xylenes were injected into the microreactor for each of the six different programs shown in Table 4.1.

4.2.6 Characteristics of Asphaltenes Particles and µPBR

A sample of 4.0 g/L asphaltenes in toluene solution mixed with n-heptane at the volume ratio of 3:2 was prepared to characterize the properties of asphaltenes solution used in this study. The kinematic viscosity of the sample was measured by a Cannon Ubbelohde viscometer to be 0.664 ± 0.002 mm^2/s. The density of the sample was measured by a density meter (Anton Paar, Model DMA 4500M) to be 0.7929 g/mL. Then the dynanmic viscosity of the sample was calculated to be 0.526 ± 0.001 mPa/s. The refractive index of the sample was measured by an Abbe refractometer to be 1.4530 with an accuracy of ± 1.0 x 10^{-4}. The particle sizes of asphaltenes aggregates in the sample were then measured by dynamic light scattering (DLS) to be around 521.1 nm. (see Appendix B) The hydraulic radius of the pore throat was calculated through the following expression:

$$r_H = \frac{\phi}{1-\phi}\frac{d_p}{6} \tag{4.1}$$

where, ϕ is the porosity and d_p is the diameter of the quartz particle. The Reynolds number for the deposition and dissolution process was calculated to be 6.59 x 10^{-3} and 6.89 x 10^{-3}, respectively. The Peclet number (Pe) of the µPBR was determined through eq 4.2 based on the particle size of asphaltenes as proposed by Lin et al., to assess the relative contributions of convection and diffusion.[22] The Pe values were calculated to be 1.47 x 10^2 and 2.14 x 10^2 for the deposition and dissolution processes, respectively.

$$Pe = \frac{2uR_P}{D_{BM}} \tag{4.2}$$

where u is the superficial velocity, R_P is the radius of the asphaltenes particles, and D_{BM} is the Brownian diffusivity, which can be determined through the Stoke-Einstein equation.

- 134 -

4.2.7 In-Line UV-vis Spectroscopy Measurements

The concentration of dissolved asphaltenes in the solvent was measured by an in-line UV-vis spectroscopy unit (Ocean Optics). Figure 4.3 shows the assembly of the microsystem during the dissolution process of asphaltenes. The house-designed flow cell was connected directly to the outlet of the reactor to increase the precision of the measurement by minimizing the dead volume to 15.7 μL. The absorbance from 300 nm to 400 nm was acquired at 10 scans/s to maximize the signal-to-noise ratio.[28] The lower detection limit of asphaltenes in xylenes was 2.95 mg/L in our experiments. The UV-Vis lamp was warmed up for at least 30 min to maintain the sable light source before each experiment.
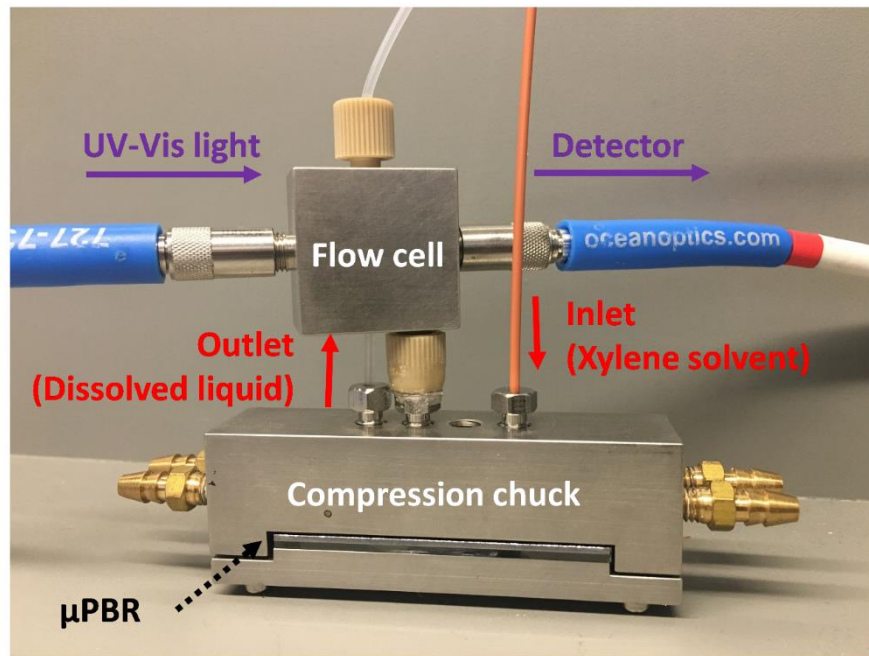
Figure 4.3 Assembly of the with in-line UV-Vis spectroscopy for asphaltenes dissolution study.

4.2.8 *in situ* Raman Spectroscopy Measurements

The Raman mappings of µPBRs were acquired by in situ Raman spectroscopy (Horiba LabRam HR evolution, Jobin-Yvon), equipped with a X-Y-Z three directional free movement sample stage. The Duoscan mode was enabled to obtain the spectra of a 50 x 50 µm^2 area as described before.[25] To cover the whole µPBR, the total mapping area was set to be 25.0 x 14.0 mm^2, which includes 35391 spectra in return. The excitation source was a Diode-Pumped Solid-State (DPSS) laser system with emitting light at 532 nm. A 10x MPlanN Olympus lens was selected as objective, while a CCD Synapse EM detector was used to acquire the spectra. The grating was 600 grooves per mm and the exposure time was 0.3 s. The deconvolution of all spectra was applied by using third party Matlab codes, such as GSTools (import '.spc' file) and iSignal (deconvolution library, created and updated by Prof. Tom O'Haver, University of Maryland). A linear baseline correction was applied to all spectra.

4.2.8.a Sheet size measurement.

As shown in Figure 4.4, the Raman spectra of asphaltene molecules could be deconvoluted into four different peaks, namely: G-band, D1-band, D2-band and D3-band.[23] It is well-known that the G-band corresponds to the stretching of sp^2 carbon atoms, which is mainly present in the aromatic core of asphaltenes molecules. The D1-band is related to the boundary of an ordered-like structure, and such is the case of asphaltenes molecules. The physical meaning of the D2-band is still not well-understood yet, while some research has assigned it to the interstitial insertion of the graphene moieties or the stacking deformation.[24] The D3-band appears as a wide band, which indicates aromatic plane of asphaltenes molecules. The ratio between the integration area of the G-band and the D1-
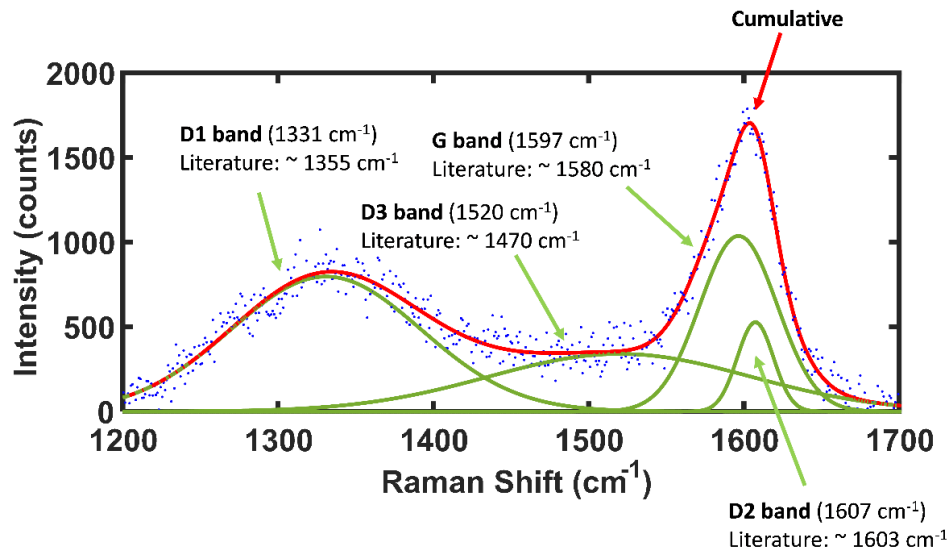
Figure 4.4 Deconvolution of Raman spectrum for asphaltenes molecules into four different peaks: G band, D1 band, D2 band, and D3 band.

band has been proved and used as a reference for asphaltenes sheet size characterization.[23–25,30,31] Here, the Tuinstra-Koenig relation was used for sheet size (La) measurement,

$$La(nm) = C(\lambda)\frac{I_G}{I_{D1}} \tag{4.3}$$

the prefactor $C(\lambda)$ is dependent on the wavelength of incident light, where $C(532nm) \cong 4.96\ nm$ in our case.[32] The concept of sheet size is similar to molecular diameter, except it is more specific to an aromatic core. It is reported that the molecular diameter of asphaltenes range from 1.2 nm to 7.6 nm.[33]

4.2.8.b Bed Occupancy Measurements

The Raman spectroscopy is a powerful characterization method, not only for chemical identification, but also in the quantitative analysis of chemicals. In this work, the dispersion of asphaltenes across the μPBR was shown as a bed occupancy map. The detailed

description and calibration of the bed occupancy of asphaltenes is previously reported.[25] In short, the concept of bed occupancy can be understood as the normalized concentration of asphaltenes. The following expression was used for local bed occupancy ϖ_i calculation:

$$\varpi_i = \frac{I_{a,i}}{I_{a,i} + mI_{q,i}} \tag{4.4}$$

where $I_{a,i}$ and $I_{q,i}$ are the corresponding integrated area of Raman peaks of asphaltenes molecules (897–1987 cm^{-1}) and quartz (400– 520 cm^{-1}), respectively. The constant m is the ratio of Raman quantification factors between asphaltenes and quartz. As indicated in the literature, Raman quantification factors have a similar definition as molar absorptivity in Beer's law.[34–36] The physical meaning of constant m originated from different molecular responses to excitation due to the different molecular properties. The value of constant m (27.33) was obtain through calibration of Raman spectra with an optical image. As the sheet size measurement and bed occupancy measurement are calculated from same spectra set, it is important to validate both data are independent to each other. (see Appendix)

4.2.9 Fluorescence Spectroscopy

The fluorescence emission spectra of the asphaltenes samples were acquired by Horiba PTI QuantaMaster 400 Fluorescent Spectrometer. The sample contain 30.0 mg/L of asphaltenes in toluene. The emission wavelength in the range from 300 nm to 800 nm was acquired at the excitation wavelength of 265 nm.

4.3 Results and Discussion

4.3.1 In-Line UV-vis Adsorption during Dissolution

The UV-vis absorbance measured provides information about the concentration of asphaltenes dissolved in the xylenes solvent. Figures 4.5 (a) & (b) are examples of in-line UV-vis absorbance versus pore volume of xylenes injected. The absorbance of asphaltenes illustrates a vertex at each program, which indicates the maximum dissolved asphaltenes
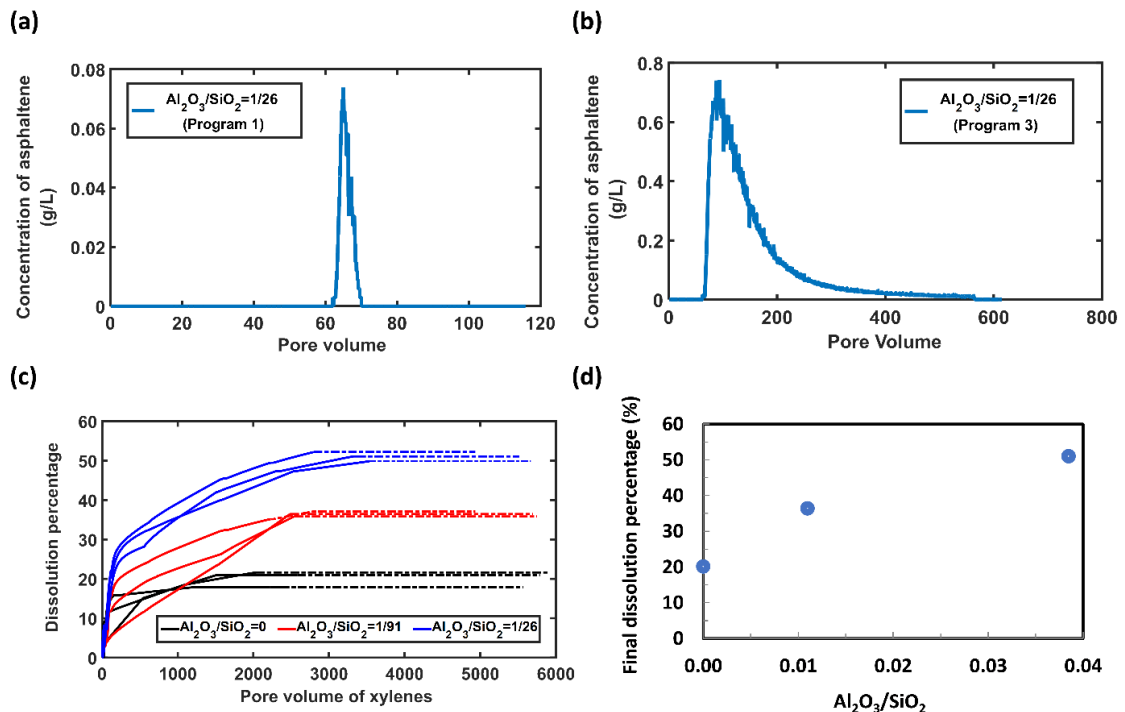
Figure 4.5 Examples of the dissolved asphaltenes concentration in xylenes acquired by UV-Vis absorbance with the presence of zeolites with $Al_2O_3/SiO_2 = 1/26$: (a) program 1 of trial 2, and (b) program 3 of trial 2. (c) The real-time accumulated asphaltenes dissolution percentage profile of all trials. (d) The final dissolution percentage of asphaltenes increases as the ratio of Al_2O_3/SiO_2 increases. (see Appendix B for outlet samples)

concentration reached by some pore volume of xylenes injected (see Figures 4.5 (a) & (b)). Note the μPBR was prewetted by cyclohexane, and the residual amount of solvent before the injection of xylenes was estimated to be 49.6 μL (or 2 pore volumes). The absorbance of asphaltenes was approximately zero after the first few pore volumes as the injected xylenes solvent front gradually displaced cyclohexane until the void volume of the μPBR was filled by xylenes. The fact that the maximum concentration was reached after 60 pore volumes indicates the influence of cyclohexane was negligible. Figure 4.5 (c) depicts the accumulative asphaltenes dissolution percentage (m / m_0) from μPBR, with respect to different pore volumes of xylenes solvent injected. Generally, the maximum dissolution percentage of asphaltenes in xylenes solvent is 51.00 ± 0.97 wt %, which is consistent with previous literature.[37]

The influence of zeolites on the dissolution of asphaltenes in xylenes could be understood by comparison of the dissolution profiles with different zeolites present. Figure 4.5 (c) indicates that more pore volumes of xylenes are necessary to obtain the maximum dissolution of asphaltenes from porous media when the Al_2O_3 content increased. Without the presence of HZSM-5, 1200−2000 pore volumes of xylenes were required to reach the maximum dissolution, while 2500−2800 pore volumes and 2800−3400 pore volumes of xylenes were required for Al_2O_3/ SiO_2 ratios of 1/91 and 1/26, respectively. In the other hand, one observes that the maximum dissolution percentage of asphaltenes in xylenes increased from 20.15 wt %, to 36.43 wt %, to 51.00 wt % when the Al_2O_3/SiO_2 ratios increased from 0, to 1/91, to 1/26. At a glance, the results seem contradictory to the fact that the affinity of asphaltenes with surface increases when the content of Al_2O_3 increases.[25] As we will soon learn, in situ Raman spectroscopy can reveal mechanistic

- 140 -

insight that explains the general observation. It is worth mentioning that the differences in molecular structure of asphaltenes can have some influence on the UV-vis absorbance spectra. For instance, the larger sheet size of asphaltenes molecules can have a red shift in the absorbance spectra. Here, we consider this effect to be negligible within the measurement range (300−400 nm) of our spectra.

4.3.2 Bed occupancy map and dissolution map.

The asphaltenes bed occupancy map provides a direct method to visualize the dispersion of asphaltene across the μPBR. Figure 4.6 (b) shows the bed occupancy maps of the μPBR damaged by deposition of asphaltenes. The results are in great consistency with optical images, except more details presented in bed occupancy maps.[25] Furthermore, the acquisition of Raman spectra of μPBR is a standardized process with enclosure chamber, which could ensure to minimize the characterization errors caused by Raman setup.

Figure 4.6 presents the dispersion of asphaltenes across the μPBR. As we already know, asphaltenes molecules can either adsorb onto the surface of the quartz or self-assemble to form nanoparticles. Either mechanism is anticipated to generate the damage illustrated in Figure 4.6 (a). The optical images are in good agreement with mechanisms described in previous works.[38–40] A closer inspection of the occupancy map of Figure 4.6 (b) reveals interesting results. The mean occupancy of the μPBR increased from 0.53 to 0.73 and 0.82 as the Al_2O_3/SiO_2 ratio of the injected zeolites increased from 0 to 1/91 and 1/26. This is mainly due to the increase in affinity between the surface and asphaltenes when there is an increase the Al_2O_3 content in the porous media. The fact that Al only has three valence electrons while Si has four valence electrons leads to the attraction of a cation onto the Al
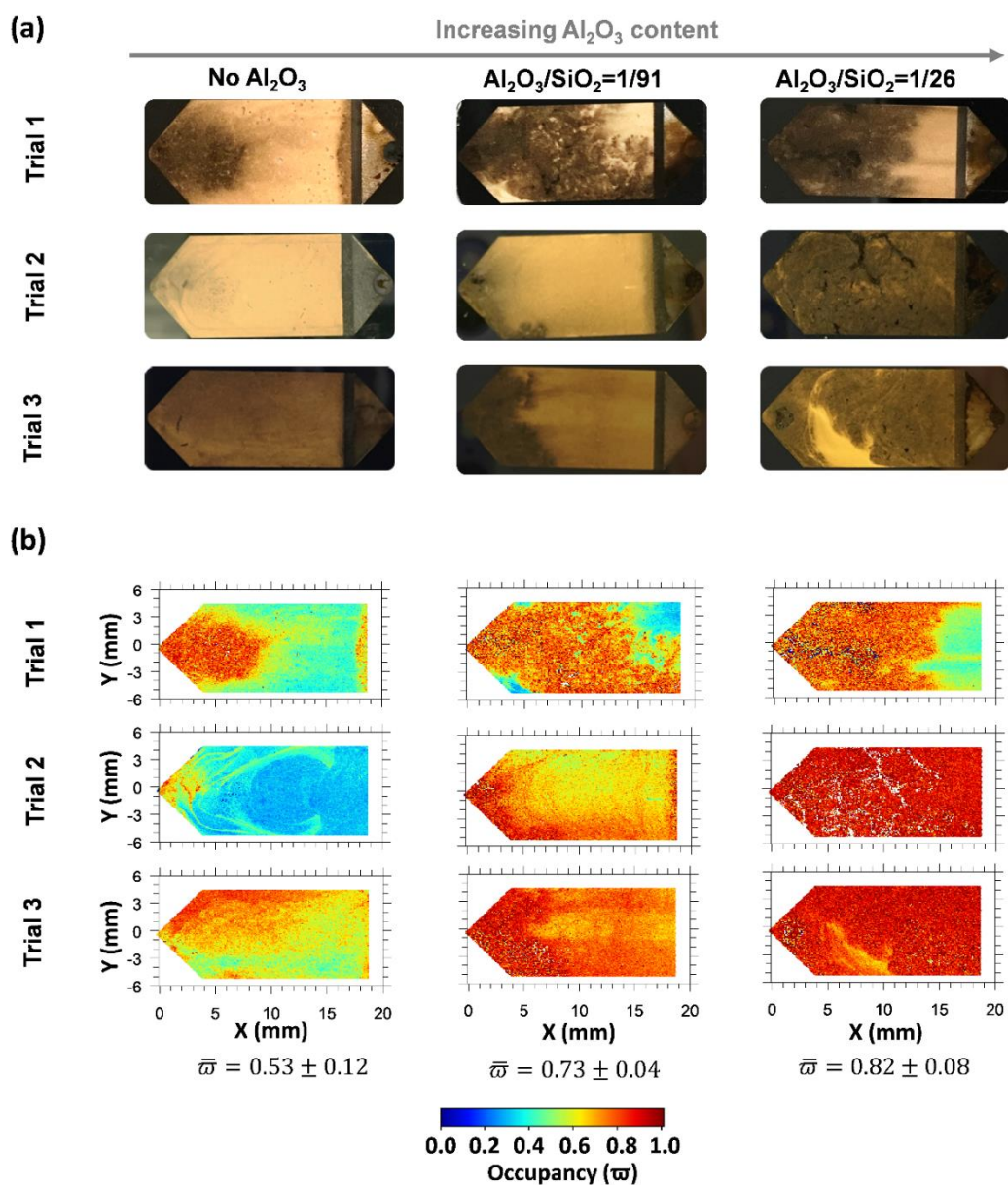
Figure 4.6 (a) Optical images of asphaltenes deposited in the μPBR. (b) Occupancy maps of asphaltenes deposited within the μPBR acquired by Raman spectroscopy. Both datasets illustrate the influence of the Al_2O_3/SiO_2 ratio.

site and the creation of Brønsted acid sites. The concentration of Brønsted acid sites in the HZSM-5 zeolites increase linearly with the Al_2O_3 content.[41] According to previous

literature, the concentrations of Brønsted acid sites are ~0.24 mol kg^{-1} and 0.71 mol kg^{-1} for Al$_2$O$_3$/SiO$_2$ ratios of 1/91 and 1/26, respectively.[41] In theory, the calculated acid number of zeolites increased from 13.46 to 39.83, when the ratio of Al$_2$O$_3$/SiO$_2$ increased from 1/91 to 1/26. (The acid number was calculated based on a 1:1 acid/base ratio.) As a result, the acid−base interaction between the zeolite's surfaces and the asphaltenes was stronger. These observations are in agreement with the reported molecular dynamic simulations of interfacial energy between asphaltenes and oxides: Al$_2$O$_3$ (4.32×10^2 kJ mol^{-1}) > SiO$_2$ (2.09×10^2 kJ mol^{-1}) at 25 °C.[42] The increase of affinity between the surfaces and asphaltenes promoted the adsorption of asphaltenes onto the surface, while competing with their self-assembly to form nanoparticles. Pore throat plugging would result in an increase of the operating pressure to maintain the constant injection rate. When surface adsorption favors self-assembly, pore-throat blockage is prolonged and a high bed occupancy results. The pressure drop measurement across the μPBR confirmed this trend.[25] Therefore, the μPBR with zeolites of highest surface acidity will have higher mean occupancy than others. These observations are in agreement with previous literature, with regard to the role of fine particles in stabilizing the asphaltenes solution.[43–46]

Figure 4.7 (a) & (b) show an optical image of asphaltenes deposition on a porous media and its corresponding occupancy map. One could clearly see that the occupancy map is well-described by the distribution of asphaltenes across the μPBR, including the quantitative details that could not be observed by optical instruments. Figures 4.7 (c) & (d) show the bed occupancy maps after injecting different pore volumes of xylenes through the μPBR. During the dissolution of asphaltenes in the aromatic solvent, the mean occupancy of the μPBR decreased as more pore volumes of xylenes flowed through. When
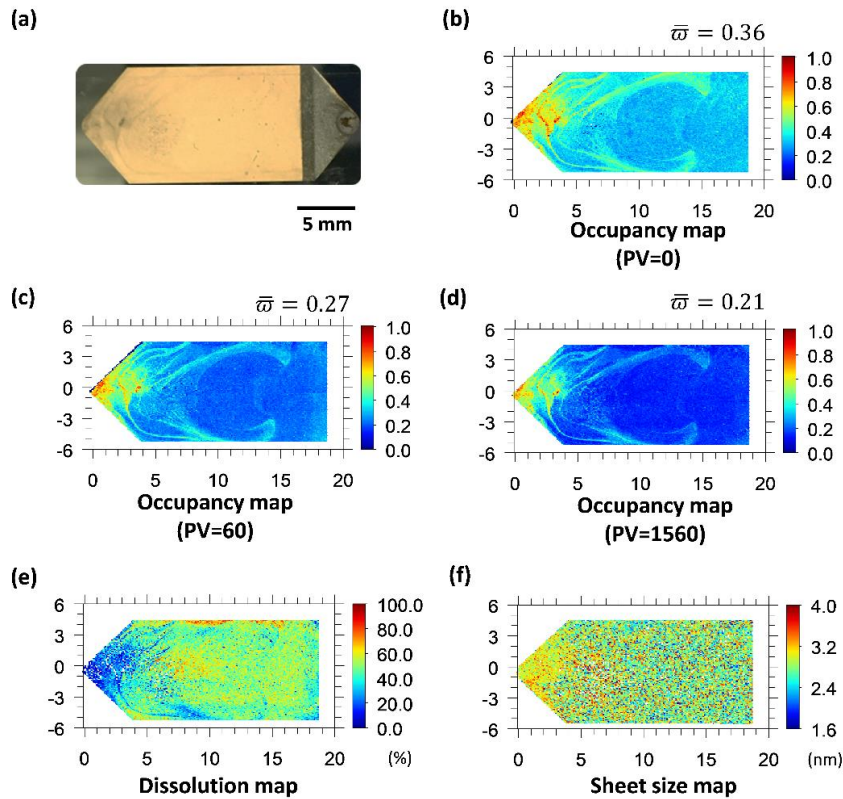
Figure 4.7 (a) Optical image of asphaltenes deposition on μPBR without the presence of zeolites (trial 2). Bed occupancy map of the μPBR after injection of different pore volume of xylenes (b) before injection of xylenes, (c) after injection of 60 pore volume of xylenes, and (d) after injection of 1560 pore volume of xylenes. Panel (e) shows a dissolution map and panel (f) shows a sheet size map.

the mean occupancy reached a constant as more xylenes were injected, the dissolution process was considered to be at equilibrium (see Figure 4.5 (c) &4.7 (d)). At the end of dissolution, less than 50 wt % of deposited asphaltenes were dissolved, which was consistent with reported value ($\leq$ 50 wt %) in the literature.[37] When comparing the different bed occupancy maps of the μPBR during the dissolution, the nonuniform

dispersion of asphaltenes across the μPBR was maintained. These results indicated that the dissolved asphaltenes in xylenes were stable and no re-deposition occurred. Otherwise, a disturbance in asphaltenes dispersion across the μPBR would be expected. The dissolution map was derived based on the bed occupancy map of the μPBR before and at the end of the dissolution, and it provides local information about the dissolution percentage. Figure 4.7 (e) illustrates the control experiment: the dissolution map of the μPBR without any zeolite. As can be seen, no channeling occurred across the μPBR, in good agreement with our previous results.[26,28,29] Furthermore, the high bed occupancy region had a tendency to have less dissolution than the low bed occupancy region. The dissolution map presents a similar pattern as the occupancy map. Based on these observations, one can infer that mechanical entrapment, such as hydrodynamic bridging, dominates in the high occupancy region and had less influence in the low occupancy region. Based on our measurement, we have the particle-to-pore throat size ratio of ∼1:19, which implies that the possibility of dendrite growth leading to hydrodynamic bridging is relatively high. Pore throat sizes much less than the resolution of the approach (or ∼100 μm) make it difficult to directly distinguish hydrodynamic bridging from adsorption. Nevertheless, we could still obtain useful insight into the mechanism. Hydrodynamic bridging corresponds to the areas where the flow pattern changed due to closing of pore throats such as check valves, thus making interstitial pore volumes inaccessible for xylenes to wet. In the other hand, adsorption of asphaltenes onto the porous media surfaces results in the attachment and stacking of asphaltenes molecules on the surfaces. Although the adsorption would also constrain the flow, the open pore throats still allow the solvent to flush through. In other words, those regions with lower occupancy allow the solvent to penetrate the pore spaces. Since less

dissolution occurs in the high occupancy regions, one can conclude that hydrodynamic bridging dominates in the high-occupancy regions. Further evidence of this phenomenon is revealed by the measurement of asphaltenes sheet sizes.

4.3.3 Sheet Size Measurements

In addition to the dispersion of asphaltenes across the μPBR, Raman spectra also provided molecular level information. Sheet size distributions of asphaltenes molecules advanced the understanding of the process of asphaltenes deposition and their dissolution. Here, the sheet size refers to the diameter of the aromatic planar sheet of asphaltenes molecules.[24] Although the mathematical relationship between the sheet size and aromaticity has yet to be reported, because of the complexity of asphaltenes molecules, the sheet size can be an indication of the degree of aromaticity. Generally speaking, the asphaltenes molecules with larger sheet sizes possess a higher degree of aromaticity than those with smaller sheet sizes.

Figure 4.8 (a) shows the mean sheet size of asphaltenes molecules across the μPBR under different Al_2O_3 contents. The term "As-deposit" refers to complete deposition of asphaltenes on the μPBR prior to their dissolution. The mean sheet size of asphaltenes molecules deposited was found to increase from 2.75 nm to 3.21 nm as the Al_2O_3/SiO_2 ratio increases from 0 to 1/26, which is consistent with our previous discussion. When increasing the affinity of asphaltenes molecules for the surface of the porous media under the same conditions, asphaltenes molecules with larger sheet size start to deposit on the surface. As a result, the mean sheet size of asphaltenes molecules deposited would increase as the Al_2O_3 content increases. This also explains why the mean sheet size of asphaltenes in the μPBR after dissolution followed the same trend (increasing from 2.59 nm to 3.03 nm

- 146 -
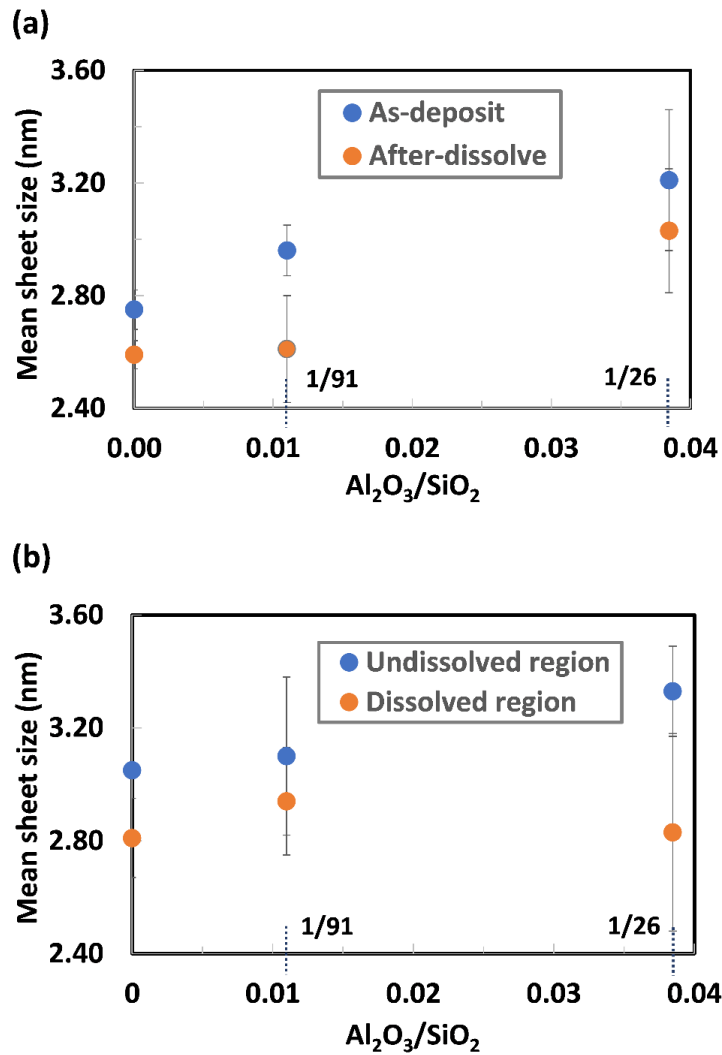
Figure 4.8 Mean sheet size of asphaltenes molecules on µPBRs with different ratios of Al$_2$O$_3$/SiO$_2$ present: (a) as-deposit and after dissolution and (b) undissolved region and dissolved region.

in Figure 4.8 (a). Here, the term "After-dissolve" refers to the maximum dissolution of asphaltenes possible within the µPBR (or the equilibrium). One also observes that the mean sheet sizes of asphaltenes in the "As-deposit" µPBRs are larger than those in the "After-dissolve" µPBRs. This observation indicates that the asphaltenes molecules with large

sheet sizes have a tendency to dissolve in the aromatic solvent, while the asphaltenes molecules with smaller sheet sizes are persistent. When asphaltenes molecules dissolved in an aromatic solvent, asphaltenes molecules with larger sheet size would have a stronger affinity with solvent molecules, because of the increase of $\pi-\pi$ interactions. In other words, the asphaltenes molecules with larger sheet sizes are more stable in the aromatic solvent than while being adsorbed on the surfaces. Molecular dynamics simulations from the literature also support that the larger asphaltenes molecules have stronger interaction with aromatic solvent than smaller asphaltenes molecules.[47] The variance in the experimental data of three trials, consistent with MD simulations, can be explained by (i) the stochastic nature of the process of asphaltenes deposition, and (ii) the complexity of the molecular structure of asphaltenes.

Using the dissolution map as the reference, we could investigate the sheet size in different dissolution regions. Here, we defined the region with a dissolution percentage of <1 wt % as the undissolved region, whereas the region with dissolution percentage of >1 wt % was defined as the dissolved region. Figure 4.8 (b) shows the comparison of the mean sheet sizes of asphaltenes molecules in the dissolved regions with those in the undissolved region. Note that the mean sheet sizes of asphaltenes molecules in the dissolved regions were smaller than those in the undissolved regions. These results could be attributed to the fact that asphaltenes molecules with larger sheet sizes are prone to form the nanoaggregates,[47–50] causing the hydrodynamic bridging in the undissolved regions. The same explanation accounts for the observed standard deviation. The fact that 8 out of 9 trials follow the same trend strengthens our point. In addition, the same trend was observed of the mean sheet size of asphaltenes molecules deposited, increasing from 3.05 nm to 3.33

nm as the acidity of the zeolite increased. Because of the competition of self-assembly of the asphaltenes and their adsorption onto the acidic zeolite, only molecules with larger sheet sizes could form the nanoaggregates. Therefore, the increase in the Al_2O_3 content would result in the increase of asphaltenes sheet size in the undissolved region. Furthermore, the mean sheet size of asphaltenes molecules in the dissolved region was independent of the Al_2O_3 content. Albeit an increase of Al_2O_3 can promote asphaltenes molecules with larger sheet sizes to deposit, recall that molecules with larger sheet size have a tendency to dissolve, because of the stronger interaction with solvent molecules. The competition of these two effects accounts for the independence of the mean sheet size and the Al_2O_3 content in the dissolved region.

4.3.4 Fluorescence Emission Spectra of Outlet Samples

The fluorescence emission spectrometer is a useful method to identify the molecular size of polycyclic aromatic hydrocarbons (PAHs), such as asphaltenes. Yosadara et al. studied the HOMO−LUMO gap as an index of molecular size and the structure of PAHs.[51,52] The work revealed that short- wavelength emissions correspond to small chromophores, while long-wavelength emissions indicate large chromophores, with regard to molecular size, rather than the number of fused rings. For instance, tetracene with a calculated HOMO−LUMO gap of 2.81 eV (440.51 nm) and a calculated size of 11.94 Å has four fused aromatic rings, while ovalene with a calculated HOMO−LUMO gap of 2.82 eV (438.79 nm) and molecular size of 11.92 Å has 10 fused aromatic rings. Another important conclusion from previous work was that the effect of the presence of the alkyl chains and heteroatoms in the asphaltenes structures on the HOMO−LUMO gap is almost negligible.[51,52] These

findings suggested that the fluorescence emission spectra would be a complementary characterization of our investigation.

The zeolite HZSM-5 has been used as a catalyst for cracking of hydrocarbon materials under high temperatures of 340−420 °C.[53–56] Although the experiments in the present work were completed under ambient temperature (20 °C), additional tests were conducted to determine whether or not any cracking or condensation of asphaltenes molecules was possible in our experiments. The asphaltenes in the present work (4.0 g/L asphaltenes in toluene) were agitated by magnetic stirrer bar with zeolite HZSM-5 for 48 h in a batch vial, which was at least 4 times longer than the exposure time of the asphaltenes to the zeolite in the packed-bed microreactors. Samples from the batch tests were collected and analyzed by fluorescence emission spectroscopy, and the results are shown in Figure 4.9 (a). At least three samples from each trial were characterized to ensure that the data were statistically significant. Figure 4.9 (a) demonstrates conclusively that HZSM-5 has a negligible effect on the asphaltenes' molecular structure.

As can be seen in Figure 4.9 (b), the fluorescence emission spectra were measured for the asphaltenes source sample and dissolved asphaltenes samples from different μPBRs with different Al_2O_3 contents. The fluorescence emission maximum of the asphaltenes source sample was ∼494 nm, relatively higher than asphaltenes samples from other sites.[48] This suggested that the asphaltenes samples used in this work have larger molecular size than those of that particular study, which is also consistent with our Raman spectra measurements of the sheet sizes. Recent mass spectrometry data also confirmed that the sample is highly aromatic and consistent with the sheet size argument.[57] Another important finding was that the dissolved asphaltenes samples from μPBRs have a red shift of 10−30
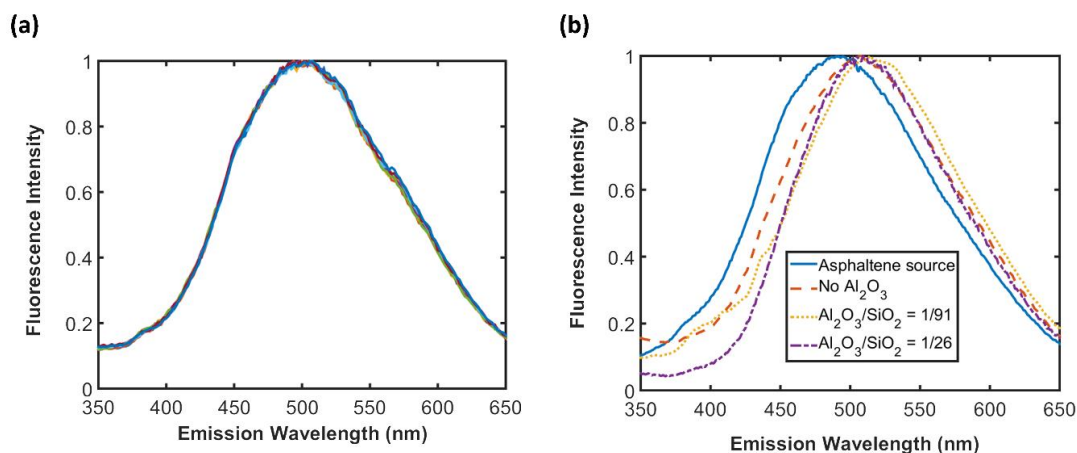
Figure 4.9 (a) Fluorescence emission spectra of asphaltenes samples with and without HZSM-5. The 0.48% of standard deviation suggests that HZSM-5 has negligible effect on the asphaltenes' molecular structure. (b) Fluorescence emission spectra of outlet samples showed a red shift, with respect to the source sample.

nm, with reference to the asphaltenes source samples. The corresponding change in HOMO−LUMO gap ranges from 0.05 eV to 0.14 eV, or 2.0% to 5.6%. (see Appendix for details) These changes are distinguishable from experimental error, which is ∼0.4%. The results implied that the dissolved asphaltenes samples have relatively larger molecular size than the asphaltenes source samples. These results support our conclusion that the asphaltenes molecules with larger sheet size have a tendency to dissolve in the aromatic solvent, while asphaltenes molecules with smaller sheet size are persistent to the surface.

4.3.5 Asphaltenes Deposition and Dissolution Mechanism

Our experimental results introduce new knowledge toward a better understanding of the deposition mechanism of asphaltenes in the porous media. Asphaltenes are attracted to

different materials through different types of interactions, for example, hydrogen bonding interaction (asphaltenes−asphaltenes, asphaltenes−zeolites, asphaltenes−quartz,), acid−base interaction (asphaltenes−zeolites, asphaltenes−asphaltenes), and π−π interaction (asphaltenes−aromatic solvent, asphaltenes−asphaltenes). However, metal coordination interactions are also possible; since no external metal was introduced into the porous media, it is reasonable to assume that metal coordination interactions, if any, were constant throughout our experiments. Since the van der Waals interaction is relatively weak (in the range of 0.4−4.0 kJ/mol, compared to 21.0 kJ/ mol in the case of O−H···O hydrogen bonding) and universal between different materials, it was also considered to have a negligible influence. When the acid−base and hydrogen bonding interactions dominate, one would expect the deposition of asphaltenes onto the surfaces, while the dissolution of asphaltenes into an aromatic solvent such as xylenes would occur when π−π interactions dominate.

Understanding the competition between the two scenarios described above can yield insight on the deposition and the dissolution mechanisms, illustrated by Figure 4.10. As noted, adsorption and mechanical entrapment are the primary mechanisms of deposition, and Figure 4.10 shows the proposed process based on the results of the present study. Since the concentration of asphaltenes solution used in our experiment (4.0 g/L) exceeds the critical nanoaggregation concentration (CNAC) of asphaltenes (150.0 mg/L), the nanoaggregation of asphaltenes molecules would be expected.[28] The surface of asphaltenes nanoaggregate would be the active site for interaction with the porous media. In other words, the affinity of asphaltenes nanoaggregates on the porous media will increase when the surface area of asphaltenes nanoaggregates increases. However, when the size of

- 152 -
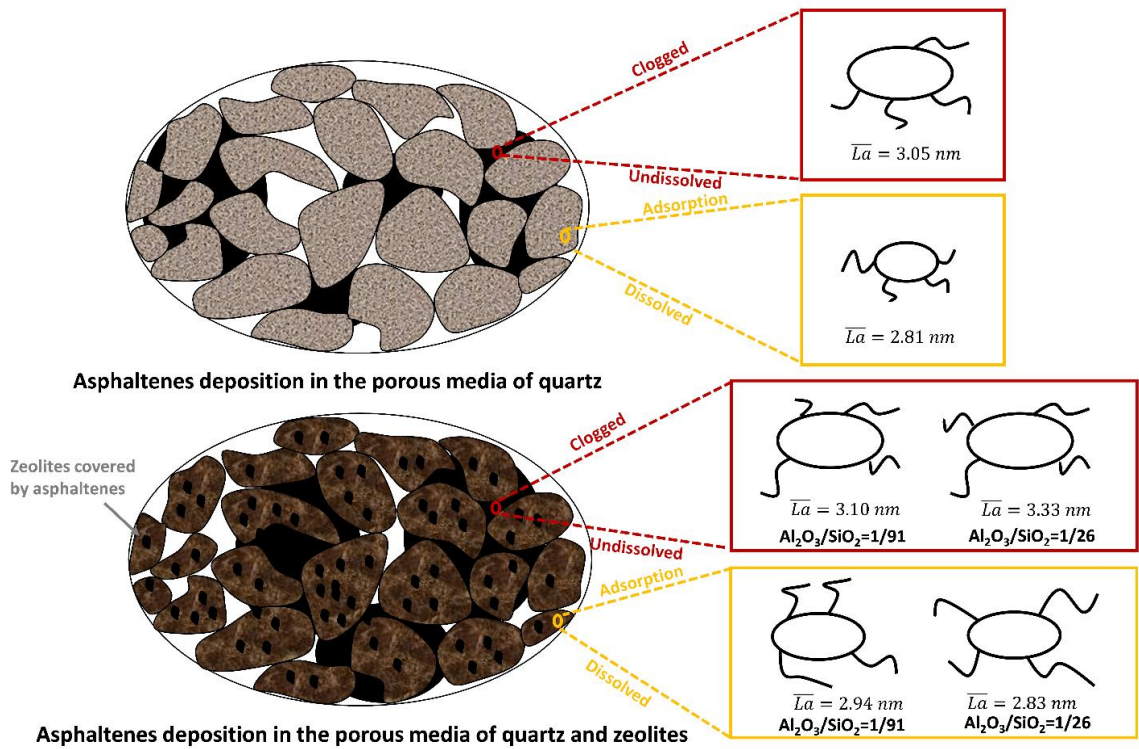
Figure 4.10 Representative elementary volume of porous media without/with the presence of zeolites. The asphaltenes molecules with different aromatic sheet sizes are presented at different locations of porous media.

asphaltenes nanoaggregate increases, the momentum of asphaltenes nanoaggregates would also increase in low *Re* flow and make it more difficult to adsorb onto the surface. Since the surface area/ volume ratio decreases as the diameter of asphaltenes nanoaggregates increase (surface/volume ratio doubles when the diameter decreases to half for a spherical particle), one would expect a greater number of the smaller-sized nanoaggregates to be adsorbed onto the surface while the larger sized nanoaggregates would cause hydrodynamic bridging. As we previously mentioned, our results show that the average sheet size of asphaltenes molecules in the dissolved region (2.86 ± 0.23 nm) is lower than those in the undissolved region (3.16 ± 0.15 nm). Compared to asphaltenes with smaller

sheet sizes, the ones with larger sheet sizes would have stronger $\pi-\pi$ interactions in addition to other interactions. As a result, this stronger affinity would promote aggregation. Therefore, in the undissolved region, where mostly likely hydrodynamic bridging occurred, one would expect the asphaltenes molecules to exhibit larger sheet sizes.

The presence of zeolites increases the affinity of asphaltenes to the surfaces of the porous media.[25] This is anticipated to have noteworthy outcomes:

(1) The large size of asphaltenes nanoaggregates would start to be adsorbed onto the surface of porous media, instead of undergoing hydrodynamic bridging;

(2) Asphaltenes molecules with larger sheet sizes themselves would deposit onto the porous media surfaces; and

(3) Prolong the deposition period by reducing hydro- dynamic bridging events, and thus result in a greater mass of asphaltenes deposited.

By a comparison with adsorption, during hydrodynamic bridging, a smaller number of pore volumes are required to achieve the same pressure drop of the system. However, introducing zeolite into the porous media delayed the pressure buildup by attracting the asphaltenes molecules with larger sheet sizes onto the surfaces. However, hydrodynamically bridged asphaltenes are more difficult to dissolve, since the flow of solvent is blocked by these regions. Based on this knowledge, we could now interpret the relationship between the asphaltenes dissolution percentage and the acidity of the porous media. There are two main reasons for this phenomenon:

(1) The asphaltenes with larger sheet sizes have a stronger affinity with the aromatic solvent xylenes than those molecules with smaller sheet sizes. Since the asphaltenes with

larger sheet sizes would have a tendency to deposition onto the surface when the acidity of porous media increases, more asphaltenes are expected to dissolve in the presence of zeolites.

(2) The stronger affinity of asphaltenes to porous media in the presence of zeolite competes with the self-assembly of asphaltenes. As a result, more asphaltenes molecules are adsorbed onto the surface instead of undergoing hydrodynamic bridging. Thus, the asphaltenes dissolution percentage is expected to increase when the hydrodynamic bridging mechanism is minimized by an increase in the acidity of the porous media.

4.4 Conclusions

The deposition within and the dissolution of asphaltenes from porous media are multicomponent processes, because of the complex chemical nature of asphaltenes molecules themselves. However, our results reveal useful information that advances our understanding of the behavior of asphaltenes molecules:

(1) The Al2O3 content in zeolite HZSM-5 can attract asphaltenes molecules with larger sheet sizes, and thus stabilize the asphaltenes in solution within porous media, because of this increase in affinity.

(2) Asphaltenes molecules with larger sheet sizes have a tendency to self-assemble, ultimately resulting in hydrodynamic bridging within the porous media.

(3) Asphaltenes molecules with larger sheet sizes are easier to dissolve in xylenes than those with smaller sheet sizes.

(4) The increase of acidity of the porous media, by introducing a model zeolite in this case, leads to an increase in the asphaltenes dissolution percentage, because of the competition between surface adsorption with self-assembly.

Our findings help to clarify the asphaltenes dissolution process, which is otherwise challenging to understand. In addition, these results imply that $\pi-\pi$ interactions are significant when considering asphaltenes physics in the porous media. Our discoveries further support that adsorption and hydrodynamic bridging are important during asphaltenes deposition. The direct measurement of either mechanism within the porous media, requiring even greater resolution than the present work, would be a powerful tool in asphaltenes science that could benefit from new innovations in in situ analytical methods and laboratory techniques designed to study asphaltenes.

Reference

(1)   Eskin, D.; Mohammadzadeh, O.; Akbarzadeh, K.; Taylor, S. D.; Ratulowski, J. Reservoir Impairment by Asphaltenes: A Critical Review. *Can. J. Chem. Eng.* **2016**, *94* (6), 1202–1217.

(2)   Mohammadi, M.; Akbari, M.; Fakhroueian, Z.; Bahramian, A.; Azin, R.; Arya, S. Inhibition of Asphaltene Precipitation by TiO2 , SiO2 , and ZrO2 Nanofluids. *Energy Fuels* **2011**, *25*, 3150–3156.

(3)   Li, R.; Du, H.; Fan, Z.; Pei, J. Molecular Dynamics Simulation to Investigate the Interaction of Asphaltene and Oxide in Aggregate. *Adv. Mater. Sci. Eng.* **2016**, *2016*, 3817123.

(4)   Chaisoontornyotin, W.; Zhang, J.; Ng, S.; Hoepfner, M. P. Rapid Heterogeneous Asphaltene Precipitation with Dispersed Solids. *Energy Fuels* **2018**, *32*, 7458–7466.

(5)   Almehaideb, R. A. Asphaltene Precipitation and Deposition in the near Wellbore Region: A Modeling Approach. *J. Pet. Sci. Eng.* **2004**, *42*, 157–170.

(6)   Chaisoontornyotin, W.; Haji-Akbari, N.; Scott Fogler, H.; Hoepfner, M. P. Combined Asphaltene Aggregation and Deposition Investigation. *Energy Fuels* **2016**, *30*, 1979–1986.

(7)   Vilas Bô, C.; Fávero, F.; Hanpan, A.; Phichphimok, P.; Binabdullah, K.; Fogler, H. S. Mechanistic Investigation of Asphaltene Deposition. *Energy Fuels* **2016**, *30*, 8915–8921.

(8)   Niaz, K.; Bahadar, H.; Maqbool, F.; Abdollahi, M. A Review of Environmental
        and Occupational Exposure to Xylene and Its Health Concerns. *EXCLI J.* **2015**, *14*,
        1167–1186.

(9)   Hartman, R. L.; McMullen, J. P.; Jensen, K. F. Deciding Whether to Go with the
        Flow: Evaluating the Merits of Flow Reactors for Synthesis. *Angew. Chem Int. Ed.*
        2011, *50* (33), 7502–7519.

(10)   Hartman, R. L.; Jensen, K. F. Microchemical Systems for Continuous-Flow
        Synthesis. *Lab Chip* **2009**, *9* (17), 2495–2507.

(11)   Marre, S.; Adamo, A.; Basak, S.; Aymonier, C.; Jensen, K. F. Design and
        Packaging of Microreactors for High Pressure and High Temperature Applications.
        Ind. Eng. Chem. Res. **2010**, *49* (22), 11310–11320.

(12)   Kjeang, E.; Djilali, N.; Sinton, D. Microfluidic Fuel Cells: A Review. *J. Power
        Sources* **2009**, *186*, 353–369.

(13)   Chen, W.; Pinho, B.; Hartman, R. L. Flash Crystallization Kinetics of Methane
        (SI) Hydrate in a Thermoelectrically-Cooled Microreactor. *Lab Chip* **2017**, *17*
        (17), 3051–3060.

(14)   Fletcher, P. D. I.; Haswell, S. J.; Zhang, X. Monitoring of Chemical Reactions
        within Microreactors Using an Inverted Raman Microscopic Spectrometer.
        Electrophoresis **2003**, *24* (18), 3239–3245.

(15)   Chan, E. M.; Mathies, R. A.; Alivisatos, A. P. Size-Controlled Growth of CdSe
        Nanocrystals in Microfluidic Reactors. *Nano Lett.* **2003**, *3* (2), 199–201.

(16)   Elvira, K. S.; i Solvas, X. C.; Wootton, R. C. R.; DeMello, A. J. The Past, Present and Potential for Microfluidic Reactor Technology in Chemical Synthesis. *Nat. Chem.* **2013**, *5*, 905–915.

(17)   Jensen, K. F. Flow Chemistry-Microreaction Technology Comes of Age. *AIChE J.* **2017**, *63* (3), 858–869.

(18)   Mcmullen, J. P.; Jensen, K. F. Rapid Determination of Reaction Kinetics with an Automated Microfluidic System. *Org. Process Res. Dev.* **2011**, *15*, 398–407.

(19)   Seong, G. H.; Heo, J.; Crooks, R. M. Measurement of Enzyme Kinetics Using a Continuous-Flow Microfluidic System. *Anal. Chem.* **2003**, *75*, 3161–3167.

(20)   Song, H.; Ismagilov, R. F. Millisecond Kinetics on a Microfluidic Chip Using Nanoliters of Reagents. *J. Am. Chem. Soc.* **2003**, *125*, 14613–14619.

(21)   Lin, Y.-J.; He, P.; Tavakkoli, M.; Thunduvila Mathew, N.; Yit Fatt, Y.; Chai, J. C.; Goharzadeh, A.; Vargas, F. M.; Lisa Biswal, S. Characterizing Asphaltene Deposition in the Presence of Chemical Dispersants in Porous Media Micromodels. *Energy Fuels* **2017**, *31*, 11660–11668.

(22)   Lin, Y.-J.; He, P.; Tavakkoli, M.; Thunduvila Mathew, N.; Yit Fatt, Y.; Chai, J. C.; Goharzadeh, A.; Vargas, F. M.; Lisa Biswal, S. Examining Asphaltene Solubility on Deposition in Model Porous Media. *Langmuir* **2016**, *32*, 8729–8734.

(23)   Abdallah, W. A.; Yang, Y. Raman Spectrum of Asphaltene. *Energy Fuels* **2012**, *26* (11), 6888–6896.

(24)   Bouhadda, Y.; Bormann, D.; Sheu, E.; Bendedouch, D.; Krallafa, A.; Daaou, M.

Characterization of Algerian Hassi-Messaoud Asphaltene Structure Using Raman Spectrometry and X-Ray Diffraction. *Fuel* **2007**, *86* (12–13), 1855–1864.

(25)   Pinho, B.; Minsariya, K.; Yen, A.; Joshi, N.; Hartman, R. L. Role of HZSM-5 Aluminosilicates on Asphaltenes Deposition by High-Throughput in Situ Characterizations of a Microreservoir. *Energy Fuels* **2017**, *31*, 11640–11650.

(26)   Hu, C.; Morris, J. E.; Hartman, R. L. Microfluidic Investigation of the Deposition of Asphaltenes in Porous Media. *Lab chip* **2014**, *14* (12), 2014–2022.

(27)   Hu, C.; Hartman, R. L. High-Throughput Packed-Bed Microreactors with In-Line Analytics for the Discovery of Asphaltene Deposition Mechanisms. *AIChE J.* **2014**, *60* (10), 3534–3546.

(28)   Hu, C.; Yen, A.; Joshi, N.; Hartman, R. L. Packed-Bed Microreactors for Understanding of the Dissolution Kinetics and Mechanisms of Asphaltenes in Xylenes. *Chem. Eng. Sci.* **2016**, *140*, 144–152.

(29)   Hu, C.; Sabio, J. C.; Yen, A.; Joshi, N.; Hartman, R. L. Role of Water on the Precipitation and Deposition of Asphaltenes in Packed-Bed Microreactors. *Ind. Eng. Chem. Res.* **2015**, *54* (16), 4103–4112.

(30)   Tuinstra, F.; Koenig, L. Raman Spectrum of Graphite. *J. Chem. Phys.* **1970**, *53* (1970), 1126–1130.

(31)   Bointon, T. H.; Barnes, M. D.; Russo, S.; Craciun, M. F. High Quality Monolayer Graphene Synthesized by Resistive Heating Cold Wall Chemical Vapor Deposition. *Adv. Mater.* **2015**, *27* (28), 4200–4206.

(32)   Matthews, M.; Pimenta, M.; Dresselhaus, G.; Dresselhaus, M.; Endo, M. Origin of Dispersive Effects of the Raman D Band in Carbon Materials. *Phys. Rev. B* **1999**, *59* (10), R6585–R6588.

(33)   Freed, D. E.; Lisitza, N. V.; Sen, P. N.; Song, Y.-Q. Molecular Composition and Dynamics of Oils from Diffusion Measurements. In *Asphaltenes, Heavy Oils, and Petroleomics*; 2007; pp 279–299.

(34)   Wopenka.B., P. J. D. Limitations to Quantitative Analysis of Fluid Inclusions in Geological Samples by Laser Raman Microprobe Spectroscopy. *Appl. Specroscopy* **1986**, *40* (2), 144–151.

(35)   Wopenka.B., P. J. D. Raman Intensities and Detection Limits of Geochemically Relevant Gas Mixtures for a Laser Raman Microprobe. *Anal. Chem.* **1987**, *59*, 2165–2170.

(36)   Sum, A. K.; Burruss, R. C.; Sloan, E. D. Measurement of Clathrate Hydrates via Raman Spectroscopy. *J. Phys. Chem. B* **1997**, *101* (38), 7371–7377.

(37)   Cimino, R.; Correra, S.; Bianco, A. Del; Lockhart, T. P. Solubility and Phase Behavior of Asphaltenes in Hydrocarbon Media. In *Asphaltenes, Fundamentals and Applications*; Sheu, E. Y., Mullins, O. C., 1st Eds.; 1995.

(38)   Boek, E. S.; Ladva, H. K.; Crawshaw, J. P.; Padding, J. T. Deposition of Colloidal Asphaltene in Capillary Flow: Experiments and Mesoscopic Simulation. *Energy Fuels* **2008**, *22*, 805–813.

(39)   Lawal, K. A.; Crawshaw, J. P.; Boek, E. S.; Vesovic, V. Experimental

Investigation of Asphaltene Deposition in Capillary Flow. *Energy Fuels* **2012**, *26*, 2145–2153.

(40) Hoepfner, M. P.; Limsakoune, V.; Chuenmeechao, V.; Maqbool, T.; Scott Fogler, H. A Fundamental Study of Asphaltene Deposition. *Energy Fuels* **2013**, *27*, 725–735.

(41) Rodríguez-González, L.; Hermes, F.; Bertmer, M.; Rodríguez-Castellón, E.; Jiménez-López, A.; Simon, U. The Acid Properties of H-ZSM-5 as Studied by NH3-TPD and 27Al-MAS-NMR Spectroscopy. *Appl. Catal. A Gen.* **2007**, *328* (2), 174–182.

(42) Sahu, K. K.; Roy, A. K.; Roy, A.; Das, K.; Singh, R. Materials for Nuclear and Fossil Energy Applications. *Adv. Mater. Sci. Eng.* **2016**, *2016*, Article ID 3817123.

(43) Langevin, D.; Argillier, J.-F. Interfacial Behavior of Asphaltenes. *Adv. Colloid Interface Sci.* **2016**, *233*, 83–93.

(44) Gafonova, O. V; Yarranton, H. W. The Stabilization of Water-in-Hydrocarbon Emulsions by Asphaltenes and Resins. *J. Colloid Interface Sci.* **2001**, *241*, 469–478.

(45) Yan, Z.; Elliott, J. A. W.; Masliyah, J. H. Roles of Various Bitumen Components in the Stability of Water-in-Diluted-Bitumen Emulsions. *J. Colloid Interface Sci.* **1999**, *220*, 329–337.

(46) Yan, N.; Gray, M. R.; Masliyah, J. H. *On Water-in-Oil Emulsions Stabilized by Fine Solids*; 2001; Vol. 193.

(47) Rogel, E. Simulation of Interactions in Asphaltene Aggregates. *Energy Fuels* **2000**, *14*, 566–574.

(48) Daaou, M.; Bendedouch, D.; Bouhadda, Y.; Vernex-Loset, L.; Modaressi, ^ A; Rogalski, M. Explaining the Flocculation of Hassi Messaoud Asphaltenes in Terms of Structural Characteristics of Monomers and Aggregates. *Energy Fuels* **2009**, *23*, 5556–5563.

(49) Sedghi, M.; Goual, L.; Welch, W.; Kubelka, J. Effect of Asphaltene Structure on Association and Aggregation Using Molecular Dynamics. *J. Phys. Chem. B* **2013**, *117*, 5765–5776.

(50) León, O.; Rogel, E.; Espidel, J.; Torres, G. Asphaltenes: Structural Characterization, Self-Association, and Stability Behavior. *Energy Fuels* **2000**, *14* (1), 6–10.

(51) Ruiz-Morales, Y. HOMO-LUMO Gap as an Index of Molecular Size and Structure for Polycyclic Aromatic Hydrocarbons (PAHs) and Asphaltenes: A Theoretical Study. I. *J. Phys. Chem. A* **2002**, *106* (46), 11283–11308.

(52) Ruiz-Morales, Y.; Mullins, O. C. Polycyclic Aromatic Hydrocarbons of Asphaltenes Analyzed by Molecular Orbital Calculations with Optical Spectroscopy. *Energy Fuels* **2007**, *21*, 256–265.

(53) Trejo, F.; Ancheyta, J.; Morgan, T. J.; Herod, A. A.; Kandiyoti, R. Characterization of Asphaltenes from Hydrotreated Products by SEC, LDMS, MALDI, NMR, and XRD. *Energy Fuels* **2007**, *21*, 2121–2128.

(54)   Derouane, E. G.; Védrine, J. C.; Pinto, R. R.; Borges, P. M.; Costa, L.; Lemos, M.
       A. N. D. A.; Lemos, F.; Ribeiro, F. R. The Acidity of Zeolites: Concepts,
       Measurements and Relation to Catalysis: A Review on Experimental and
       Theoretical Methods for the Study of Zeolite Acidity. *Catal. Rev.* **2013**, *55* (4),
       454–515.

(55)   Alshareef, A. H.; Scherer, A.; Tan, X.; Azyat, K.; Stryker, J. M.; Tykwinski, R. R.;
       Gray, M. R. Formation of Archipelago Structures during Thermal Cracking
       Implicates a Chemical Mechanism for the Formation of Petroleum Asphaltenes.
       Energy Fuels **2011**, *25* (5), 2130–2136.

(56)   Adams, J. J.; Schabron, J. F.; Boysen, R. Quantitative Vacuum Distillation of
       Crude Oils to Give Residues Amenable to the Asphaltene Determinator Coupled
       with Saturates, Aromatics, and Resins Separation Characterization. *Energy Fuels*
       2015, *29*, 2774–2784.

(57)   Juyal, P.; Mckenna, A. M.; Fan, T.; Cao, T.; Rueda-Velásquezvelásquez, R. I.;
       Fitzsimmons, J. E.; Yen, A.; Rodgers, R. P.; Wang, J.; Buckley, J. S.; et al. Joint
       Industrial Case Study for Asphaltene Deposition. *Energy Fuels* **2013**, *27*, 1899–
       1908.

Chapter 5

An Automated Microfluidic System for the Investigation of Asphaltenes Deposition and Dissolution in Porous Media

5.1 Introduction

While the lighter components of hydrocarbons, such as saturates and aromatic compounds, are well characterized in their chemical structures, the heavier, more complex components, such as asphaltenes and resins, are often considered as by-products in refining, thus are unmerited in being characterized in a practical fashion.[1–3] Asphaltenes remain a problem in the petroleum industry. They can precipitate in the near well-bore region, resulting in permeability losses of the rock formation (formation damage), deposition on equipment and tubing, and an overall decline in production. These operational Issues not only lead to safety hazards, but they also increase the cost of petroleum production.

Nowadays the definition of asphaltenes is widely accepted by its solubility properties, which are defined as being soluble in toluene and insoluble in n-alkanes. Nonetheless, this broad definition makes asphaltenes molecules more difficult to study than most molecules, which are defined by their chemical properties. Exacerbating their characterization, asphaltenes, depending on their geological formation or origin, can vary widely in composition. Numerous reports have shown that their hydrogen-to-carbon ratio is relatively consistent, suggesting that asphaltenes have a definitive structured backbone. However, the composition of the heteroatoms has been seen to vary quite significantly.[4] These reasons alone make the study of asphaltenes either very time-consuming or not extendable, creating both practical and scientific demand for high through-put laboratory methodologies in this field of study.

In our previous investigations, we have reported improvements in the experimental efficiency from weeks and months with traditional methodologies, to days and hours by designing microfluidics.[5–10] Characterizations of asphaltenes' nanosheet sizes and their occupancy within porous media is also possible using *in-situ* Raman spectroscopy.[9–11] However, even with miniaturization and *in-situ* Raman spectroscopy, typical experiment times are in the range of 6 hours (at 0.3 s per spectrum) to characterize a 2D porous media having a 25 x 14 mm^2 cross-sectional area.[9,10] These long acquisition times and the vast amount of parameters necessary to study call for a new approach in the design of microfluidics to study asphaltenes in porous media.

Automation of microfluidic systems has advanced science and engineering in the last decade. High through-put screening of various parameters in biology, chemistry, and materials science can build a wealth of knowledge in a short period of time.[12–20] The 'micropilot', for example, aides in the analysis of biological processes by automatically detecting the cells of interest and performs complex image sequencing to gather statistically significant data sets.[15] The discovery of new active pharmaceutical ingredients (API) from natural sources require a tremendous amount of effort, and is often extremely time-consuming. With the integration of automated liquid chromatography-mass spectroscopy (LC-MS) systems, the process becomes expedited.[17] Autonomous robotics have been applied to perform traditional synthesis of materials in order to optimize the reaction conditions necessary for nanoparticle selectivity and synthesis.[19] In recent years, the method of applying automation to research has been gaining much traction in order to efficiently better

- 167 -
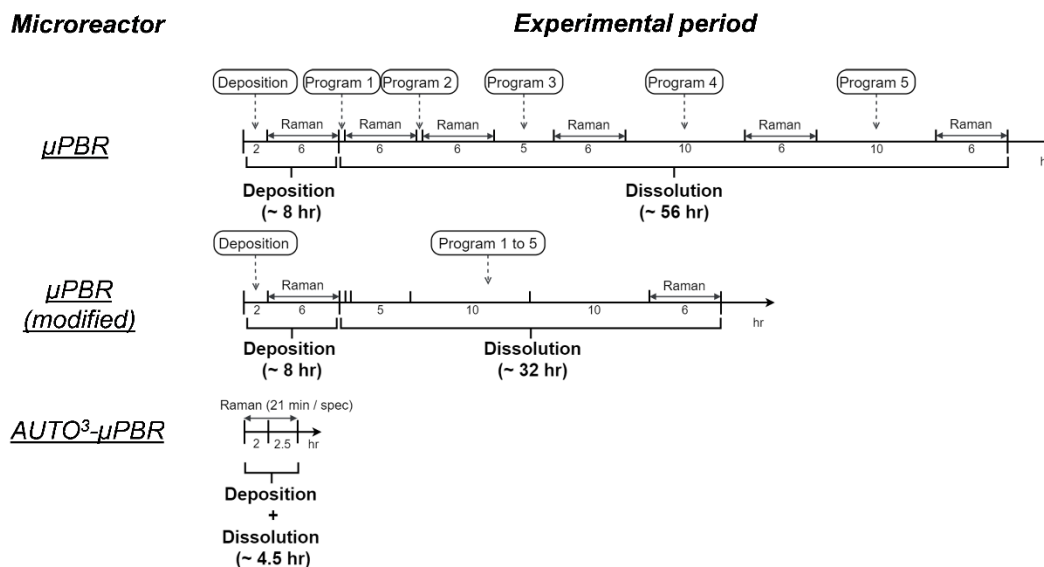
Figure 5.1 Comparison of total experimental period for previous micro-packed bed reactor(µPBR), and automated micro-packed bed reactor (AUTO³-µPBR).

understand reaction chemistry.[21-34] Research combined with automation not only saves researchers from tedious repetition but also provides an efficient platform to spearhead studies in complex chemistries, such as asphaltenes science.

In the present work, an automated microfluidic system was designed to study asphaltenes in porous media, making accessible in hours and minutes information on the deposition and dissociation processes. Figure 5.1 shows the reduction of total experimental period for the automated micro-packed bed reactor (AUTO³-µPBR) when compare to previous microreactor. This study introduces three independent, parallel, packed-bed microreactors on the same chip. Operation in parallel, increases the statistical significance of data, which is critical in the study of complex phenomena. In-situ characterizations made possible the real-time acquisition of transient, high-fidelity information of the temperature effect on asphaltenes

deposition and dissociation in porous media. Our findings could generate deeper understanding of asphaltenes science.

5.2 Experimental section

5.2.1 Materials and Chemicals

Toluene (>99.9%, purity) was purchased from BDH Chemicals VWR. Ethanol (>99.5%, purity), isopropanol (99.7%, purity), and acetone (99.8%, purity) were purchased from Milipore. n-Heptane (99%, purity), Xylenes (>98.5%, purity), and cyclohexane (>99.7%, purity) were purchased from Alfa Aesar.

Quartz particles (30-40 mesh) were purchased from VWR International. To reduce the particle size, particles were ground up in a ceramic mortar with pedestal and deionized water until a smooth consistency was achieved. The slurry was then oven dried at 60 °C for 30 min or until completely dried. Once dried the quartz was sieved using a sonic sifter (L3P, Advantech Manufacturing Inc., New Berlin, WI, USA) through filters of sizes 38, 25, and 20 microns. Particles in the range of 25-20 microns were collected for use in the packed-bed microreactors. The quartz was then transferred to a vial with excess deionized water and sonicated to loosen fines. The mixture was then gravity separated for one minute to ensure that only the larger particles remained. After 1 min, the aqueous solution containing the small particles was decanted out and fresh deionized water added. This procedure was completed three times to ensure that the larger particles were completely isolated. The quartz was then left to dry in an oven at 60 °C until dry and transferred to a vial.

The crude oil was kindly provided by Nalco Champion, Sugar Land, TX, USA. The preparation of asphaltenes from the crude oil was described in previous work.[5] In brief, the hydrocarbon sample was first dissolved in toluene. The solution was then treated in an ultrasonic bath for 20 min, followed by a 30-min rest. The resulting solution was filtered through Whatman grade 1 filter to get rid of the non-soluble impurities. Twice the volume of n-heptane was added to the solution to precipitate the asphaltenes overnight. The asphaltenes samples were then obtained by filtering the solution through Whatman grade 1 filter paper. The samples were then oven dried at 60 °C for 24 hrs and collected in a vial for future use.

5.2.2 Microfluidics design and packaging

5.2.2.a Design and fabrication of AUTO^3-µPBR.

Figures 5.2 (a) and (b) illustrate the assembled automated microfluidic system and the two-dimensional pattern of the AUTO^3-µPBR, which were designed using AutoCAD software. The AUTO^3-µPBR has three independent micro-packed bed channels on-chip, which can operate either in series or in parallel. Each micro packed-bed features a 4.5 µL packing zone and downstream micropillars (25 rows x 30 columns of 20 µm diameter micropillars each spaced 20 µm apart) near the exit of the packing zone to immobilize the quartz particles. The devices were fabricated using traditional micro-electronics-mechanical-system (MEMS) processing techniques (refer to Appendix C). Microchannels (304.3 ± 8.4 µm) were etched by deep-reactive ion etching a 1.0 mm thick silicon wafer. A 1.5 mm thick Pyrex glass was then anodically bonded on the top of the silicon to seal the microchannels.

- 170 -
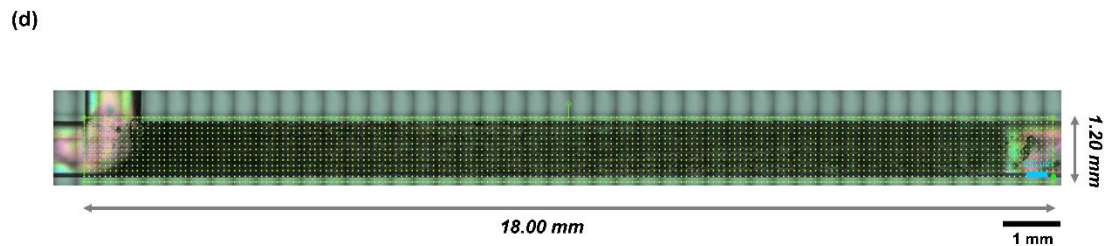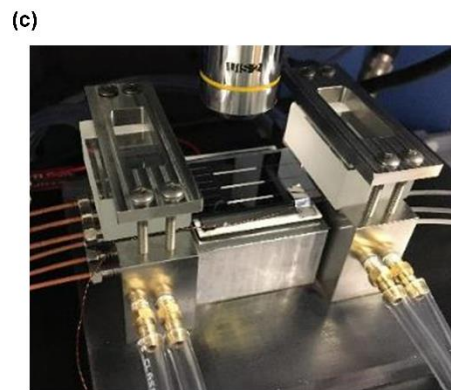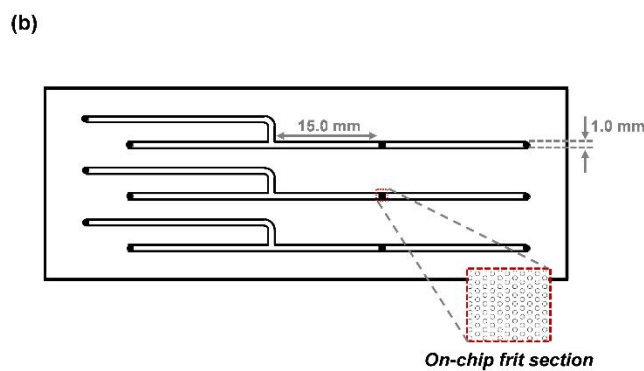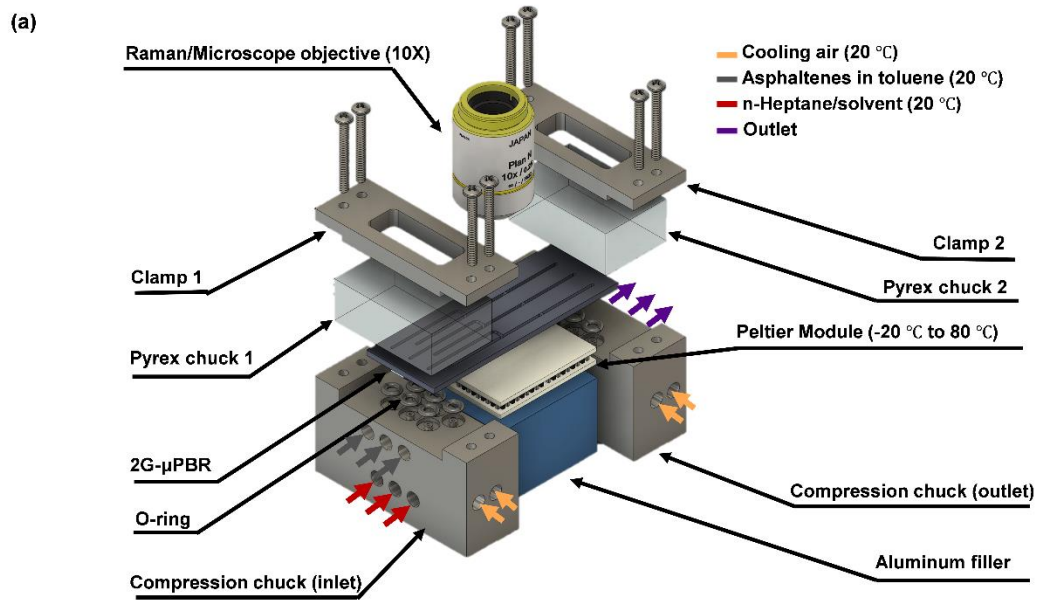
Figure 5.2 (a) Schematic diagram of assembly of the automated microfluidic system. (b) 2D design of the automated packed-bed microreactor (AUTO^3-µPBR). (c) Photo of the packaged microfluidic system under the in-situ Raman spectroscopy. (d) Raman mapping with 18.00 mm x 1.20 mm area to ensure the coverage of the entire porous media. The acquisition time is approximately 20.58 min per mapping.

5.2.2.b RTD measurement of porous media

The mean residence time distributions (RTD) were measured for the micro packed-beds using a pulse tracer method. A continuous in-line UV-Visible Spectroscopy system (Ocean Optics, Dunedin, FL, USA) was used to measure the concentration of acetone tracer in n-heptane at the outlet. The carrier fluid was injected into the system using a 10 ml Hamilton 1010 glass syringe and syringe pump (PHD 2000, Harvard Apparatus, Holliston, MA, USA), while the acetone tracer was injected using a microinjector (IDEX Health & Science, Oak Harbor, WA, USA) with a
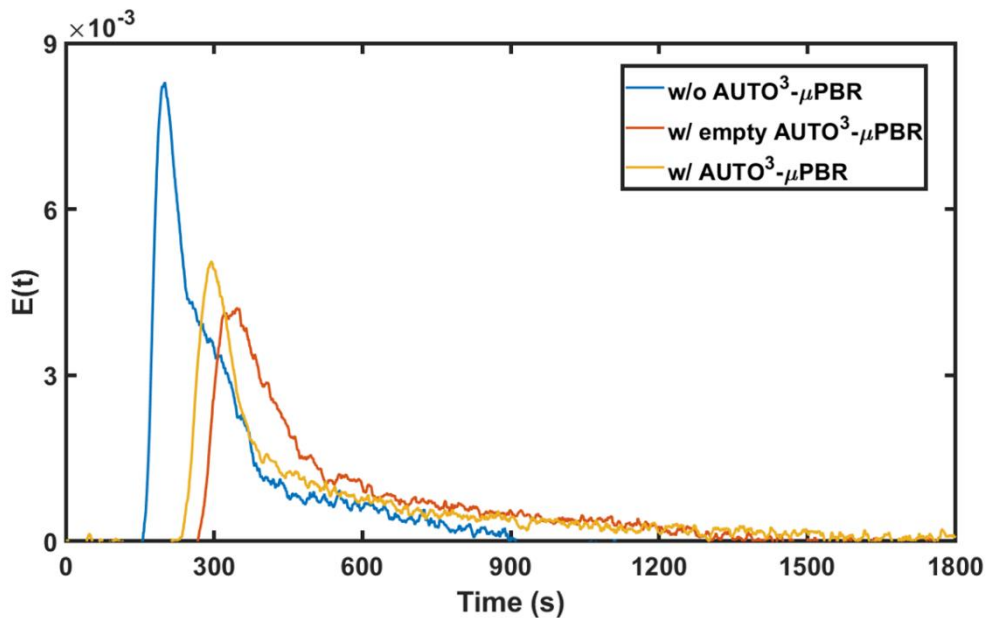
Figure 5.3 Residence time distribution (RTD) measurements of 2G-μPBR under three different setups: the system without 2G-μPBR, with empty 2G-μPBR, and with packed 2G-μPBR. The volume of the system was calculated by flow rate and mean residence time. The volume of microsystem, 2G-μPBR and packing were calculated to be 87.08 μL,16.43 μL and 2.48 μL respectively. The resultant porosity is about 44.85%.

sample loop of 1.0 µL. To optimize the signal to noise ratio a peak absorbance wavelength of 283nm was selected for the UV-Vis system output. Figure 5.3 shows the results of RTD measurement. Convolution of the RTDs confirmed that each packed-bed region is approximately 2.48 µL with a void fraction of 0.45 and a mean residence time of 3.72 seconds.

5.2.2.c Packaging, system controls, and automation

Figures 5.2 (a) and (c) illustrate the assembly and packing of the microfluidic system. Stainless-steel compression chucks designed in AutoCAD and manufactured by Xometry connect the device to upstream and downstream peripherals/controls. Cooling air at ambient temperature was circulated through the compression chucks to ensure the temperature of the fluidic inlets and outlets remained constant. The temperature on-chip in the packed-beds was maintained by contacting the silicon-side to a thermoelectric module (TEC, TE Technology HP-127-1.4-1.5-74, max. 65 W) controlled by a PID controller (TE Technology RS485) with a thermistor probe (TE Technology MP-2444). Computational fluid dynamic simulations (COMSOL Multiphysics 5.3) of the temperature profiles are in excellent agreement with measured values obtained by an IR thermal camera (ICI 9640P) (refer to Appendix C for more details). Pressure drop tests using deionized water confirmed that the average pressure drop of the AUTO^3-µPBR was 0.05 bar without packing (see Appendix C).

Figure 5.4 shows the process flow diagram of automated fluid delivery system. Three high-pressure syringe pumps (Teledyne ISCO 65DM) were used to deliver the asphaltenes in toluene (4 g/L) solution, n-heptane, and xylenes into the
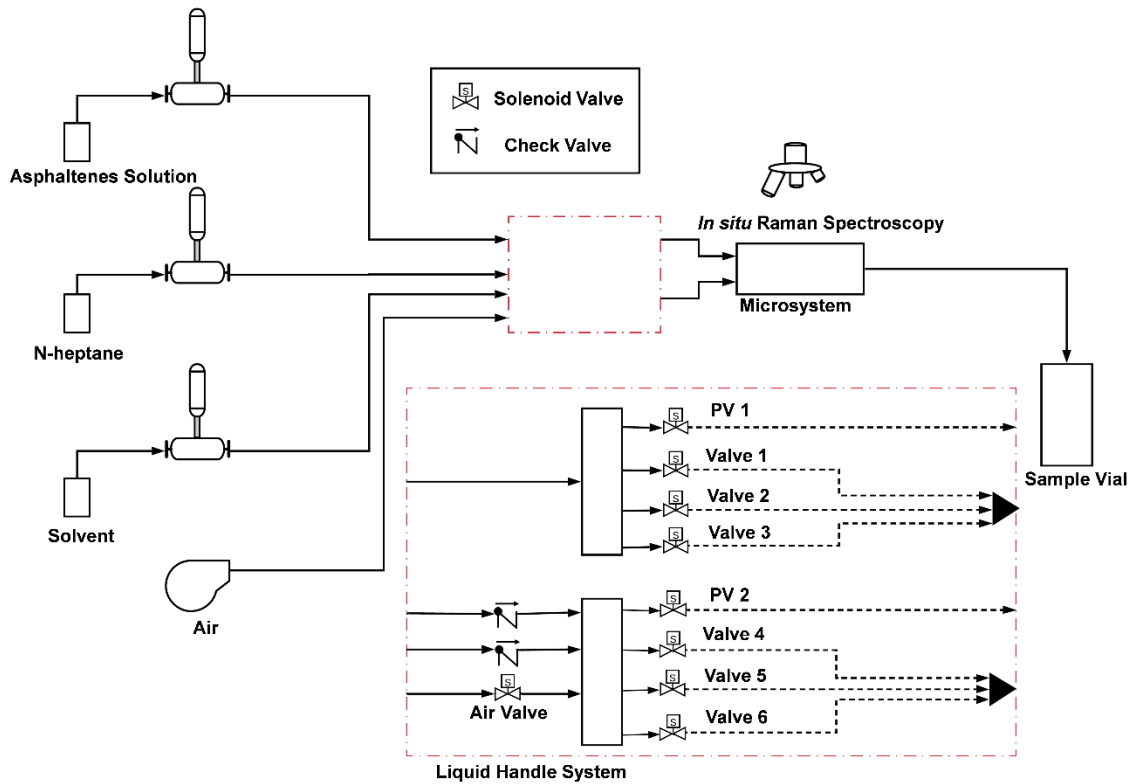
Figure 5.4 Process flow diagram of automated fluid delivery system.

microfluidic device. The distribution of the fluids into the three-different packed-beds was managed by a comprehensive liquid handle system, which consisted of solenoid valves and customized manifolds. The stepwise deposition and dissolution experimental procedures are briefly described below:

System initialization:

1) The temperature of the system was adjusted and stabilized to a set point for at least 12 minutes to ensure isothermal operation.

2) The manifolds and solenoid valves of the n-heptane and asphaltenes solution lines were purged at 1000.00 μL/min for 5 min through purge valve 1 (PV1) and

purge valve 2 (PV2) to remove potential air bubbles, which may pose pressure drop issues.

Deposition:

1) *System priming.* The corresponding pumps for delivering n-heptane (Pump B) and asphaltenes solution (Pump C) were operated at 500.00 µL/min and 300.00 µL/min, respectively, for 3 mins with all valves closed. This procedure increased the pressure of the system to 0.3 bar. Once primed, the corresponding valves (Valves 1 and 4 for reactor 1, Valves 2 and 5 for reactor 2, and Valves 3 and 6 for reactor 3) were simultaneously open to achieve a stable interface at the tee intersection.

2) *Deposition.* After priming, the flowrates of n-heptane and asphaltenes solution were adjusted to the desired values of 25.00 µL/min and 15.00 µL/min. The ratio of flowrates was determined by the approximate ratio of fluid densities to ensure the stable interface. *In-situ* Raman spectroscopy was then initiated. The deposition process lasted for 2 hrs. At the end of deposition, vacuum was applied to outlet of the reactor to terminate the deposition process by purging the remaining fluids out of the bed.

Process switching:

1) *Air purging.* The manifolds and solenoid valves (at the n-heptane/solvent line) were purged by air for 10 min through the air valve and purge valve 2. The purpose of this step is to remove any remaining n-heptane that may influence the dissolution process.

2) ***System purging (solvent).*** The manifolds and solenoid valves at solvent line were purged with xylenes at 1000.00 µL/min for 5 min through purge valve 2 (PV2). The purpose of this step is to remove air bubbles in the system. The inlets of the asphaltenes line were also closed to prevent any further injection of fresh asphaltenes into the porous media during the dissolution process.

Dissolution:

1) ***System priming.*** The pump for solvent delivery (Pump A) was operated at 500.00 µL/min for 5 mins with all valves closed. This increased the pressure of the system to 0.5 bar. Once primed, the corresponding valves (Valve 4 for reactor 1, Valve 5 for reactor 2, and Valve 6 for reactor 3) were opened to create stable flow into the porous media.

2) ***Dissolution.*** After system priming, the flowrate of the solvent was adjusted to a set point of 80.00 µL/min. A total xylenes pore volume equivalent of 4752 was injected through the damaged packed bed. The characterization methodology was initiated to characterize the entire dissolution process in real-time. At the end of dissolution, vacuum was applied to the outlet of the device to terminate the dissolution process by discharging the fluids from the packed bed.

The automation of the fluid delivery system, data acquisition, and *in-situ* Raman characterization were controlled by an in-house LabView program.

5.2.3 *In-situ* Raman spectroscopy measurements

An *in-situ* Raman spectroscopy system (Horiba LabRam HR evolution, Jobin-Yvon) was used to map of the Auto-µPBR during asphaltenes deposition and dissolution.

A diode-pumped solid-state (DPSS) laser system with an excitation line of 532 nm and power output of 40 mW was used as the incident light source. A 10X MplanN Olympus lens was used with a CCD Synapse EM detector to collect spectral shifts. A 600-grooves/mm grating filter was chosen, while the acquisition time was set to 0.3 s. A 18 mm x 1.2 mm region with step sizes of 100 µm was selected to cover the entire packed-bed region and part of the upstream entrance and the downstream exit (see Figure 1 (d)). The mapping time for each micro packed-bed was 20.58 mins. Automation of Raman acquisition was achieved by built-in software provided by Horiba, while deconvolution of Raman spectra were performed using third-party MATLAB codes, such as GSTools (import ".spc" file) and iSignal (deconvolution library, created and updated by Prof. Tom O'Haver, University of Maryland). The linear baseline correction was applied to all spectra.

5.2.3.a Occupancy measurements

The distribution of asphaltenes in the AUTO[3]-µPBR was provided by measurement of the bed occupancy on quartz,[9]

$$\varpi_i = \frac{I_{a,i}}{I_{a,i} + m I_{q,i}} \tag{5.1}$$

where $I_{a,i}$ and $I_{q,i}$ are the corresponding integrated area of Raman peaks of asphaltenes (897-1987 cm^{-1}) and quartz (400-520 cm^{-1}), respectively. The physical meaning of the pre-factor m derived from different molecular responses to excitation due to the different molecular properties. A detailed description of the methodology, including its calibration, was previously reported.[9]

5.2.3.b Nanosheet size measurements

- 177 -

The nanosheet sizes of asphaltenes by Raman spectroscopy has been reported.[35,36] Convolution of the Raman spectra results in G, D1, D2, and D3 shifts. The physical meaning and description of each peak can be found in previous literature.[35] The sheet size information of asphaltenes molecules could then be derived from integrating areas of peak G (I_G) and peak D (I_{D1}) through the Tuinstra-Koenig relation,[37]

$$La(nm) = C(\lambda)\frac{I_G}{I_{D1}} \tag{5.2}$$

where, $C(\lambda)$ is a pre-factor that depends on the wavelength of incident light.[38] In the present work, $C(532\ nm) = 4.96$ nm was applied to the calculation.

5.2.3.c Xylenes distribution

The distribution of xylenes in the AUTO[3]-μPBR was also revealed by *in-situ* Raman spectroscopy. Since the xylenes used in this work were a mixture of o-xylenes, m-xylenes and p-xylenes, it is expected to have some variation in the Raman shift. Here, the Raman shifts of 1001 cm^{-1} and 1028 cm^{-1} were used as the signature peaks to identify the presence of xylenes. This is due to the presence of these distinct peaks in all xylene isotopes. Note these shifts correspond to out-of-plane methyl CCH bending and in-plane methyl CCH bending.[39] Figure 5.5 shows an example of a xylene shift measured inside the AUTO[3]-μPBR. Here the palpable regions are defined as the areas in which xylenes are clearly detected, and impalpable regions as where xylenes were undetectable or unrecognized.

- 178 -
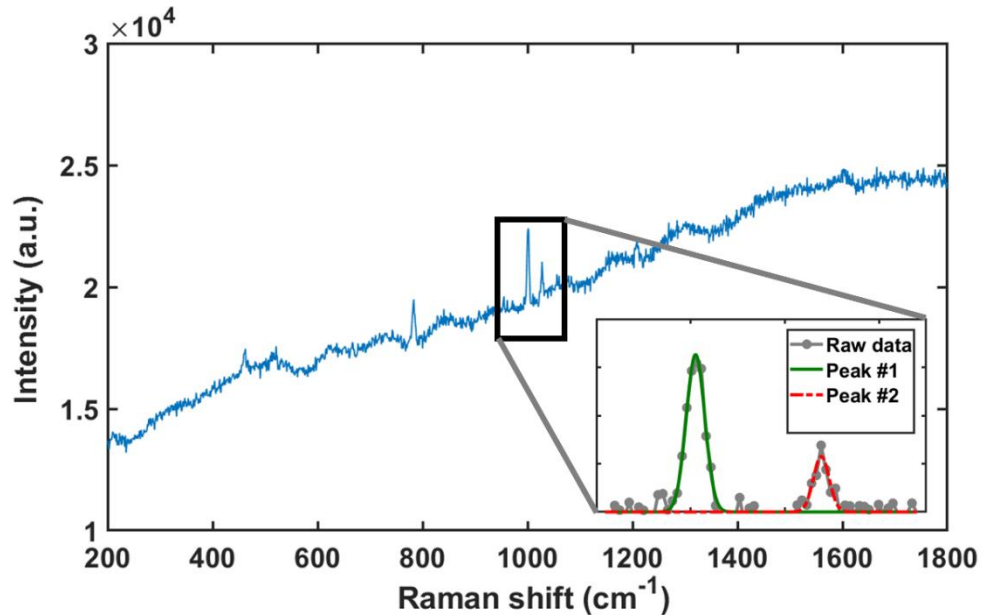
Figure 5.5 An example of xylenes Raman spectrum obtained during the dissolution process. Peaks of 1001 cm^{-1} and 1028 cm^{-1} were chosen as criteria to determine the presence of xylenes.

5.3 Results and discussion

5.3.1 Deposition of asphaltenes in the AUTO^3-μPBR

5.3.1.a Visualization by Raman spectroscopy of asphaltenes deposition

Figure 5.6 shows an example of the Raman spectra and corresponding occupancy changes on the quartz surface at the coordinates of [7.8 mm, 0.3 mm] in the porous media during the asphaltenes deposition. Note that the time information used here is relative to the start time of each mapping. It took about 3.85 min for the XY-stage
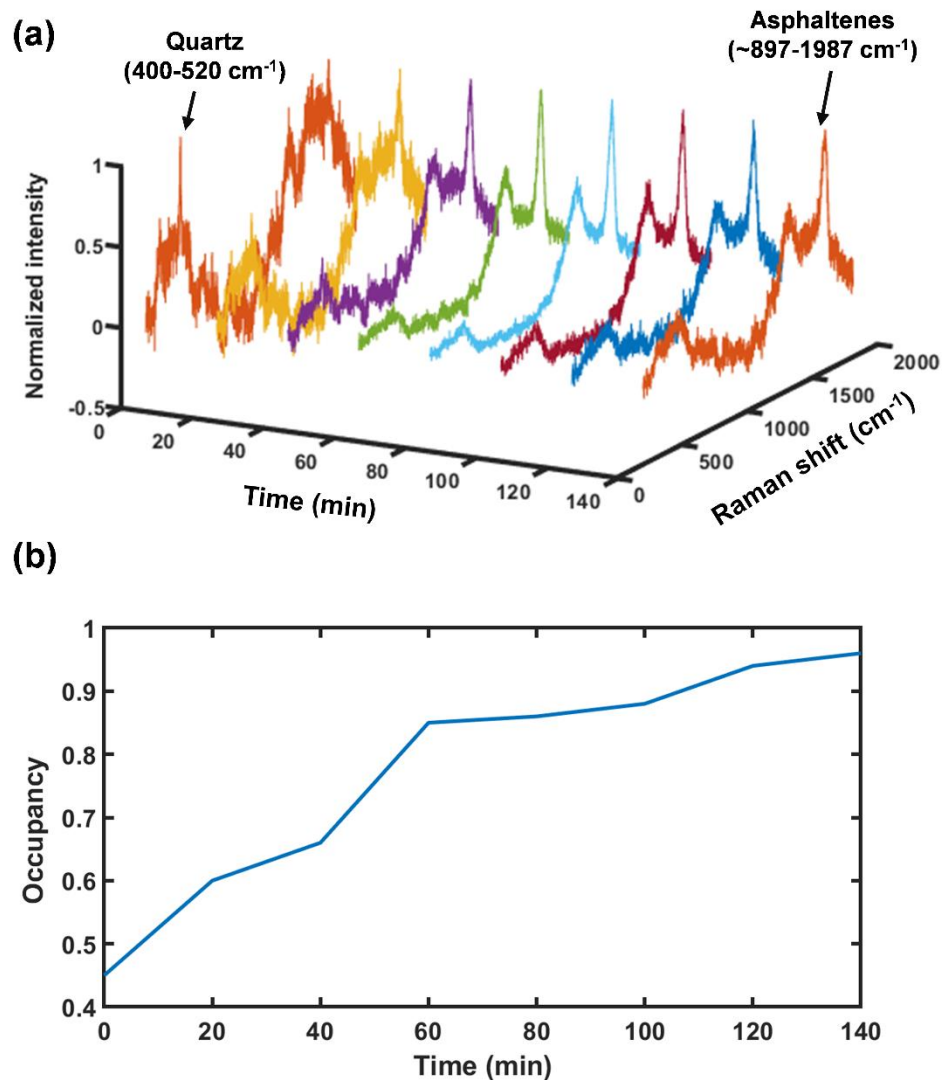
Figure 5.6 (a) Raman spectra at the location of [7.8 mm, 0.3 mm] inside the porous media at different periods of deposition. The peaks at the Raman shift of $400 – 520$ cm^{-1} were assigned to quartz peaks, while shifts of $897 – 1987$ cm^{-1} are assigned to asphaltenes peaks. As deposition continued, the normalized intensity of quartz peaks decreased, while the peaks of asphaltenes became more distinct. (b) The corresponding occupancy for (a) increased as the deposition proceeded.

to reach the coordinates in the example of Figure 5.6. At the beginning of the experiment, a distinct Raman peak of quartz (460 cm^{-1}) was shown on the spectrum, while an indistinct peak of asphaltenes indicated the presence of a trace amount of asphaltenes. The results indicated that the deposition process begins within several minutes. As the deposition proceeds, the normalized intensity of quartz decreased, whereas the normalized intensity of asphaltenes increased. This meant that the occupancy of asphaltenes on the quartz surface was expected to increase since the measurement of occupancy relates the ratio between peaks of quartz and asphaltenes as shown previously in equation (1). This methodology provides the ability to monitor the process of asphaltenes deposition inside the porous media.

The method was then applied to monitor the deposition process of asphaltenes at different experimental temperatures; an important consideration in geological reservoirs. An isothermal AUTO^3-μPBR can be validated by the solution to the Graetz-Nusselt problem for two worst-case scenarios. The time required to increase the centre-line fluid temperature to that of the microchannel wall (or the quartz surface for a capillary bundle model) is given by,[40]

$$t = \frac{\rho C_p R^2}{\kappa} \tag{5.3}$$

where, ρ, C_p, and κ are the density, heat capacity, and thermal conductivity of the fluids, respectively. The inner diameter of the cross-section R is seen to have the greatest impact on the heating time. Here, we used the density value of 870 kg/m^3 (toluene), heat capacity value of 2.25 kJ/kg·K (n-heptane), and thermal conductivity value of 0.14 W·m·K (n-heptane). The time required for the fluid to reach the system

- 181 -
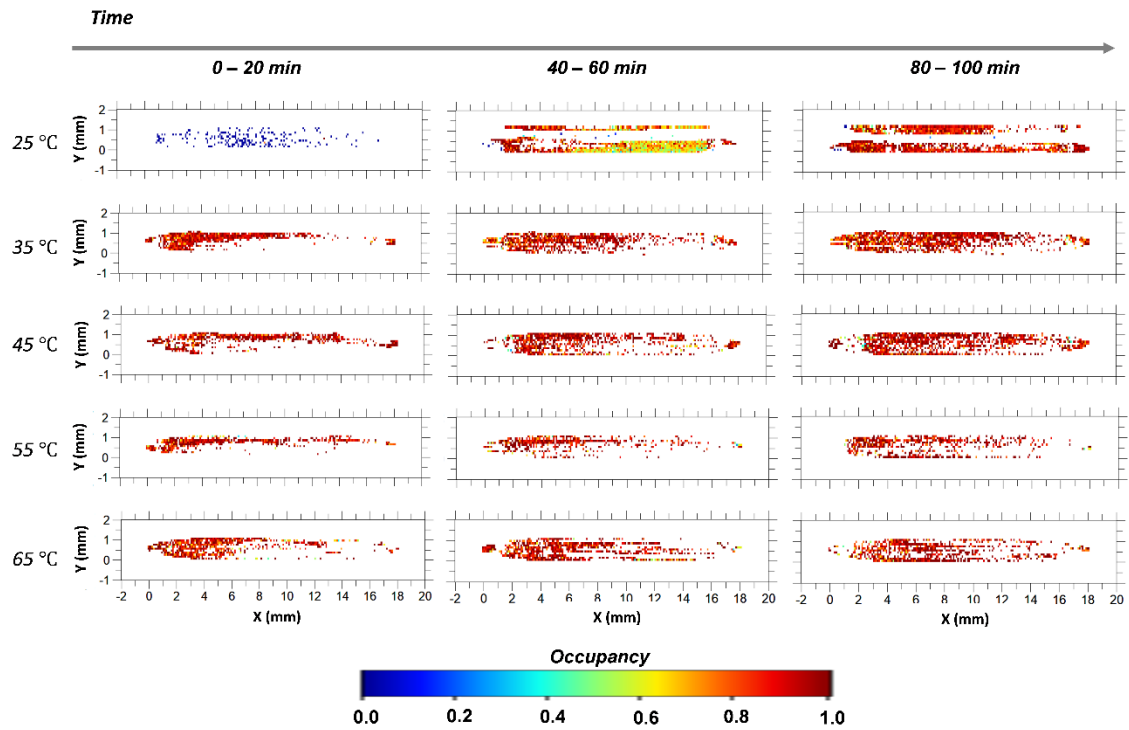
Figure 5.7 The occupancy maps of the AUTO^3-μPBR at different times and deposition temperatures. At elevated temperatures (> 35 °C), the deposition occurred within the first 20 min. Channelling was observed in several of the samples, e.g., at 25 °C and 45 °C.

temperature without the present of the quartz packing was estimated to be 1.25 s. With the addition of the packed-bed the heating time was further reduced to 0.11 ms. Compared with the resident time of 3.72 s, the time required for heating the fluid could be considered as negligible. It is therefore appropriate to assume isothermal operation of the AUTO^3-μPBR.

Figure 5.7 reports occupancy maps of the AUTO^3-μPBR during the deposition process at different system temperatures. At a deposition temperature of 25 °C, the occupancy within the first 20 min of deposition was low, as indicated by the blue colour. Channelling appeared later during the deposition (or after 20 min), meaning

that the fluid showed a preferential pathway along the pack-bed due to either the distribution of native pore throat sizes or by the deposition mechanism. At higher deposition temperatures, for instance at 35 °C, the occupancy map shows a high average occupancy (>0.8) from the beginning of the deposition. These results indicated that higher temperatures lead to faster deposition of asphaltenes onto the porous media, in good agreement with some observations in the literature that says the onset time for flocculation of asphaltenes was shorter at a higher temperature.[41]

Removal of the solvent from the micro packed-beds strengthened our initial observation. Figure 5.8 (a) shows photographs of the air-dried AUTO^3-µPBR damaged by asphaltenes. As can be seen, "Depo25", "Depo35", "Depo45", "Depo55", and "Depo65" correspond to deposition operating temperatures of 25, 35, 45, 55, and 65 °C, respectively. At lower deposition temperatures, for instance at 25 °C, the asphaltenes were distributed throughout the AUTO^3-µPBR. However, at higher deposition temperatures the asphaltenes accumulated at the entrance of the packed-bed. Occupancy maps of the corresponding samples can be seen in Figure 5.8 (b). Not only are these occupancy maps in excellent agreement with the optical photographs, but they could also provide more quantifiable information on the damaged packed-beds.

Figure 5.8 (c) reports the average occupancy of asphaltenes along the axial direction of the porous media. Here, we segmented the porous media at 1 mm intervals and only considered the occupancy inside the porous media. Within the first axial 3 mm of the porous media, there is no significant difference in the occupancy between the different samples. However, as one moves down the
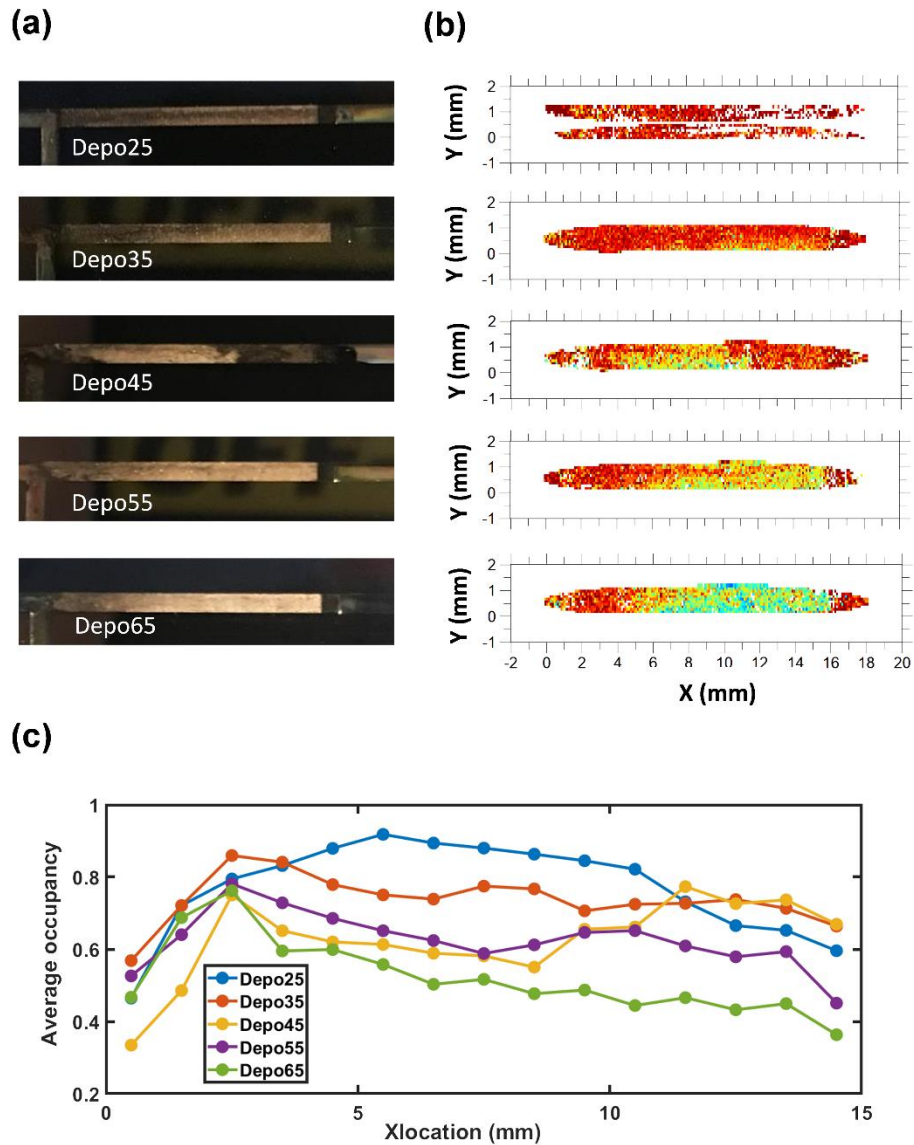
Figure 5.8 (a) Photographs of asphaltenes deposited within the porous media at different temperatures. Depo25, Depo35, Depo45, Depo55 and Depo65 correlates to the samples deposited at temperatures of 25 °C, 35 °C, 45 °C, 55 °C, and 65 °C, respectively. (b) The corresponding occupancy maps of the AUTO^3-μPBR. (c) The average occupancy changes in the axial direction. The average occupancy is calculated along the 1.00 mm width-wise direction. With increases in the deposition temperature the asphaltenes are seen to accumulate at the beginning of the micro packed-bed.

- 184 -

higher temperatures, this decrease in occupancy occurs more rapidly than at lower temperatures. This result is in good agreement with our previous observation that deposited asphaltenes inside the porous media were distributed throughout the micro packed-beds more at lower temperatures.

5.3.1.b Effect of deposition temperature on asphaltenes nanoaggregation

From the results shown in Figure 5.8, it is apparent that temperature has a profound impact on asphaltenes deposition, or the nanoaggregation process. From the images, at lower temperatures the asphaltene aggregates tend to be highly distributed throughout the bed, resulting in a uniform dark bed colour. Increasing to deposition temperatures up to 65 °C leads to more aggregation on the forward front end of the packed-bed where the asphaltenes are first introduced into the packing. This restricts the nanoaggregates transport throughout the bed, and it results in a dark to light colour gradient in the axial direction. The phenomenon can be attributed to temperature effects on the asphaltenes' nanoaggregation.

As previously described in literature, temperature alters the physical characteristics of asphaltenes nanoaggregation by reducing the onset time, increasing the fractal dimension of aggregates, and increasing the mean particle size of flocculated aggregates.[42–46] Any three of these effects may play an important role in our results. The onset time can be described as the period at which asphaltene aggregates reach a mean particle size of 5 μm, and thus a direct correlation exists between the temperature and the rate of flocculation. As the temperature increases the rate of precipitation also increases. Maqbool, *et al* showed that higher temperatures result in a larger mean particle size of nanoaggregates, primarily due

to the increase in their solubility.[41] Although this result may seem counterintuitive, it appears as though the increase in solubility prevents the smaller aggregates from forming, while the larger particles stay stable and are not dissociated back into solution. This conclusion agrees with our observations primarily because our pore throats, in the range of 7 μm, are on the same order of magnitude as the developed stable aggregates, in the range 5 – 10 μm. The asphaltenes physically cannot flow through the bed once the aggregates are formed, and hence confined into the pore space.

The fractal dimension, as previously discovered in literature, increases with an increase in the temperature, creating a more ordered and dense agglomerates of asphaltenes.[47–49] These tightly packed clusters have a higher resistance to fractionation due to convective forces than their loose/porous counterparts that are formed at lower temperatures. This could explain why, at higher temperatures, that even though the pressure drop is higher, resulting in larger convective forces due to pore throat constriction, the asphaltene deposits did not fractionate and flow along the fluid path. The abovementioned observations could explain the intense accumulation of asphaltenes on the forward front of the reactor at higher temperatures.

5.3.1.c Effect of deposition temperature on hydrodynamic conditions

Besides its effect on asphaltenes nanoaggregation and their deposition, temperature also influences the hydrodynamic properties of the fluid. When fluid flows along a solid boundary, such as our quartz surface, a shear stress occurs at that boundary. The presence of shear stresses can potentially lead to local fractionation and break

up loose deposits of asphaltenes, resulting in reduced surface thicknesses. According to Newton's law of viscosity, the shear stress τ is proportional to the viscosity of the fluid, μ and the velocity gradient where,

$$\tau = \mu \frac{\partial u}{\partial y} \qquad (4)$$

Here, we could assume the velocity gradient remained constant at different experimental temperatures because the total volumetric flow rate was the same between different experiments. Hence, shear stress of the fluid is proportional to the viscosity of the fluid.

It is well known that the presence of dispersed solid particles or liquid droplets, such as asphaltenes aggregates, will alternate the viscosity of the solution.[50–52] The relative viscosity of a solution μ_r increases with the concentration of solute c,

$$\mu_r = \frac{\mu}{\mu_0} = 1 + [\mu]c + K_v c^2 + \cdots \qquad (5)$$

where, μ_0 is the viscosity of the dispersant phase, $[\mu]$ is the intrinsic viscosity and K_v is a pre-factor. For instance, an increase of asphaltenes volume fraction from 5.08 to 13.50 vol.% could lead to relative viscosity increases from 2.6 to 20.8 at 20 °C, which is an order of magnitude higher.[53] This increase in viscosity is a result of the increase in the number of interactions between asphaltenes particles due to the increase in their concentration. In the present work, the volume fraction of asphaltenes in the mixture solution was constant at 0.125 vol. % for all experimental conditions. Thus, the solutions were dilute. For dilute solutions, the differences in concentration due to the deposition of asphaltenes onto the quartz surface was

- 187 -

considered to have a negligible effect onto the fluid viscosity. Therefore, we assume the relative viscosity as unity throughout our experimental conditions according to equation (5), under the condition where $c \cong 0$. In other words, the viscosity of the fluid is solely dependent on the dispersant fluid viscosity.

Besides the concentration, temperature can also play a significant role in changing the fluid's viscosity. According to Eyring's theory of viscosity, the correlation between the fluid's viscosity and temperature is described by an Arrhenius relationship,[54]

$$\frac{\mu(T)}{\mu(T_0)} = exp\left[\frac{E_a}{R}\left(\frac{1}{T} - \frac{1}{T_0}\right)\right] \qquad (6)$$

where, E_a is the activation energy for viscous flow, and R is the gas constant. The value of the activation energy E_a is reported to increase with increasing the asphaltenes' volume fraction. The enhancement of interactions between an increased amount of asphaltenes particles increases the energy barrier towards a more viscous flow. For a dilute solution, we could assume the activation energy remained constant at our experimental conditions. The measured values of activation energy could be different depending on the source of asphaltenes samples.[53,55] Table 5.1 reports the calculated viscosity ratio based on two previously reported activation energies, at different temperatures, with the viscosity value at 65 °C being the reference. When the temperature decreased from 65 °C to 25 °C, the increase in the solutions viscosity ranged from 5 times to more than 17 times. According to equation (4), the shear stress could decrease drastically when the deposition temperature increases in our experimental conditions. This decrease in shear stress provides

another explanation of why the deposition of asphaltenes was distributed throughout the micro packed-bed at lower deposition temperatures.

Table 5.1 Relative viscosity change (μ/μ_0) as a function of temperature.

Temperature	$(\mu/\mu_0)_1$ *	$(\mu/\mu_0)_2$ **
25°C	17.52	5.10
35°C	7.99	3.26
45°C	3.83	2.15
55°C	1.92	1.45

* Calculated based on Ea = 60 kJ/mol

** Calculated based on Ea = 34.14 kJ/mol

5.3.2 Dissolution of deposited asphaltenes by xylenes

5.3.2.a Visualization by Raman spectroscopy of asphaltenes dissolution.

Raman spectroscopy, being a diverse characterization method, can also provide insights on how significant the deposition temperature is to the dissolution process. Figure 5.9 reports the occupancy maps of different AUTO³-μPBRs during the dissolution process. It is important to note that compared with a mean residence time of 3.72 s, the acquisition time of each mapping is considerably large. Therefore, even on the same occupancy map, different sample spots would also have time information associated with its coordinates. In other words, the occupancy map contains transient information of the asphaltenes distribution.

Within each occupancy map, a total xylenes pore volume equivalency of 792 was flowed through the porous media. From the mappings, we can observe that the high occupancy regions become impregnated with xylenes resulting in segmentation into

- 189 -
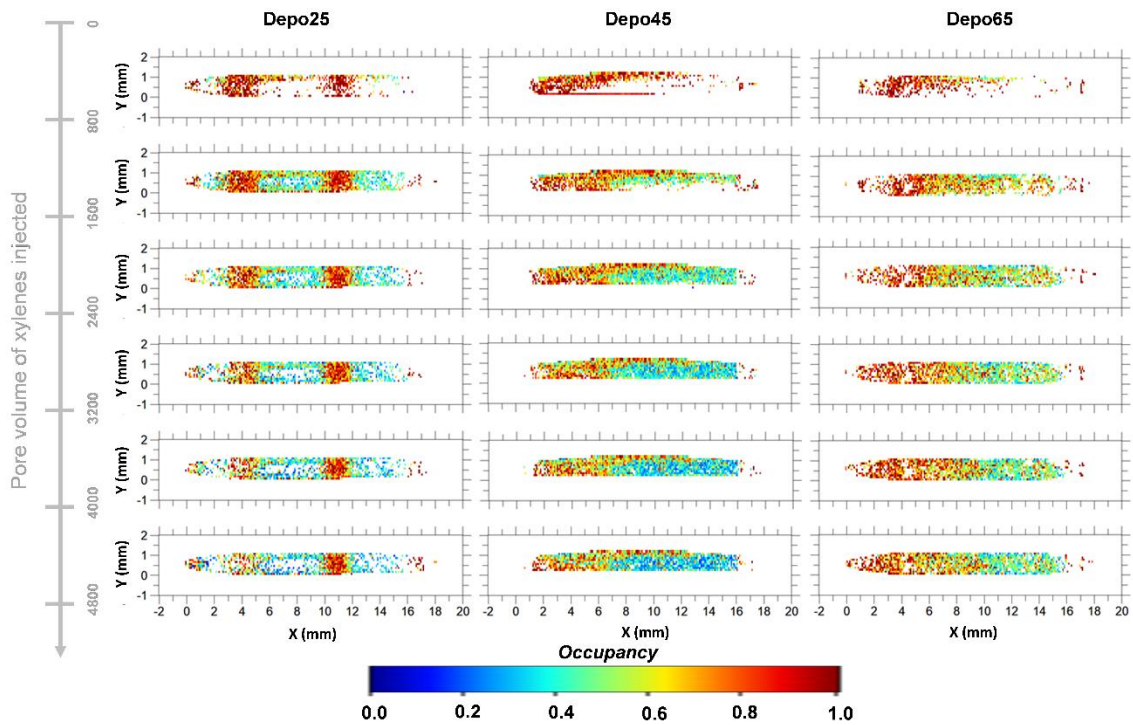
Figure 5.9 Occupancy maps of the AUTO^3-μPBR during the dissolution of asphaltenes. When increasing the amount of xylenes exposed to the system the occupancy is seen to decrease, particularly in the low occupancy regions. The regions of high occupancy have the tendency of breaking down into the low occupancy regime. Some areas of high occupancy are stable throughout the dissolution.

smaller highly packed clusters in the localized zone as dissolution continued. The lower occupancy regions follow a general trend of gradual reduction which is seen throughout the dissolution process. These two behaviours will be further discussed in the next section.

It is important to point out that when comparing the first occupancy maps to the second, there is an obvious difference between the two mappings that can be a result of the system priming step in the operating procedure. The first mapping contains

- 190 -
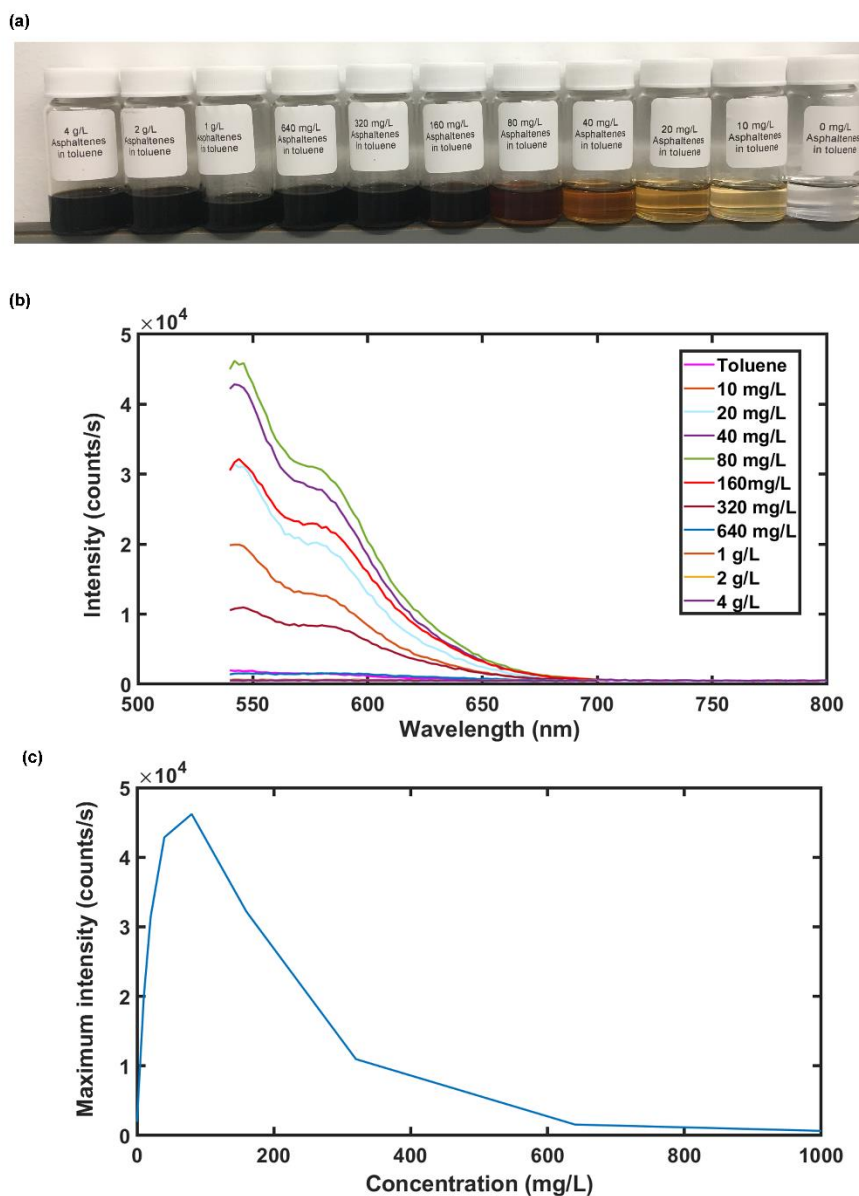
Figure 5.10 (a) Optical images of asphaltenes in toluene samples at different concentration. (b) Fluorescence emission spectra of asphaltenes samples with different concentration at the incident light of 532 nm. When the concentration is below 80 mg/L, the fluorescence intensity increases as the concentration increase. When the concentration is larger than 80 mg/L, the fluorescence intensity decreases as the concentration increase. At concentration above 640 mg/L, the fluorescence intensity is negligible.

areas that are void, meaning that in those areas there was a lack of meaningful signal and the CCD detector was saturated, resulting in noise. We speculated that the asphaltenes dissolved in the solution were emitting florescence signals that were causing this saturation. Because of this phenomenon, experiments were conducted to measure the fluorescence intensity at an incident laser wavelength of 532nm (same as incident laser in Raman) to test our theory. Figure 5.10 shows the fluorescence emission spectrum of asphaltenes at different concentration. Fluorescence spectroscopy results show that, compared to toluene, asphaltenes emit increasing fluorescence intensity as the concentration is also increased. Once the concentration reaches the threshold value of about 80 mg/L there is a sharp decrease in the fluorescence intensity. At concentrations of 2 g/L and 4 g/L the fluorescence emissions are quenched to intensities below that of toluene. Goncalves, *et al* showed that asphaltenes in solution emit fluorescence signals in a pattern that closely reflects our results, in that there is a certain threshold concentration that promotes an inverse relationship between the asphaltenes concentration and the emitted fluorescence intensity.[56] This sharp drop in the fluorescence intensity is due to the formation of asphaltenes aggregates. By removing the molecule out of the solution and into physical particles the number of potential fluorophores, fluorescence emitters, is also reduced.

From our first occupancy map we can see that the cause of this noise likely arose from the impact of system priming. Figure 5.11 shows the photos of reaction channel after the system priming step. As described in the experimental section, the ISCO pump for the delivery of the solvent was pressurized to 0.5 bar prior to flowing
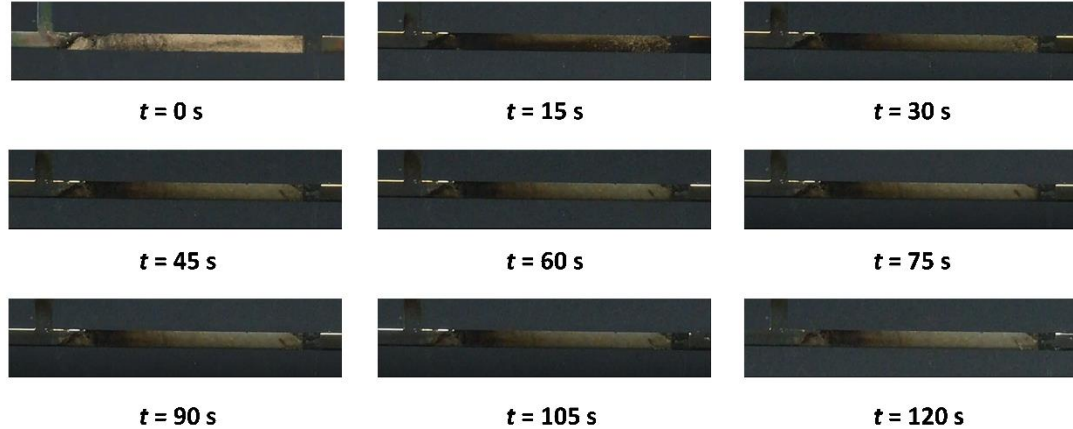
Figure 5.11 Photos of the reaction channel after the system priming step. The priming step cleans out the low occupancy regions and provides a baseline for dissolution.

xylenes into the microsystem to minimize the presence of any air pockets that may be inside the lines. According to the Hagen-Poiseuille law, this increase in pressure leads to at least a 5-fold increase in the flow rate, which also directly results in an increase in shear stresses during the dissolution. These shear stresses caused the immediate dissolution of the low occupancy regions; however, they also fractionate the high occupancy areas resulting in segmentation and a quicker dissolution. The asphaltenes from these areas dissociate into the solution and enter the concentration regime below that of the threshold and emit fluorescence signals which cause the noise that is seen in the first occupancy mapping. As the dissolution proceeds the total pressure drop equilibrates and the flow rate reaches the target of 80 μL/min. At this point the dissolution slows down and local concentration within the packed-bed is small enough for the fluorescence to be filtered out. Good agreement with our previous UV-Vis results add a level of confidence in our speculation.[10]

5.3.2.b Influence of xylenes distribution on the dissolution

Figure 5.12 shows the distribution of xylenes inside the porous media during dissolution. As the dissolution process progressed, the distribution of xylenes inside the porous media increased. Here, we could apply the bundle of capillary model with Laplace's equation to describe the xylenes distribution change inside the porous media,[57]

$$p_c = (4\gamma \cos\theta)/\delta_c \qquad (5.7)$$
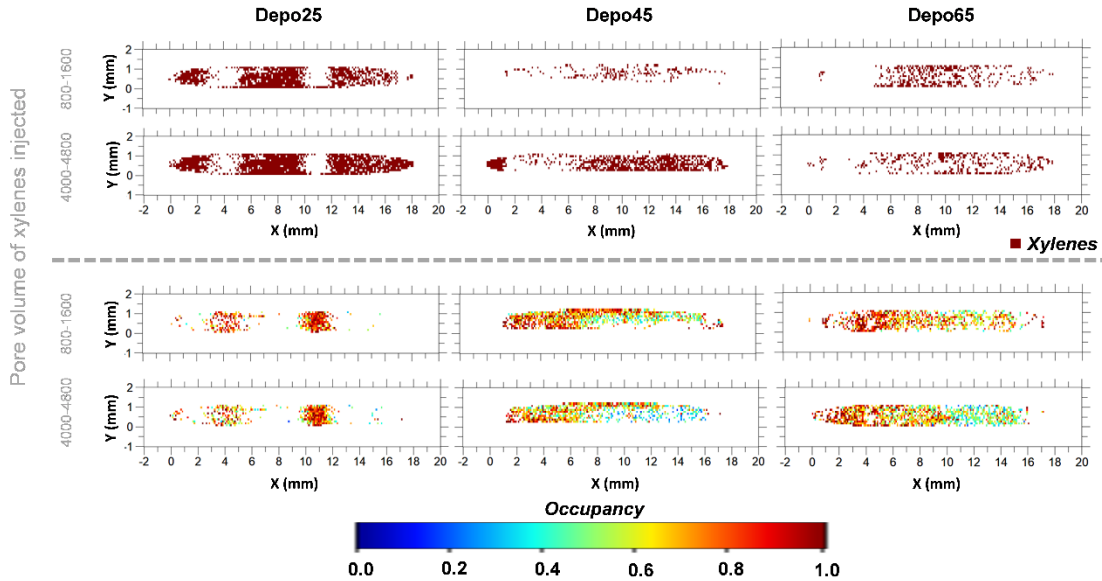
Figure 5.12 Top: Distribution of xylenes within the AUTO^3-μPBR during the dissolution process. The xylenes distribution in AUTO^3-μPBR decreased as the deposition temperature of the sample increased. Bottom: The occupancy map of asphaltenes at the xylenes impalpable regions. In the Depo25 sample, the xylenes impalpable region is mostly located at highly occupied regions, whereas in sample of Depo45 and Depo65, the impalpable region can occur at the low occupancy region.

$$s = \int_{\delta=(4\gamma\cos\theta)/p}^{\infty} \alpha(\delta)d\delta \qquad (5.8)$$

where p is the pressure of the system, γ is the surface tension of the fluid, θ is the contact angle, s is the saturation of fluid inside the porous media, δ is the pore size, and α is the distribution of pore size. For a system with a constant capillary pressure of p_c, only the pores with sizes above the critical pore size $\delta_c = (4\gamma\cos\theta)/p_c$ would allow the fluid to pass through. Therefore, the increase in xylenes distribution inside the porous media could be described by an increase in the pore sizes during the dissolution of asphaltenes.

Furthermore, we can segment the AUTO³-μPBR into two different regions: (i) xylenes palpable region and (ii) xylenes impalpable region. Here, we define the xylenes palpable region as the areas where distinct peaks of xylenes from the Raman spectra are identified, while the xylenes impalpable regions are the areas in which the peaks are not present or unrecognized. The occupancy of the xylenes impalpable region during the dissolution can be seen in Figure 5.12. Most of the impalpable regions are located at the high occupancy areas. However, in the AUTO³-μPBR damaged by higher temperatures (*e.g.*, Depo45 and Depo65), the impalpable region starts to appear at the low occupancy regions. Two different possible mechanisms may account for the restriction of xylenes through the pores. According to equation (5.7), the two main factors that influence the xylenes' accessibility are the fluid dynamics and the pore size. When the fluid dynamics are held constant then the pore size is the only determining variable that constrains the flow of the solvent. Higher pressures would be required to enter the smaller pore sizes and as the asphaltenes are dissolved, new pores are opened, or existing pores grow larger. This complex

nature causes the fluid path to alternate directions resulting in older pathways to become more stagnant. Another possible explanation for xylenes restriction is the modification of the local surface chemistry. As asphaltenes deposit or dissolve the surface transforms both chemically and topologically. This result influences changes in the contact angle between the solid and liquid phase, that may cross a threshold of flow restriction. As a result, the impalpable regions located at high occupancy areas are dominated by pore throat restrictions while the low occupancy regions are most likely dominated by surface chemistry changes.

Figure 5.13 reports the histogram of occupancy at the different regions. For better data presentation, points that have an occupancy < 0.1 were excluded from the
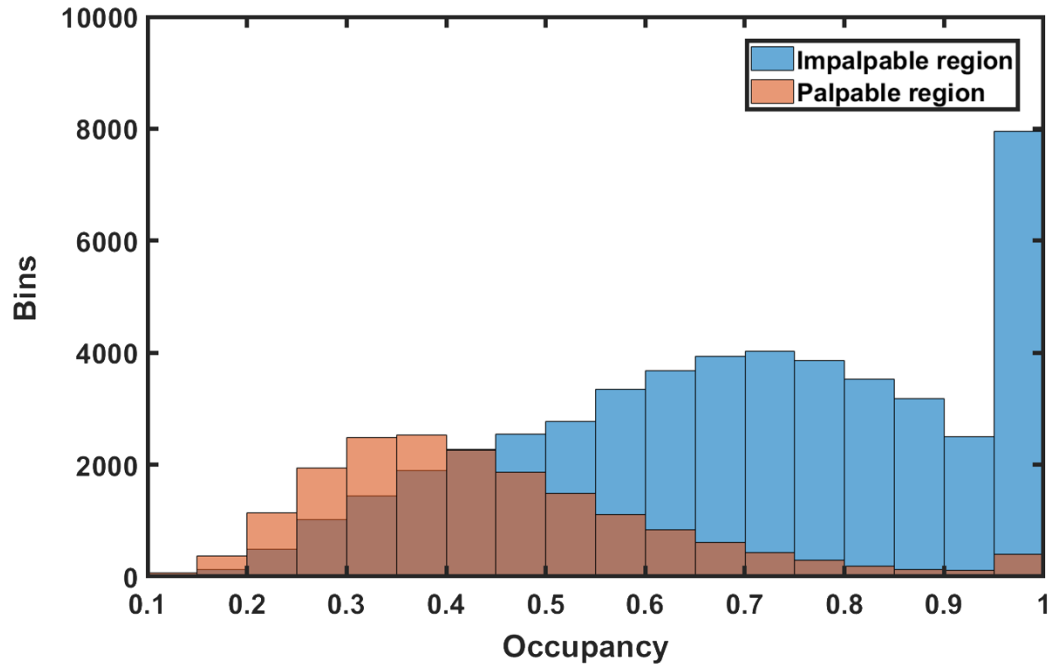
Figure 5.13 Histogram of occupancy at different regions of the packed bed. The xylenes impalpable region showed an average occupancy of 0.66, whereas the xylenes palpable region had an average occupancy of 0.41 (excluding the ones with occupancy under 0.1).

figure. (see Appendix C for complete data set) There are 27180 points for xylenes palpable region with occupancy under 0.1, which is expected for the dissolution process. If we are to exclude these regions, the average occupancy at the xylenes impalpable region is 0.66, while the average occupancy at the xylenes palpable region is 0.41. These results confirm that the impalpable regions are located at higher occupancy areas. It is important to note that there is not a clear threshold value of occupancy between different regions, which could be attributed to the pore size distribution in the porous media. These results imply that the limitation of pore sizes plays a more significant role than surface chemistry alteration during the dissolution.

To better understand the dissolution, we could investigate the influence of the xylenes' distribution on the dissolution of asphaltenes from the $AUTO^3$-µPBR. Figure 5.14 shows the relation between the final average occupancy of $AUTO^3$-µPBR deposited at different temperatures and the xylenes distribution percentage inside the $AUTO^3$-µPBR. The final dissolution occupancy can be used as an indicator of the extent of dissolution. A high value of the final dissolution occupancy expresses the difficulty of cleaning the $AUTO^3$-µPBR. As can be seen in Figure 5.14, the final dissolution occupancy decreased as the xylenes' distribution percentage inside the porous media increased, which could be expected. This increase in the xylenes' distribution percentage leads to increases in overall contact area between the solvent and deposited asphaltenes, which results in a better dissolution efficiency. Furthermore, the increase in dissolution efficiency could cause the pore size to increase, resulting in a higher xylenes distribution percentage.

- 197 -
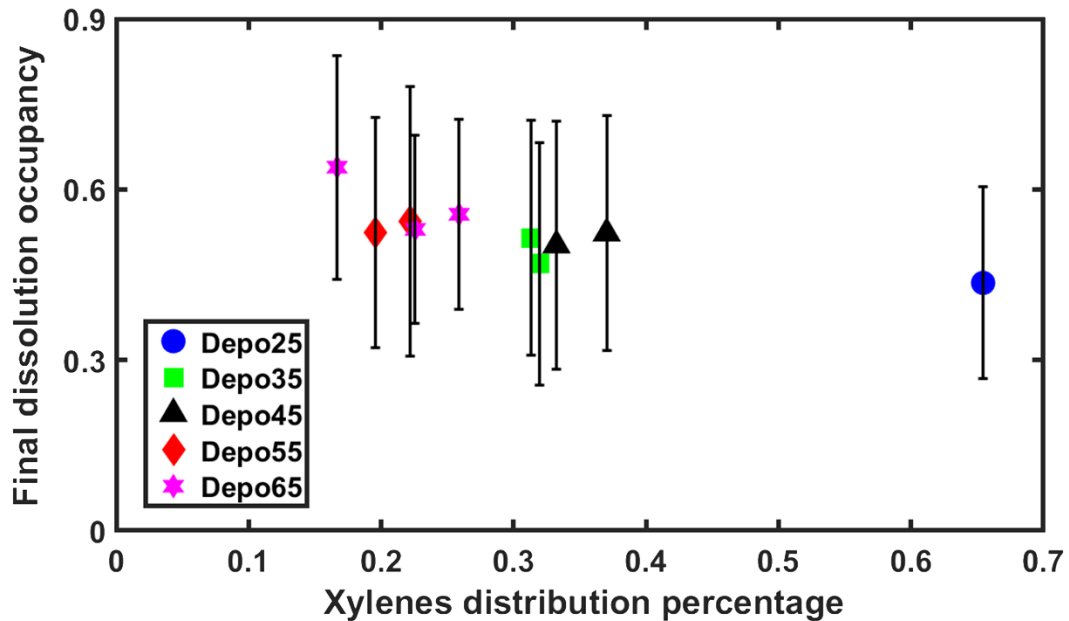
Figure 5.14 Final dissolution occupancy and xylenes distribution percentage of different samples. When increasing the deposition temperature of the sample, the xylenes distribution percentage decreased, and final dissolution occupancy increased.

A very clear trend can be seen from the graph that shows that deposition at higher temperatures also results in higher overall occupancies and lower xylenes distribution percentages. Indicating that it is more challenging to clean the porous media where asphaltenes are deposited at higher temperatures than the regions deposited at lower temperatures. It is noteworthy to mention that the large deviations are greatly influenced by interplay of both pore size limitation and surface limitation mechanisms. From another prospective the increase in the fractal dimension of formed aggregates due to the increase in the deposition temperature provided a greater resistance to the internal diffusion of xylenes, which in turn inhibited

dissolution from within the nanostructures. This reasoning interconnects the effects of the deposition temperature on the final dissolution.

5.3.2.c Nanosheet sizes of asphaltenes at different regions

Besides the microscale information from the occupancy maps, we can also estimate molecular information of the nanosheet sizes of asphaltenes at different regions. Figure 5.15 reports that asphaltenes molecules at the impalpable region had slightly larger nanosheet sizes (2.99-3.08 nm) than the ones at the palpable region (2.90 – 3.03 nm). This result is consistent with our previous work.[10] Due to the enhanced π-π interaction between aromatic solvent and asphaltenes molecules with larger sheet
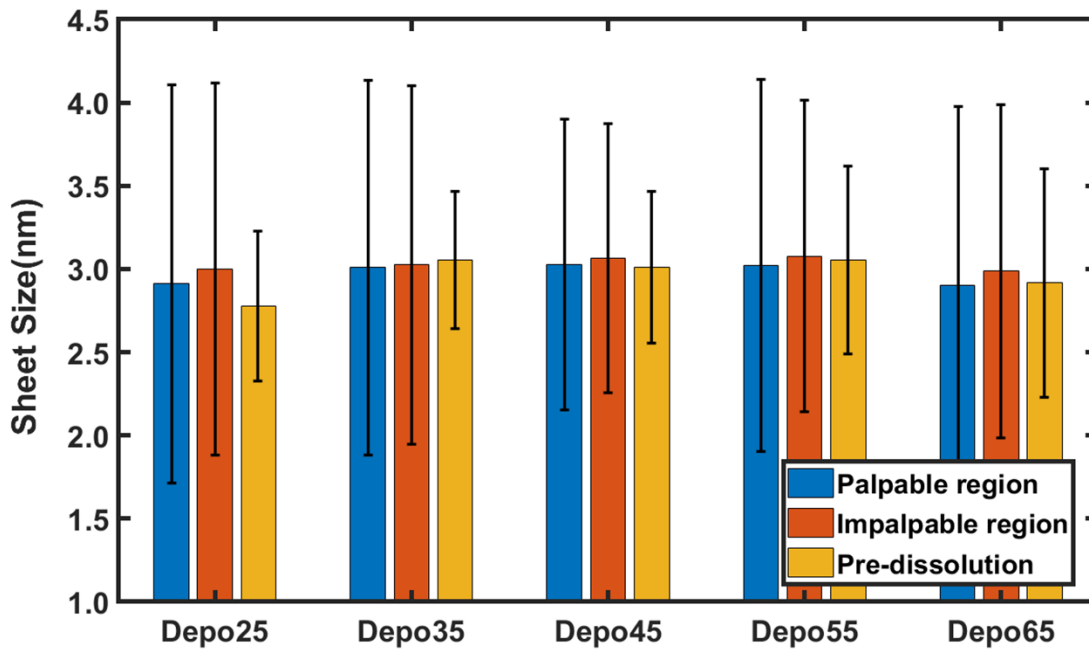
Figure 5.15 Average sheet size of asphaltenes molecules before dissolution and during dissolution at different regions. The asphaltenes molecules at impalpable regions showed a slight increase in sheet sizes when compared with the ones at palpable regions. (refer to Appendix C for distribution)

sizes, asphaltenes with smaller sheet sizes are expected at the xylenes palpable region. Noteworthy, the standard deviations are due to the size-distributions of asphaltenes molecules, and thus estimation of the nanosheet sizes provides qualitative insight that could potentially be applied to other asphaltenes deposits.

5.4 Conclusion

In the present work, a novel automated microfluidic system for research on asphaltenes deposition and dissolution in porous media was designed, generating an unprecedented level of data acquisition. This system has access to real-time *in-situ* characterization during the deposition and dissolution processes. The occupancy map of asphaltenes obtained by convolution of the asphaltenes spectra enabled us to visualize the distribution of asphaltenes during experiments. The combination of the silicon-based microfluidic device with thermoelectric heating enabled us to create a well-controlled isothermal environment for all conditions studied. Here, we utilized the advanced automated microsystem to study the temperature effect on asphaltenes deposition within the porous media. Our findings provided better understanding of the behaviour of asphaltenes:

1) Asphaltenes from a Wyoming sample (field deposits) deposited at higher temperatures tend to accumulate at the beginning of the porous media, while at lower temperatures, the deposition was distributed throughout the porous media. Two possible explanations for this phenomenon include the temperature effect on asphaltenes nanoaggregation and hydrodynamic conditions. An increase in the deposition temperature can form asphaltenes with larger aggregates and

- 200 -

higher fractal dimensions in shorter periods. In contrast, increasing the deposition temperature from 25 °C to 65 °C could lead to decreases in shear stresses ranging from 1/5 to 1/17 the reference.

2) During the dissolution of asphaltenes, xylenes have a much easier time accessing the regions of low occupancy compared to regions with high occupancy. At low deposition temperatures, the xylenes are mainly restricted by pore size limitations, while at higher temperatures the alteration of the surface chemistry dominates the xylenes fluid path through the pores.

3) As the distribution of xylenes inside the porous media increases, the dissolution of asphaltenes also increases. An increase in the deposition temperature increased the difficulty of removing the deposited asphaltenes from porous media for the same number of pore volumes of solvent injected. At low occupancy regions, it is possible to flush out asphaltenes with higher flow rates. At high occupancy regions, the immersion time of the solvent plays an important role in the dissolution.

4) Asphaltenes molecules in the impalpable region tended to have larger sheet sizes than the ones in the palpable region.

Our findings could help to discover more efficient remediation strategies where asphaltenes deposit in upstream energy production operations. As an example, a solvent shut-in would favour the dissolution of highly occupied regions, while a high-pressure flush with high flowrates could clean the low occupied regions. Towards the future perspective, the automated high throughput microfluidic system supplemented with a database and a more sophisticated data analysis method, such

- 201 -

as artificial intelligent and supervised machine learning could advance the asphaltenes science to an even deeper level of molecular understanding.

Reference

(1)   Sheu, E. Y.; Mullins, O. C. *Asphaltenes Fundamentals and Applications*, 1st. Edn.; Springer Science+ Business Media, LLC, 1995.

(2)   Mullins, O. C. The Asphaltenes. *Annu. Rev. Anal. Chem.* **2011**, *4* (1), 393–418.

(3)   Akbarzadeh, K.; Hammami, A.; Kharrat, A.; Zhang, D.; Allenson, S.; Creek, J.; Kabir, S.; Jamaluddin, J.; Marshall, A.; Rodgers, R.; et al. Asphaltenes-Problematic but Rich in Potential. *Oilf. Rev.* **2007**, 22–43.

(4)   Kaminski, T. J.; Fogler, H. S.; Wolf, N.; Wattana, P.; Mairal, A. Classification of Asphaltenes via Fractionation and the Effect of Heteroatom Content on Dissolution Kinetics. *Energy Fuels* **2000**, *14* (1), 25–30.

(5)   Hu, C.; Morris, J. E.; Hartman, R. L. Microfluidic Investigation of the Deposition of Asphaltenes in Porous Media. *Lab chip* **2014**, *14* (12), 2014–2022.

(6)   Hu, C.; Hartman, R. L. High-Throughput Packed-Bed Microreactors with In-Line Analytics for the Discovery of Asphaltene Deposition Mechanisms. *AIChE J.* **2014**, *60* (10), 3534–3546.

(7)   Hu, C.; Garcia, N. C.; Xu, R.; Cao, T.; Yen, A.; Garner, S. A.; Macias, J. M.; Joshi, N.; Hartman, R. L. Interfacial Properties of Asphaltenes at the Heptol-Brine Interface. *Energy Fuels* **2016**, *30* (1), 80–87.

(8)   Hu, C.; Yen, A.; Joshi, N.; Hartman, R. L. Packed-Bed Microreactors for Understanding of the Dissolution Kinetics and Mechanisms of Asphaltenes in Xylenes. *Chem. Eng. Sci.* **2016**, *140*, 144–152.

(9)   Pinho, B.; Minsariya, K.; Yen, A.; Joshi, N.; Hartman, R. L. Role of HZSM-5 Aluminosilicates on Asphaltenes Deposition by High-Throughput in Situ

Characterizations of a Microreservoir. *Energy Fuels* **2017**, *31*, 11640–11650.

(10)   Chen, W.; Vashistha, P.; Yen, A.; Joshi, N.; Kapoor, Y.; Hartman, R. L.
       Asphaltenes Dissolution Mechanism Study by In-Situ Raman Characterization of a
       Packed-Bed Microreactor with HZSM-5 Aluminosilicates. *Energy Fuels* **2018**, *32*
       (12), 12205–12217.

(11)   Luiza, M.; Pereira, O.; Grasseschi, D.; Toma, H. E. Photocatalytic Activity of
       Reduced Graphene Oxide–Gold Nanoparticle Nanomaterials: Interaction with
       Asphaltene and Conversion of a Model Compound. *Energy Fuels* **2018**, *32*, 2673–
       2680.

(12)   Stevens, R. C. High-Throughput Protein Crystallization Stevens 559. *Curr. Opin.
       Struct. Biol.* **2000**, *10* (5), 558–563.

(13)   Hopfgartner, G.; Bourgogne, E. Quantitative High-Throughput Analysis of Drugs
       in Biological Matrices by Mass Spectrometry. *Mass Spectrom. Rev.* **2003**, *22* (3),
       195–214.

(14)   Pepperkok, R.; Ellenberg, J. High-Throughput Fluorescence Microscopy for
       Systems Biology. *Nat. Rev. Mol. Cell Biol.* **2006**, *7* (9), 690–696.

(15)   Conrad, C.; Wünsche, A.; Tan, T. H.; Bulkescher, J.; Sieckmann, F.; Verissimo,
       F.; Edelstein, A.; Walter, T.; Liebel, U.; Pepperkok, R.; et al. Micropilot:
       Automation of Fluorescence Microscopy-Based Imaging for Systems Biology.
       Nat. Methods **2011**, *8* (3), 246–249.

(16)   Jones, R. V.; Godorhazy, L.; Varga, N.; Szalay, D.; Urge, L.; Darvas, F.
       Continuous-Flow High Pressure Hydrogenation Reactor for Optimization and
       High-Throughput Synthesis. *J. Comb. Chem.* **2006**, *8* (1), 110–116.

(17)   Smithson, D.; Shelat, A. A.; Guy, K.; Yan, B.; Khan, I. A.; Nelson, C.; Ruan, H.;
       Walker, L.; Brown, K. M.; Smillie, T.; et al. Automated High-Throughput System
       to Fractionate Plant Natural Products for Drug Discovery. *J. Nat. Prod.* **2010**, *73*
       (4), 751–754.

(18)   Churski, K.; Korczyk, P.; Garstecki, P. High-Throughput Automated Droplet
       Microfluidic System for Screening of Reaction Conditions. *Lab Chip* **2010**, *10* (7),
       816–818.

(19)   Chan, E. M.; Xu, C.; Mao, A. W.; Han, G.; Owen, J. S.; Cohen, B. E.; Milliron, D.
       J. Reproducible, High-Throughput Synthesis of Colloidal Nanocrystals for
       Optimization in Multidimensional Parameter Space. *Nano Lett.* **2010**, *10* (5),
       1874–1885.

(20)   Chan, E. M. Combinatorial Approaches for Developing Upconverting
       Nanomaterials: High-Throughput Screening, Modeling, and Applications. *Chem.
       Soc. Rev.* **2015**, *44* (6), 1653–1679.

(21)   Goodell, J. R.; Mcmullen, J. P.; Zaborenko, N.; Maloney, J. R.; Ho, C.-X.; Jensen,
       K. F.; Porco, J. A.; Beeler, A. B. Development of an Automated Microfluidic
       Reaction Platform for Multidimensional Screening: Reaction Discovery
       Employing Bicyclo[3.2.1]Octanoid Scaffolds. *J. Org. Chem* **2009**, *74*, 6169–6180.

(22)   Mcmullen, J. P.; Jensen, K. F. Integrated Microreactors for Reaction Automation:
       New Approaches to Reaction Development. *Annu. Rev. Anal. Chem.* **2010**, *3*, 19–
       42.

(23)   Schneider, M. H.; Sieben, V. J.; Kharrat, A. M.; Mostowfi, F. Measurement of
       Asphaltenes Using Optical Spectroscopy on a Microfluidic Platform. *Anal. Chem.*

2013, *85* (10), 5153–5160.

(24)   Sieben, V. J.; Tharanivasan, A. K.; Ratulowski, J.; Mostowfi, F. Asphaltenes Yield
        Curve Measurements on a Microfluidic Platform. *Lab Chip* **2015**, *15* (20), 4062–
        4074.

(25)   Sieben, V. J.; Tharanivasan, A. K.; Andersen, S. I.; Mostowfi, F. Microfluidic
        Approach for Evaluating the Solubility of Crude Oil Asphaltenes. *Energy Fuels*
        2016, *30* (3), 1933–1946.

(26)   Sieben, V. J.; Stickel, A. J.; Obiosa-Maife, C.; Rowbotham, J.; Memon, A.;
        Hamed, N.; Ratulowski, J.; Mostowfi, F. Optical Measurement of Saturates,
        Aromatics, Resins, and Asphaltenes in Crude Oil. *Energy Fuels* **2017**, *31* (4),
        3684–3697.

(27)   Mcmullen, J. P.; Jensen, K. F. An Automated Microfluidic System for Online
        Optimization in Chemical Synthesis. *Org. Process Res. Dev.* **2010**, *14*, 1169–1176.

(28)   Mcmullen, J. P.; Jensen, K. F. Rapid Determination of Reaction Kinetics with an
        Automated Microfluidic System. *Org. Process Res. Dev.* **2011**, *15*, 398–407.

(29)   Nieuwland, P. J.; Koch, K.; Van Harskamp, N.; Wehrens, R.; Van Hest, J. C. M.;
        Rutjes, F. P. J. T. Flash Chemistry Extensively Optimized: High-Temperature
        Swern-Moffatt Oxidation in an Automated Microreactor Platform. *Chem. Asian. J.*
        2010, *5* (4), 799–805.

(30)   Garcia-Egido, E.; Spikmans, V.; Wong, S. Y. F.; Warrington, B. H. Synthesis and
        Analysis of Combinatorial Libraries Performed in an Automated Micro Reactor
        System. *Lab Chip* **2003**, *3*, 73–76.

(31)   Stefan, H.; Roland, Z. Microfluidic Platforms for Lab-on-a-Chip Applications. *Lab*

Chip **2007**, *7*, 1094–1110.

(32)   Chung, K.; Crane, M. M.; Lu, H. Automated On-Chip Rapid Microscopy,

Phenotyping and Sorting of C. Elegans. *Nat. Methods* **2008**, *5* (7), 637–643.

(33)   Sugimoto, A.; Fukuyama, T.; Rahman, M. T.; Ryu, I. An Automated-Flow

Microreactor System for Quick Optimization and Production: Application of 10-

and 100-Gram Order Productions of a Matrix Metalloproteinase Inhibitor Using a

Sonogashira Coupling Reaction. *Tetrahedron Lett.* **2009**, *50* (46), 6364–6367.

(34)   Krishnadasan, S.; Brown, R. J. C.; DeMello, A. J.; DeMello, J. C. Intelligent

Routes to the Controlled Synthesis of Nanoparticles. *Lab Chip* **2007**, *7*, 1434–

1441.

(35)   Abdallah, W. A.; Yang, Y. Raman Spectrum of Asphaltene. *Energy Fuels* **2012**,

26 (11), 6888–6896.

(36)   Bouhadda, Y.; Bormann, D.; Sheu, E.; Bendedouch, D.; Krallafa, A.; Daaou, M.

Characterization of Algerian Hassi-Messaoud Asphaltene Structure Using Raman

Spectrometry and X-Ray Diffraction. *Fuel* **2007**, *86* (12–13), 1855–1864.

(37)   Tuinstra, F.; Koenig, L. Raman Spectrum of Graphite. *J. Chem. Phys.* **1970**, *53*

(1970), 1126–1130.

(38)   Matthews, M.; Pimenta, M.; Dresselhaus, G.; Dresselhaus, M.; Endo, M. Origin of

Dispersive Effects of the Raman D Band in Carbon Materials. *Phys. Rev. B* **1999**,

59 (10), R6585–R6588.

(39)   Lindenmaier, R.; Scharko, N. K.; Tonkyn, R. G.; Nguyen, K. T.; Williams, S. D.;

Johnson, T. J. Improved Assignments of the Vibrational Fundamental Modes of

Ortho-, Meta-, and Para-Xylene Using Gas- and Liquid-Phase Infrared and Raman

- 207 -

Spectra Combined with Ab Initio Calculations: Quantitative Gas-Phase Infrared Spectra for Detection. *J. Mol. Struct.* **2017**, *1149*, 332–351.

(40)   Yen, K. H. B. Microfluidic Reactors for the Synthesis of Nanocrystals, Massachusetts Institute of Technology, 2007.

(41)   Maqbool, T.; Srikiratiwong, P.; Fogler, H. S. Effect of Temperature on the Precipitation Kinetics of Asphaltenes. *Energy Fuels* **2011**, *25*, 694–700.

(42)   Chaisoontornyotin, W.; Bingham, A. W.; Hoepfner, M. P. Reversibility of Asphaltene Precipitation Using Temperature-Induced Aggregation. *Energy Fuels* **2017**, *31*, 3392–3398.

(43)   Headen, T. F.; Hoepfner, M. P. Predicting Asphaltene Aggregate Structure from Molecular Dynamics Simulation: Comparison to Neutron Total Scattering Data. *Energy Fuels* **2019**, *33*, 3787–3795.

(44)   Vilas Bôas Fávero, C.; Maqbool, T.; Hoepfner, M.; Haji-Akbari, N.; Fogler, H. S. Revisiting the Flocculation Kinetics of Destabilized Asphaltenes. *Adv. Colloid Interface Sci.* **2017**, *244*, 267–280.

(45)   Maqbool, T.; Raha, S.; Hoepfner, M. P.; Fogler, H. S. Modeling the Aggregation of Asphaltene Nanoaggregates in Crude Oil-Precipitant Systems. *Energy Fuels* **2011**, *25*, 1585–1596.

(46)   Hoepfner, M. P.; Fávero, C. V. B.; Haji-Akbari, N.; Fogler, H. S. The Fractal Aggregation of Asphaltenes. *Langmuir* **2013**, *29*, 8799–8808.

(47)   Torkaman, M.; Bahrami, M.; Dehghani, M. Influence of Temperature on Aggregation and Stability of Asphaltenes. I. Perikinetic Aggregation. *Energy Fuels* **2017**, *31*, 11169–11180.

(48) Torkaman, M.; Bahrami, M.; Dehghani, M. R. Influence of Temperature on Aggregation and Stability of Asphaltenes. II. Orthokinetic Aggregation. *Energy Fuels* **2018**, *32*, 6144–6154.

(49) Mohammadi, S.; Rashidi, F.; Mousavi-Dehghani, S. A.; Ghazanfari, M. H. On the Effect of Temperature on Precipitation and Aggregation of Asphaltenes in Light Live Oils. *Can. J. Chem. Eng.* **2016**, *94* (9), 1820–1829.

(50) Reerink, H. Size and Shape of Asphaltene Particles in Relationship to High-Temperature Viscosity. *Ind. Eng. Chem. Prod. Res. Dev.* **1973**, *12* (1), 82–88.

(51) Storm, D. A.; Barresi, R. J.; Sheu, & E. Y. Flocculation of Asphaltenes in Heavy Oil at Elevated Temperatures. *Fuel Sci. Technol. Int.* **1996**, *14*, 243–260.

(52) Wargadalam, V. J.; Norinaga, K.; Iino, M. Size and Shape of a Coal Asphaltene Studied by Viscosity and Diffusion Coefficient Measurements. *Fuel* **2002**, *81*, 1403–1407.

(53) Luo, P.; Gu, Y. Effects of Asphaltene Content on the Heavy Oil Viscosity at Different Temperatures. *Fuel* **2007**, *86*, 1069–1078.

(54) Bird, R. B.; Stewart, W. E.; Lightfoot, E. N. *Transport Phenomena*, 2nd Edn.; John Wiley & Sons, Ltd., 2002.

(55) Ghanavati, M.; Shojaei, M.-J.; Ramazani, A. Effects of Asphaltene Content and Temperature on Viscosity of Iranian Heavy Crude Oil: Experimental and Modeling Study. *Energy Fuels* **2013**, *27*, 7217–7232.

(56) Goncalves, S.; Castillo, J.; Fernández, A.; Hung, J. Absorbance and Fluorescence Spectroscopy on the Aggregation Behavior of Asphaltene-Toluene Solutions. *Fuel* **2004**.

(57)   Larson, R. G.; Morrow, N. R. Effects of Sample Size on Capillary Pressures in

Porous Media. *Powder Technol.* **1981**, *30* (2), 123–138.

Chapter 6

Conclusion and Future Development

6.1 Conclusion

Fossil fuel energy will still play a critical role in global energy consumption for the next few decades, despite the progressive development of renewable energy. Compared with coal and natural gas, petroleum has the advantages of less pollution when burnt, easy to handle and transport, and high energy density. However, the easy-to-access light crude oil is draining. The development in advanced technology, such as hydraulic fracturing and deep-water construction, enables the exploitation of crude oil from unconventional regions. However, these sophisticated facilities also increase the cost of construction and maintenance. Flow assurance is the top technology problem in terms of economic impacts. The hydrate formation during the deep-water oil exploration and asphaltenes deposition during heavy oil collection are two of the most important flow assurance issues. The knowledge of kinetics and mechanisms would contribute to the development of better remediation strategy. The thermodynamics information for both processes was well understood in the laboratory scale. However, the requirement of precise control over the system for kinetics study might not be satisfied in the traditional laboratory setups. Furthermore, the measurement for a matrix of multi-conditions kinetics information could be time-consuming. Therefore, novel laboratory systems with access to high throughput, high fidelity information are desired to tackle these problems in energy science. In response, three microfluidic systems integrated with *in situ* Raman spectroscopy were applied to study the kinetics of methane hydrate crystallization/dissociation, and mechanisms of asphaltenes deposition and dissolution in porous media.

In the study of methane hydrate, a novel thermoelectrically-cooled microsystem was designed and built to enable the swift (1.0 K/s) and precise (up to ±0.01 K) temperature control of the microreactor. Benefit from the advanced temperature control, the experiment time was reduced from hours-to-days to seconds-to-minutes. The non-linear relationship of the propagation rate of methane hydrate and sub-cooling temperature at low sub-cooling region (< 4.0 K) was detected for the first time. A comprehensive model derived from first principles provides the explanation for this relationship through the consideration of diffusive flux during the crystallization. The dimensionless analysis confirmed that besides intrinsic crystallization kinetics, both mass transfer and heat transfer resistances could not be neglected. Asides from crystallization, the dissociation kinetics of methane hydrate were investigated by *in situ* Raman spectroscopy at unusual sensitivity, within a tenth of a degree near the thermodynamic phase boundary. The Raman characterization was optimized for the first time to decrease the heat effect of laser light to where it could be neglected. The transient dissociation kinetics information was determined through the normalized Raman scattering intensity of methane hydrate. A comprehensive model derived from first principles reveals the fact that the contribution of heat transfer and intrinsic kinetics to the dissociation process is transient, depending on the initial thickness of the crystal, the temperature of the system and dissociation time. In the meanwhile, the model indicates the origin of the "memory effect", referenced in hydrate science, comes from the dominance of intrinsic kinetics at the end of dissociation. This work not only leads to a deeper understanding of the kinetics of methane hydrate crystallization and dissociation but

also shows the exclusive advantages of using microfluidics as a platform to access the high-fidelity transient information.

In the mechanistic study of asphaltenes dissolution, a combination of quartz and HZSM-5 particles constitutes the porous media in a micro-packed bed reactor (μPBR). The dispersion profile and chemical information of asphaltenes molecules are obtained through *in situ* Raman characterization of the μPBR. By comparing the Raman mapping results of the μPBR after different pore volume of xylenes flowing through, invaluable insights are obtained:

(1) The Al_2O_3 content in zeolite HZSM-5 can attract asphaltenes molecules with larger sheet sizes, and thus stabilize the asphaltenes in solution within porous media, because of this increase in affinity.

(2) Asphaltenes molecules with larger sheet sizes have a tendency to self-assemble, ultimately resulting in hydrodynamic bridging within the porous media.

(3) Asphaltenes molecules with larger sheet sizes are easier to dissolve in xylenes than those with smaller sheet sizes.

(4) The increase of acidity of the porous media, by introducing a model zeolite in this case, leads to an increase in the asphaltenes dissolution percentage, because of the competition between surface adsorption with self-assembly.

These findings imply that $\pi-\pi$ interactions are significant when considering asphaltenes physics in the porous media. To further improve the experimental efficiency, a novel automated microfluidic system featured three independent packed-bed reactors was designed and built. In addition, the system has access to real-time *in situ* Raman

characterization on the asphaltenes deposition and dissolution processes for the first time. With the temperature control by the thermoelectric module, the system was utilized to study the temperature effect on asphaltenes deposition within the porous media. The results provide a better understanding of the behavior of asphaltenes in porous media:

(1) Asphaltenes from a Wyoming sample (field deposits) deposited at higher temperatures tend to accumulate at the beginning of the porous media, while at lower temperatures, the deposition was distributed throughout the porous media.

(2) During the dissolution of asphaltenes, xylenes have a much easier time accessing the regions of low occupancy compared to regions with high occupancy. At low deposition temperatures, the xylenes are mainly restricted by pore size limitations, while at higher temperatures the alteration of the surface chemistry dominates the xylenes fluid path through the pores.

(3) An increase in the deposition temperature increased the difficulty of removing the deposited asphaltenes from porous media for the same number of pore volumes of solvent injected. At low occupancy regions, it is possible to flush out asphaltenes with higher flow rates. At high occupancy regions, the immersion time of the solvent plays an important role in the dissolution.

(4) Asphaltenes molecules in the impalpable region tended to have larger sheet sizes than the ones in the palpable region.

Our findings in both studies not only provide a deeper understanding towards phase behaviours of hydrate and asphaltenes in the pipeline or near wellbore region but also could be served as guidance for the development of practical remediation strategy.

6.2 Future development

The increased experimental efficiency in hydrate study through the microsystem presents the possibility of high throughput screening for various parameters and additives. In a realistic scenario, natural gas is a mixture of eight possible components. It would be challenging to determine the phase behaviors of natural gas hydrate in the traditional setup without *in situ* characterization. However, it is possible to measure the thermodynamic behavior of a mixture of natural gas with a similar composition to nature, which could be obtained through mixing inside the microreactor, under the presence of water at various conditions. Couple with *in situ* Raman characterization, the microsystem could provide important insights towards the natural gas hydrate formation, such as the species, the crystal structures, the thermodynamic behaviors, and even the kinetics. Based on specific compositions, operation conditions in each production site, the microsystem could help to determine the fatal issues caused the formation of the hydrate.

Besides the diagnostic process, the microsystem also could be served as a platform for high throughput screening of the effectiveness of additives. There are at least three types of additives: thermodynamic inhibitors, kinetic inhibitors, and promoters. In the case of remediation, risk management is the preferred method over hydrate avoidance in terms of cost efficient. The former method uses kinetics inhibitors, while the latter method uses thermodynamic inhibitors. The effectiveness of additives could be determined through their influences on hydrate formation kinetics. Besides inhibitors, the promoters could be tested as well. Compared with compressed natural gas, the natural gas hydrate has the advantages over handling, storage, and transportation. However, the transformation of natural gas to hydrate could be of low efficiency due to the stochastic nature of nucleation,

and diffusive limitation during crystallization. Therefore, the use of optimum promoters could help to release the potential of application of hydrate.

The novel automated microsystem, AUTO^3-μPBR, brings the experimental efficiency of asphaltenes study to an unprecedented level. It allows building a wealth of high-fidelity data in a short period. Due to this capability, it is ideal for the diagnostic application in asphaltenes problem. Although asphaltenes are varied depending on the sample source, they still have some properties in common. Therefore, a database would be a valuable reference. However, the asphaltenes deposition is a complicated problem, which requires to consider from multi perspectives, such as the chemical nature of asphaltenes molecules, the chemical environment of porous media, and the hydraulic condition during production. Combined with all characterization information, the size of data for asphaltenes will be gigantic, which requires a more sophisticated data management.

With the huge size of data, it could be overwhelmed for a scientist to search for a pattern. The advanced analysis technique is desired for this application, such as artificial intelligence (AI) data analysis. Although it is not a new concept, artificial intelligence has only become more applicable in recent years with the growing power of computation and the availability of cloud-based services. AI machine learning is one of the most promising techniques for data analysis, with the ability to make assumptions, build models, test assumptions and learn the details autonomously. Furthermore, it could provide large-scale predictions based on a panoramic view of data. The implement of AI could contribute to understanding the asphaltenes behaviors from different, even unexpected perspectives.

Appendix A. Dissociation kinetics calculated based on equilibrium reaction and mass transfer rate

A.1 Derivation of intrinsic kinetics based on equilibrium reaction

The intrinsic kinetics could be viewed as the equilibrium reaction between the methane hydrate dissociation and crystallization when operation is close to the phase boundary (*i.e.*, within 0.1 K). In this scenario, the dissociation rate should consider the re-crystallization of methane hydrate based on equilibrium constant K_{eq},

$$\frac{dn_H}{dt} = -k_d n_H + k_b \cdot C_m \cdot C_W^{5.75} \qquad (A1)$$

$$K_{eq} = \frac{C_m \cdot C_W^{5.75}}{n_H} = \frac{k_d}{k_b} \qquad (A2)$$

where k_b is the rate constant for methane hydrate crystallization, C_m and C_w are the concentration of methane and water, respectively. Here, we assume the crystallization is elementary. From equations (A1) and (A2), we could now derive the expression for overall dissociation rate,

$$\frac{n_D}{n_0} = 1 - \left(\exp(-k_d t) \cdot \left(1 - \frac{C_m \cdot C_W^{5.75}}{K_{eq} \cdot n_0}\right) + \frac{C_m \cdot C_W^{5.75}}{K_{eq} \cdot n_0}\right) \qquad (A3)$$

Replacing equation (3.7) with equation (A3) for intrinsic kinetics, we could obtain the modified expression for dissociation based on heat transfer and intrinsic kinetics as

$$\frac{n_H}{n_0} = 1 - \frac{1}{\frac{l}{\sqrt{\frac{2t \cdot \kappa \cdot \Delta T}{\rho_H \cdot \Delta H}}} + \frac{1}{1 - (\exp(-k_d t)) \cdot \left(1 - \frac{C_m \cdot C_W^{5.75}}{K_{eq} \cdot n_0}\right) - \frac{C_m \cdot C_W^{5.75}}{K_{eq} \cdot n_0}}} \qquad (A4)$$

here, we have l, k_d, and K_{eq} as three fitting parameters. The initial mass of methane hydrate could be estimated as $n_0 = l \cdot A \cdot \rho_H$. Table A.1 Shows the results of fitting by using equation (A4).

Table A.1 Fitting parameters of the mixed heat transfer and intrinsic kinetic model (equation (A4)).

Experimental conditions	Initial methane hydrate thickness l (µm)	Intrinsic kinetic constant k_d (s^{-1})	Equilibrium constant K_{eq} mol$^{5.75}$/(m$^{17.25}$ kg))
60.2 bar, ΔT=0.1 K	133.70	0.045	1.5 x 10^{45}
60.2 bar, ΔT=0.2 K	2.75	0.047	1.5 x 10^{45}
60.2 bar, ΔT=0.3 K	8.68	0.042	1.5 x 10^{45}
70.3 bar, ΔT=0.1 K	15.69	0.055	1.5 x 10^{45}
70.3 bar, ΔT=0.2 K	2.25	0.070	1.5 x 10^{45}
70.3 bar, ΔT=0.3 K	11.27	0.051	1.5 x 10^{45}
80.1 bar, ΔT=0.1 K	2.78	0.060	1.5 x 10^{45}
80.1 bar, ΔT=0.2 K	8.67	0.060	1.5 x 10^{45}
80.1 bar, ΔT=0.3 K	7.22	0.064	1.5 x 10^{45}

The fitting results indicate that the dissociation rate is dominating. In other words, the formation rate of methane hydrate from the supercritical thin film could be assumed to be negligible at the temperature above the phase boundary ($\frac{C_m \cdot C_w^{5.75}}{K_{eq} \cdot n_0} \cong 1.07 \times 10^{-3} \cong 0$). Therefore, the equation (A4) could be simplified into equation (3.7).

A.2 Calculation of mass transfer rate

The rate of methane transfer ($\frac{dm}{dt}$) through the thin layer at the interface of methane hydrate and liquid water could be calculated through the following expression,

$$\frac{dm}{dt} = k_c \cdot A \cdot \Delta C \qquad \text{(A5)}$$

where, k_c is the mass transfer coefficient, which could be estimated through the diffusivity of methane in water (D, 1.0 x 10^{-9} m^2/s @ 10 ºC) and thin film thickness (l, estimated as 10 μm); A is the interface area; ΔC is the concentration difference of methane in methane hydrate and water bulk region. The amount of methane released by methane hydrate dissociation could be calculated as followed,

$$\frac{dm}{dt} = r \cdot \rho_H \cdot \omega_m \qquad \text{(A6)}$$

where, r is the dissociation rate, which could be estimated through linear dissociation rate ($\frac{dx}{dt}$) and interface area (A); ρ_H (920 kg/m^3) is the density of methane hydrate; and ω_m (0.13) is the mass weight fraction of methane in methane hydrate. The linear dissociation rate based on mass transfer could be estimated to be 102.3 μm/s. The linear dissociation rate based on heat transfer could be derived from equation (3.4)

$$\frac{dx}{dt} = \frac{1}{2}\sqrt{\frac{2 \cdot \kappa \cdot \Delta T}{\rho_H \cdot \Delta H \cdot t}} \qquad \text{(A7)}$$

which increases as ΔT increase and decrease as t increase. When $\Delta T = 0.1\,K$, t needs to be less than 0.0069 s to be comparable to dissociation rate calculated by mass transfer. When $\Delta T = 0.3\,K$, t needs to be less than 0.021 s. Both cases are in orders of magnitude

difference of time scale with our experimental time, which is 10 s. Therefore, the mass transfer could be ignored.

Appendix B. Pressure drop measurement of asphaltenes deposition in porous media, validation of bed occupancy and sheet size measurement, characterization of asphaltenes samples

B.1 Pressure drop measurement of asphaltenes deposition in porous media
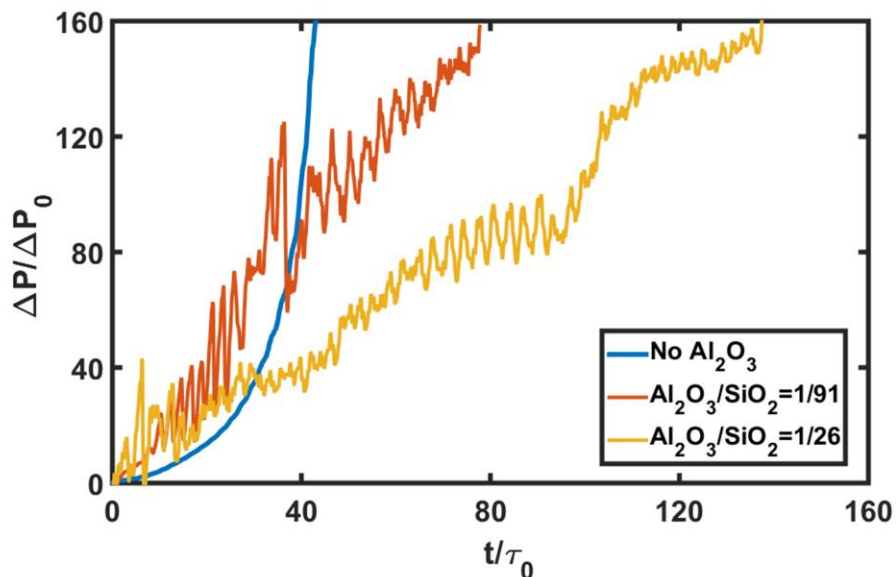
Figure B.1 Dimensionless pressure drop against dimensionless time for different Al_2O_3/SiO_2 ratios. ΔP_0 is the initial pressure drop across the µPBR and τ_0 is the initial residence time. The time required to achieve the final pressure (6.0 bar) increases as the Al_2O_3 content increase.

B.2 Validation of bed occupancy and sheet size measurement

Our experimental results demonstrate that the introduction of Al_2O_3 in the system could attract the large sheet size and result in higher bed occupancy. Both bed occupancy and sheet size measurements are analyzed by the same data set. As showed in Figure B.2, the random-scattered pattern suggests that two measurement are independent of one another.
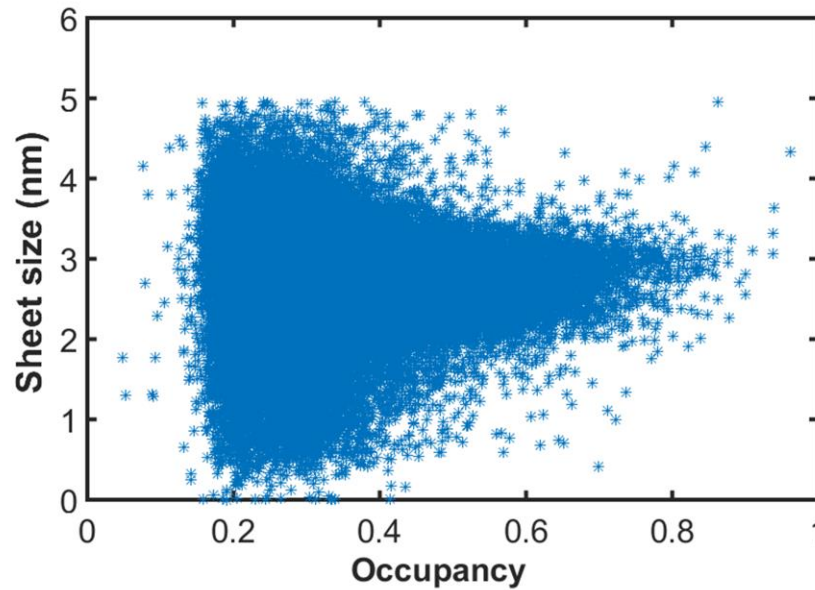
Figure B.2 Relationship between bed occupancy and sheet size measurements analyzed by the same data set.

B.3 Characterization of asphaltenes samples

B.3.1 Dynamic light scattering measurement of asphaltenes particle

The size of asphaltenes particles were measured by using Malvern Nano Series Zetasizer ZS90 at a 90 degree scattering angle. The sample was prepared by adding 20 ml of n-heptane to 30 ml of asphaltenes in toluene solution (4.0 g/l) and leaving it for overnight. The kinematic viscosity of the sample was measured using a Cannon Ubbelohde viscometer. The density of the sample was measured using a Anton Paar DMA 4500M densiometer. The dynamic viscosity was then calculated through kinematic viscosity and density of the sample. The refractive index of the sample was measured by an Abbe
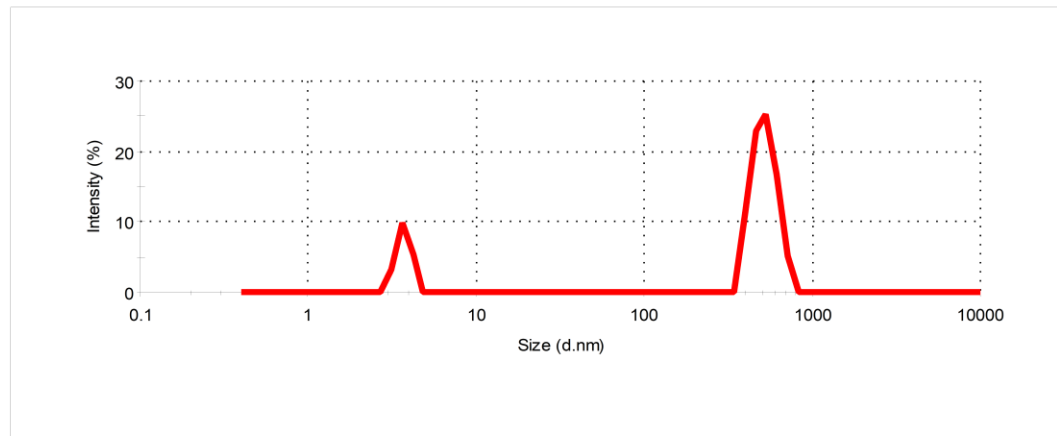
Figure B.3 Particle size distribution obtained by dynamic light scattering measurement. The results show two distinct size distributions of asphaltenes particles. The primary distribution of particles (81.4%) have an average size of 521.1 nm. The secondary distribution of particles (18.6%) have an average size of 3.7 nm, which is consistent with the size of asphaltenes nanoaggregates.

refractormeter. The dynamic viscosity and refractive index values were the input parameters for dynamic light scattering (DLS) measurement.

B.3.2 Outlet samples of asphaltenes dissolved from porous media
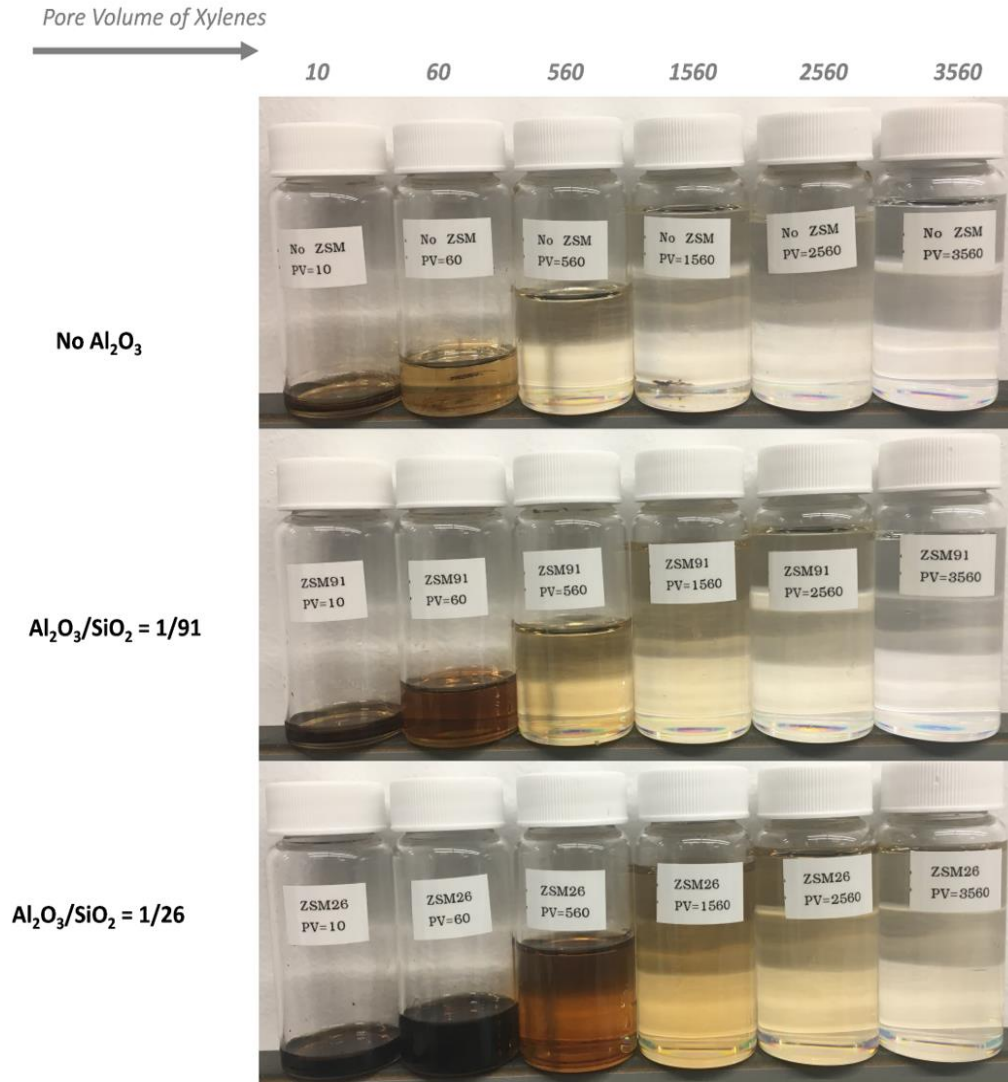
Figure B.4 Outlet samples of asphaltenes dissolved from micro-packed-bed reactors with respect to different programs.

B.3.3 Sheet size characterization of asphaltenes molecules

Table B.1 Mean sheet size of asphaltene molecules across the micro-packed bed reactor before and after dissolution with xylenes solvent.

Trial #	Mean sheet size before dissolution (nm)	Mean sheet size after dissolution (nm)
No zeolites (1)	2.70	2.49
No zeolites (2)	2.81	2.64
No zeolites (3)	2.74	2.63
$Al_2O_3/SiO_2 = 1/91$ (1)	2.70	2.66
$Al_2O_3/SiO_2 = 1/91$ (2)	3.13	2.69
$Al_2O_3/SiO_2 = 1/91$ (3)	3.05	2.48
$Al_2O_3/SiO_2 = 1/26$ (1)	2.92	2.70
$Al_2O_3/SiO_2 = 1/26$ (2)	3.45	3.30
$Al_2O_3/SiO_2 = 1/26$ (3)	3.26	3.10

Table B.2 Mean sheet size of asphaltene molecules at undissolved and dissolved regions
of the packed-bed microreactor.

Trial #	Mean sheet size at undissolved region (nm)	Mean sheet size at dissolved region (nm)
No zeolites (1)	3.05	2.64
No zeolites (2)	3.04	2.80
No zeolites (3)	3.06	2.98
$Al_2O_3/SiO_2 = 1/91$ (1)	2.80	2.67
$Al_2O_3/SiO_2 = 1/91$ (2)	3.40	3.10
$Al_2O_3/SiO_2 = 1/91$ (3)	3.01	3.06
$Al_2O_3/SiO_2 = 1/26$ (1)	3.15	2.83
$Al_2O_3/SiO_2 = 1/26$ (2)	3.54	2.40
$Al_2O_3/SiO_2 = 1/26$ (3)	3.29	3.25

Table B.3 Fluorescence emission wavelength and corresponding HOMO-LUMO gap of outlet samples of asphaltenes dissolved from a packed-bed microreactor.

Trial #	Fluorescence emission wavelength λ_{max} (nm)	Calculated HOMO-LUMO gap ΔE_{H-L} (eV)
Source sample	494.5	2.5073
No zeolites (1)	519.5	2.3866
No zeolites (2)	508	2.4406
No zeolites (3)	516	2.4028
$Al_2O_3/SiO_2 = 1/91$ (1)	524.5	2.3639
$Al_2O_3/SiO_2 = 1/91$ (2)	514	2.4121
$Al_2O_3/SiO_2 = 1/91$ (3)	532	2.3305
$Al_2O_3/SiO_2 = 1/26$ (1)	524.5	2.3639
$Al_2O_3/SiO_2 = 1/26$ (2)	520	2.3843
$Al_2O_3/SiO_2 = 1/26$ (3)	509.5	2.4335

Appendix C. Fabrication and characterization of AUTO^3-µPBR, distribution of bed occupancy and sheet size at different regions

C.1 Fabrication Procedure for the AUTO^3-µPBR

C.1.1 Materials and chemicals

The silicon wafers with diameter of 100 mm (4 inch), and thickness of 1.0 mm were purchased from NOVA Electronic. The Schott Borofloat 33 Glass with diameter of 100 mm, and thickness of 1.5 mm were purchased from UniversityWafer Inc. The positive photomask made of chrome and quartz was obtained from Front Range Photomask. The negative photomask made of Mylar Emulsion was obtained from Advance Reproduction Corp. The positive photoresist AZ9260 was purchased through Integrated Micro Materials (IMM). The rest of the chemicals, including AZ 400K (developer for AZ9260), Hexamethyldisilazane (HMDS, Sigma Aldrich, primer) SU-8 50 or SU-8 2025 (MicroChem, negative photoresist), and SU-8 developer were kindly provided by CUNY ASRC NanoFabrication Lab.

C.1.2 Instrument and facility list

Table C.1 List of instrument models for fabrication procedure

Category	Procedure	Instrument model
Photolithography*	Spin coating	Brewer Science Cee Spin Coaters
	Patterning	EVG620 Mask Aligner
	UV-Ozone cleaning	The SAMCO UV-2
Etching*	Deep reactive ion etching (DRIE)	Oxford PlasmaPro System 100 Cobra
Oxidation*	Plasma enhanced chemical vapor deposition	Oxford PlasmaPro System 100 PECVD
	Oxidation	Tystar Furnace Stack
Bonding**	Rinse and cleaning	Verteq SuperClean 1600-3
	Anodically bonding	EVG 510 Wafer Bonder
Backend*	Tape mounting	Ultron UH114
	Dicing	Disco DAD3220
Metrology*	Photoresist thickness measurement	Burker Dektak-XT (stylus profiler)
	Etching depth measurement	Burker Contour GT-I (optical interferometric microscope)
	Oxide layer thickness measurement	Filmetrics F20
	Profile inspection	Nikon Cclipse Inspection Microscopes
	Profile inspection	FEI Nova NanoSEM (high resolution scanning electron microscope)

* Nanofabrication Lab at Advanced Science Research Center, CUNY

** Quattrone Nanofabrication at Singh Center for nanotechnology, UPenn

C.1.3 Fabrication procedure of AUTO^3-µPBR

Figure C.1 shows the schematic of the fabrication. The fabrication of the microfluidic device followed a standard micro-electronic-mechanical system (MEMS) process briefly described below:

I.   **Negative Photoresist Patterning:** The negative photoresist SU-8 50 is spin coated onto the first side of the silicon wafer at spinner rate of 3000 RPM for 45 s. The coated silicon wafer is then soft baked in an oven at 65 °C for 5 mins and 95 °C for 15 mins in that order. The baked silicon wafer is then exposed to a constant dosage of 220 mJ/cm^2 UV source. A 1-min and 6-min post-exposure bake is applied to the exposed silicon wafer in an oven at 65 °C and 95°C, respectively. The 54-µm thick pattern is developed by immersing the silicon wafer into SU-8 developer for 6 mins.

II. **Deep Reactive Ion Etching (DRIE):** The patterned silicon wafer is etched at a rate of about 2.8 µm/min for a total 250 min through the BOSCH process. The etching rate could be different depending on the cleaness condition in the chamber. It is suggested to do a step etching and measure the depth profile of the etching by optical interferometric microscope. After the completion of the etching process, the residual photoresist is cleaned by Piranha solution.

III. **Positive Photoresist Patterning:** The primer, hexamethyldisilazane (HMDS), is first spin coated onto the second side of the silicon wafer at spinner rate of 3000 RPM for 45s. The silicon wafer is then heated at 110 °C on the hotplate for 5 min to remove excess primer. The positive photoresist AZ9260 is then spin coated onto the primed silicon wafer. The coated silicon wafer was then soft baked in an

oven at 65 °C for 5 mins and 95 °C for 30 mins in that order. Leave the baked silicon wafer in the photolithography room for at least 1 hour for rehydration. (Note: the humidity should be kept between 40 % and 50 %) The rehydrated silicon wafer is exposed to a constant dosage of 1600 mJ/cm2 UV source through the EVG620 Mask Aligner. The 14.2-μm thick pattern is developed by immersing the silicon wafer into AZ-400K for 6 mins. (Note: dark erosion will occur if develop for too long) A hard bake at 110 °C for 2 min is applied afterward. The baked silicon wafer could be cleaned by UV-ozone to remove the debris of undeveloped photoresist.

IV. **Deep Reactive Ion Etching (DRIE):** The patterned silicon wafer is etched at the rate around 2.8 μm/min for 110 min through the BOSCH process. The depth profile is characterized by optical interferometric microscope to ensure reached the desired depth. After the completion of etching process, the residual of photoresist was cleaned by Piranha solution.

V. **Formation of oxide layer:** A thin layer of 0.5 μm silicon dioxide was deposited onto the second side of the silicon wafer through plasma-enhanced chemical vapor deposition (PECVD). This process could be replaced by oxidize the surface of silicon wafer through thermal furnace. However, an RCA cleaning should be applied prior thermal oxidation process.

VI. **Bonding and dicing:** Prior bonding, apply piranha cleaning and rinse to the etched silicon wafer as need to remove any chemical residuals and dust from surface. The stack of clean etched silicon wafer and 1.5 mm thick Pyrex glass wafer is then applied at high voltage (up to 700 V) and at high temperature

- 232 -

(300 °C) for anodically bonding. The AUTO^3-µPBRs are then obtained by dicing the stack of wafers.

(1) 1.0 mm Si-wafer with SU-8 photo resist

(2) UV exposure with mask

(3) Development

(4) 700 µm DRIE dry etching

(5) Removal of photo-resist layer

(6) Backside with AZ 9260 photo resist

(7) UV exposure with mask

(8) Development

(9) 300 µm DRIE dry etching

(10) Removal of photo-resist layer

(11) Deposit 0.5 µm silicon oxide in PECVD

(12) Anodically bond with 1.5 mm Borofloat 33

(13) Dice and separation of chips

Figure C.1 Schematic of fabrication of AUTO^3- µPBRs
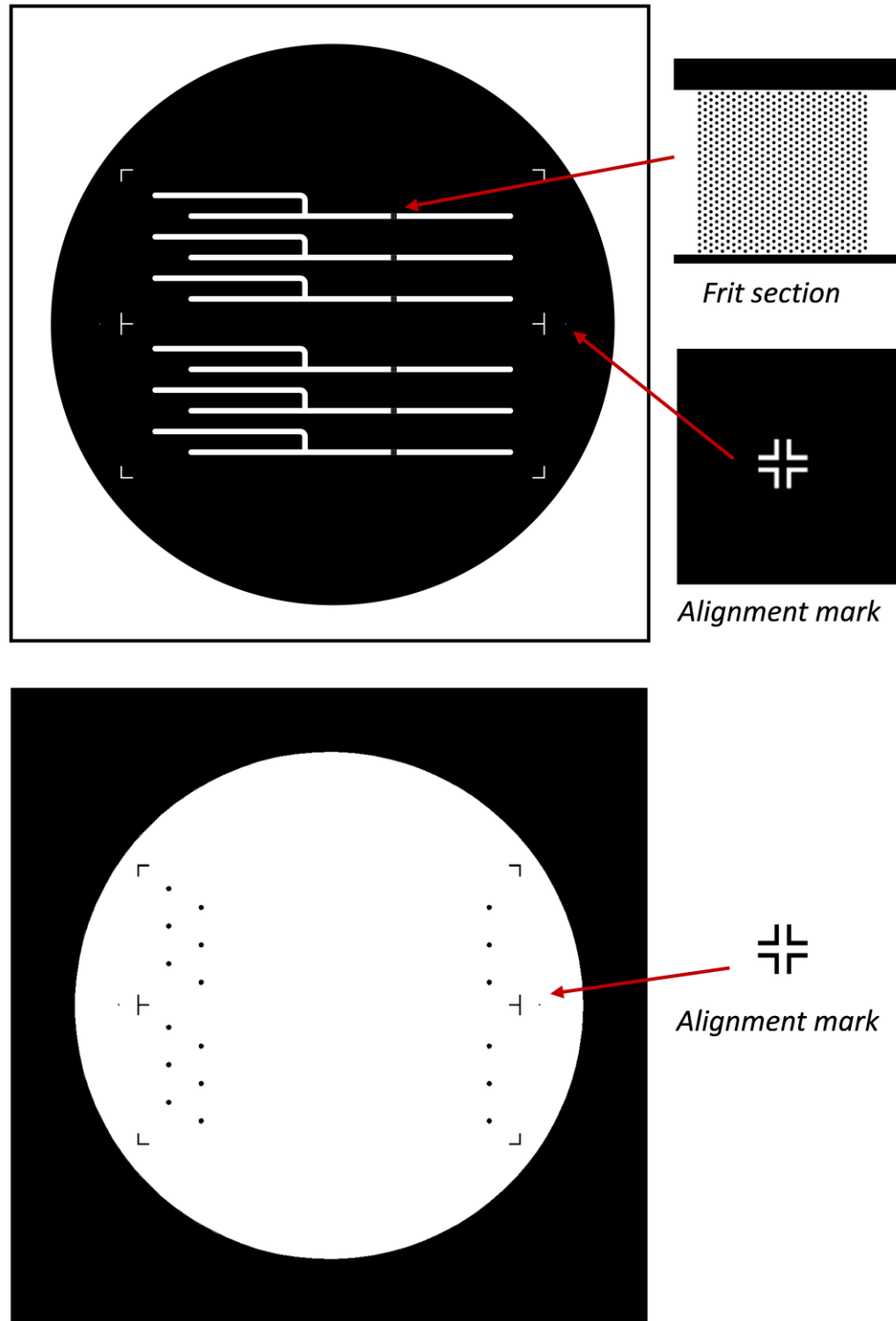
Figure C.2 Schematic of photomasks used in the fabrication of AUTO^3-µPBR. Top is the photomask for positive photoresist in right read chrome side down configuration (RRCD). Bottom is the photomask for negative photoresist in RRCD configuration.

C.2 Characterization of AUTO^3-µPBR

C.2.1 Pressure test and pressure drop measurement of AUTO^3- µPBR

The pressure test was done by pumping DI water at flowrate of 200 µL/min through the microsystem at testing pressure. The delivery of DI water was realized by an ISCO pump (Teledyne), while the testing pressure was adjusted through a back-pressure regulator (BPR, Equilibar). Two pressure transducers were installed at upstream and downstream of the microsystem each to monitor the pressure drop of the system. As shown in figure C.2, the sudden drop of the pressure indicated the maximum pressure rating of the AUTO^3-µPBR is around 15.39 bar.
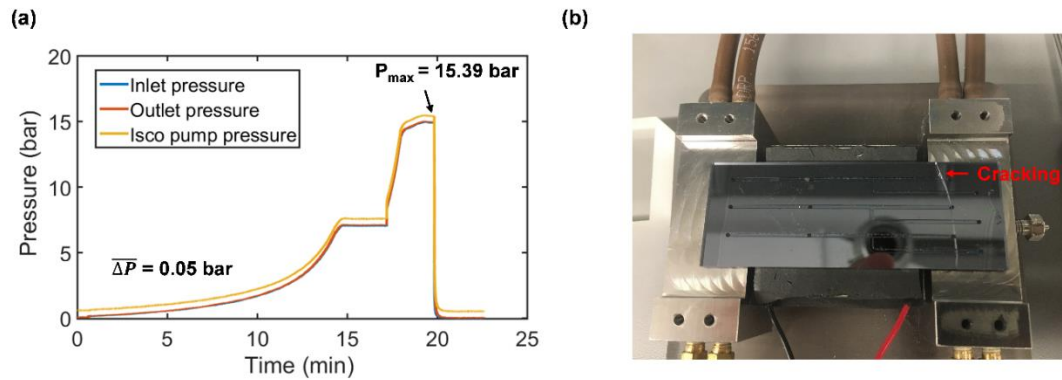
Figure C.3 (a) Pressure test of the AUTO^3-µPBR. The ultimate operating pressure was seen at 15.39 bar, after this the reactor cracked at the inlet of the channels. (b) Photo of the resulting crack from the pressure test.

C.2.2 COMSOL simulation of temperature profile

During the design of the microsystem, the temperature profile of the system was simulated by using COMSOL Multiphysics. The coolant with room temperature (293 K) was set to circulate at the inlet and outlet chucks of the microsystem at flowrate of 1 ml/min. The temperature of the microreactor was controlled by a Peltier Module with maximum power of 65 W. The mixture of toluene and n-heptane was flowed through the microchannels at the rate of 40 µL/min. Figure C.3 shows the result of the COMSOL simulation.
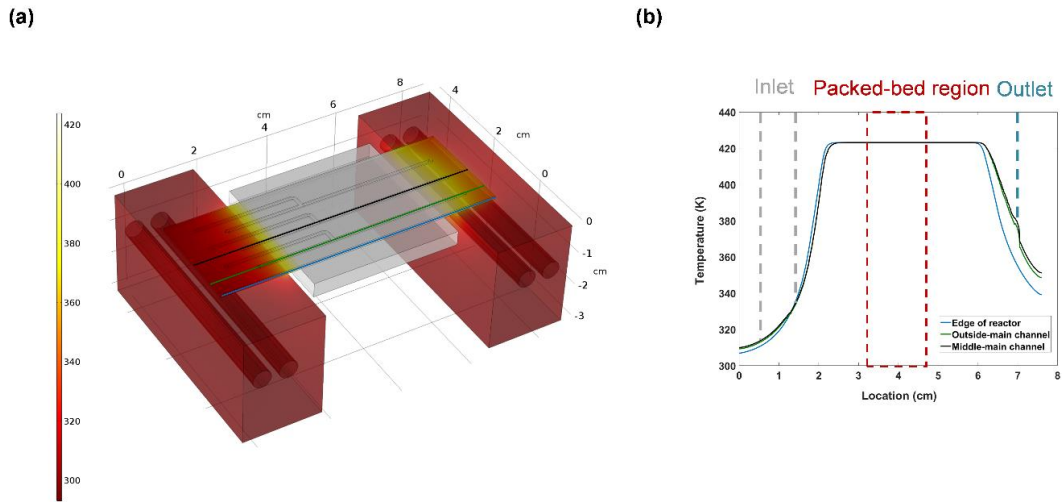
Figure C.4 (a) Temperature profile of microsystem at set temperature of 423 K. The results are simulated by COMSOL Multiphysics. (b) Temperature profile of different regions of the AUTO^3-µPBR.

C.2.3 Temperature test

As shown in figure C.4(a), the microsystem was assembled as design for temperature testing. The temperature test was conducted at set temperature of 60 °C and temperature profile of AUTO^3-µPBR was characterized by an IR camera. A standard Peltier Module (up to 80 °C) was used for the temperature testing. The higher experimental temperature could be achieved by using High Temperature Peltier Module (up to 150 °C). As shown in figure C.4(b), 50 sample points were chosen to measure the temperature profile. Figure C.5 shows the IR images for the initial 120 s and after 10 hrs. The images show the prompt response and swift temperature change of the microsystem. The temperature profile of the microsystem was stable after around 120 s till 10 hrs. Figure C.6 shows the

(a) Setup for temperature testing

(b) Infrared images with locations of testing points
(T= 60 °C)
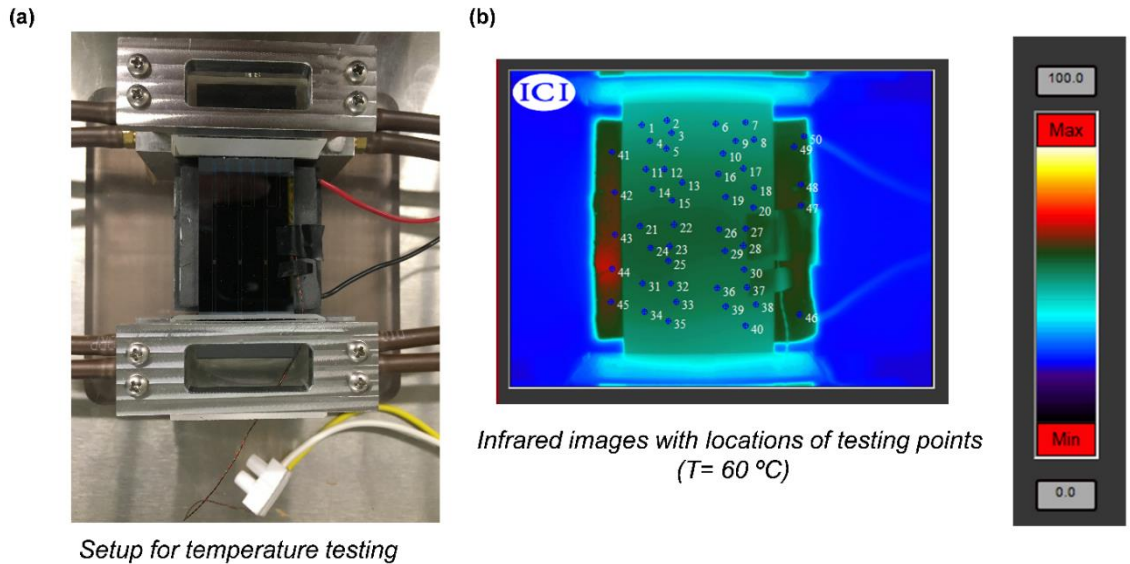
Figure C.5 (a) Photo of the temperature test setup done for the AUTO^3-µPBR. (b) IR imaging was used in testing the homogeneity of the temperature distributions and the stabilization time for a set temperature of 60 °C. The images show a homogenous temperature distribution within our reaction zone.

temperature profile of all 50 sample points. The maximum temperature appeared on the surface of Peltier Module at around 69 °C, whereas the minimum temperature appeared at the inlet region of the AUTO³-μPBR at around 52 °C as expect. The maximum temperature difference across the packed-bed region (point 21-30) was 0.30 °C, which was in the acceptable range (< 1%). The temperature fluctuation during 10-hour period was 0.13 °C.
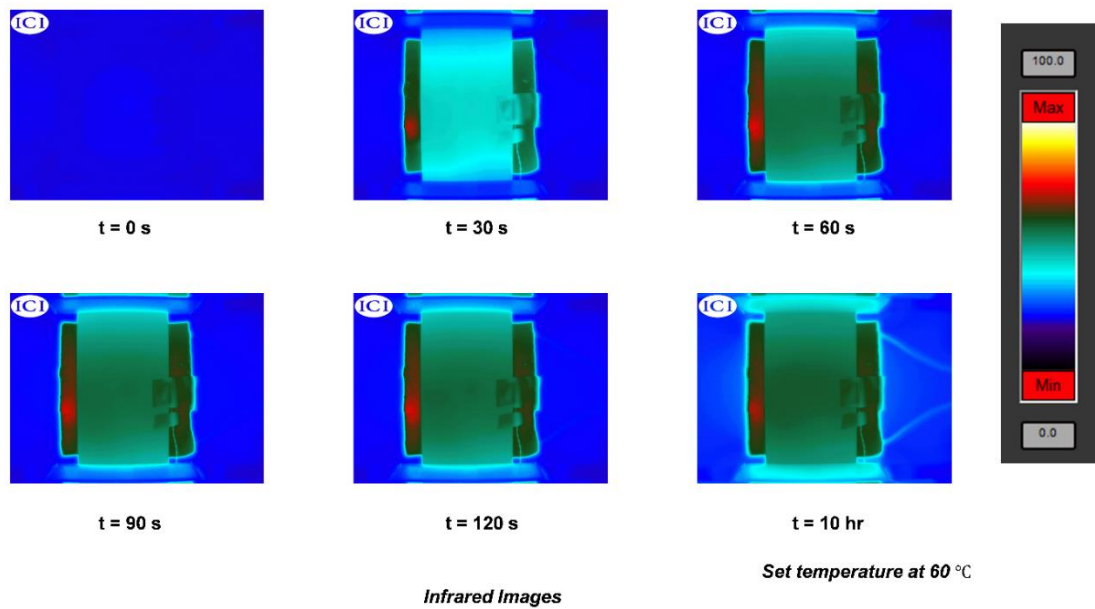
Figure C.6 IR images of the temperature distribution at different times. The reactor took a total of about 60 seconds to reach the target temperature and about 12 minutes to reach temperature stabilization (<1°C fluctuations).
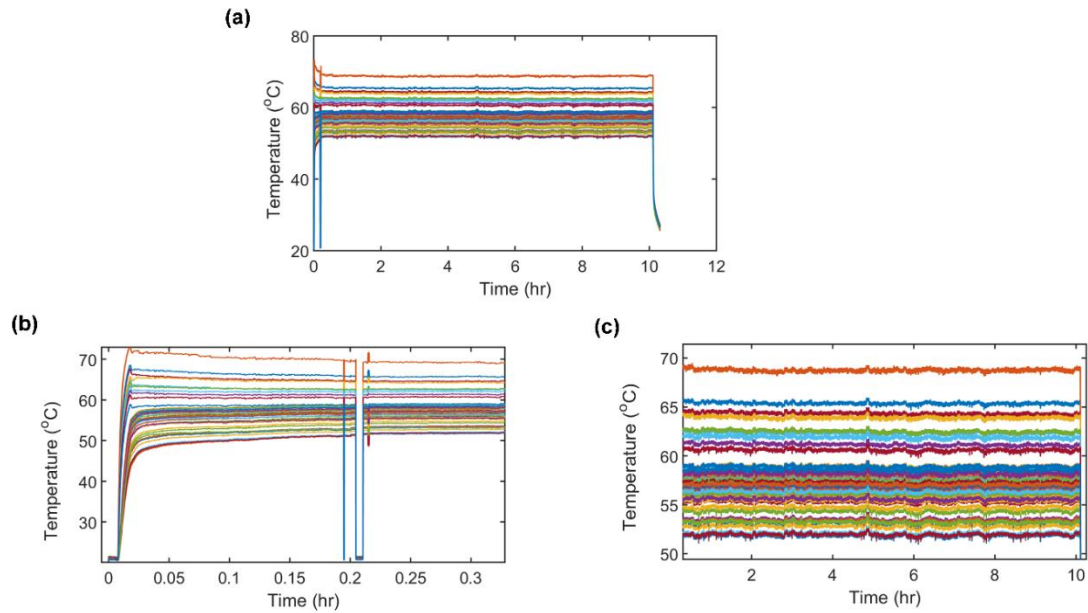
Figure C.7 (a) Temperature fluctuations from IR images up to 10-hour period. (b) Temperature graphs for one-hour period. Sharp temperature declines were seen at the 0.2-hour mark due to a slight malfunction of the temperature sensor, swift corrections were implemented and corrected the detachment of the sensor. (c) Close up image of the temperature graph for 10-hour period.

C.2.4 Resident time distribution (RTD) characterization of AUTO^3-µPBR for porosity measurement

The RTD of the AUTO^3-µPBR was obtained using a traditional pulse tracer method. To start, the mean residence time was first experimentally measured for the RTD system without the reactor and chuck by direct connection of tubing with an inner diameter of 0.005" at a constant flow rate of 40 µl/min. The tracer species, acetone was injected using a microinjector (IDEX Health & Science, Oak Harbor, WA, USA) with a sample loop of 1.0 µl. The injection was tracked for a total of 30 minutes, noting that the time starts once the acetone is introduced into the main line, upstream of the region of interest. The absorbance values were directly translated as concentration measurements and were converted into unitless E(t) values by the following:

$$E(t) = \frac{C(t)_i}{\sum C(t)_i} \tag{C1}$$

The reactor and chuck were then connected to the region of interest and the mean residence time was measured using the same procedure described above for an empty reactor (EµPBR) and packed bed reactor(µPBR). The mean residence time was calculated for each set of data by the following equation:

$$\tau = \int tE(t) \tag{C2}$$

It was found that the RTD system, without the reactor connected to it, had a residence time of 10.04 minutes. Once the reactor chuck was connected this time was extended to 12.22 minutes and the inclusion of the packed bed resulted in a residence time of 12.15 minutes. From these measurements it is clear that the time difference between the EµPBR

and μPBR reflects the packed bed region and translates to approximately 2.48 μl, which gives us a void fraction for the packed bed of 0.45 and a residence time of 3.72 seconds.

C.3 Bed occupancy distribution at different regions during dissolution of asphaltenes from porous media
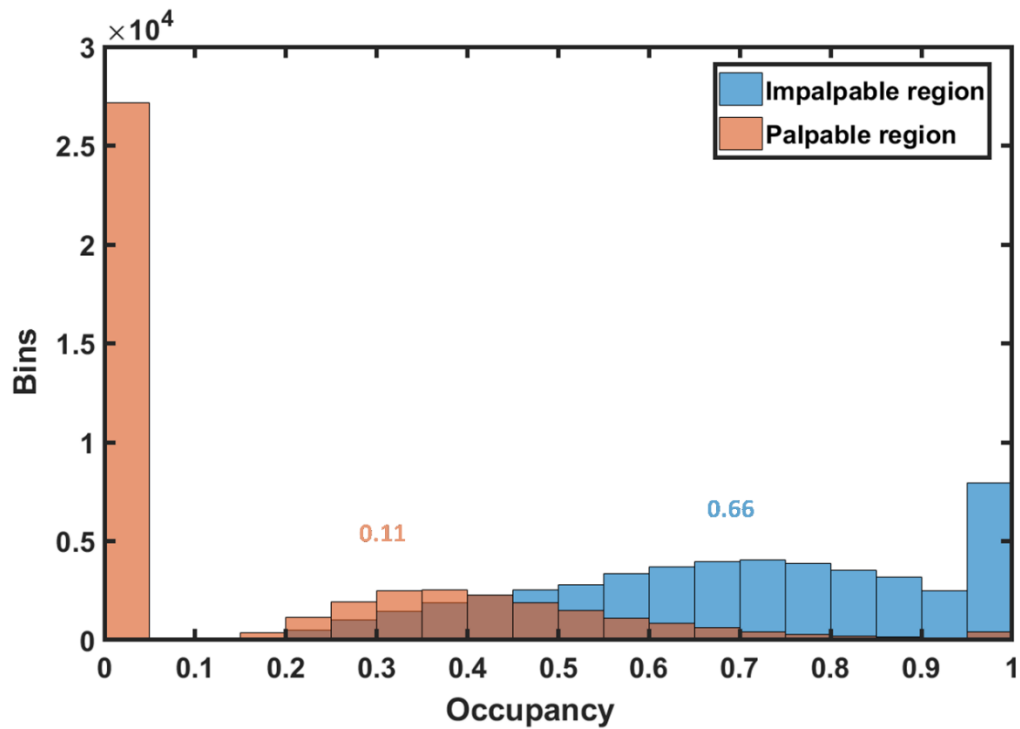
Figure C. 8 Histogram of bed occupancy at different regions on AUTO^3-μPBR.

C.4 Sheet size distribution of asphaltenes molecules at different regions
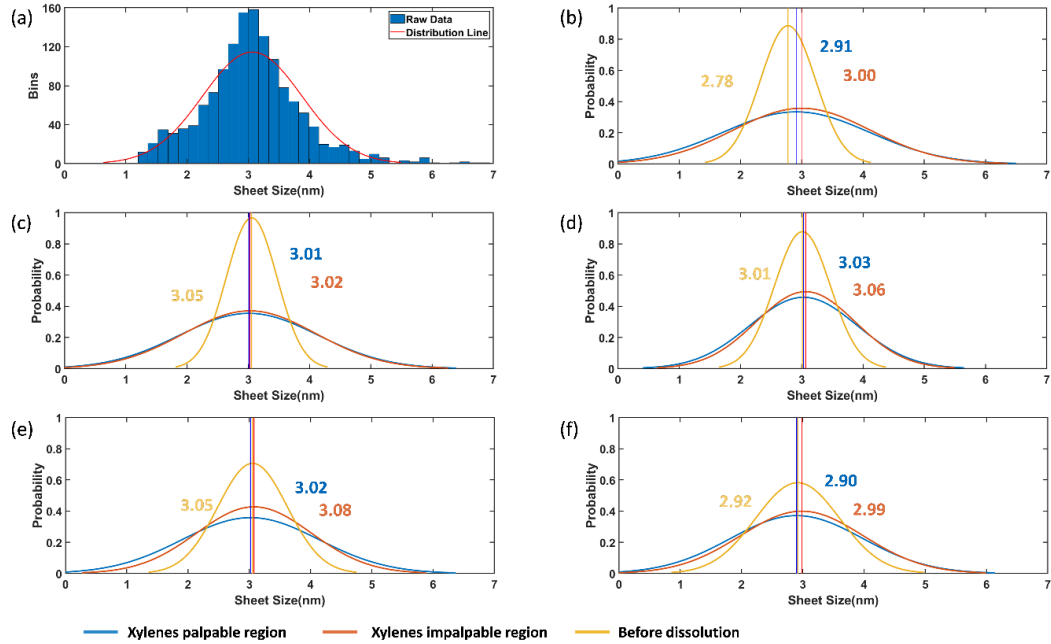
Figure C.9 (a) An example of histogram of sheet sizes at xylenes palpable region and its corresponding normalized distribution for Depo45. The normalized distribution of sheet size at xylenes palpable region, impalpable region, and before dissolution for (b) Depo25, (c) Depo35, (d) Depo45, (e) Depo 55, and (f) Depo 65.

Appendix D. MATLAB codes

The source codes of MATLAB for data analysis in asphaltenes study are summarized here. The origin versions of *main.m, Raman_analyzer.m, baseline_correction.m*, were developed by Dr. Pinho and used in the paper: Pinho, B., Minsariya, K., Yen, A., Joshi, N., and Hartman, R.L., Role of HZSM-5 Aluminosilicates on Asphaltenes Deposition by High-Throughput in Situ Characterizations of a Microreservoir, Energy Fuels, 2017, 31, 11640-11650.

D.1 Deconvolution of Raman spectra, calculation of bed occupancy and sheet size of asphaltenes

"Main.m"

Description: This code is used to import multiple Raman mapping data and apply universal deconvolution operation to each spectrum. Note that the universal deconvolution operation requires known fitting parameters, such as baseline correction, number of peaks, shape of peaks, and so on. The information of bed occupancy, sheet size and location are the results.

```
%% Initialize program
clc;
close all;
cd('Z:\...');
clear textprogressbar;  %Terminate progression bar
clear;
warning('off');
disp('///////////////////////////////////')
disp('U003 data analysis is starting')
disp('///////////////////////////////////')

%//////////////////////////////////////////////////////////////////
```

```matlab
%% Input parameters
Display_Raman='no';
offset_graph_Y=500; % Offset for a 2D graphic
Display_3D='no'; % Offset for a 3D graphic
Raman_shift_min=200;
Raman_shift_max=1800;
Raman_intensity_min=0;
Raman_intensity_max=6.5E4;
overexpovalue=35000; %% threshold value for over exposure
fiterrvalue=10; %% threshold value for not well fitting
if ispc
   Raman_chromatograme_path= {'Z:...'};
end
        folder={'2019-04-24'}; % Folder where the .spc files are located
       filenames={
          'example1.spc'
          'example2.spc'
          'example3.spc' };

%/////////////////////////////////////////////////////////////////////
%%   Raman processing
%%   Bulk deconvolution
n=size(filenames);
startvalue=1;

for h=1:n
   Raman_folder=folder;
   Raman_filename=filenames(h);
   [Raman_data] =
Raman_analyser(Display_3D,Raman_chromatograme_path,offset_graph_Y,Raman_filen
ame,Raman_folder,Raman_shift_min,Raman_shift_max,Raman_intensity_min,Raman_i
ntensity_max);

   [results,La,endvalue] =
deconvolution_function(startvalue,Raman_data,overexpovalue,fiterrvalue);

       for i=1:2353
             wq=i-1;
                 for q=1:7
                 total(startvalue+wq,q)=results(i,q);
                 end
                 for w=1:5
                 ss(startvalue+wq,w)=La(i,w);
                 end
       end
```

```
     startvalue=endvalue;
end
keepvars = {'total','ss'};
clearvars('-except', keepvars{:});
disp('[Operation complete]')


return;
```
"Raman_analyser.m"

Description: This function enables to read .spc file and import into MATLAB. In the

meantime, the Raman spectra could be plotted in 3D. The Raman spectra data is the

output.

```
function [Raman_data] =
Raman_analyser(Display_3D,chromatograme_path,offset_graph_Y,Raman_filename,Ra
man_folder,Raman_shift_min,Raman_shift_max,Raman_intensity_min,Raman_intensity
_max)

%//////////////////////////////////////////////////////////////////
current_directory=pwd;
Raman_data=struct('Name',{" "},'Spectrum',{" "});
for i=1:length(Raman_filename)

    if ispc
        temp=char(strcat(chromatograme_path,Raman_folder{i},'\',Raman_filename{i}));
    else
        temp =
        char(strcat(chromatograme_path,Raman_folder{i},'/',Raman_filename{i}));
    end
        Raman_data(i).Spectrum=GSSpcRead(temp,-1,'false');
%This file ("GSSpcRead.m") is part of GSTools.
%GSTools is free software: you can redistribute it and/or modify
%it under the terms of the GNU General Public License as published by
%the Free Software Foundation, either version 3 of the License, or
%(at your option) any later version.
%Copyright (c) 2004-2009, Kris De Gussem
%All rights reserved.

        Raman_data(i).Name=Raman_data(i).Spectrum.Name;
end

if isempty(Raman_data)
    disp(' ')
    disp('No Raman data in the date chosen')
else
```

```matlab
figure_width=8*2.5;
figure_height=6*4;
Ramanf = figure; clf;
%window configurations and properties of the graphic window
   set(Ramanf, 'units', 'centimeters', 'pos', [0 0 figure_width figure_height])
   set(Ramanf, 'PaperPositionMode', 'auto');
   set(Ramanf, 'Color', [1 1 1]); % Sets figure background
   set(Ramanf, 'Color', [1 1 1]); % Sets axes background
   set(Ramanf, 'Renderer', 'painters');
   grid on;
   j=0;

   if isempty(Raman_data(2).Name)
      cycle_loop=1;
   else
      cycle_loop=length(Raman_data);
   end

   for i=1:cycle_loop
       % Peak graph
       ax1=subplot(3,1,1:2);
       temp=strrep(char(Raman_data(i).Spectrum.Name),'_',' ');
       if strcmp(Display_3D,'Yes') || strcmp(Display_3D,'yes') ||
strcmp(Display_3D,'Y') || strcmp(Display_3D,'YES')
           number_spectrum(1:size(Raman_data(i).Spectrum.xaxis,2))=i;

           if isfield(Raman_data(1).Spectrum,'spectra')
           else
              plot3(Raman_data(i).Spectrum.xaxis, number_spectrum,
Raman_data(i).Spectrum.data,'DisplayName',temp);
           end

             view(26, 42)
           box on;
           hold all;
           clearvars number_spectrum;
           hTitle1= title ('Raman spectrum');
           hXLabel1=xlabel('Raman Shift (cm^{-1})');
           hZLabel1=zlabel('Intensity (counts)');
           axis([Raman_shift_min Raman_shift_max 0 cycle_loop
Raman_intensity_min Raman_intensity_max]);
        else

           if isfield(Raman_data(1).Spectrum,'spectra')
```

```matlab
            else
Raman_graph=plot(Raman_data(i).Spectrum.xaxis,Raman_data(i).Spectrum.data+offset_
graph_Y*i,'DisplayName',temp);
            end
            hold all;
            axis([Raman_shift_min Raman_shift_max Raman_intensity_min
Raman_intensity_max]);
            hTitle1= title ('Raman spectrum');
            hXLabel1=xlabel('Raman Shift (cm^{-1})');
            hYLabel1=ylabel('Intensity (counts)');
          end
      end
      Raman_legend=legend('show');
      plotbrowser('off');
      set(Raman_legend,'Position',[0.11 0.2 0.45 0.13]);
end

cd(current_directory);
end
```

"deconvolution_function.m"

Descrption: This function enables the deconvolution of single Raman mapping. The bed

occupancy and sheet size are calculated from the deconvolution results. The information

of bed occupancy, sheet size of asphaltenes, and location are the output.

```matlab
function
[results,ss,endvalue]=deconvolution_function(startvalue,Raman_data,oevalue,fevalue)

%///////////////////////////////////////////////////////////////////
    clc;
    close all;
    max_intensity=-10000000;
    min_intensity=10000000;
    center=1420;
    window=600;
    autozero=1;
    threholdvalue=oevalue; % threhold value for over exposure
    PeakFIT_DATA=struct('FitResults',{" "},'FitError',{" "},'Coef',{" "});
    clear textprogressbar;
    textprogressbar('Generating analysing the data: ');

%///////////////////////////////////////////////////////////////////
 %% Data deconvolution

for i=1:size(Raman_data(1).Spectrum.spectra,2)

    if mean(Raman_data(1).Spectrum.spectra(i).data)<threholdvalue
       pix(i)=1;

       if i==1;
        textprogressbar(round(i/size(Raman_data(1).Spectrum.spectra,2)*100));
       elseif mod(i,10)==0;
        textprogressbar(round(i/size(Raman_data(1).Spectrum.spectra,2)*100));
       end

signal=[Raman_data(1).Spectrum.spectra(1).xaxis;Raman_data(1).Spectrum.spectra(i).data];
       [xx,yy]=baseline_correction(signal,center,window,autozero);
       Raman_data(1).Spectrum.spectra(i).data_xbaseline=xx;
       Raman_data(1).Spectrum.spectra(i).data_ybaseline=yy;

       if max(yy)>max_intensity
        max_intensity=max(yy);
```

```matlab
        end

        if min(yy)<min_intensity
         min_intensity=min(yy);
        end

 [FitResults,FitError,baseline_temp,coeff]=peakfit(signal,1442.2714,545.1261,4,1,16,1,
[1324.7473    143.2665    1513.2709    186.7327    1594.1218    53.342111
1609.0294    26.407572], 1, [77.5], 1 ,0,1.1169,5.4513);
      % "peakfit.m" Copyright (c) 2015, Thomas C. O'Haver
      % For more details, see
      % http://terpconnect.umd.edu/~toh/spectrum/CurveFittingC.html and
      % http://terpconnect.umd.edu/~toh/spectrum/InteractivePeakFitter.html

      PeakFIT_DATA(i).FitResults=FitResults;
      PeakFIT_DATA(i).FitError=FitError;
      PeakFIT_DATA(i).Coef=coeff;

        if FitError<fevalue
           pix(i)=1;
        else
           pix(i)=-1;
        end

      else
         pix(i)=-2;
      end

        y_location(i)=Raman_data(1).Spectrum.spectra(i).ycoordinate;
        x_location(i)=Raman_data(1).Spectrum.spectra(i).xcoordinate;
end
    textprogressbar(100);
    textprogressbar(' ');
    x_location_temp=x_location;

%//////////////////////////////////////////////////////////////////////
%% Occupancy and sheet size calculation
    j=1;

    for i=1:size(Raman_data(1).Spectrum.spectra,2)
signal=[Raman_data(1).Spectrum.spectra(1).xaxis;Raman_data(1).Spectrum.spectra(i).da
ta];
      [xx,yy]=baseline_correction(signal,1442.2714,545.1261,1);
      area_asphaltenes(i,j)=simps(xx,yy);
%  "simps.m" -- Damien Garcia -- 08/2007, revised 11/2009
%  Website: http://www.biomecardio.com
```

- 249 -

```matlab
        [xx,yy]=baseline_correction(signal,460,60,1);
        area_quartz(i,j)=simps(xx,yy);

        if pix(i)==1
        pix(i)=area_asphaltenes(i,j)/(area_asphaltenes(i,j)+27.33*area_quartz(i,j));
        ss(i,j+4)=
4.96*PeakFIT_DATA(i).FitResults(3,5)/PeakFIT_DATA(i).FitResults(1,5);

            if pix(i)>1
                pix(i)=1;
            end

        end
        x_location_matrix(i,j)=x_location(i);
        y_location_matrix(i,j)=y_location(i);
        results(i,j)=x_location_matrix(i,j);
        results(i,j+1)=y_location_matrix(i,j);
        results(i,j+2)=x_location_matrix(i,j)/1000;
        results(i,j+3)=y_location_matrix(i,j)/1000;
        results(i,j+4)=area_asphaltenes(i,j);
        results(i,j+5)=area_quartz(i,j);
        results(i,j+6)=pix(i);
        ss(i,j)=x_location_matrix(i,j);
        ss(i,j+1)=y_location_matrix(i,j);
        ss(i,j+2)=x_location_matrix(i,j)/1000;
        ss(i,j+3)=y_location_matrix(i,j)/1000;
    end

    endvalue=startvalue+i;
end
```

"baseline_correction.m"

Descrption: This function enables the performance of baseline correction to single Raman

spectrum.

```matlab
function [xx,yy]=baseline_correction(signal,center,window,AUTOZERO)

%//////////////////////////////////////////////////////////////////
% format short g
format compact
warning off all
datasize=size(signal);

if datasize(1)<datasize(2)
    signal=signal';
end

datasize=size(signal);

if datasize(2)==1, %  'signal' is a vector; Must be peakfit(Y-vector)
    X=1:length(signal); % Create an independent variable vector
    Y=signal;
else
    % 'signal' is a matrix. Must be peakfit(DataMatrix)
    X=signal(:,1); % Split matrix argument
    Y=signal(:,2);
end
X=reshape(X,1,length(X)); % Adjust X and Y vector shape to 1 x n (rather than n x 1)
Y=reshape(Y,1,length(Y));
% If necessary, flip the data vectors so that X increases

if X(1)>X(length(X)),
    disp('X-axis flipped.')
    X=fliplr(X);
    Y=fliplr(Y);
End

xoffset=0;
k=0;
kk=0;

for i=1:length(X)

    if X(i)>center-window/2;
        k=1+k;
```

```matlab
        if k==1
            n1=i;
        end

    end

    if X(i)>center+window/2;
        kk=1+kk;

        if kk==1
            n2=i-1;
        end

    end

end

if window==0
    n1=1;n2=length(X)
end

xx=X(n1:n2)-xoffset;
yy=Y(n1:n2);
ShapeString='Gaussian';
coeff=0;
CLIPHEIGHT=max(Y);
LOGPLOT=0;
baseline=0;
bkgcoef=0;
bkgsize=round(length(xx)/10);

if bkgsize<2
    bkgsize=2;
end

lxx=length(xx);

if AUTOZERO==0, % Flat autozero operation
    XX1=xx(1:round(lxx/bkgsize));
    XX2=xx((lxx-round(lxx/bkgsize)):lxx);
    Y1=yy(1:(round(length(xx)/bkgsize)));
    Y2=yy((lxx-round(lxx/bkgsize)):lxx);
    yy=yy;
end

if AUTOZERO==1, % linear autozero operation
```

```matlab
   XX1=xx(1:round(lxx/bkgsize));
   XX2=xx((lxx-round(lxx/bkgsize)):lxx);
   Y1=yy(1:(round(length(xx)/bkgsize)));
   Y2=yy((lxx-round(lxx/bkgsize)):lxx);
   bkgcoef=polyfit([XX1,XX2],[Y1,Y2],1);  % Fit straight line to sub-group of points
   bkg=polyval(bkgcoef,xx);
   yy=yy-bkg;
end

if AUTOZERO==2, % Parabolic autozero operation
   XX1=xx(1:round(lxx/bkgsize));
   XX2=xx((lxx-round(lxx/bkgsize)):lxx);
   Y1=yy(1:round(length(xx)/bkgsize));
   Y2=yy((lxx-round(lxx/bkgsize)):lxx);
   bkgcoef=polyfit([XX1,XX2],[Y1,Y2],2);  % Fit parabola to sub-group of points
   bkg=polyval(bkgcoef,xx);
   yy=yy-bkg;
end

if AUTOZERO==3, % Quadratic autozero operation
   [M,I]=min(yy);

   if I>size(yy,2)-10
      background=mean(yy(I-10:I));
   elseif I<size(yy,2)+10
      background=mean(yy(I:I+10));
   else
      background=mean(yy(I-5:I+5));
   end

   yy=yy-background;
end

end
```

D.2 Time-dependent study of asphaltenes molecules at different regions during deposition and dissolution processes

"Compile_data.m"

Description: This code enables the compilation of all deconvoluted results and turn into a 3-dimension matrix.

```matlab
clc;
load ('Z:\...') % load deconvoluted data from folder

%//////////////////////////////////////////////////////////////////////
%% Deposition from Raw
totoccu = cat(3,total1,total2,total3);
[x,y,z] = size(totoccu);

for h = 1:z
    for i = 1:7
        for j = 1:(x/y)
                occu(j,i,h) = totoccu(((i-1)*2353)+j,y,h);
        end
    end
end

occu_1 = occu(:,:,1);
occu_2 = occu(:,:,2);
occu_3 = occu(:,:,3);
totss = cat(3,ss1,ss2,ss3);
[x,y,z] = size(totoccu);

for h = 1:z
    for i = 1:7
        for j = 1:(x/y)
                ss(j,i,h) = totss(((i-1)*2353)+j,y,h);
        end
    end
end

ss_1 = ss(:,:,1);
ss_2 = ss(:,:,2);
ss_3 = ss(:,:,3);

%//////////////////////////////////////////////////////////////////////
```

www.manaraa.com

```matlab
%% Dissolution from Raw
clc;
totoccu = cat(3,total1);   %input variable names
[x,y,z] = size(totoccu);

for h = 1:z
   for i = 1:7
      for j = 1:(x/7)
              occu(j,i,h) =  totoccu(((i-1)*2353)+j,y,h);
      end
   end
end
occu_1 = occu(:,:,1);
occu_2 = occu(:,:,2);
occu_3 = occu(:,:,3);
totss = cat(3,ss1);        % input variable names
[x,y,z] = size(totss);

for h = 1:z
   for i = 1:7
      for j = 1:(x/7)
              ss(j,i,h) =  totss(((i-1)*2353)+j,y,h);
      end
   end
end

ss_1 = ss(:,:,1);
ss_2 = ss(:,:,2);
ss_3 = ss(:,:,3);
totsat = cat(3,sat1);     %input variable names
[x,y,z] = size(totsat);

for h = 1:z
   for i = 1:7
      for j = 1:(x/7)
              sat(j,i,h) =  totsat(((i-1)*2353)+j,y,h);
      end
   end
end
sat_1 = sat(:,:,1);
sat_2 = sat(:,:,2);
sat_3 = sat(:,:,3);

%/////////////////////////////////////////////////////////////////////
%% Refined to 3d Matrix sheetsize
ss_25 = cat(3,ss_25_1,ss_25_2,ss_25_3);
```

- 255 -

```matlab
ss_35 = cat(3,ss_35_1,ss_35_2,ss_35_3);
ss_45 = cat(3,ss_45_1,ss_45_2,ss_45_3);
ss_55 = cat(3,ss_55_1,ss_55_2,ss_55_3);
ss_65 = cat(3,ss_65_1,ss_65_2,ss_65_3);
ss = cat(3,ss_25,ss_35,ss_45,ss_55,ss_65);
disp("Complete");


%////////////////////////////////////////////////////////////////////
%% Refined to 3d Matrix occupancy
occu_25 = cat(3,occu_25_1,occu_25_2,occu_25_3);
occu_35 = cat(3,occu_35_1,occu_35_2,occu_35_3);
occu_45 = cat(3,occu_45_1,occu_45_2,occu_45_3);
occu_55 = cat(3,occu_55_1,occu_55_2,occu_55_3);
occu_65 = cat(3,occu_65_1,occu_65_2,occu_65_3);
occu = cat(3,occu_25,occu_35,occu_45,occu_55,occu_65);
disp("Complete");


%////////////////////////////////////////////////////////////////////
%% Refined to 3d Matrix xyl
xyl_25 = cat(3,xyl_25_1,xyl_25_2,xyl_25_3);
xyl_35 = cat(3,xyl_35_1,xyl_35_2,xyl_35_3);
xyl_45 = cat(3,xyl_45_1,xyl_45_2,xyl_45_3);
xyl_55 = cat(3,xyl_55_1,xyl_55_2,xyl_55_3);
xyl_65 = cat(3,xyl_65_1,xyl_65_2,xyl_65_3);
xyl = cat(3,xyl_25,xyl_35,xyl_45,xyl_55,xyl_65);

disp("Complete");
```

"ultimate_analysis.m"

Description: This code enables the analysis of transient data from asphaltenes deposition

process. It could divide the porous media into different regions based on preset definition,

such as growing region and non-growing region. The bed occupancy and sheet size at

different regions are analyzed and plotted.

```matlab
%% Initialize program
clc;
clear;
load('Z:\...'); % load complied MATLAB data

%/////////////////////////////////////////////////////////////////////////
%% define of growing region and nongrowing region
tolerance=-0.03;
th_gr=3;
th_nongr=3;
temp=zeros(2353,7);

for i=1:15
   temp=occ(:,:,i);
[gr_region(:,i),nongr_region(:,i),time]=depo_region_analysis(tolerance,th_gr,th_nongr,temp);
   disp(strcat('>>>>>>',num2str(i/15*100),'% complete <<<<<<'));
end

for i=1:15
   for j=1:2353

     if isnan(gr_region(j,i))
        gr_region(j,i)=0;
     end

     if isnan(nongr_region(j,i))
        nongr_region(j,i)=0;
     end

   end
end

for i=1:15
   for j=1:7
   gr_ss(:,j)=gr_region(:,i).*SS(:,j,i);      %% growing region sheet size
```

- 257 -

```matlab
    non_ss(:,j)=nongr_region(:,i).*SS(:,j,i);   %% non growing region sheet size
    end

    if i>1
        ul_ss=cat(3,ul_ss,gr_ss);
        ulnon_ss=cat(3,ulnon_ss,non_ss);
    else
        ul_ss=cat(3,gr_ss);
        ulnon_ss=cat(3,non_ss);
    end

end

for i=1:15
subplot(4,4,i)
plot(time,ul_ss(:,:,i),'bo','LineStyle','no','MarkerSize',3);
hold on
plot(time,ulnon_ss(:,:,i),'ro','LineStyle','no','MarkerSize',3);
hold off
end

%/////////////////////////////////////////////////////////////////////////
 %% Location information mask

for i=1:2353

    if location(i,3)<0.99
        mask(i,1)=NaN;
    elseif location(i,3)>16.01
        mask(i,1)=NaN;
    else
        mask(i,1)=1;
    end

    if location(i,4)<0.09
        mask(i,2)=NaN;
    elseif location(i,4)>1.01
        mask(i,2)=NaN;
    else
        mask(i,2)=1;
    end

end

for i=1:15
    occ_filter(:,i)=occ(:,7,i).*mask(:,1).*mask(:,2);
```

- 258 -

```
      end
for h=1:15
  for i=1:13
    for j=1:181
       k=(i-1)*181+j;
       axial_location(j)=(j-1)*0.1;

       if isnan(occ_filter(k,h))
          occ_axial(i,j,h)=0;
       else
          occ_axial(i,j,h)=occ_filter(k,h);
       end

    end
  end
end


%//////////////////////////////////////////////////////////////////////////
%% Alignment and axial direction occupancy

for j=1:15
 for i=11:161
   h=i-10;
   direc_occ1(j,h)=sum(occ_axial(:,i,j));
   reactor_loc(h)=axial_location(i);
 end
end

segment=10;
k=round(151/segment);

for x=1:15
  for i=1:k
    diss(x,i)=0;
    xlocation(i)=(segment/2+(i-1)*segment)/10;

    for j=1:segment
       h=(i-1)*segment+j;
      diss(x,i)=diss(x,i)+direc_occ1(x,h);
    end

  end
end

figure,
n=[2,6,8,12,15];
```

```matlab
for j=1:5
plot(xlocation,diss(n(j),:));
hold on
end

xlabel('Xlocation (mm)');
ylabel('Total occupancy at axial direction');
axis([0 16 0 100]);

%/////////////////////////////////////////////////////////////////
%% Mean value occupancy

for i=1:15
    for j=1:7
        for k=1:2353

            if occ(k,j,i)<0
                occ(k,j,i)=NaN;
            elseif occ(k,j,i)>1
                occ(k,j,i)=NaN;
            end

        end
    end
end

for i=1:15
    for j=1:7
        av_occ(j,i)=nanmean(occ(:,j,i));
    end
end

%/////////////////////////////////////////////////////////////////
%% Mean values sheet size
for i=1:15
    for j=1:7
        for k=1:2353

            if ul_ss(k,j,i)<1.2
                ul_ss(k,j,i)=NaN;
            elseif ul_ss(k,j,i)>7.6
                ul_ss(k,j,i)=NaN;
            end

            if ulnon_ss(k,j,i)<1.2
```

```
        ulnon_ss(k,j,i)=NaN;
      elseif ulnon_ss(k,j,i)>7.6
        ulnon_ss(k,j,i)=NaN;
      end


    end
  end
end

mean_temp_ss = zeros(2353,15);
mean_temp_nonss = zeros(2353,15);

for i = 1:15
  mean_temp_ss(:,i) = ul_ss(:,7,i);
  mean_temp_nonss(:,i) = ulnon_ss(:,7,i);
  for j = 1:2353

    if mean_temp_ss(j,i) == 0
      mean_temp_ss(j,i) = NaN;
    end

    if mean_temp_nonss(j,i) == 0
      mean_temp_nonss(j,i) = NaN;
    end

  end
end

for i = 1:5
  tot_mean_ss(:,i) = vertcat(mean_temp_ss(:,(i-1)*3 + 1),mean_temp_ss(:,(i-1)*3 +
2),mean_temp_ss(:,(i-1)*3 + 3));
  tot_mean_nonss(:,i) = vertcat(mean_temp_nonss(:,(i-1)*3 + 1),mean_temp_nonss(:,(i-
1)*3 + 2),mean_temp_nonss(:,(i-1)*3 + 3));
  total_mean_ss(i) = nanmean(tot_mean_ss(:,i));
  total_mean_nonss(i) = nanmean(tot_mean_nonss(:,i));
  error_bar_ss(i) = nanstd(tot_mean_ss(:,i));
  error_bar_nonss(i) = nanstd(tot_mean_nonss(:,i));
end

%////////////////////////////////////////////////////////////////////
%% Bar graph of sheet size results at diffferent regions
count_ss = [1 2 3 4 5];
bar([total_mean_ss(:),total_mean_nonss(:)]);
hold on
er = errorbar(count_ss - 0.15,total_mean_ss,error_bar_ss,error_bar_ss);
er.Color = [0 0 0];
```

- 261 -

```
er.LineStyle = 'none';
er = errorbar(count_ss + 0.15,total_mean_nonss,error_bar_nonss,error_bar_nonss);
er.Color = [0 0 0];
er.LineStyle = 'none';
set(gca,'xticklabel',{'25C', '35C', '45C', '55C', '65C'});
ylabel('Sheet Size(nm)');
legend('Deposition Growing Region','Deposition Non-growning Region');
hold off
total_mean_ssdepo = total_mean_ss;
totam_mean_nonssdepo = total_mean_nonss;
error_bar_ssdepo = error_bar_ss;
error_bar_nonssdepo = error_bar_nonss;
clearvars -except total_mean_ssdepo total_mean_nonssdepo error_bar_ssdepo
error_bar_nonssdepo

return
```

"depo_region_analysis.m"

Description: This function enables the identification of locations, analysis the bed occupancy and sheet size information at asphaltenes growing region and non-growing region. In the meantime, the results will be plotted.

```matlab
function
[adlocation,nongrlocation,time]=depo_region_analysis(tolerance,th_gr,th_nongr,occ)

%///////////////////////////////////////////////////////////////////
%% filter ==> -1,-2 to NaN

for i=1:7
   for j=1:2353

      if occ(j,i)<0
         occ(j,i)=NaN;
      elseif occ(j,i)>1
         occ(j,i)=NaN;
      end

      time(j,i)=(0.5247*j+(i-1)*20.58*60)/60;
      region_gr(j,i)=NaN;
      region_nongr(j,i)=NaN;
      jcc(j,i)=occ(j,i);

   end
end
%///////////////////////////////////////////////////////////////////
%% identify growing region vs. non-growing region
ads=0;
bbs=0;

for i=1:2353;
   count=0;
   discount=0;
      for j=1:5
         a=occ(i,j);
         b=occ(i,j+1);

         if isnan(a)
            a=b;
         else
            k=j+1;
```

```matlab
        for h=k:6
            if isnan(b)
             k=k+1;
             b=occ(k);
            end
        end

        if isnan(b)
        else
            if a<b+tolerance
                count=count+1;
            else
                discount=discount+1;
            end
        end

    end

    end

    if count>th_gr
        region_gr(i,:)=occ(i,:);
        ads=ads+1;
        adlocation(i,1)=1;
    else
        adlocation(i,1)=NaN;
    end

    if discount>th_nongr
        region_nongr(i,:)=occ(i,:);
        nongrlocation(i,1)=1;
        bbs=bbs+1;
    else
        nongrlocation(i,1)=NaN;
    end

    per=num2str(i/2353*100);
    disp(strcat('>>>>>>>>>',per,'%
Complete','<<<<<<<<',num2str(ads),',',num2str(bbs)));
end

%/////////////////////////////////////////////////////////////////
%% plot of results
subplot(1,3,1)

for i=1:2353
```

```matlab
    plot(time(i,:),region_gr(i,:),'bo','LineStyle','no');
    hold on
end
xlabel('Time(min)');
ylabel('Occupancy');
axis([0 120 0.5 1]);
subplot(1,3,2)

for i=1:2353
    plot(time(i,:),region_nongr(i,:),'bo','LineStyle','no');
    hold on
end

xlabel('Time(min)');
ylabel('Occupancy');
axis([0 120 0.5 1]);
subplot(1,3,3)

for i=1:2353
    plot(time(i,:),jcc(i,:));
    hold on
end

xlabel('Time(min)');
ylabel('Occupancy');
axis([0 120 0.5 1]);

end
```

"ultimate_analysis_dissolution.m"

Description: This code enables the analysis of transient data from asphaltenes dissolution process. It could divide the porous media into different regions based on preset definition, such as xylene palpable region and impalpable region. The bed occupancy and sheet size at different regions are analyzed and plotted.

```matlab
%///////////////////////////////////////////////////////////////////
clc;
clear;
load('Z:\...') %%% load complied MATLAB data
%% Data analysis

for i=1:15
[loc_xyl(:,:,i),loc_nonxyl(:,:,i),occ_xyl(:,:,i),occ_nonxyl(:,:,i),ss_xyl(:,:,i),ss_nonxyl(:,:,i),
time]=dissolution_sat_analysis(occu(:,:,i),ss(:,:,i),xyl(:,:,i),location);
disp(strcat('>>>>>>>>>',num2str(i/15*100),'% complete','<<<<<<<<<<'));
end

%///////////////////////////////////////////////////////////////////
%% Filter of location

for i=1:2353

    if location(i,3)<0.99
       mask(i,1)=NaN;
    elseif location(i,3)>16.01
       mask(i,1)=NaN;
    else
       mask(i,1)=1;
    end

    if location(i,4)<0.09
       mask(i,2)=NaN;
    elseif location(i,4)>1.01
       mask(i,2)=NaN;
    else
       mask(i,2)=1;
    end

end

%///////////////////////////////////////////////////////////////////
```

```matlab
%% x ==> xylene percentage  ,  y ==> average occupancy
for i=1:15
  for j=1:7
    for k=1:2353

      if occu(k,j,i)<0
          occu(k,j,i)=NaN;
      elseif occu(k,j,i)>1
          occu(k,j,i)=NaN;
      end

    end
  end
end

for i=1:15
  for j=1:7
    x(i,j)=nansum(xyl(:,j,i).*mask(:,1).*mask(:,2))/1661;
    y(i,j)=nanmean(occu(:,j,i).*mask(:,1).*mask(:,2));
    error(i,j) = nanstd(occu(:,j,i).*mask(:,1).*mask(:,2));
  end
end

%//////////////////////////////////////////////////////////////////
%% Plot xylenes distribution and final average occupancy
time = 7;
sat25 = x(1:3,6);
sat35(:) = x(4:6,6);
sat45(:) = x(7:9,6);
sat55(:) = x(10:12,6);
sat65(:) = x(13:15,6);
occu25 = y(1:3,time);
occu35(:) = y(4:6,time);
occu45(:) = y(7:9,time);
occu55(:) = y(10:12,time);
occu65(:) = y(13:15,time);
errorloc = [sat25,sat35,sat45,sat55,sat65];
errorlocy = [occu25,occu35,occu45,occu55,occu65];
error25 = error(1:3,time);
error35(:) = error(4:6,time);
error45(:) = error(7:9,time);
error55(:) = error(10:12,time);
error65(:) = error(13:15,time);
error_bars = [error25,error35,error45,error55,error65];
plot(sat25,occu25,'bo','MarkerFaceColor','b');
hold on
```

```matlab
plot(sat35,occu35,'gs','MarkerFaceColor','g');
plot(sat45,occu45,'k^','MarkerFaceColor','k','LineStyle','no');
plot(sat55,occu55,'rd','MarkerFaceColor','r','LineStyle','no');
plot(sat65,occu65,'mh','MarkerFaceColor','m','LineStyle','no');
axis([0 0.7 0 1])
er = errorbar(errorloc,errorlocy,error_bars,error_bars);
er.Color = [0 0 0];
er.LineStyle = 'none';
xlabel('Xylenes distribution percentage');
ylabel('Final dissolution occupancy');
legend('Depo25','Depo35','Depo45','Depo55','Depo65','Location','SouthEast');
hold off

%/////////////////////////////////////////////////////////////////////
%%% axial direction occupancy

for i=1:15
    occu_axial(:,i)=occu(:,7,i).*mask(:,1).*mask(:,2);
end

 for i=1:13
    for j=1:181
        k=(i-1)*181+j;
        location(j)=(j-1)*0.1;

        if isnan(total(k))
            occ(i,j)=0;
        else
            occ(i,j)=total(k);
        end

    end
end

%/////////////////////////////////////////////////////////////////////
%%% Sheet size distribution at different region
mean_temp_ss = zeros(2353,15);
mean_temp_nonss = zeros(2353,15);

for i = 1:15
    mean_temp_ss(:,i) = ss_xyl(:,1,i);
    mean_temp_nonss(:,i) = ss_nonxyl(:,1,i);
    for j = 1:2353

        if or(mean_temp_ss(j,i)<1.2,mean_temp_ss(j,i)>7.6)
            mean_temp_ss(j,i) = NaN;
```

- 268 -

```matlab
        end

        if or(mean_temp_nonss(j,i)<1.2,mean_temp_nonss(j,i)>7.6)
            mean_temp_nonss(j,i) = NaN;
        end

    end
end

for i = 1:5
    tot_mean_ss(:,i) = vertcat(mean_temp_ss(:,(i-1)*3 + 1),mean_temp_ss(:,(i-1)*3 +
2),mean_temp_ss(:,(i-1)*3 + 3));
    tot_mean_nonss(:,i) = vertcat(mean_temp_nonss(:,(i-1)*3 + 1),mean_temp_nonss(:,(i-
1)*3 + 2),mean_temp_nonss(:,(i-1)*3 + 3));
    total_mean_ss(i) = nanmean(tot_mean_ss(:,i));
    total_mean_nonss(i) = nanmean(tot_mean_nonss(:,i));
    error_bar_ss(i) = nanstd(tot_mean_ss(:,i));
    error_bar_nonss(i) = nanstd(tot_mean_nonss(:,i));
    total_mean(i) = nanmean(total(:,i));
end

for i = 1:5
    figure
    h = histfit(tot_mean_ss(:,i));
    h1 = h(2,1).YData;
    h2 = h(2,1).XData;
    h3 = h1/trapz(h2,h1);
    hold on
    g = histfit(tot_mean_nonss(:,i));
    g1 = g(2,1).YData;
    g2 = g(2,1).XData;
    g3 = g1/trapz(g2,g1);
    k = histfit(tot(:,i));
    k1 = k(2,1).YData;
    k2 = k(2,1).XData;
    k3 = k1/trapz(k2,k1);
    xlabel('Sheet Size(nm)');
    ylabel('Bins');
    hold off
    figure
    alpha = plot(h2,h3,g2,g3,k2,k3);
    xlabel('Sheet Size(nm)');
    ylabel('Probability');
    axis([0 7 0 1]);
    ax = gca;
    set(alpha,'linewidth',3);
```

```matlab
        set(ax,'fontweight','bold','fontsize',24,'linewidth',2);
        set(gcf,'position',[10 10 550 400]);
        hold on
        palp = vline([mean(h2) mean(g2) mean(k2)] ,{'b','r','y'});
        set(palp,'linewidth',1);
        hold off
end

figure
histfit(tot_mean_nonss(:,3))
xlabel('Sheet Size(nm)');
ylabel('Bins');
legend('Raw Data','Distribution Line')
interval = 0.09;
count_ss = [1 2 3 4 5];

return
```

"dissolution_sat_analysis.m"

Description: This function enables the identification of locations, analysis the bed occupancy and sheet size information at xylenes palpable region and impalpable region. In the meantime, the results will be plotted.

```
function
[loc_xyl,loc_nonxyl,occ_xyl,occ_nonxyl,ss_xyl,ss_nonxyl,time]=dissolution_sat_analysis(occ,ss,xyl,location)

%///////////////////////////////////////////////////////////////////////
%% filter ==> -1,-2 to NaN

for i=1:7
    for j=1:2353

        if occ(j,i)<0
            occ(j,i)=NaN;
        elseif occ(j,i)>1
            occ(j,i)=NaN;
        end

        if isnan(xyl(j,i))
            anti_xyl(j,i)=1;
        else
            anti_xyl(j,i)=NaN;
        end

        time(j,i)=(0.5247*j+(i-1)*20.58*60)/60;
        if ss(j,i)<1.2
            ss(j,i)=NaN;
        elseif ss(j,i)>7.6
            ss(j,i)=NaN;
        end

    end
end

%///////////////////////////////////////////////////////////////////////
%% Filter of location

for i=1:2353

    if location(i,3)<0.99
```

```matlab
        mask(i,1)=NaN;
    elseif location(i,3)>16.01
        mask(i,1)=NaN;
    else
        mask(i,1)=1;
    end

    if location(i,4)<0.09
        mask(i,2)=NaN;
    elseif location(i,4)>1.01
        mask(i,2)=NaN;
    else
        mask(i,2)=1;
    end

end

%/////////////////////////////////////////////////////////////////////////
%% location of xylenes/non-xylenes
figure

for i=1:6
    loc_xyl(:,1)=xyl(:,i).*location(:,3).*mask(:,1).*mask(:,2); % xlocation
    loc_xyl(:,2)=xyl(:,i).*location(:,4).*mask(:,1).*mask(:,2); % ylocation
    loc_nonxyl(:,1)=anti_xyl(:,i).*location(:,3).*mask(:,1).*mask(:,2); % xlocation
    loc_nonxyl(:,2)=anti_xyl(:,i).*location(:,4).*mask(:,1).*mask(:,2); % ylocation
    subplot (2,3,i)
    plot(loc_xyl(:,1),loc_xyl(:,2));
    title('Location of Xylenes');
end

%/////////////////////////////////////////////////////////////////////////
%% occupancy of xylenes/non-xylenes
figure

for i=1:6
    occ_xyl(:,i)=xyl(:,i).*occ(:,i).*mask(:,1).*mask(:,2); % xlocation
    occ_nonxyl(:,i)=anti_xyl(:,i).*occ(:,i).*mask(:,1).*mask(:,2); % xlocation
    subplot (2,3,i)
    histogram(occ_xyl);
    hold on
    histogram(occ_nonxyl);
    hold off
    title('Occupancy');
end
```

```matlab
%////////////////////////////////////////////////////////////////////////
%%% sheetsize of asphaltenes at xylenes palpable/xylenes impalpable regions
figure

for i=1:6
    ss_xyl(:,1)=xyl(:,i).*ss(:,i).*mask(:,1).*mask(:,2);
    ss_nonxyl(:,1)=anti_xyl(:,i).*ss(:,i).*mask(:,1).*mask(:,2);
    a(i)=nanmean(ss_xyl);
    b(i)=nanmean(ss_nonxyl);
    subplot (2,3,i)
    histogram(ss_xyl);
    hold on
    histogram(ss_nonxyl);
    hold off
    diff(i)=b(i)-a(i);
    title ('Sheet Size');
end

    ss_xyl(:,1)=xyl(:,6).*ss(:,7).*mask(:,1).*mask(:,2);
    ss_nonxyl(:,1)=anti_xyl(:,6).*ss(:,7).*mask(:,1).*mask(:,2);
    c=nanmean(ss_xyl);
    d=nanmean(ss_nonxyl);
    figure
    histogram(ss_xyl);
    hold on
    histogram(ss_nonxyl);
    hold off
    title('Dry bed')

end
```